

**Synergies between Effective Field Theories: Global analyses  
of the Minimal Flavour Violating SMEFT and subleading  
NLO analysis of  $b \rightarrow s\gamma$  transitions**

*Dissertation*  
*zur Erlangung des Grades*  
*„Doktor der Naturwissenschaften“*

am Fachbereich Physik, Mathematik und Informatik  
der Johannes Gutenberg-Universität Mainz



JOHANNES GUTENBERG  
UNIVERSITÄT MAINZ

**Riccardo Bartocci**  
geboren in Ancona (Italien)

Mainz, 2025

This work is licensed under the Creative Commons Attribution 4.0 International License  
(CC-BY-4.0).

**Synergies between Effective Field Theories: Global analyses  
of the Minimal Flavour Violating SMEFT and subleading  
NLO analysis of  $b \rightarrow s\gamma$  transitions**

**Betreuer und erster Gutachter:** Prof. Dr. Tobias Hurth  
**Zweiter Gutachter:** Prof. Dr. Stefan Weinzierl  
**Tag der mündlichen Prüfung:** 21. Januar 2026  
**Prüfungsvorsitz:** Prof. Dr. Van Loock

**Prüfungskommission:**

Prof. Dr. Tobias Hurth  
Prof. Dr. Stefan Weinzierl  
Prof. Dr. Sebastian Böser  
Prof. Dr. Friederike Schmid



# Abstract

The Standard Model (SM) of particle physics, despite its remarkable predictive power, is widely recognised as incomplete. Effective Field Theories (EFTs) provide a systematic framework to explore physics beyond the SM, both through searches for new heavy particles within the Standard Model Effective Field Theory (SMEFT) and through precision studies at low energy using the Soft-Collinear Effective Theory (SCET). A central theme of this thesis is the consistent inclusion of higher-order effects, specifically Next-to-Leading Order (NLO) corrections and Renormalisation Group Evolution (RGE), which are essential for achieving reliable theoretical predictions and for connecting different energy scales. In the SMEFT part of this work, I developed and critically assessed a global analysis that combines theoretical and experimental information across multiple observables. Unlike purely data-driven approaches, this analysis was performed within a flavour-symmetric UV-inspired framework. Building on this foundation, I systematically incorporated NLO corrections and RGE effects, showing their significant impact on Wilson coefficient determinations, their correlations, and ultimately the interpretation of new physics constraints. In the flavour-physics sector, I investigated the inclusive decay  $\bar{B} \rightarrow X_s \gamma$  within SCET. In this context, I focused on the non-local contributions, which appear only at the NLO in  $1/m_b$ , and currently constitute one of the largest sources of uncertainty in this inclusive decay rate. In particular, the numerically dominant non-local contribution arises from the interference of the two electroweak operators  $Q_1^q$  and  $Q_{7\gamma}$ . To this end, I computed previously unknown  $\mathcal{O}(\alpha_s)$  corrections to the functions entering the factorisation theorem of this non-local contribution. Important advances include the determination and analysis of the RGE of the non-perturbative soft function  $g_{17}$ , enabling the resummation of large logarithms, as well as the computation of the NLO (two-loop)  $\bar{n}$ -jet function. These technically demanding calculations not only improve the theoretical predictions but also provide novel insights into the structure of SCET factorisation. Together, these results significantly enhance the precision and scope of EFT analyses, both in constraining new physics through global fits and in improving the precision of key flavour observables predictions.



# Zusammenfassung

Das Standardmodell (SM) der Teilchenphysik gilt trotz seiner bemerkenswerten Vorhersagekraft weithin als unvollständig. Effektive Feldtheorien (EFTs) bieten einen systematischen Rahmen, um Physik sowohl innerhalb als auch jenseits des SM zu erforschen, durch die Suche nach neuen schweren Teilchen innerhalb der Standard Model Effective Field Theory (SMEFT) oder durch Präzisionsuntersuchungen bei niedrigen Energien mithilfe der Soft-Collinear Effective Theory (SCET). Ein zentrales Thema dieser Arbeit ist die konsistente Berücksichtigung höherer Ordnungen, insbesondere der Next-to-Leading Order (NLO)-Korrekturen und der Renormierungsgruppenevolution (RGE). Diese sind für zuverlässige theoretische Vorhersagen und die konsistente Verknüpfung verschiedener Energieskalen unverzichtbar. Im SMEFT-Teil dieser Arbeit habe ich eine globale Analyse, die theoretische und experimentelle Informationen mehrerer Observablen kombiniert, entwickelt und kritisch analysiert. Im Gegensatz zu rein datengetriebenen Ansätzen wurde diese Analyse in einem UV-inspirierten, flavoursymmetrischen Kontext durchgeführt. Aufbauend darauf habe ich systematisch NLO-Korrekturen und RGE-Effekte einbezogen und gezeigt, dass sie einen erheblichen Einfluss auf die Bestimmung der Wilson-Koeffizienten, deren Korrelationen und letztlich auf die Interpretation von Beschränkungen neuer Physik haben. Im Bereich der Flavour-Physik habe ich den inklusiven Zerfall  $\bar{B} \rightarrow X_s \gamma$  mit Hilfe der SCET untersucht. Ich habe mich hierbei auf die nichtlokalen Beiträge konzentriert. Sie treten erst in nächstführender Ordnung in  $1/m_b$  auf und gehören momentan zu den größten Unsicherheiten in der inklusiven Zerfallsrate. Der numerisch wichtigste nichtlokale Beitrag resultiert aus der Interferenz der beiden elektroschwachen Operatoren  $Q_1^q$  und  $Q_{7\gamma}$ . Hierzu habe ich deshalb zuvor unbekannte  $\mathcal{O}(\alpha_s)$ -Korrekturen zu den Funktionen, die in das Faktorisierungstheorem dieses nichtlokalen Beitrags eingehen, berechnet. Wichtige Fortschritte umfassen die Bestimmung und Analyse der RGE der nichtperturbativen Soft-Funktion  $g_{17}$ , die die Aufsummierung großer Logarithmen ermöglicht, sowie die Berechnung der NLO- (Zwei-Schleifen-)  $\bar{n}$ -Jetfunktion. Diese technisch anspruchsvollen Rechnungen verbessern nicht nur die theoretischen Vorhersagen, sondern liefern auch neue Einblicke in die Struktur der SCET-Faktorisierung. Zusammengefasst erweitern die vorliegenden Ergebnisse die Präzision und Reichweite von EFT-Analysen, sowohl bei der Einschränkung neuer Physik durch globale Fits als auch bei der Verbesserung der Vorhersagen zentraler Flavour-Observablen.



# Contents

<b>Preface</b>	<b>xiii</b>
<b>1 The State of the Standard Model</b>	<b>1</b>
1.1 The Standard Model of Particle Physics . . . . .	1
1.2 Flavour Physics: Probing the Standard Model with Low Energy Observables	4
1.3 Collider Physics: Probing the Standard Model with High Energy Observables	5
<b>2 Effective Field Theories</b>	<b>9</b>
2.1 Effective Field Theories: A General Framework . . . . .	9
2.2 The Weak Effective Theory . . . . .	12
2.3 The Standard Model Effective Field Theory . . . . .	15
2.4 The Heavy Quark Effective Theory . . . . .	18
2.5 The Soft-Collinear Effective Theory . . . . .	20
<b>I Global Analyses of the <i>Minimal</i> MFV SMEFT</b>	<b>25</b>
<b>3 Introduction to Global Analyses</b>	<b>27</b>
3.1 The Importance of Global Analyses in the SMEFT . . . . .	27
3.2 Present Status of Global Analyses . . . . .	28
3.3 Statistical Framework of Global Analyses in the SMEFT . . . . .	31
3.4 Input Schemes in the SMEFT . . . . .	32
<b>4 Global Analysis at LO</b>	<b>35</b>
4.1 The <i>Minimal</i> MFV SMEFT . . . . .	35
4.2 Experimental Input . . . . .	36
4.2.1 Electroweak Precision Observables . . . . .	36
4.2.2 Higgs and Electroweak Boson Observables . . . . .	37
4.2.3 Top Observables . . . . .	38
4.2.4 Parity Violation Experiments and Lepton Scattering . . . . .	38
4.2.5 Drell-Yan Observables . . . . .	38
4.2.6 Flavour Observables . . . . .	38
4.3 Dijets+ $\gamma$ Production . . . . .	39
4.4 LO Results . . . . .	40

<b>5</b>	<b>Global Analysis with NLO Contributions</b>	<b>43</b>
5.1	SMEFT Predictions at NLO . . . . .	43
5.1.1	EWPO . . . . .	43
5.1.2	Top . . . . .	44
5.1.3	Higgs . . . . .	44
5.2	Comparison Between LO and NLO Results . . . . .	44
5.3	Interplay and Correlations . . . . .	46
5.3.1	EWPO and PVE Datasets . . . . .	49
5.3.2	Drell-Yan, PVE and Flavour Datasets . . . . .	50
5.3.3	Top, Flavour and Dijet Datasets . . . . .	52
<b>6</b>	<b>RGE Improved Global Analysis</b>	<b>55</b>
6.1	Inclusion of the RGE . . . . .	56
6.2	The Impact of RGE on the Global Analysis . . . . .	59
6.2.1	Operators Contributing to EWPO at LO . . . . .	60
6.2.2	Four-Lepton Operators . . . . .	62
6.2.3	Higgs Sector . . . . .	62
6.2.4	Semileptonic Operators . . . . .	63
6.2.5	Four-Quark Operators . . . . .	64
<b>7</b>	<b>Conclusion of Part I</b>	<b>67</b>
<b>II</b>	<b>NLO Analysis of the <math>Q_1^q - Q_{7\gamma}</math> Interference in <math>\bar{B} \rightarrow X_s \gamma</math> at Subleading Power</b>	<b>69</b>
<b>8</b>	<b>Introduction to <math>\bar{B} \rightarrow X_s \gamma</math> at Subleading Power</b>	<b>71</b>
8.1	Motivations . . . . .	71
8.2	The Factorisation Formula . . . . .	74
8.3	The Known Functions at NLO: $H$ and $J^{(n)}$ . . . . .	75
8.3.1	The Hard Function at NLO . . . . .	75
8.3.2	The $n$ -Jet Function at NLO . . . . .	78
<b>9</b>	<b>RGE of the Shape Function <math>g_{17}</math></b>	<b>79</b>
9.1	UV Singularities of $\mathcal{O}_{17}$ . . . . .	80
9.1.1	Abelian Contributions . . . . .	83
9.1.2	Non-Abelian Contributions . . . . .	86
9.1.3	Cut Diagrams and the Relevance of $\Delta Z_{17}$ . . . . .	89
9.2	Analytic Solution to the Renormalisation-Group Equation . . . . .	91
9.2.1	Abelian Part . . . . .	92
9.2.2	Non-Abelian Part . . . . .	94
9.2.3	Phenomenological Implications . . . . .	95
9.3	The Exclusive Counterpart $\Phi_G$ . . . . .	98
9.3.1	Anomalous Dimension . . . . .	99
9.3.2	Solution to the “Reduced” RG Equation . . . . .	101
9.3.3	Phenomenological Implications . . . . .	103

---

<b>10 The <math>\bar{n}</math>-Jet Function at NLO</b>	<b>107</b>
10.1 The $\bar{n}$ -Jet Function at One Loop . . . . .	107
10.1.1 Massless Amplitude at LO . . . . .	108
10.1.2 Massive Amplitude at LO . . . . .	111
10.1.3 Massless $u$ -Dependent Amplitude at LO . . . . .	112
10.1.4 Massive $u$ -Dependent Amplitude at LO . . . . .	115
10.2 The $\bar{n}$ -Jet Function at Two Loops . . . . .	116
10.3 Full $u$ -Dependence of the $\bar{n}$ -Jet Function at NLO . . . . .	124
<b>11 Cancellation of Singularities among the NLO-Improved Functions</b>	<b>131</b>
<b>12 Conclusion of Part II</b>	<b>135</b>
<b>Epilogue</b>	<b>137</b>
<b>Appendices</b>	<b>141</b>
A Observables . . . . .	141
B Numerical Results for Chapters 4 and 5 . . . . .	145
C Numerical Results for Chapter 6 . . . . .	147
D Evanescent Operators in the BBL Basis . . . . .	150
E Results for the Finite Terms of the $u$ -Dependent $\bar{n}$ -Jet Function . . . . .	151
F Details and Results for the Computation of Master Integrals . . . . .	152



# Preface

The Standard Model (SM) of fundamental interactions stands as one of the most successful theories in modern physics, having been confirmed with remarkable precision by a vast array of experiments. Nevertheless, despite its extraordinary predictive power, it is widely recognised that the SM cannot be the ultimate theory of nature. There are both theoretical motivations and phenomenological indications that point to the necessity of extending the SM, in order to account for phenomena currently unexplained and to address conceptual limitations inherent in the model itself.

In the landscape of particle physics, two complementary approaches have emerged to investigate physics beyond the SM. The first is a direct approach, which seeks to discover new particles or interactions at high energies, typically accessible at large particle accelerators. The second is an indirect approach, which aims at improving the precision of suitable SM predictions, thereby enabling the identification of subtle deviations from experimental data that may signal new physics effects even in the absence of direct evidence. Although different in methodology, these two strategies are deeply interconnected and mutually reinforcing. In this thesis, both the high- and low-energy approaches are analysed and discussed.

A common and fundamental tool in both these strategies is the use of Effective Field Theories (EFTs). EFTs provide a systematic framework to separate energy scales relevant to the physical problem, allowing a controlled exploration of new physics effects or higher order corrections in a given process. For example, they offer a coherent theoretical setting for analysing beyond the SM signals via higher-dimensional operators, as in the Standard Model Effective Field Theory (SMEFT), as well as for performing high-precision calculations at lower energy scales, such as those involving soft and collinear dynamics within the Soft-Collinear Effective Theory (SCET).

Within the EFT framework, corrections beyond the leading order play a crucial role. In particular, Next-to-Leading Order (NLO) corrections in the strong and electroweak coupling constants, together with the Renormalisation Group Evolution (RGE), are essential to ensure reliable theoretical predictions and to correctly match theories valid at different energy scales. The systematic inclusion of these effects is indispensable for the internal consistency of EFTs and for meaningful quantitative comparisons with experimental measurements.

In this thesis, the significance of these corrections is explicitly demonstrated in both the aforementioned contexts. On one hand, we study the impact of NLO contributions and RGE effects within the SMEFT framework, highlighting how these corrections can substantially affect the interpretation of new physics constraints in SMEFT global analyses. On the other hand, we examine the inclusive decay  $\bar{B} \rightarrow X_s \gamma$ , where SCET provides an accurate description in terms of a factorisation theorem, emphasising the crucial role of NLO corrections and RGE to reduce the theoretical uncertainty and improve the SM predictions.

Within the SMEFT framework, a crucial first step involves the construction and critical assessment of global datasets combining experimental and theoretical information across

multiple observables. This includes studying correlations among observables, identifying blind directions in the parameter space, and improving the global fit by incorporating new theoretical calculations. A first component of this thesis is devoted to such improvements, providing refined theoretical inputs that strengthen the reliability and scope of global analyses. In this context, we perform a global fit of the SMEFT within a UV-inspired flavour symmetry framework, in contrast to more “data-driven” approaches in the literature where operators not directly contributing to the considered observables are simply omitted. Once a consistent global fit is established, it becomes crucial to include higher-order effects, such as NLO corrections and RGE, to properly connect different energy scales. These corrections, often neglected in global analyses, are investigated here and shown to significantly affect not only the uncertainties on the Wilson coefficients, but also their correlations, thereby impacting the interpretation of experimental constraints.

In the context of the inclusive decay  $\bar{B} \rightarrow X_s \gamma$  within SCET, previous work has established the LO analysis of the non-local power-suppressed contribution arising from the interference between the weak effective operators  $Q_1^q$  and  $Q_{7\gamma}$ , which represents the dominant source of theoretical uncertainty. Therefore, the goal of this thesis is to go beyond this level by incorporating NLO corrections, in the strong coupling  $\alpha_s$ , together with the effects of RGE. The analysis starts from a factorisation theorem, which systematically disentangle short- and long-distance dynamics. Building on this, a central element of this work is the computation of previously unknown  $\mathcal{O}(\alpha_s)$  corrections to the functions entering the factorisation formula, crucial for improving theoretical precision. Achieving this involves technically demanding one- and two-loop calculations and the solution of RG equations to resum large logarithms. Beyond their direct impact on precision, these computations also provide new insights into the internal structure of the theory, uncovering technical subtleties that are of fundamental importance for future progress in this field.

The thesis is organised as follows. In Chapter 1, we review the Standard Model, highlighting its main features and intrinsic limitations, while also introducing the flavour sector and discussing how the SM can be probed at colliders. Chapter 2 provides an overview of the general framework of Effective Field Theories, with particular attention to the EFTs that are central to this work.

Part I: [Global Analyses of the \*Minimal\* MFV SMEFT](#) is devoted to the global analysis of the SMEFT. In Chapter 3, we discuss the motivations, the current status, and the statistical framework of global analyses. Chapter 4 introduces the construction of the likelihood required for the global fit, including the evaluation of dijet production, and presents the first results. Chapters 5 and 6 explore the impact of NLO corrections and RGE on the analysis. Part I is concluded in Chapter 7.

Part II: [NLO Analysis of the  \$Q\_1^q - Q\_{7\gamma}\$  Interference in  \$\bar{B} \rightarrow X\_s \gamma\$  at Subleading Power](#) focuses on the computation of NLO corrections to the  $Q_1^q - Q_{7\gamma}$  interference contribution in  $\bar{B} \rightarrow X_s \gamma$ . Chapter 8 presents the motivations for this calculation and reviews the existing literature. Chapter 9 is dedicated to the renormalisation of the shape function  $g_{17}$  and the solution of its RG equation. In Chapter 10, we compute the  $\bar{n}$ -jet function at both LO and NLO, while in Chapter 11 we demonstrate the cancellation of all singularities among the functions computed in this part. Part II concludes in Chapter 12.

# The State of the Standard Model

## Contents

---

1.1	The Standard Model of Particle Physics . . . . .	1
1.2	Flavour Physics: Probing the Standard Model with Low Energy Observables . . . . .	4
1.3	Collider Physics: Probing the Standard Model with High En- ergy Observables . . . . .	5

---

## 1.1 The Standard Model of Particle Physics

The Standard Model (SM) of particle physics is a relativistic quantum field theory based on the gauge symmetry group

$$G_{\text{SM}} = SU(3)_C \times SU(2)_L \times U(1)_Y, \tag{1.1}$$

which successfully describes three of the four known fundamental interactions: the electromagnetic, weak, and strong forces. Within this framework, matter is composed of spin- $\frac{1}{2}$  fermions, organised in three generations of quarks and leptons, while the interactions are mediated by gauge bosons: the photon ( $\gamma$ ), the weak bosons ( $W^\pm$ ,  $Z^0$ ), and the gluons ( $g$ ). The electroweak unification is achieved via the Glashow–Weinberg–Salam model [1–3], and spontaneous symmetry breaking is implemented through the Brout–Englert–Higgs mechanism [4, 5], which introduces a scalar Higgs field responsible for giving mass to the  $W$  and  $Z$  bosons, as well as to fermions via Yukawa couplings.

The Lagrangian of the SM is renormalisable and has been extensively tested experimentally, with predictions confirmed to a high degree of precision. The discovery of the Higgs boson in 2012 at CERN’s Large Hadron Collider (LHC) marked a major milestone, completing the particle spectrum predicted by the theory [6, 7].

Despite its empirical success, the Standard Model is widely regarded as an effective low-energy theory, rather than a fundamental one. Several unresolved issues and theoretical limitations point to the necessity of physics beyond the Standard Model (BSM), including:

- Gravity: The SM does not incorporate gravity, which is described by General Relativity and is not compatible with quantum field theory in its current form.

- **Neutrino Masses:** In its minimal formulation, the SM assumes neutrinos to be massless. However, the observation of neutrino oscillations implies that they must have non-zero masses, requiring an extension of the model.
- **Dark Matter (DM) and Dark Energy:** The Standard Model provides no viable candidate for dark matter particles capable of accounting for the observed DM energy density, and it does not explain the accelerated expansion of the Universe, which is attributed to dark energy.
- **Matter-Antimatter Asymmetry:** The CP violation present in the SM is insufficient to explain the observed baryon asymmetry of the Universe.

These open questions have motivated numerous theoretical proposals, such as supersymmetry (SUSY) [8], grand unified theories (GUTs) [9], extra dimensions [10], composite Higgs models [11], dark sectors [12], and various models of neutrino mass generation (e.g., seesaw mechanisms) [13, 14]. Although the exact scale of new physics remains unknown, theoretical considerations such as the hierarchy problem suggest that it should emerge not far above the electroweak scale. Experimental efforts, including precision measurements and high-energy collider searches, continue to probe the SM and search for signatures of new physics.

Before introducing the full Lagrangian, it is useful to present the field content of SM.

- **Fermions:**

The SM contains three generations of spin- $\frac{1}{2}$  fermions, referred to us as quarks and leptons. Left-handed fermions are arranged in  $SU(2)_L$  doublets

$$Q_L^i(3, 2, +\frac{1}{6}) = \begin{pmatrix} u_L^i \\ d_L^i \end{pmatrix}, \quad L_L^i(1, 2, -\frac{1}{2}) = \begin{pmatrix} \nu_L^i \\ e_L^i \end{pmatrix}, \quad (1.2)$$

while the right-handed components are  $SU(2)_L$  singlets

$$u_R^i(3, 1, +\frac{2}{3}), \quad d_R^i(3, 1, -\frac{1}{3}), \quad e_R^i(1, 1, -1). \quad (1.3)$$

The numbers in parentheses denote the representations under  $G_{\text{SM}}$ , and the index  $i = 1, 2, 3$  labels the generation (or flavour). Each generation contains one charged lepton ( $e, \mu, \tau$ ) and its corresponding neutrino ( $\nu_e, \nu_\mu, \nu_\tau$ ), as well as two quarks: one with electric charge  $+\frac{2}{3}$  ( $u, c, t$ ) and one with charge  $-\frac{1}{3}$  ( $d, s, b$ ). Therefore, particles of the same charge differ for the mass. The mass spectrum is extremely hierarchical: the lightest fermion is the electron with  $m_e = 0.511$  MeV, while the heaviest is the top quark with  $m_t \approx 170$  GeV.

- **Higgs Scalar:**

The Higgs field is a complex scalar transforming as an  $SU(2)_L$  doublet with hypercharge  $Y = +\frac{1}{2}$ :

$$\Phi(1, 2, +\frac{1}{2}). \quad (1.4)$$

Its vacuum expectation value breaks the electroweak symmetry:

$$SU(2)_L \times U(1)_Y \rightarrow \times U(1)_{\text{EM}}. \quad (1.5)$$

This mechanism, known as electroweak symmetry breaking, generates masses for both gauge bosons and fermions while preserving gauge invariance.

- Gauge Fields:

The gauge sector includes the following vector fields:

$$G_\mu = G_\mu^a \lambda^a, \quad W_\mu = W_\mu^i \tau^i, \quad B_\mu, \quad (1.6)$$

where  $\lambda^a$  are the Gell-Mann matrices of  $SU(3)_C$  and  $\tau^i$  the Pauli matrices of  $SU(2)_L$ .

The corresponding field strengths are:

$$G_{\mu\nu} = \partial_\mu G_\nu - \partial_\nu G_\mu + ig_s [G_\mu, G_\nu], \quad (1.7)$$

$$W_{\mu\nu} = \partial_\mu W_\nu - \partial_\nu W_\mu + ig [W_\mu, W_\nu], \quad (1.8)$$

$$B_{\mu\nu} = \partial_\mu B_\nu - \partial_\nu B_\mu, \quad (1.9)$$

where  $g_s$ ,  $g$ , and  $g'$  are the coupling constants of  $SU(3)_C$ ,  $SU(2)_L$ , and  $U(1)_Y$ , respectively.

After electroweak symmetry breaking, the  $W_\mu^3$  and  $B_\mu$  fields mix via the Weinberg angle  $\theta_W$  to form the physical bosons:

- $W_\mu^\pm = \frac{1}{\sqrt{2}}(W_\mu^1 \mp iW_\mu^2)$ : charged weak bosons,
- $Z_\mu = \cos \theta_W W_\mu^3 - \sin \theta_W B_\mu$ : neutral weak boson,
- $A_\mu = \sin \theta_W W_\mu^3 + \cos \theta_W B_\mu$ : photon (electromagnetic interaction).

Once the field content is specified, the Standard Model is formulated as a renormalisable quantum field theory whose dynamics are governed by the principle of local gauge invariance. The underlying gauge symmetry is given by the product group  $G_{\text{SM}}$ , defined in (1.1). Here,  $SU(3)_C$  denotes the special unitary group of colour, associated with Quantum Chromodynamics (QCD), which governs the interactions among quarks and gluons through the exchange of eight massless gluons. The electroweak sector is described by the gauge group  $SU(2)_L \times U(1)_Y$ , where  $SU(2)_L$  corresponds to weak isospin and  $U(1)_Y$  to weak hypercharge. Based on this fundamental principle and based on the particle content, the SM is given by the most general symmetric Lagrangian (up to mass dimension 4) which can be written as:

$$\mathcal{L}_{\text{SM}} = \mathcal{L}_{\text{kin}} + \mathcal{L}_H + \mathcal{L}_Y, \quad (1.10)$$

where the Lagrangian terms are defined as follows.

- Kinetic and Interaction Terms:

$$\mathcal{L}_{\text{kin}} = -\frac{1}{4}G_{\mu\nu}^a G^{a\mu\nu} - \frac{1}{4}W_{\mu\nu}^i W^{i\mu\nu} - \frac{1}{4}B_{\mu\nu} B^{\mu\nu} + \sum_f \bar{\psi}_f i \not{D} \psi_f, \quad (1.11)$$

with  $D_\mu = \partial_\mu - i\frac{g_s}{2}\lambda_a G_\mu^a - i\frac{g}{2}\tau_i W_\mu^i - i\frac{g'}{2}Y B_\mu$  the covariant derivative and  $\psi_f$  a generic fermion field. We note that the covariant derivative generates interactions between bosons and fermions.

- Higgs Sector:

$$\mathcal{L}_H = (D_\mu \Phi)^\dagger (D^\mu \Phi) - \mu^2 \Phi^\dagger \Phi - \lambda (\Phi^\dagger \Phi)^2, \quad (1.12)$$

where  $\mu^2$  and  $\lambda$  are real parameters. This Lagrangian term contains the Higgs self interactions and the interactions with Gauge bosons. The aforementioned electroweak symmetry breaking happens when the Higgs field acquires its vacuum expectation value

$$\langle \Phi \rangle = \begin{pmatrix} 0 \\ \frac{v}{\sqrt{2}} \end{pmatrix}, \quad \text{with } v = \sqrt{\frac{-\mu^2}{\lambda}}, \quad (1.13)$$

which generates masses for the gauge bosons.

- Yukawa Interactions:

$$\mathcal{L}_Y = -Y_u^{ij} \bar{Q}_{Li} u_{Rj} \tilde{\Phi} - Y_d^{ij} \bar{Q}_{Li} d_{Rj} \Phi - Y_e^{ij} \bar{L}_{Li} e_{Rj} \Phi + \text{h.c.}, \quad (1.14)$$

where  $\tilde{\Phi} = i\tau_2 \Phi^*$  is the conjugate Higgs doublet, while  $Y_u$ ,  $Y_d$ , and  $Y_e$  are the Yukawa coupling matrices. This term is responsible for fermion mass generation and encodes the full flavour structure of the SM, which is analysed in the following section.

## 1.2 Flavour Physics: Probing the Standard Model with Low Energy Observables

Flavour physics studies the structure and dynamics associated with the replication of fermion families and the transitions between different generations (or flavours). In the Standard Model, flavour is encoded in the fermionic sector through the Yukawa couplings, which are the only source of flavour and CP violation.

The Yukawa sector of the SM Lagrangian is responsible for giving mass to the charged fermions via spontaneous electroweak symmetry breaking. After the Higgs field acquires its vacuum expectation value (VEV) as in Equation (1.13), the Yukawa couplings induce mass terms:

$$\mathcal{L}_{\text{mass}} = -\bar{u}_L^i (M_u)^{ij} u_R^j - \bar{d}_L^i (M_d)^{ij} d_R^j - \bar{e}_L^i (M_e)^{ij} e_R^j + \text{h.c.}, \quad (1.15)$$

where the mass matrices are defined as

$$M_u = \frac{v}{\sqrt{2}} Y_u, \quad M_d = \frac{v}{\sqrt{2}} Y_d, \quad M_e = \frac{v}{\sqrt{2}} Y_e. \quad (1.16)$$

The mass matrices are, in general, complex and non-diagonal, but they can be diagonalised by bi-unitary transformations:

$$U_{uL}^\dagger M_u U_{uR} = \text{diag}(m_u, m_c, m_t), \quad U_{dL}^\dagger M_d U_{dR} = \text{diag}(m_d, m_s, m_b). \quad (1.17)$$

While these rotations leave the neutral current interactions flavour-diagonal, the charged-current interactions in the weak sector couple the left-handed quark doublets:

$$\mathcal{L}_{CC} = \frac{g}{\sqrt{2}} \bar{u}_L^i \gamma^\mu d_L^i W_\mu^+ + \text{h.c.} \quad (1.18)$$

After rotating to the mass eigenbasis, the charged-current Lagrangian becomes:

$$\mathcal{L}_{CC} = \frac{g}{\sqrt{2}} \bar{u}_L^i \gamma^\mu (V_{\text{CKM}})^{ij} d_L^j W_\mu^+ + \text{h.c.}, \quad (1.19)$$

where the Cabibbo-Kobayashi-Maskawa (CKM) [15, 16] matrix is defined as:

$$V_{\text{CKM}} = U_{uL}^\dagger U_{dL}. \quad (1.20)$$

This unitary matrix encodes all the flavour-changing processes among quarks in the SM and is responsible for CP violation in the quark sector.

The CKM matrix contains 9 complex elements, subject to unitarity constraints. After removing unphysical phases by field redefinitions, it can be parameterised by three mixing angles and one CP-violating phase. A commonly used parameterisation is:

$$V_{\text{CKM}} = \begin{pmatrix} c_{12}c_{13} & s_{12}c_{13} & s_{13}e^{-i\delta} \\ -s_{12}c_{23} - c_{12}s_{23}s_{13}e^{i\delta} & c_{12}c_{23} - s_{12}s_{23}s_{13}e^{i\delta} & s_{23}c_{13} \\ s_{12}s_{23} - c_{12}c_{23}s_{13}e^{i\delta} & -c_{12}s_{23} - s_{12}c_{23}s_{13}e^{i\delta} & c_{23}c_{13} \end{pmatrix},$$

with  $c_{ij} = \cos \theta_{ij}$ ,  $s_{ij} = \sin \theta_{ij}$ , and  $\delta$  the Dirac CP-violating phase.

An alternative and phenomenologically useful parameterisation, which makes the hierarchy of the entries explicit, is provided by the Wolfenstein expansion [17]:

$$V_{\text{CKM}} = \begin{pmatrix} 1 - \frac{\lambda^2}{2} & \lambda & A\lambda^3(\rho - i\eta) \\ -\lambda & 1 - \frac{\lambda^2}{2} & A\lambda^2 \\ A\lambda^3(1 - \rho - i\eta) & -A\lambda^2 & 1 \end{pmatrix} + \mathcal{O}(\lambda^4), \quad (1.21)$$

with  $\lambda \simeq 0.225$ ,  $A \simeq 0.8$ , and  $(\rho, \eta)$  governing CP violation.

At tree level, the SM forbids flavour-changing neutral currents (FCNCs) due to the unitarity of the CKM matrix and the flavour universality of gauge interactions. FCNCs only appear at loop level (e.g., box and penguin diagrams), leading to strong suppression known as the GIM mechanism (Glashow–Iliopoulos–Maiani) [18].

Examples of FCNC processes include:

- $K^0 - \bar{K}^0$ ,  $B^0 - \bar{B}^0$  mixing,
- Rare decays such as  $b \rightarrow s\gamma$ ,  $B \rightarrow \mu^+\mu^-$ ,
- Kaon and B-meson CP violation.

These processes provide sensitive probes of physics beyond the Standard Model (BSM), as new heavy particles in loops may generate observable deviations. Such deviations can be systematically parameterised within Effective Field Theories (EFTs) through higher-dimensional operators. At the same time, the EFT framework is widely used in flavour physics to improve theoretical predictions for complex hadronic transitions. We address these topics in the next chapter, while the following section focuses on probing the Standard Model at high energies rather than in low-energy flavour processes.

### 1.3 Collider Physics: Probing the Standard Model with High Energy Observables

Collider physics is the branch of particle physics that studies the fundamental constituents of matter and their interactions by accelerating particles to relativistic energies and colliding them. Colliders provide the necessary energy to probe short-distance phenomena, access new degrees of freedom, and test the predictions of the SM and its extensions.

The most relevant quantity in high-energy collisions is the center-of-mass (CM) energy  $\sqrt{s}$ , defined for two colliding particles with four-momenta  $p_1^\mu$  and  $p_2^\mu$  as:

$$s = (p_1 + p_2)^2. \quad (1.22)$$

In hadron colliders like the LHC, protons are composed of quarks and gluons, and the actual interactions occur between their partonic constituents. Thus, the relevant quantity is the partonic center-of-mass energy:

$$\hat{s} = x_1 x_2 s, \quad (1.23)$$

where  $x_1$  and  $x_2$  are the momentum fractions carried by the interacting partons, governed by the Parton Distribution Functions (PDFs)  $f_{i/p}(x, Q^2)$  [19].

The fundamental observable in collider physics is the cross section, which quantifies the probability of a given process to occur. For a process  $a + b \rightarrow X$ , the total cross section at hadron level is obtained by convoluting the partonic cross section  $\hat{\sigma}_{ab \rightarrow X}(\hat{s})$  with the PDFs:

$$\sigma_{pp \rightarrow X}(s) = \sum_{a,b} \int_0^1 dx_1 dx_2 f_{a/p}(x_1, Q^2) f_{b/p}(x_2, Q^2) \hat{\sigma}_{ab \rightarrow X}(\hat{s}). \quad (1.24)$$

The expected number of events for a given process is then given by:

$$N = L \cdot \sigma, \quad (1.25)$$

where  $L$  is the integrated luminosity.

Partonic cross sections are computed using perturbation theory in quantum field theory. At leading order (LO), the cross section is related to the squared amplitude:

$$\hat{\sigma} \propto \frac{1}{2\hat{s}} \int d\text{PS}_n \overline{|\mathcal{M}|^2}, \quad (1.26)$$

where  $d\text{PS}_n$  is the  $n$ -body phase space measure, and  $\overline{|\mathcal{M}|^2}$  is the matrix element squared, averaged (summed) over initial (final) quantum numbers.

For example, the Drell–Yan process at LO involves the partonic reaction  $q\bar{q} \rightarrow \ell^+\ell^-$  via an intermediate  $\gamma^*/Z$  boson, with the differential cross section:

$$\frac{d\hat{\sigma}}{d\hat{t}} \propto \frac{e^4 Q_q^2}{\hat{s}^2}, \quad (1.27)$$

where  $Q_q$  is the electric charge of the quark.

QCD corrections are essential in collider physics due to the strong interactions of initial-state partons. These include:

- Virtual corrections: loop diagrams contributing to the same process;
- Real emissions: extra gluons or quarks in the final state;
- Infrared divergences: handled through cancellation (KLN theorem [20, 21]).

To achieve higher precision, cross sections are computed at Next-to-Leading Order (NLO) or Next-to-Next-to-Leading Order (NNLO), and in many cases they are matched with parton shower simulations using frameworks such as POWHEG [22] or MC@NLO [23]. Collider experiments reconstruct final-state particles by identifying the different types of objects produced in the collision. Leptons, such as electrons and muons, are detected through tracks in the tracking systems and energy deposits in calorimeters. Jets, which appear as collimated sprays of hadrons, are reconstructed using clustering algorithms like “anti- $k_T$ ” [24] or “Cambridge/Aachen” [25, 26]. Missing transverse energy ( $\cancel{E}_T$ ) is measured to infer the presence of neutrinos or possible dark matter candidates. These reconstructed objects are then characterised by kinematic variables such as transverse momentum ( $p_T$ ), pseudorapidity ( $\eta$ ), and invariant masses (e.g.,  $m_{\ell\ell}$ ), which are essential to define signal regions and suppress background contributions. The hadronic final states observed in the detector arise from a sequence of well-understood steps. The hard scattering process is described by perturbative QCD, setting the initial parton-level configuration. Parton showering resums soft and collinear emissions, producing a realistic distribution of outgoing partons. Hadronisation, a non-perturbative process modelled through string or cluster models, converts partons

into observable hadrons. Finally, detector simulation incorporates the finite resolution and efficiencies of the experimental apparatus, allowing for a realistic prediction of the measured final-state signatures.

This entire chain is simulated via Monte Carlo event generators such as PYTHIA [27], HERWIG [28], or SHERPA [29], which model the full evolution from parton-level events to hadron-level final states, including parton showers and hadronisation. In addition, tools like MADGRAPH5\_AMC@NLO [30] are used to compute the hard scattering matrix elements at LO or NLO in perturbation theory, and can be interfaced with parton shower generators for full event simulation.

Collider physics is not only a testbed for the SM but also a powerful probe for Beyond Standard Model (BSM) physics. Signatures may include:

- Resonances: peaks in invariant mass distributions (e.g.,  $Z' \rightarrow \ell^+ \ell^-$ );
- Deviations in cross sections: modifications in angular distributions or tails of kinematic distributions;
- Missing energy signals: arising from weakly interacting particles;
- Long-lived particles: displaced vertices or non-standard time-of-flight.

Effective Field Theories are the perfect framework to investigate physics BSM in a model-independent way and to parametrise possible deviations, from the SM expectation, also in collider experiments.

Given the importance of EFTs in both collider and flavour physics, and their role in precision computations as well as NP parameterisation, we provide a broad overview and a more technical introduction to these frameworks in the next chapter.



# Effective Field Theories

## Contents

---

<b>2.1</b>	<b>Effective Field Theories: A General Framework . . . . .</b>	<b>9</b>
<b>2.2</b>	<b>The Weak Effective Theory . . . . .</b>	<b>12</b>
<b>2.3</b>	<b>The Standard Model Effective Field Theory . . . . .</b>	<b>15</b>
<b>2.4</b>	<b>The Heavy Quark Effective Theory . . . . .</b>	<b>18</b>
<b>2.5</b>	<b>The Soft-Collinear Effective Theory . . . . .</b>	<b>20</b>

---

## 2.1 Effective Field Theories: A General Framework

EFTs provide a powerful and systematic approach to describe physical phenomena when there is a possible separation of energy scales. The central idea is to focus on the relevant degrees of freedom at a given energy scale, while systematically accounting for the effects of high-energy, or ultraviolet (UV), physics through an expansion in local operators.

The construction of an EFT relies on a few key assumptions:

- There exists a hierarchy of scales: a low-energy scale  $E$  at which we probe the system, and a high-energy cutoff  $\Lambda \gg E$  where new degrees of freedom become active<sup>1</sup>.
- The heavy fields with masses of order  $\Lambda$  can be integrated out, leaving an effective Lagrangian involving only light fields.
- The dynamics at low energy can be encoded in a Lagrangian organised as a series of operators consistent with the symmetries of the underlying theory, suppressed by powers of  $1/\Lambda$ .

The structure of an EFT Lagrangian, expanded in the mass parameter  $\Lambda$ , reads as follows:

$$\mathcal{L}_{\text{EFT}} = \mathcal{L}_{\text{ren}} + \sum_i \frac{c_i^{(5)}}{\Lambda} \mathcal{O}_i^{(5)} + \sum_i \frac{c_i^{(6)}}{\Lambda^2} \mathcal{O}_i^{(6)} + \dots, \quad (2.1)$$

where  $\mathcal{L}_{\text{ren}}$  is the renormalisable part (typically the Standard Model or another low-energy renormalisable theory), while the operators  $\mathcal{O}_i^{(d)}$  are operators of dimension  $d > 4$ , respecting

---

<sup>1</sup>In the EFTs employed in this thesis, more than two scales are usually present, but for illustrative purposes, in this section we focus on the case where only two scales are relevant.

the underlying symmetry, built from the low-energy fields, and the  $c_i^{(d)}$  are dimensionless Wilson coefficients encoding the UV physics. An EFT expansion is meaningful as long as the typical energy scale of the process satisfies  $E \ll \Lambda$ . Corrections from higher-dimensional operators are suppressed as:

$$\delta \sim \left(\frac{E}{\Lambda}\right)^{d-4}, \quad (2.2)$$

which provides a natural expansion parameter. The number of operators grows rapidly with the operator dimension, and symmetry considerations (gauge, Lorentz, flavour, etc.) play a crucial role in organising and selecting the relevant operators.

When constructing an EFT from an UV complete theory, one performs a procedure called matching to determine the Wilson coefficients  $c_i^{(d)}$  by requiring that the low-energy observables match between the full theory and the EFT:

$$\mathcal{A}_{\text{full}}(E \ll \Lambda) = \mathcal{A}_{\text{EFT}}(E \ll \Lambda). \quad (2.3)$$

In practice, the matching procedure can be performed at tree level or at loop level, depending on the precision required. Loop-level matching is essential when the leading contribution to an operator appears only radiatively, or when one wishes to control subleading effects necessary for precision predictions. Matching calculations often require careful regularisation and renormalisation schemes to ensure consistency between the full theory and the EFT [31]. The matching is most appropriately carried out at the high scale  $\Lambda$ , where potential large logarithms do not arise.

Once matched at a scale  $\mu \sim \Lambda$ , the EFT can be evolved down to lower energy scales via Renormalisation Group Evolution (RGE). This scale evolution is crucial because physical processes are typically probed at energy scales  $E \ll \Lambda$ , and the Wilson coefficients  $c_i^{(d)}(\mu)$ , which encode the effects of UV physics, run with the renormalisation scale  $\mu$  due to quantum corrections.

The scale dependence of the Wilson coefficients is governed by a coupled system of differential equations of the form:

$$\mu \frac{d}{d\mu} c_i(\mu) = \gamma_{ij}(\mu) c_j(\mu), \quad (2.4)$$

where  $\gamma_{ij}(\mu)$  is the anomalous dimension matrix, which encodes how the operator basis mixes under renormalisation. The matrix elements  $\gamma_{ij}$  can be computed perturbatively as expansions in the coupling constants (e.g.  $\alpha_s$  in QCD):

$$\gamma_{ij}(\mu) = \frac{\alpha_s(\mu)}{4\pi} \gamma_{ij}^{(0)} + \left(\frac{\alpha_s(\mu)}{4\pi}\right)^2 \gamma_{ij}^{(1)} + \dots \quad (2.5)$$

The non-trivial structure of  $\gamma_{ij}$  reflects that renormalisation can mix operators with the same quantum numbers, so even if some operators are absent at the matching scale, they can be generated at lower scales through this mixing.

The need for RGE arises from the presence of large logarithms in perturbative expansions, which spoil fixed-order convergence. Consider a generic observable whose perturbative expansion contains terms of the form:

$$\alpha_s^n \log^m \frac{\Lambda}{\mu}, \quad m \leq n, \quad (2.6)$$

where  $\Lambda$  is the high scale (e.g. matching scale) and  $\mu$  a low scale (typical of the process). When  $\log(\Lambda/\mu) \gg 1$ , these logarithms can invalidate naive perturbation theory since terms like  $\alpha_s \log(\Lambda/\mu)$  may become of order one.

The RGEs allow one to resum these logarithms to all orders by solving the scale evolution of the Wilson coefficients. At leading-log (LL) accuracy, one resums terms  $(\alpha_s \log)^n$ ; next-to-leading-log (NLL) accuracy resums terms  $\alpha_s(\alpha_s \log)^n$ , and so forth. This restores the validity of the perturbative expansion and ensures its reliability at low energies.

Once the EFT Lagrangian is constructed, it typically contains a large number of higher-dimensional operators. However, not all these operators correspond to independent physical effects. Many operators are related by redundancies that arise due to the freedom of performing field redefinitions, integration by parts, or the use of the classical equations of motion (EOM) of the low-energy fields. The systematic elimination of such redundant operators is essential to obtain a minimal and physically meaningful set of operators known as an operator basis.

Consider an effective Lagrangian of the form

$$\mathcal{L}_{\text{EFT}} = \mathcal{L}_{\text{ren}} + \sum_i \frac{c_i}{\Lambda^{d_i-4}} \mathcal{O}_i, \quad (2.7)$$

where  $\mathcal{O}_i$  are local operators of dimension  $d_i > 4$ . A field redefinition

$$\phi \rightarrow \phi + \frac{1}{\Lambda^{d-4}} \delta\phi, \quad (2.8)$$

where  $\delta\phi$  is a functional of the fields and their derivatives, modifies the effective action by terms proportional to the equations of motion of the original fields:

$$\delta\mathcal{L} = \frac{\delta\mathcal{L}}{\delta\phi} \delta\phi + \text{total derivatives}. \quad (2.9)$$

Since physical observables are invariant under such redefinitions (they amount to a change of variables in the path integral), operators proportional to the EOM can be eliminated or reshuffled into other operators of the same or higher dimension.

Integration by parts in the action allows the transfer of derivatives between fields, reducing the number of independent operators by relating superficially different operators. For example,

$$\int d^4x (\partial_\mu A) B = - \int d^4x A (\partial_\mu B) + \text{boundary terms}, \quad (2.10)$$

and since boundary terms do not affect the equations of motion, operators differing by total derivatives are physically equivalent and redundant.

The classical equations of motion derived from the renormalisable Lagrangian  $\mathcal{L}_{\text{ren}}$  take the schematic form

$$\frac{\delta\mathcal{L}_{\text{ren}}}{\delta\phi} = 0. \quad (2.11)$$

Operators that vanish upon use of these EOM can be removed from the basis, as their effects can be absorbed into redefinitions of other operators or Wilson coefficients.

The combined use of field redefinitions, integration by parts, and EOM relations leads to a minimal and non-redundant set of operators, commonly called an operator basis. This reduces the complexity of the EFT parameter space and avoids ambiguities in interpreting experimental constraints.

For example, in the context of the Standard Model Effective Field Theory, the so-called Warsaw basis [32] represents a complete and independent set of dimension-six operators consistent with the Standard Model gauge symmetries and flavour structure. This basis is widely adopted due to its systematic construction and suitability for global fits of Wilson coefficients to experimental data.

Similarly, in the Weak Effective Theory, which describes flavour-changing processes at scales below the electroweak scale, complete bases of four-fermion and dipole operators have been systematically constructed [33].

A paradigmatic example of an EFT is the Fermi theory of weak interactions [34], which describes low-energy charged-current processes such as beta decay. In the full electroweak Standard Model, the process  $d \rightarrow ue^- \bar{\nu}_e$  proceeds via exchange of a virtual  $W$  boson with mass  $M_W$ . For energies much smaller than  $M_W$ , the  $W$  propagator can be expanded in powers of  $q^2/M_W^2$ , leading to an effective four-fermion interaction:

$$\mathcal{L}_{\text{Fermi}} = -\frac{4G_F}{\sqrt{2}} (\bar{u}\gamma^\mu P_L d) (\bar{e}\gamma_\mu P_L \nu_e), \quad (2.12)$$

where the Fermi constant is given by  $G_F/\sqrt{2} = g^2/(8M_W^2)$ , and  $P_L = (1 - \gamma^5)/2$  is the left-handed projector. This effective interaction correctly reproduces low-energy weak processes such as nuclear beta decay, with deviations from the full theory suppressed by powers of  $E^2/M_W^2$ .

This historical example illustrates the power of EFTs: even without knowing the details of the UV theory (in this case, the electroweak theory with massive vector bosons), low-energy phenomena can be accurately described using only the relevant degrees of freedom and symmetry principles. Additionally, these EFTs can act as a bridge, providing guidance on the structure and symmetries of the underlying UV theory. Modern EFTs extend this idea to a wide range of contexts each tailored to the appropriate energy regime and physical processes.

In the following sections, we provide a detailed overview of the EFTs relevant to this work: the Weak Effective Theory, the Standard Model Effective Field Theory, the Heavy Quark Effective Theory, and the Soft-Collinear Effective Theory.

## 2.2 The Weak Effective Theory

The Weak Effective Theory (WET) [35], also known as the Low-Energy Effective Theory (LEFT) [36], is an effective field theory designed to describe processes mediated by weak interactions at energies much below the electroweak scale, typically  $E \ll M_W$ . In this regime, the heavy degrees of freedom of the Standard Model (namely the  $W^\pm$ ,  $Z$ , the Higgs boson  $H$ , and the top quark  $t$ ) are integrated out, and the resulting theory involves only the light fermions (up to the  $b$  quark), gluons, and photons, along with a tower of local, non-renormalisable operators encoding the effects of the heavy fields.

The general structure of the WET Lagrangian is given by:

$$\mathcal{L}_{\text{WET}} = \mathcal{L}_{\text{QCD+QED}}^{(5 \text{ quarks})} + \sum_i C_i(\mu) Q_i, \quad (2.13)$$

where:

- $\mathcal{L}_{\text{QCD+QED}}^{(5 \text{ quarks})}$  is the renormalisable Lagrangian of QCD and QED with five active quark flavours ( $u, d, s, c, b$ ),

- $Q_i$  are dimension-six (or higher) effective operators constructed from the light fields,
- $C_i(\mu)$  are the Wilson coefficients, which carry the information of the short-distance physics and evolve with the renormalization scale  $\mu$ .

This formulation provides an efficient description of FCNC, CP violation, and rare decays of mesons and baryons. Since the weak interactions are mediated by the exchange of heavy  $W^\pm$  and  $Z$  bosons, they appear in WET as local four-fermion operators after integrating out these massive gauge bosons.

The operators in the WET are classified by their flavour structure, chirality, and gauge quantum numbers. A relevant example for the following is the  $\Delta F = 1$  effective Hamiltonian [37, 38] describing FCNC processes such as  $b \rightarrow s\gamma$ ,  $b \rightarrow s\ell^+\ell^-$  or  $s \rightarrow d\nu\bar{\nu}$  transitions:

$$\mathcal{H}_{\text{eff}}^{\Delta F=1} = -\frac{4G_F}{\sqrt{2}}V_{tb}V_{ts}^* \sum_i C_i(\mu)Q_i(\mu) + \text{h.c.} \quad (2.14)$$

Here,  $G_F$  is the Fermi constant,  $V_{ij}$  are CKM matrix elements, and  $Q_i$  are local dimension-six operator. A comprehensive list is provided in Table 2.1. We typically refer to these operators as follows.

- Current-current (four-quark) operators (e.g.,  $Q_1^q, Q_2^q$ ),
- QCD and electroweak penguin operators (e.g.,  $Q_3 - Q_{10}$ ),
- Magnetic and chromomagnetic dipole operators (e.g.,  $Q_{7\gamma}, Q_{8g}$ ),
- Semileptonic operators (e.g.,  $Q_9, Q_{10}, Q_S, Q_P$ ),
- Neutrino operators (e.g.,  $Q_{\nu\bar{\nu}}$ ),
- Scalar and tensor operators, in extensions beyond the SM.

Each of these operators has well-defined transformation properties under Lorentz and gauge symmetries and can interfere in specific processes depending on the helicity structure of the external states.

The WET is constructed by performing a matching calculation between the Standard Model (or the Standard Model Effective Theory) and the WET at a high scale, typically  $\mu \sim M_W$  or  $\mu \sim m_t$ , in order to avoid large logarithms. At this scale, the full theory is matched onto the WET by equating Green's functions computed in both theories, ensuring that physical amplitudes are continuous across the threshold. As explained in the previous section, the matching procedure can be performed at tree-level or loop-level depending on the desired precision. At tree level, as fully computed in [36], the WET reproduces the well-known Fermi theory that successfully describes processes such as nuclear  $\beta$ -decay. In this regime, the weak interaction can be understood as an effective four-fermion contact interaction obtained after integrating out the  $W$  boson. Moving to the one-loop level, the picture becomes considerably richer. As shown in [39, 40], loop corrections generate FCNC processes, which are absent at tree level in the Standard Model. A paradigmatic example is the transition  $b \rightarrow s\gamma$ , mediated by loop diagrams involving heavy virtual particles. Such processes are particularly important because they are highly suppressed in the SM and therefore serve as sensitive probes of possible new physics contributions.

The RGE matrix governs the mixing of operators under QCD and QED corrections and has been systematically computed at one loop [41, 42] and implemented in various

1, 2 : $Q_1^q, Q_2^q$		3, 4 : $Q_3, Q_4$	
$Q_1^q$	$(\bar{s}_\alpha \gamma^\mu P_L q_\beta)(\bar{q}_\beta \gamma_\mu P_L b_\alpha)$	$Q_3$	$(\bar{s}_\alpha \gamma^\mu P_L b_\alpha) \sum_q (\bar{q}_\beta \gamma_\mu P_L q_\beta)$
$Q_2^q$	$(\bar{s}_\alpha \gamma^\mu P_L q_\alpha)(\bar{q}_\beta \gamma_\mu P_L b_\beta)$	$Q_4$	$(\bar{s}_\alpha \gamma^\mu P_L b_\beta) \sum_q (\bar{q}_\beta \gamma_\mu P_L q_\alpha)$
5, 6 : $Q_5, Q_6$			
$Q_5$	$(\bar{s}_\alpha \gamma^\mu P_L b_\alpha) \sum_q (\bar{q}_\beta \gamma_\mu P_R q_\beta)$		
$Q_6$	$(\bar{s}_\alpha \gamma^\mu P_L b_\beta) \sum_q (\bar{q}_\beta \gamma_\mu P_R q_\alpha)$		
7, 8 : $Q_{7\gamma}, Q_{8g}$		9, 10 : $Q_9, Q_{10}$	
$Q_{7\gamma}$	$\frac{e}{16\pi^2} m_b (\bar{s}_\alpha \sigma^{\mu\nu} P_R b_\alpha) F_{\mu\nu}$	$Q_9$	$\frac{e^2}{16\pi^2} (\bar{s} \gamma^\mu P_L b) (\bar{\ell} \gamma_\mu \ell)$
$Q_{8g}$	$\frac{g_s}{16\pi^2} m_b (\bar{s}_\alpha \sigma^{\mu\nu} P_R T_{\alpha\beta}^a b_\beta) G_{\mu\nu}^a$	$Q_{10}$	$\frac{e^2}{16\pi^2} (\bar{s} \gamma^\mu P_L b) (\bar{\ell} \gamma_\mu \gamma_5 \ell)$
S, P : $Q_S, Q_P$			
$Q_S$	$\frac{e^2}{16\pi^2} (\bar{s} P_R b) (\bar{\ell} \ell)$		
$Q_P$	$\frac{e^2}{16\pi^2} (\bar{s} P_R b) (\bar{\ell} \gamma_5 \ell)$		
T, T5 : $Q_T, Q_{T5}$		$\ell\ell'$ : $Q_{\ell\ell'}^{(V)}, Q_{\ell\ell'}^{(S)}$	
$Q_T$	$\frac{e^2}{16\pi^2} (\bar{s} \sigma^{\mu\nu} b) (\bar{\ell} \sigma_{\mu\nu} \ell)$	$Q_{\ell\ell'}^{(V)}$	$(\bar{s} \gamma^\mu P_L b) (\bar{\ell} \gamma_\mu \ell')$
$Q_{T5}$	$\frac{e^2}{16\pi^2} (\bar{s} \sigma^{\mu\nu} b) (\bar{\ell} \sigma_{\mu\nu} \gamma_5 \ell)$	$Q_{\ell\ell'}^{(S)}$	$(\bar{s} P_R b) (\bar{\ell} \ell')$
$\ell\ell'$ : $Q_{\ell\ell'}^{(T)}$			
$Q_{\ell\ell'}^{(T)}$	$(\bar{s} \sigma^{\mu\nu} b) (\bar{\ell} \sigma_{\mu\nu} \ell')$		

**Table 2.1:** List of common dimension-six operators in the WET, relevant for flavour-changing processes. Color indices  $\alpha, \beta$  are shown where relevant,  $T^a$  denotes the  $SU(3)$  generators,  $\sigma_{\mu\nu} = \frac{i}{2}[\gamma_\mu, \gamma_\nu]$  is the antisymmetric combination of Dirac matrices, and  $P_{L(R)} = (1 \mp \gamma_5)/2$  are the left-handed and right-handed chirality projectors.

programmes such as `Wilson` [43] or `DsixTools` [44]. In some phenomenologically interesting processes, such as rare radiative  $B$ -meson decays or rare leptonic modes like  $B_s \rightarrow \ell^+ \ell^-$ , it is imperative to perform matching onto the WET beyond the one-loop level. As an example the two-loop electroweak corrections to the radiative decays of the  $B$  meson in the SM are computed in [45]. At yet higher orders, the three-loop QCD matching of dipole operators relevant for  $b \rightarrow s\gamma$  has been computed [46], and three-loop QCD corrections to the Wilson coefficient of the quark–lepton operator governing  $B_s \rightarrow \ell^+ \ell^-$  have been evaluated in [47]. These higher-loop calculations are essential to mitigate perturbative uncertainties, capture sizeable mixed QCD–electroweak effects, and achieve the theoretical precision required by current and forthcoming experiments.

For example, in  $b \rightarrow s$  transitions, the electromagnetic dipole operator  $Q_{7\gamma}$  mixes with four-quark operators such as  $Q_1^q$  and  $Q_2^q$  under renormalisation. This mixing significantly affects predictions for processes like  $\bar{B} \rightarrow X_s \gamma$ .

The WET has a remarkably broad range of applications in flavour physics and low-energy phenomenology. A first domain of interest, as mentioned above, is provided by rare decays, such as  $B \rightarrow K^{(*)} \ell^+ \ell^-$ ,  $K \rightarrow \pi \nu \bar{\nu}$  or  $B_s \rightarrow \mu^+ \mu^-$ . Another important area concerns CP violation, probed for instance through observables like  $\epsilon_K$  in kaon mixing or the direct asym-

metries  $A_{CP}$  in  $B$ -meson decays. The precise study of CP-violating quantities is essential for testing the CKM paradigm and may also shed light on the baryon asymmetry of the Universe. The WET also provides the natural framework to investigate lepton flavour violation. Processes such as  $\mu \rightarrow e\gamma$ ,  $\mu \rightarrow eee$ , or similar  $\tau$ -lepton decays are strictly forbidden in the Standard Model with massless neutrinos and remain extremely suppressed even after accounting for neutrino masses. As such, they represent golden channels in the search for new physics. In addition, the theory allows one to study electric dipole moments (EDMs) of hadrons and nuclei, which serve as ultra-sensitive probes of CP violation beyond the Standard Model. Any non-zero measurement of an EDM at current experimental sensitivities would provide unambiguous evidence for new sources of CP violation. Finally, a central application of the WET lies in the global fits of Wilson coefficients to experimental data. By systematically combining measurements from different processes, one can constrain the parameter space of possible new physics contributions and identify consistent patterns that may point towards specific ultraviolet completions.

In many cases, deviations from the Standard Model predictions in the WET coefficients can signal the presence of physics beyond the SM, even if the underlying dynamics occur at scales well above the reach of current colliders.

While the WET provides an effective description of processes below the electroweak scale, the study of high-energy phenomena near or above this scale, as well as the inclusion of information about electroweak symmetry breaking and the UV structure of possible new physics, requires the framework of the Standard Model Effective Field Theory, which will be introduced in the next section.

## 2.3 The Standard Model Effective Field Theory

The Standard Model Effective Field Theory (SMEFT) [48, 49] is a powerful extension of the SM, which parameterises the effects of hypothetical heavy new physics beyond the SM in a model-independent framework. Assuming that new physics resides at a high energy scale  $\Lambda$  much larger than the electroweak scale  $v \simeq 246$  GeV, SMEFT allows one to study possible deviations from SM predictions by expanding the Lagrangian in higher-dimensional operators constructed solely from SM fields, while preserving the full  $SU(3)_C \times SU(2)_L \times U(1)_Y$  gauge symmetry and Lorentz invariance.

The SMEFT Lagrangian is organised as a series expansion in inverse powers of the high-energy scale  $\Lambda$ :

$$\mathcal{L}_{\text{SMEFT}} = \mathcal{L}_{\text{SM}} + \sum_{d>4} \frac{1}{\Lambda^{d-4}} \sum_i C_i^{(d)} \mathcal{O}_i^{(d)}, \quad (2.15)$$

where  $\mathcal{L}_{\text{SM}}$  is the renormalisable dimension-four SM Lagrangian, and the additional operators  $\mathcal{O}_i^{(d)}$  are local, gauge-invariant combinations of SM fields with canonical mass dimension  $d > 4$ . Each operator is multiplied by a Wilson coefficient  $C_i^{(d)}$  whose magnitude reflects the strength of the associated new physics contribution at low energies. These coefficients carry implicit dependence on the UV dynamics and encode the imprint of heavy degrees of freedom integrated out at the matching scale  $\Lambda$ .

In practical applications, this expansion is typically truncated at dimension six, since dimension-five effects are highly constrained (notably leading to Majorana neutrino masses via the Weinberg operator), dimension-seven operators are related to lepton number violation and dimension-eight or higher operators are suppressed by additional powers of  $\Lambda$ , making their contributions subleading in most observables.

The SMEFT is constructed under a set of well-motivated theoretical assumptions. First, it is assumed that the underlying UV theory is a decoupling extension of the SM, meaning that the new degrees of freedom are heavy compared to the electroweak scale and their effects can be captured via local operators at low energies. This assumption allows for the use of the Appelquist-Carazzone theorem [50], which justifies integrating out heavy fields. Secondly, the particle content of the low-energy theory is restricted to the SM fields. In particular, no additional light states (such as light scalars, sterile neutrinos, or vector-like fermions) are assumed to be present below the cutoff<sup>2</sup>. Furthermore, the full gauge invariance of the SM, namely  $SU(3)_C \times SU(2)_L \times U(1)_Y$ , is preserved in the effective theory, even after electroweak symmetry breaking, by constructing the operators in the unbroken phase. Finally, it is assumed that the Higgs boson is part of an exact  $SU(2)_L$  doublet, and that electroweak symmetry breaking proceeds linearly through the acquisition of a VEV by the Higgs field, as in the SM.

Should any of these assumptions fail in a given UV completion, for instance in models with a composite Higgs, non-linear EWSB, or light hidden sectors, the SMEFT may no longer provide the appropriate description. While in certain limits SMEFT can still offer a valid approximation even in composite scenarios, in general alternative frameworks such as the Higgs Effective Field Theory (HEFT) [49] become more suitable.

A central task in formulating the SMEFT is identifying a complete, non-redundant set of independent operators at each dimension. This process is highly nontrivial due to the presence of several redundancies as explained in Section 2.1. The most commonly adopted basis (also in this work) at dimension six is known as the *Warsaw basis*, introduced in [32]. It is a minimal, non-redundant, and complete set of operators up to dimension six, constructed from the SM fields with all redundancies properly removed. In the case of a single fermion generation and assuming baryon-number conservation, the Warsaw basis contains 59 operators. When all three generations of fermions are included, and no flavour symmetry is imposed, the number of independent operators grows rapidly, reaching 2499 in the dimension-six sector alone.

The leading BSM contributions to physical processes in SMEFT typically stem from the dimension-six operators. The dimension-five sector is limited to a single operator, the Weinberg operator, which induces Majorana neutrino masses and violates lepton number by two units:

$$\mathcal{O}_\nu^{(5)} = (\bar{L}^c \tilde{H}^*)(\tilde{H}^\dagger L), \quad (2.16)$$

where  $L$  denotes the lepton doublet and  $\tilde{H} = i\sigma_2 H^*$  is the conjugate Higgs doublet.

At dimension six, a wide variety of operators appear. These can be broadly categorised according to their field content and physical effects. One finds operators that modify the Higgs potential and kinetic terms, such as  $|H|^6$  and  $|D_\mu H|^2 |H|^2$ , which can affect Higgs self-interactions and electroweak symmetry breaking. Other operators involve fermion-Higgs couplings, such as  $(H^\dagger H)(\bar{L} H e_R)$ , which lead to corrections to Yukawa interactions and thus to fermion mass and coupling deviations. Four-fermion operators, of the type  $(\bar{L} \gamma^\mu L)(\bar{L} \gamma_\mu L)$  or  $(\bar{Q} \gamma^\mu Q)(\bar{d}_R \gamma_\mu d_R)$ , induce new contact interactions that can mediate flavour-changing processes and affect scattering amplitudes. In addition, dimension-six operators also affect gauge boson dynamics. These include corrections to triple gauge couplings (TGCs), such as those involving  $W$  and  $Z$  bosons, and dipole-type operators of the form  $(\bar{Q} \sigma^{\mu\nu} u_R) \tilde{H} B_{\mu\nu}$ , which introduce electromagnetic moments and modify rare decays. These operators lead to

<sup>2</sup>However, recently, several studies have addressed the inclusion of light new degrees of freedom, such as light scalars [51] and light sterile neutrinos [52] in SMEFT.

observable consequences in precision electroweak tests, Higgs couplings, flavour physics, and more.

As explained in the previous sections, to connect the SMEFT with observables measured at low energies, one must perform the matching procedure. This involves integrating out the heavy SM particles, such as the top quark, Higgs boson,  $W^\pm$ , and  $Z$ , to obtain an appropriate low-energy EFT, typically the WET. Matching is carried out at a scale  $\mu \sim M_W$ , and determines the boundary conditions for the Wilson coefficients of the lower-energy theory in terms of those in SMEFT. The full matching expressions at one-loop are reported in [39]. The Wilson coefficients  $C_i^{(6)}$  evolve with the renormalisation scale  $\mu$  due to quantum corrections. The full one-loop anomalous dimension matrix for SMEFT has been computed in a series of works [53–55], enabling the consistent running of coefficients from the high scale  $\Lambda$  down to the electroweak scale. This running resums large logarithms of the form  $\log(\Lambda/M_W)$  and accounts for operator mixing, which is essential for accurate phenomenological predictions.

When considering the full flavour structure of SMEFT with three generations of fermions, the number of independent Wilson coefficients grows dramatically. In this general flavour setup, the Wilson coefficients can carry generation indices and be complex-valued, introducing a multitude of new sources of flavour and CP violation beyond those present in the SM. To manage this proliferation of parameters, various symmetry assumptions are often introduced [56]. The choice we employ in this work is to assume a  $U(3)^5$  global flavour symmetry acting on the five SM fermion multiplets:  $Q$ ,  $u_R$ ,  $d_R$ ,  $L$ , and  $e_R$ . Under this assumption, the number of independent parameters is greatly reduced at the high scale. This assumption is embedded within the more general framework of Minimal Flavour Violation (MFV), which postulates that the only sources of flavour and CP violation are the SM Yukawa couplings. This ensures that new physics contributions are aligned with the SM flavour structure and automatically satisfies strong experimental constraints from meson mixing, rare decays, and electric dipole moments. We provide a comprehensive list of flavour symmetric and CP invariant operators at dimension six in Table 2.2.

SMEFT has become a unifying framework for analysing a wide range of experimental data. Its operator basis enables a consistent interpretation of precision measurements from various sectors of particle physics. In the Higgs and electroweak sectors, SMEFT operators modify Higgs couplings, triple gauge vertices, and electroweak precision observables, providing constraints from LEP, Tevatron, and LHC data. In flavour physics, operators involving quarks and leptons contribute to meson decays, lepton flavour universality tests, and CP violation observables, offering sensitivity to very high scales due to loop and helicity suppression in the SM. Additionally, dipole operators influence the anomalous magnetic moments of leptons and electric dipole moments of the neutron and electron. Finally, top quark interactions, neutrino scattering cross sections, and low-energy weak processes can all be impacted by SMEFT operators.

A significant body of work has been dedicated to performing global fits of SMEFT coefficients using experimental data from different processes like low-energy experiments [57], electroweak precision tests [58–62] and top physics [63–67], as well as combinations thereof [68–71]. These fits aim to identify the allowed regions of parameter space, determine correlations among Wilson coefficients, and extract the most stringent constraints on the scale  $\Lambda$  of new physics. The SMEFT framework thus serves as a bridge between experimental data and high-scale theories, allowing systematic searches for BSM signals in a model-independent setting. Part I of this thesis is dedicated to the understanding and the improvement of global analysis following the discussions reported in [68, 72]. In contrast, Part II makes extensive use of the Heavy Quark Effective Theory and the Soft-Collinear Effective Theory,

1 : $X^3$		2 : $H^6$		3 : $H^4 D^2$	
$\mathcal{O}_G$	$f^{ABC} G_\mu^{A\nu} G_\nu^{B\rho} G_\rho^{C\mu}$	$\mathcal{O}_H$	$(H^\dagger H)^3$	$\mathcal{O}_{H\Box}$	$(H^\dagger H)\Box(H^\dagger H)$
$\mathcal{O}_W$	$\epsilon^{IJK} W_\mu^{I\nu} W_\nu^{J\rho} W_\rho^{K\mu}$			$\mathcal{O}_{HD}$	$(H^\dagger D_\mu H)^* (H^\dagger D_\mu H)$
4 : $X^2 H^2$		7 : $\psi^2 H^2 D$			
$\mathcal{O}_{HG}$	$H^\dagger H G_{\mu\nu}^A G^{A\mu\nu}$	$\mathcal{O}_{Hl}^{(1)}$	$(H^\dagger i \overleftrightarrow{D}_\mu H)(\bar{l}_p \gamma^\mu l_p)$		
$\mathcal{O}_{HW}$	$H^\dagger H W_{\mu\nu}^I W^{I\mu\nu}$	$\mathcal{O}_{Hl}^{(3)}$	$(H^\dagger i \overleftrightarrow{D}_\mu^I H)(\bar{l}_p \tau^I \gamma^\mu l_p)$		
$\mathcal{O}_{HB}$	$H^\dagger H B_{\mu\nu} B^{\mu\nu}$	$\mathcal{O}_{He}$	$(H^\dagger i \overleftrightarrow{D}_\mu H)(\bar{e}_p \gamma^\mu e_p)$		
$\mathcal{O}_{HWB}$	$H^\dagger \tau^I H W_{\mu\nu}^I B^{\mu\nu}$	$\mathcal{O}_{Hq}^{(1)}$	$(H^\dagger i \overleftrightarrow{D}_\mu H)(\bar{q}_p \gamma^\mu q_p)$		
		$\mathcal{O}_{Hq}^{(3)}$	$(H^\dagger i \overleftrightarrow{D}_\mu^I H)(\bar{q}_p \tau^I \gamma^\mu q_p)$		
		$\mathcal{O}_{Hu}$	$(H^\dagger i \overleftrightarrow{D}_\mu H)(\bar{u}_p \gamma^\mu u_p)$		
		$\mathcal{O}_{Hd}$	$(H^\dagger i \overleftrightarrow{D}_\mu H)(\bar{d}_p \gamma^\mu d_p)$		
8 : $(\bar{L}L)(\bar{L}L)$		8 : $(\bar{R}R)(\bar{R}R)$		8 : $(\bar{L}L)(\bar{R}R)$	
$\mathcal{O}_{\ell\ell}$	$(\bar{l}_p \gamma_\mu l_p)(\bar{l}_s \gamma^\mu l_s)$	$\mathcal{O}_{ee}$	$(\bar{e}_p \gamma_\mu e_p)(\bar{e}_s \gamma^\mu e_s)$	$\mathcal{O}_{le}$	$(\bar{l}_p \gamma_\mu l_p)(\bar{e}_s \gamma^\mu e_s)$
$\mathcal{O}'_{\ell\ell}$	$(\bar{l}_p \gamma_\mu l_s)(\bar{l}_s \gamma^\mu l_p)$	$\mathcal{O}_{uu}$	$(\bar{u}_p \gamma_\mu u_p)(\bar{u}_s \gamma^\mu u_s)$	$\mathcal{O}_{lu}$	$(\bar{l}_p \gamma_\mu l_p)(\bar{u}_s \gamma^\mu u_s)$
$\mathcal{O}_{qq}^{(1)}$	$(\bar{q}_p \gamma_\mu q_p)(\bar{q}_s \gamma^\mu q_s)$	$\mathcal{O}'_{uu}$	$(\bar{u}_p \gamma_\mu u_s)(\bar{u}_s \gamma^\mu u_p)$	$\mathcal{O}_{ld}$	$(\bar{l}_p \gamma_\mu l_p)(\bar{d}_s \gamma^\mu d_s)$
$\mathcal{O}_{qq}^{(3)}$	$(\bar{q}_p \gamma_\mu \tau^I q_p)(\bar{q}_s \gamma^\mu \tau^I q_s)$	$\mathcal{O}_{dd}$	$(\bar{d}_p \gamma_\mu d_p)(\bar{d}_s \gamma^\mu d_s)$	$\mathcal{O}_{qe}$	$(\bar{q}_p \gamma_\mu q_p)(\bar{e}_s \gamma^\mu e_s)$
$\mathcal{O}_{qq}^{(1)'}$	$(\bar{q}_p \gamma_\mu q_s)(\bar{q}_s \gamma^\mu q_p)$	$\mathcal{O}'_{dd}$	$(\bar{d}_p \gamma_\mu d_s)(\bar{d}_s \gamma^\mu d_p)$	$\mathcal{O}_{qu}^{(1)}$	$(\bar{q}_p \gamma_\mu q_p)(\bar{u}_s \gamma^\mu u_s)$
$\mathcal{O}_{qq}^{(3)'}$	$(\bar{q}_p \gamma_\mu \tau^I q_s)(\bar{q}_s \gamma^\mu \tau^I q_p)$	$\mathcal{O}_{eu}$	$(\bar{e}_p \gamma_\mu e_p)(\bar{u}_s \gamma^\mu u_s)$	$\mathcal{O}_{qu}^{(8)}$	$(\bar{q}_p \gamma_\mu T^A q_p)(\bar{u}_s \gamma^\mu T^A u_s)$
$\mathcal{O}_{\ell q}^{(1)}$	$(\bar{l}_p \gamma_\mu l_p)(\bar{q}_s \gamma^\mu q_s)$	$\mathcal{O}_{ed}$	$(\bar{e}_p \gamma_\mu e_p)(\bar{d}_s \gamma^\mu d_s)$	$\mathcal{O}_{qd}^{(1)}$	$(\bar{q}_p \gamma_\mu q_p)(\bar{d}_s \gamma^\mu d_s)$
$\mathcal{O}_{\ell q}^{(3)}$	$(\bar{l}_p \gamma_\mu \tau^I l_p)(\bar{q}_s \gamma^\mu \tau^I q_s)$	$\mathcal{O}_{ud}^{(1)}$	$(\bar{u}_p \gamma_\mu u_p)(\bar{d}_s \gamma^\mu d_s)$	$\mathcal{O}_{qd}^{(8)}$	$(\bar{q}_p \gamma_\mu T^A q_p)(\bar{d}_s \gamma^\mu T^A d_s)$
		$\mathcal{O}_{ud}^{(8)}$	$(\bar{u}_p \gamma_\mu T^A u_p)(\bar{d}_s \gamma^\mu T^A d_s)$		

**Table 2.2:** Flavour symmetric and CP even dimension-six SMEFT operators in the Warsaw basis.

which we introduce in the following two sections.

## 2.4 The Heavy Quark Effective Theory

The Heavy Quark Effective Theory (HQET) [73–75], is an effective field theory tailored to describe the low-energy dynamics of hadrons containing a single heavy quark, such as bottom mesons. Its conceptual foundation lies in the observation that, in the limit where the heavy quark mass  $m_Q$  is much larger than the QCD confinement scale  $\Lambda_{\text{QCD}}$ , certain simplifications arise in the structure of QCD. These simplifications manifest themselves as new approximate symmetries that are not evident in the full QCD Lagrangian. HQET provides a systematic framework to exploit these symmetries by organising the dynamics of heavy-light systems in an expansion in powers of  $\Lambda_{\text{QCD}}/m_Q$ .

In full QCD, the Lagrangian for a heavy quark field  $Q(x)$  is given by

$$\mathcal{L}_{\text{QCD}}^{\text{heavy}} = \bar{Q}(i\not{D} - m_Q)Q, \quad (2.17)$$

where  $D_\mu$  denotes the covariant derivative including the gluon field. However, when  $m_Q \gg \Lambda_{\text{QCD}}$ , the heavy quark cannot be excited far off its mass shell by soft QCD interactions. This suggests that its dynamics can be effectively separated into a fast-moving, on-shell part, and small residual fluctuations due to interactions with the light degrees of freedom.

To make this separation explicit, one writes the heavy quark momentum as  $p^\mu = m_Q v^\mu + k^\mu$ , where  $v^\mu$  is the four-velocity of the hadron (with  $v^2 = 1$ ), and  $k^\mu$  is a small residual momentum associated with the motion of the heavy quark inside the hadron. The field  $Q(x)$  is then decomposed into velocity-dependent fields via the field redefinition

$$Q(x) = e^{-im_Q v \cdot x} [h_v(x) + H_v(x)], \quad (2.18)$$

where  $h_v(x)$  is the so-called large component field, and  $H_v(x)$  is the small component field, both depending on the residual momentum  $k^\mu$ . This decomposition allows the integration out of the small component  $H_v(x)$ , which is off-shell by an amount of order  $2m_Q$ , yielding the effective HQET Lagrangian.

At leading order in the  $1/m_Q$  expansion, the HQET Lagrangian reads

$$\mathcal{L}_{\text{HQET}}^{(0)} = \bar{h}_v i v \cdot D h_v, \quad (2.19)$$

which describes a static color source moving with velocity  $v^\mu$ . This Lagrangian exhibits an emergent spin-flavour symmetry: in the heavy quark limit, the interactions of the heavy quark with gluons do not depend on its spin or mass, as long as the velocity is fixed. Consequently, hadronic matrix elements become independent of the heavy quark flavour (e.g.,  $b$  or  $c$ ), and of the spin of the heavy quark. This leads to powerful relations among observables such as decay constants and form factors, notably those involved in  $B \rightarrow D^{(*)} \ell \nu$  transitions.

Corrections to the leading-order Lagrangian are systematically incorporated by expanding in powers of  $1/m_Q$ . At order  $1/m_Q$ , two additional operators appear:

$$\mathcal{L}_{\text{HQET}}^{(1)} = \frac{1}{2m_Q} [\mathcal{O}_{\text{kin}} + \mathcal{O}_{\text{mag}}] = \frac{1}{2m_Q} \left[ \bar{h}_v (iD_\perp)^2 h_v + C_{\text{mag}}(\mu) \bar{h}_v \frac{g_s}{2} \sigma^{\mu\nu} G_{\mu\nu} h_v \right], \quad (2.20)$$

where  $D_\perp^\mu = D^\mu - v^\mu (v \cdot D)$  projects onto directions orthogonal to  $v^\mu$ , and  $G_{\mu\nu}$  is the gluon field strength tensor. The operator  $\mathcal{O}_{\text{kin}}$  encodes the residual kinetic energy of the heavy quark inside the hadron, while  $\mathcal{O}_{\text{mag}}$  accounts for spin-dependent chromomagnetic interactions that break heavy quark spin symmetry. The coefficient  $C_{\text{mag}}(\mu)$  captures short-distance QCD corrections and is determined by matching HQET to full QCD at a scale  $\mu \sim m_Q$ .

The effective theory thus organises physical amplitudes as a power series in  $\Lambda_{\text{QCD}}/m_Q$ :

$$\mathcal{A} = \mathcal{A}^{(0)} + \frac{\Lambda}{m_Q} \mathcal{A}^{(1)} + \left( \frac{\Lambda}{m_Q} \right)^2 \mathcal{A}^{(2)} + \dots, \quad (2.21)$$

where each term can be computed within HQET and matched to experimental data or lattice QCD results. In processes involving heavy-to-heavy transitions, such as  $B \rightarrow D^{(*)} \ell \nu$ , the leading-order matrix elements are governed by a single universal form factor known as the Isgur-Wise function  $\xi(w)$  [76], which depends only on the velocity transfer  $w = v \cdot v'$ . All other form factors receive corrections suppressed by  $1/m_Q$  or higher powers.

Another important application of HQET lies in the analysis of heavy meson spectroscopy. The mass of a heavy-light meson can be expanded as

$$M_{H_Q} = m_Q + \bar{\Lambda} - \frac{\lambda_1}{2m_Q} + d_H \frac{\lambda_2}{2m_Q} + \mathcal{O}\left(\frac{1}{m_Q^2}\right), \quad (2.22)$$

where  $\bar{\Lambda}$  denotes the residual mass of the light degrees of freedom,  $\lambda_1$  is associated with the kinetic operator, and  $\lambda_2$  with the chromomagnetic interaction. The coefficient  $d_H$  depends on the total spin of the hadron. This relation successfully explains the observed pattern of hyperfine splittings, such as the mass difference between  $B$  and  $B^*$  mesons.

HQET also plays a key role in the extraction of CKM matrix elements, particularly  $|V_{cb}|$ , from exclusive semileptonic decays. By providing model-independent relations among form factors and constraining their normalisation at zero recoil, HQET significantly reduces theoretical uncertainties in the interpretation of experimental data.

Renormalisation in HQET introduces its own set of challenges. Since the effective theory breaks Lorentz invariance explicitly due to the presence of a fixed velocity vector  $v^\mu$ , operator mixing under renormalisation becomes more intricate. The running of Wilson coefficients is again governed by renormalisation group equations, allowing large logarithms of the form  $\log(m_Q/\mu)$  to be resummed via RGE.

The relevance of HQET for this thesis resides in the fact that HQET offers a systematic framework to incorporate non-perturbative effects in the calculation of the inclusive  $\bar{B} \rightarrow X_s \gamma$  decay rate. Within this approach, hadronic matrix elements can be expanded in inverse powers of  $m_b$ , and each term in the expansion is governed by a finite number of HQET parameters. Although these parameters cannot be determined analytically, they are process-independent due to heavy-quark symmetries, thus ensuring a degree of universality. The leading term in the expansion reproduces the partonic result, while power corrections to the total rate emerge only at  $\mathcal{O}(1/m_b^2)$  [77]. Nonetheless, the breakdown of the local operator product expansion (OPE) in the kinematic endpoint region necessitates a non-local treatment, which is captured through the introduction of the so called shape function. While this addresses the limitations of the OPE, the inclusion of radiative corrections within this framework remains subtle. A more rigorous treatment of these subtleties, particularly in the endpoint region, requires the formalism of Soft-Collinear Effective Theory which will be the focus of the next section.

## 2.5 The Soft-Collinear Effective Theory

Soft-Collinear Effective Theory (SCET) [78, 79] is an effective field theory that provides a systematic framework to describe processes involving energetic light degrees of freedom, especially when they propagate close to the light cone. It is particularly well-suited to treat processes, such as  $B$ -meson decays into light final-state particles. Unlike HQET, which focuses on the static limit of heavy quarks, SCET addresses the dynamics of energetic light quarks and gluons and their interactions with soft and collinear degrees of freedom. It achieves this by performing an expansion in a small parameter  $\lambda$ , which characterises the hierarchy between the hard, collinear, and soft scales in the problem.

Before delving into the construction of SCET, it is useful to briefly discuss the strategy of regions [80]. This technique provides a systematic framework for performing asymptotic expansions of loop integrals in dimensional regularisation around various kinematic limits. The integration domain is decomposed into distinct momentum regions, and the integrand

is correspondingly expanded according to the characteristic scaling of the loop momenta in each region. In SCET, these regions are promoted to distinct dynamical fields of the effective theory, representing soft and collinear degrees of freedom. The integrals obtained through the method of regions then correspond to Feynman diagrams computed within the effective theory in dimensional regularisation. While for simple perturbative expansions the strategy of regions alone may suffice, the use of an effective field theory offers several additional advantages: it provides a systematic framework for deriving factorisation theorems and enables the resummation of logarithmically enhanced contributions to all orders via the renormalisation group. Furthermore, gauge invariance is manifest in the effective Lagrangian, and power-suppressed corrections can be organised in a consistent and controlled expansion.

To construct SCET, one begins by identifying relevant momentum modes and organising the dynamics according to the power counting in  $\lambda \ll 1$ . A generic light-like momentum can be decomposed using two light-cone vectors  $n^\mu$  and  $\bar{n}^\mu$ , satisfying

$$n^2 = \bar{n}^2 = 0, \quad n \cdot \bar{n} = 2. \quad (2.23)$$

Given any four-momentum  $p^\mu$ , one can decompose it as

$$p^\mu = \frac{1}{2}(n \cdot p)\bar{n}^\mu + \frac{1}{2}(\bar{n} \cdot p)n^\mu + p_\perp^\mu, \quad (2.24)$$

where  $p_\perp^\mu$  denotes the components transverse to both  $n^\mu$  and  $\bar{n}^\mu$ .

In the context of SCET, one typically considers collinear momenta aligned with a direction  $n^\mu$ , satisfying the scaling

$$p_c^\mu \sim Q(\lambda^2, 1, \lambda), \quad (2.25)$$

where the components are given in terms of  $(n \cdot p, \bar{n} \cdot p, p_\perp)$ , and  $Q$  is a hard scale in the process, such as the  $b$ -quark mass  $m_b$  or the large energy of the final-state light meson. The soft momenta, describing soft gluons and light quarks, scale as

$$p_s^\mu \sim Q(\lambda, \lambda, \lambda), \quad (2.26)$$

while the hard modes (integrated out of the theory) scale as

$$p_H^\mu \sim Q(1, 1, 1). \quad (2.27)$$

The effective degrees of freedom in SCET include:

- Collinear quark fields  $\xi_n(x)$  moving along the  $n^\mu$  direction.
- Collinear gluon fields  $A_n^\mu(x)$  with similar scaling.
- Soft fields  $q_s(x), A_s^\mu(x)$  describing low-momentum modes.
- Ultrasoft (usoft) fields in the original SCET formulation, which are now more often described by soft modes due to field redefinitions.

Collinear quarks obey the constraint

$$\frac{\not{n}\not{\eta}}{4}\xi_n = \xi_n, \quad (2.28)$$

which projects onto the appropriate spinor components that propagate in the  $n^\mu$  direction.

The SCET Lagrangian is organised as an expansion in powers of  $\lambda$ . At leading order, the collinear quark Lagrangian reads:

$$\mathcal{L}_{\xi_n}^{(0)} = \bar{\xi}_n \left( in \cdot D + i\cancel{D}_{\perp c} \frac{1}{i\bar{n} \cdot D_c} i\cancel{D}_{\perp c} \right) \frac{\cancel{n}}{2} \xi_n, \quad (2.29)$$

where  $D_c^\mu = \partial^\mu - igA_n^\mu$  is the covariant derivative with respect to collinear gluons. The Lagrangian is manifestly gauge-invariant under collinear gauge transformations.

For soft quark fields, the leading-order Lagrangian is simply the QCD Lagrangian restricted to soft momenta:

$$\mathcal{L}_{q_s}^{(0)} = \bar{q}_s i\cancel{D}_s q_s, \quad (2.30)$$

where  $D_s^\mu = \partial^\mu - igA_s^\mu$  is the soft covariant derivative.

To preserve gauge invariance under both collinear and soft transformations, SCET introduces Wilson lines. For collinear gauge invariance, one defines the collinear Wilson line:

$$W_c(x) = \mathbf{P} \exp \left( ig \int_{-\infty}^0 ds \bar{n} \cdot A_c(x + s\bar{n}) \right), \quad (2.31)$$

where  $\mathbf{P}$  is the path ordering of colour matrices. Similarly, the soft Wilson line ensures soft gauge invariance and describes the eikonal interactions between soft gluons and energetic partons:

$$S_n(x) = \mathbf{P} \exp \left( ig \int_{-\infty}^0 ds n \cdot A_s(x + sn) \right). \quad (2.32)$$

These Wilson lines appear in operator definitions and factorised amplitudes and play a central role in encoding gauge invariance and in resummation.

A crucial property of SCET is that, at leading power, soft and collinear degrees of freedom decouple in the Lagrangian via field redefinitions:

$$\xi_n(x) \rightarrow S_n(x) \xi_n^{(0)}(x), \quad A_n^\mu(x) \rightarrow S_n(x) A_n^{(0)\mu}(x) S_n^\dagger(x). \quad (2.33)$$

In this rotated basis, the Lagrangian factorises into independent soft and collinear parts, and interactions between them are confined to external operators and Wilson lines. This decoupling is the foundation of factorisation theorems in SCET, allowing one to compute short-distance coefficients separately from long-distance nonperturbative matrix elements.

One of the central pillars of the SCET formalism is the use of matching and RGE to disentangle physics at different energy scales. The separation of scales is exploited by systematically integrating out heavy (hard) degrees of freedom, and encoding their effects in operators with scale-dependent Wilson coefficients.

Matching in this effective theory refers to the procedure of equating full QCD matrix elements with corresponding SCET matrix elements at a common scale  $\mu \sim Q$ , where both descriptions are valid. Since the hard modes with virtuality  $\sim Q^2$  are not dynamical in SCET, their effects are encoded into Wilson coefficients multiplying effective operators. The matching condition takes the schematic form:

$$\langle \mathcal{O}_{\text{QCD}} \rangle = C(\mu) \langle \mathcal{O}_{\text{SCET}}(\mu) \rangle + \mathcal{O} \left( \frac{\lambda}{Q} \right), \quad (2.34)$$

where  $C(\mu)$  is a short-distance matching coefficient and  $\mathcal{O}_{\text{SCET}}$  is a gauge-invariant operator constructed from SCET fields. Matching is typically performed at fixed order in  $\alpha_s$  by

evaluating both sides of the equation perturbatively using on-shell external states, with IR divergences canceling between the two sides, and UV divergences absorbed into  $C(\mu)$ .

As an example, consider the matching of a full QCD current like  $\bar{q}\gamma^\mu b$  onto SCET:

$$\bar{q}(x)\gamma^\mu b(x) \rightarrow C(\mu) \cdot [\bar{\xi}_n(x)W_n(x)\gamma^\mu h_v(x)] + \mathcal{O}(\lambda), \quad (2.35)$$

where  $h_v$  is the HQET field for the  $b$ -quark, and  $W_n$  is the collinear Wilson line ensuring gauge invariance.

Once hard modes are integrated out, the RG evolution governs how the Wilson coefficients evolve from the hard matching scale  $\mu_H \sim Q$  to lower scales associated with collinear or soft modes (e.g.,  $\mu_c \sim Q\lambda$ ,  $\mu_s \sim Q\lambda^2$ ). This evolution sums large logarithms of scale ratios  $\log(\mu_H/\mu)$  that appear in fixed-order calculations.

In many applications, multiple matching steps are required. For example:

- First, matching full QCD onto SCET<sub>I</sub> at  $\mu \sim m_b$ .
- Then, matching SCET<sub>I</sub> onto SCET<sub>II</sub> at an intermediate hard-collinear scale  $\mu \sim \sqrt{m_b\Lambda_{\text{QCD}}}$ , if present.
- Finally, evolving down to a hadronic scale  $\mu \sim 1$  GeV, where matrix elements are computed or parametrised.

The running of operators and Wilson coefficients is typically governed by cusp anomalous dimensions and other universal RG structures, especially in processes involving light-like Wilson lines [81, 82]. These allow for all-order resummation of Sudakov double logarithms [83] via evolution equations.

The combination of all of these tools allows SCET to cleanly factorise physical observables into distinct components, typically factorisation reads as

$$\text{Observable} = H(Q, \mu_H) \cdot J(\mu_J) \cdot S(\mu_S), \quad (2.36)$$

where  $H$  is a hard coefficient from matching,  $J$  is a jet function describing collinear dynamics, and  $S$  is a soft function encoding long-distance physics. The resummation of large logarithms of the ratios  $Q^2/\mu_J^2$  and  $\mu_J^2/\mu_S^2$  is achieved by solving the respective RG equations separately for each component.

This systematic separation of scales and resummation of logarithms is a major strength of SCET, enabling precision predictions for a wide class of QCD processes involving heavy hadron decays or jets.

In the context of inclusive  $B$ -meson decays, SCET is particularly powerful providing a framework for analysing the decay  $\bar{B} \rightarrow X_s\gamma$  in the kinematic region where the photon energy is near its endpoint. In this regime, the decay rate is dominated by configurations in which the hadronic final state is composed of energetic, collinear partons recoiling against the photon. SCET enables the derivation of a factorisation theorem valid at leading power in  $\Lambda_{\text{QCD}}/m_b$ , which separates contributions from different energy scales. At leading order, the differential decay rate admits the schematic form [82, 84]:

$$\frac{d\Gamma(\bar{B} \rightarrow X_s\gamma)}{dE_\gamma} \sim H \cdot J \otimes S, \quad (2.37)$$

where  $H$  is the hard function encoding short-distance physics at the scale  $\mu_H \sim m_b$ ,  $J$  is the jet function describing collinear dynamics at the intermediate scale  $\mu_J \sim \sqrt{m_b\Lambda_{\text{QCD}}}$ ,

and  $S$  is the non-perturbative shape function capturing soft physics at the hadronic scale  $\mu_S \sim \Lambda_{\text{QCD}}$ . The symbol  $\otimes$  denotes a convolution in light-cone momentum.

This framework also sets the stage for systematic improvements. On the perturbative side, the hard and jet functions can be computed to higher orders in  $\alpha_s$ . While on the power expansion side, the factorisation theorem can be extended beyond the leading power in  $\Lambda_{\text{QCD}}/m_b$ , allowing for a more accurate description of subleading effects. These higher-order corrections, both perturbative and power-suppressed, are crucial for pushing theoretical predictions to match the experimental precision. Part II of this thesis is dedicated to computing the NLO (in  $\alpha_s$ ) corrections to the interference term between the operators  $Q_1^q$  and  $Q_{7\gamma}$  at subleading power in the  $1/m_b$  expansion, following partially the discussion in [85, 86].

Part I

Global Analyses of the *Minimal*  
MFV SMEFT



# Introduction to Global Analyses

## Contents

---

<b>3.1</b>	<b>The Importance of Global Analyses in the SMEFT . . . . .</b>	<b>27</b>
<b>3.2</b>	<b>Present Status of Global Analyses . . . . .</b>	<b>28</b>
<b>3.3</b>	<b>Statistical Framework of Global Analyses in the SMEFT . . . . .</b>	<b>31</b>
<b>3.4</b>	<b>Input Schemes in the SMEFT . . . . .</b>	<b>32</b>

---

## 3.1 The Importance of Global Analyses in the SMEFT

As we discussed in Chapter 2, in the SMEFT framework, the effects of heavy new physics are parameterised through higher-dimensional operators. These operators are multiplied by Wilson coefficients that encapsulate the underlying ultraviolet dynamics in a model-independent way. However, given the large dimensionality of the operator basis at dimension six, especially once flavour, CP-violating, and baryon/lepton number violating sectors are fully taken into account, the task of extracting meaningful and consistent bounds on the Wilson coefficients requires a systematic and comprehensive approach. Generic NP models match on a multitude of Wilson coefficients, especially when loop matching is considered [87], therefore in order to extract phenomenologically relevant bounds all the coefficients compatible with symmetry information must be taken into account. This is the core motivation behind global SMEFT analyses. The term global analysis refers to the simultaneous fit of multiple experimental observables to the full set of relevant Wilson coefficients. These observables can span diverse energy regimes and physical sectors, including EWPO, Higgs measurements, diboson production, top-quark couplings, flavour-changing neutral currents, low-energy effective couplings, and parity-violating observables. Importantly, many SMEFT operators contribute simultaneously to multiple observables across these sectors, often inducing correlations that are both numerically and phenomenologically significant.

One of the main reasons global fits are indispensable is that they account for interferences and degeneracies among operator contributions. In a theory with so many effective operators, the impact of any single operator on a given observable can often be compensated or masked by the contributions of others. These correlations can arise from the LO contribution to the physical amplitudes, but also from operator mixing under RGE or NLO contributions. By fitting all relevant operators simultaneously, global analyses can correctly capture these correlation patterns and provide bounds that reflect the true sensitivity of

current data, avoiding the overly stringent and often misleading constraints obtained under the one-operator-at-a-time assumption.

Moreover, global analyses are designed to incorporate experimental correlations across measurements, which are typically encoded in published covariance matrices. These correlations can significantly affect the shape of the likelihood in the multidimensional space of Wilson coefficients, especially when different observables are derived from the same experimental dataset or share systematic uncertainties. Ignoring these correlations would compromise the statistical consistency of the fit and misrepresent the true reach of the data.

Another essential virtue of the global approach lies in its capacity to coherently combine measurements across disparate energy scales. Observables in SMEFT are typically computed at different scales but Wilson coefficients are defined at the high scale  $\Lambda$  where the new physics is integrated out. To relate the coefficients to physical observables, one must perform RGE and matching, accounting for operator mixing and threshold corrections. Global fits enforce this consistency across scales by solving the full RG flow and matching equations at the required loop order, ensuring that the extracted bounds are physically meaningful and robust under scale variations.

As experimental precision continues to improve, especially with LHC Run 3 data and future high-luminosity runs, another critical challenge emerges: the critical study of subleading effects in the EFT expansion [88]. These include quadratic contributions from dimension-six operators (important when linear effects are suppressed), as well as dimension-eight corrections that may not be negligible in high-energy tails of distributions. A well-constructed global fit must explicitly check the validity of the EFT expansion in the kinematic regions under consideration, often imposing energy cuts to maintain control over truncation errors.

Lastly, global SMEFT fits offer a unique and model-independent bridge between experimental data and ultraviolet completions. Once bounds on Wilson coefficients are extracted from data, one can map them onto specific BSM scenarios via tree-level or loop-level matching, effectively translating the results into constraints on heavy particle masses and couplings. This procedure allows global fits to be used both as discovery tools, by highlighting tensions or deviations from the SM, and as diagnostic tools, by identifying which operator combinations are most sensitive to future data.

In summary, global analyses constitute a cornerstone of modern SMEFT phenomenology. They integrate a broad and diverse set of measurements within a consistent EFT framework, account for theoretical and experimental correlations, and provide reliable and informative constraints on physics BSM. As we are moving into an era of precision-driven discovery, such analyses will remain central to interpreting data and guiding theoretical exploration.

## 3.2 Present Status of Global Analyses

Having assessed the role of global analyses in the previous section, we now turn to a discussion of their current status and the challenges that remain. Global analyses within the SMEFT have rapidly evolved from exploratory, process-specific studies to comprehensive, multi-observable programmes that aim to map out the space of possible low-energy imprints of high-scale UV physics in a model-independent way. The conceptual groundwork for this enterprise is the systematic operator expansion itself: beginning with the early effective-Lagrangian enumerations and made rigorous in contemporary operator bases, the field now routinely organises effects at dimension six and beyond through well-defined bases such as the Warsaw basis we introduced in Chapter 2. This operator classification both clarifies the counting of independent directions in theory space and provides a common language for

comparing results across different fits.

Building on this foundation, the literature over the last decade has produced a variety of global fits that differ in scope, assumptions and methodology. Initial efforts typically focused on restricted subsectors like low-energy experiments [57], electroweak precision tests and Higgs physics [58–62] or top [63–67], exploiting process-specific observables to obtain robust bounds on a limited set of Wilson coefficients. Over time these separate analyses have been merged into genuinely global programmes that combine low-energy precision data, electroweak observables, Higgs measurements, top and diboson processes, flavour constraints and collider differential distributions. This transition has been made possible both by the accumulation of high-precision experimental results and by advances in the theoretical machinery for predicting SMEFT effects across disparate processes. In this thesis, we present a combined fit of a wide range of observables with the aim of constraining the *minimal* MFV SMEFT, defined by imposing a  $U(3)^5$  flavour symmetry on dimension-six operators [56]. This constitutes a further step forward, since most existing fits are largely data-driven, where the choice of relevant operators is dictated by the available measurements. By contrast, in this work the operator set is determined by a well-motivated symmetry assumption, in a UV-inspired manner, and we then assemble the dataset required to test and constrain this hypothesis.

Methodologically, the field today stands on several pillars. First, there has been a clear movement towards open, software-based toolchains that codify the fit logic, data ingestion, basis rotations and uncertainty propagation in reproducible frameworks. The SMEFiT [89] project, for example, exemplifies this software-first approach: it supplies a flexible, open implementation for performing high-dimensional inference in SMEFT that can accommodate different operator bases, sampling algorithms, and post-processing diagnostics, thereby reducing analyst bias and enabling global community validation. Other projects developing along the same lines are: *Fitmaker* [69], *Sfitter* [90], *HEPfit* [91] and *Smelli* [92].

Second, only very recently in the framework of global analyses, there is growing possibility to pursue a consistent global programme explicitly accounting for higher-order theoretical effects and RGE. Neglecting such corrections can result in a misestimation of constraints, especially when observables probe widely separated energy scales. Recent studies have therefore incorporated NLO SMEFT corrections [68, 93–101] together with RGE running [72, 102–110], thereby improving theoretical control and enabling meaningful comparisons between low- and high-energy data. This thesis contributes to this line of work by including both partial NLO corrections and RGE, with a particular emphasis on assessing their impact on the outcome of the global analysis. Here, we will not only show the impact of these corrections on the bounds but also on correlations and global interpretations.

Third, modern global fits rely on a broad suite of statistical techniques, ranging from nested sampling [111] and Markov Chain Monte Carlo [112] to systematic use of profiling, principal-component analysis, and closure tests, in order to characterise correlations, degeneracies, and the effective number of constrained directions within the high-dimensional Wilson-coefficient space. The following section provides an introduction to this statistical framework, which is highly relevant for this thesis.

Despite these advances, several recurring challenges define the current frontier. The first is dimensionality and degeneracy: even restricting to dimension-six operators the parameter space is large and, once flavour indices are counted, rapidly becomes enormous (2499 independent operators); this abundance of directions generates near-flat combinations that are only weakly constrained by present data, so that physical conclusions often depend sensitively on flavour assumptions. Imposing symmetry assumptions (for instance minimal flavour violation or  $U(3)^5$  flavour symmetry) is a pragmatic and theoretically motivated way to re-

strict the study to well-defined classes of UV models and to reduce the parameter count. Recent works, including this one, have explored both the benefits and the biases introduced by such assumptions. This thesis provides a foundation for extending global analyses to increasingly general flavour assumptions, particularly within the framework of MFV. A second major difficulty is theoretical precision. Many observables used in global fits require Standard Model predictions at high perturbative accuracy and with well-quantified uncertainties; correspondingly, SMEFT predictions should include NLO corrections, operator mixing under RGE, and a careful treatment of the EFT truncation uncertainty (i.e., the omitted higher-dimension terms). The interplay between experimental precision and theoretical systematics means that pushing sensitivity to subtle deviations often demands significant theoretical investment, both analytic and computational, to avoid biasing the fits. While, as discussed above, higher-loop corrections are now being included in global analyses, another important conceptual and practical issue concerns the treatment of contributions beyond the linear dimension-six approximation. At order  $\mathcal{O}(1/\Lambda^4)$ , two types of effects arise: the quadratic terms of dimension-six operators and the interference of dimension-eight operators with the SM. While global fits have traditionally focused on linear dimension-six effects, the neglect of higher-order contributions can bias constraints, especially in regions of parameter space where quadratic terms become numerically comparable to the linear ones. This problem is exacerbated in observables that are accidentally suppressed at interference level, such as certain diboson or four-fermion processes, where the squared dimension-six amplitudes may provide the leading SMEFT sensitivity [89]. On the other hand, retaining dimension-six squared terms without including dimension-eight operators raises issues of consistency, since both contribute at the same EFT order. The literature has therefore debated whether quadratic dimension-six terms can be pragmatically included as an estimate of sensitivity, or whether this approach risks overstating the validity of the EFT expansion. Recent studies [113–115] have highlighted that systematic inclusion of dimension-eight operators is still a complicated problem, due to the large operator basis and the lack of complete matching calculations, but progress is being made in classifying their phenomenological impact and in developing strategies for truncation-error estimates [116–119]. In the following, we perform a linear fit at dimension six, while critically addressing the potential impact of sizeable quadratic contributions. This issue becomes particularly relevant in the computation of dijet production, which will be discussed later in this chapter. Looking ahead, future collider programmes are expected to play a decisive role in advancing global SMEFT analyses. High-luminosity upgrades such as the HL-LHC will greatly improve the statistical power and precision of key observables, thereby tightening constraints on many Wilson coefficients. Beyond that, proposed machines like the FCC-ee, ILC, EIC, or CEPC, with their clean experimental environments and per-mille level precision, are uniquely suited to probe electroweak and Higgs observables where SMEFT effects manifest most clearly. Hadron colliders at higher energies, such as the FCC-hh, will extend the reach to new kinematic regimes, enhancing sensitivity to operators that grow with energy and allowing complementary constraints to those from lepton colliders. Together, these facilities will not only reduce existing degeneracies in the Wilson-coefficient space but also enable systematic exploration of currently inaccessible directions. Incorporating projected measurements from future colliders into global fits thus represents a natural and powerful step toward a more complete and robust mapping of the SMEFT parameter space [120–122].

### 3.3 Statistical Framework of Global Analyses in the SMEFT

The extraction of meaningful bounds on the Wilson coefficients  $C_i$  in the SMEFT relies on a rigorous statistical treatment of the available experimental data. In the context of global fits, this is achieved through the construction of a likelihood function, or equivalently a  $\chi^2$  function, which compares theoretical SMEFT predictions to experimental measurements, taking into account the full covariance structure of the data. We define the  $\chi^2$  function as

$$\chi^2(C_i) = \left( \vec{d} - \vec{p}(C_i) \right)^T V^{-1} \left( \vec{d} - \vec{p}(C_i) \right), \quad (3.1)$$

where:

- $\vec{d}$  is the vector of experimental data,
- $\vec{p}(C_i)$  is the vector of SMEFT predictions, which depend linearly (or at times quadratically) on the Wilson coefficients  $C_i$ ,
- $V$  is the covariance matrix encoding experimental (and potentially theoretical) uncertainties and their correlations.

Predictions in terms of the Wilson coefficients  $C_i$ , can be written as:

$$\vec{p}(C_i) = \vec{p}^{\text{SM}} + \sum_i \frac{C_i}{\Lambda^2} \vec{p}_i^{(1)} + \sum_{i,j} \frac{C_i C_j}{\Lambda^4} \vec{p}_{ij}^{(2)} + \dots, \quad (3.2)$$

where  $\vec{p}^{\text{SM}}$  is the Standard Model prediction, and the remaining terms encode SMEFT corrections at linear and quadratic order.

In a global fit, we are typically interested in placing bounds on individual coefficients (or subsets of them), while marginalising or profiling over the remaining directions in parameter space. Profiling involves maximising the likelihood (or minimising the  $\chi^2$ ) with respect to the nuisance parameters and remaining coefficients for fixed values of the coefficients of interest. In our setup, this is done using the toy Monte Carlo (MC) method.

The toy MC approach consists of generating synthetic datasets  $\vec{d}^{\text{toy}}$  from the known experimental distribution, typically assuming a multivariate Gaussian with central value  $\vec{d}$  and covariance  $V$ . The best fit value is obtained minimising the  $\chi^2$  and for each pseudo-experiment, the fit is repeated. The best-fit values of the parameter of interest are recorded, and a cumulative histogram of these values is constructed.

The procedure can be summarised as follows:

1. Generate  $N$  toy datasets  $\{\vec{d}^{(k)}\}$  from  $\mathcal{N}(\vec{d}, V)$ .
2. For each toy, minimise  $\chi^2(C_i)$  with respect to the vector of Wilson coefficients.
3. Build a multi-dimensional histogram collecting all the minima previously evaluated, which in linear fits distribute as a Gaussian.
4. Determine the confidence interval for  $C_i$  by finding the values of the standard deviations of these Gaussian distributions.

While this method gives us access directly to the bounds and the correlations, in order to study how linear combinations of coefficients are constrained in the fit we need another

statistical method: the Fisher information matrix. Assuming a Gaussian likelihood, the Fisher matrix is defined as

$$F_{ij} = \frac{1}{2} \frac{\partial^2 \chi^2(C)}{\partial C_i \partial C_j} \Big|_{C=0}. \quad (3.3)$$

In the linear SMEFT regime, this reduces to

$$F_{ij} = \left( \vec{p}_i^{(1)} \right)^T V^{-1} \vec{p}_j^{(1)}, \quad (3.4)$$

where  $\vec{p}_i^{(1)} = \partial \vec{p} / \partial C_i$  is the SMEFT shift in the observables due to the operator  $\mathcal{O}_i$ . The Fisher matrix captures the curvature of the likelihood around the SM point and determines the shape and orientation of the confidence ellipsoids in parameter space.

The inverse of the Fisher matrix (when it exists) approximates the covariance matrix of the parameter estimates:

$$\text{Cov}[C_i, C_j] \approx (F^{-1})_{ij}. \quad (3.5)$$

Therefore, eigenvalues and eigenvectors of  $F$  also provide insight into the most and least constrained directions in parameter space, through a procedure called Principal Component Analysis (PCA). PCA is used in SMEFT fits to identify optimal linear combinations of Wilson coefficients that are constrained by the data. Given the Fisher matrix (or the full posterior covariance from the fit), one diagonalises it to obtain eigenvectors  $v^{(k)}$  and corresponding eigenvalues  $\lambda_k$ . The directions with the largest eigenvalues (smallest variances) are the best constrained combinations of operators:

$$F v^{(k)} = \lambda_k v^{(k)}. \quad (3.6)$$

The eigenvectors define new orthogonal coordinates in parameter space:

$$C_i = \sum_k \alpha_k v_i^{(k)}, \quad (3.7)$$

where the coefficients  $\alpha_k$  represent projections onto the principal components. This decomposition is particularly useful because it clarifies the effective information that can be extracted from the data. In particular, it makes it possible to quantify how many independent directions in the parameter space are genuinely constrained, while at the same time exposing potential degeneracies or flat directions, corresponding to null eigenvalues of the covariance matrix. Moreover, it naturally provides a physically motivated basis for presenting the results of the fit, for instance by quoting bounds on the combinations of operators that are actually best constrained.

### 3.4 Input Schemes in the SMEFT

An additional physics aspect that deserves consideration is the choice of the electroweak input parameters. In our analysis, we employ the input parameter set  $\{\alpha, M_Z, G_F\}$  to fix the electroweak sector of the SM. These three quantities are experimentally measured with very high precision and serve as a convenient and theoretically consistent basis for computing observables within both the SM and the SMEFT framework.

The three input parameters are defined as:

- $\alpha \equiv \alpha_{\text{em}}(0)$ : the electromagnetic fine-structure constant at zero momentum transfer,
- $M_Z$ : the physical mass of the  $Z$  boson,
- $G_F$ : the Fermi constant extracted from the muon lifetime via the relation

$$\frac{1}{\tau_\mu} = \frac{G_F^2 m_\mu^5}{192\pi^3} (1 + \text{radiative corrections}). \quad (3.8)$$

This input scheme is commonly referred to as the  $\{\alpha, M_Z, G_F\}$  scheme and is one of several viable choices (others include the  $\{M_W, M_Z, G_F\}$  or  $\{\alpha, M_Z, M_W\}$  schemes). The choice of input schemes affects how the remaining electroweak parameters, such as the weak mixing angle and the  $W$ -boson mass, are computed [123].

From the input parameters, one can determine other electroweak quantities at tree level. For instance, the sine of the weak mixing angle  $\theta_W$  is defined via:

$$\sin^2 \theta_W^{(0)} = 1 - \frac{M_W^2}{M_Z^2}, \quad (3.9)$$

while the relation between the Fermi constant and the gauge couplings at tree level is given by:

$$G_F = \frac{\pi\alpha}{\sqrt{2}M_W^2 \sin^2 \theta_W}. \quad (3.10)$$

Combining these equations yields a tree-level prediction for the  $W$ -boson mass in the SM:

$$M_W^{(0)} = M_Z \left( \frac{1}{2} + \sqrt{\frac{1}{4} - \frac{\pi\alpha}{\sqrt{2}G_F M_Z^2}} \right)^{1/2}. \quad (3.11)$$

In the SMEFT, dimension-6 operators modify the relations among electroweak parameters, leading to shifts in derived quantities like  $M_W$  and  $\sin^2 \theta_W$ , which can be tested against precision measurements.

The input parameters  $\{\alpha, M_Z, G_F\}$  are matched onto the Lagrangian parameters  $g, g'$ , and  $v$  but the presence of higher-dimensional operators induces corrections to this matching. Schematically, one has:

$$\alpha \rightarrow \alpha^{\text{SM}} + \delta\alpha(C_i), \quad (3.12)$$

$$M_Z^2 \rightarrow M_Z^{2,\text{SM}} + \delta M_Z^2(C_i), \quad (3.13)$$

$$G_F \rightarrow G_F^{\text{SM}} + \delta G_F(C_i), \quad (3.14)$$

where  $\delta X(C_i)$  denotes SMEFT corrections involving Wilson coefficients  $C_i$ . For example, the operator

$$\mathcal{O}_{\ell\ell} = (\bar{\ell}_i \gamma_\mu \ell_j)(\bar{\ell}_k \gamma^\mu \ell_l) \quad (3.15)$$

modifies the muon decay amplitude and hence shifts the relation between  $G_F$  and the vacuum expectation value  $v$ . Similarly, operators like

$$\mathcal{O}_{H\ell}^{(1)} = (H^\dagger i \overleftrightarrow{D}_\mu H)(\bar{\ell}_i \gamma^\mu \ell_j), \quad \mathcal{O}_{HD} = |H^\dagger D_\mu H|^2 \quad (3.16)$$

contribute to the  $Z$ -pole observables and shift the relations among electroweak couplings.

Therefore, when employing the  $\{\alpha, M_Z, G_F\}$  input set, one must consistently compute the SMEFT corrections to all derived observables (e.g.,  $M_W$ ,  $\Gamma_W$ ,  $\sin^2 \theta_{\text{eff}}$ , etc.) using the shifted input-parameter relations. Neglecting these corrections would lead to inconsistent use of the SMEFT expansion and potentially misleading conclusions.

Although physical observables must be independent of the input parameter scheme, the interpretation of SMEFT constraints may vary depending on the chosen set [124]. This is due to the fact that SMEFT corrections shift both the input parameters and the observables, and different schemes distribute these corrections differently between input and prediction sectors. The difference between the schemes is reduced when we introduce higher orders.

# Chapter 4

## Global Analysis at LO

### Contents

<b>4.1</b>	<b>The <i>Minimal</i> MFV SMEFT . . . . .</b>	<b>35</b>
<b>4.2</b>	<b>Experimental Input . . . . .</b>	<b>36</b>
<b>4.3</b>	<b>Dijets+<math>\gamma</math> Production . . . . .</b>	<b>39</b>
<b>4.4</b>	<b>LO Results . . . . .</b>	<b>40</b>

In the literature, several global analyses are data-driven, meaning that chosen a specific observable, only the operator contributing there are considered. However, the choice of the operators should come from the UV physics and most likely affects most of the known observables. We decide therefore to adopt a more “UV inspired” operator selection. Once the symmetry on NP is specified these must be respected in the matching onto the SMEFT. Therefore, after selecting the symmetry that we define as the *minimal* MFV our goal is to bound all the operators allowed by this symmetry. The aim of this chapter is to build a likelihood based on experimental data both at high and low energy able to fit all the Wilson coefficients allowed by the chosen symmetry. In order to do this we need to recollect and recast the known collider results, compute flavour observables via RGE and matching onto the LEFT and computing a previously unknown prediction for dijet+ $\gamma$  production. At the end of the chapter, we will show that this likelihood is enough to perform a global fit without surviving flat directions and we provide results for it.

### 4.1 The *Minimal* MFV SMEFT

We have already treated the different flavour symmetry choices for the SMEFT operators in Chapter 2. We now define more precisely the specific framework we work in. A priori, there are no restrictions on the flavour structure in the SMEFT. However, the fact that explicit flavour violation is experimentally extremely constrained [125, 126] makes it natural to assume symmetries suppressing these contributions. We consider a  $U(3)^5$  symmetry of the SMEFT, namely

$$U(3)^5 = U(3)_\ell \times U(3)_q \times U(3)_e \times U(3)_u \times U(3)_d, \tag{4.1}$$

where  $\{\ell, q, e, u, d\}$  represent the SM fermions [56]. The  $U(3)^5$  symmetric SMEFT contains only the minimum and non-removable amount of flavour violation which results from the

SM Yukawa couplings. Under this assumption, there are 47 independent SMEFT operators. Note that the contraction of the flavour indices of flavour-generic operators can result in two independent  $U(3)^5$  singlets in some cases. This is the case for four-fermion operators with two fermion currents of the same chirality:  $\mathcal{O}_{qq}^{(1)}$ ,  $\mathcal{O}_{qq}^{(3)}$ ,  $\mathcal{O}_l$ ,  $\mathcal{O}_{dd}$  and  $\mathcal{O}_{uu}$ . For these operators, we hence introduce unprimed and primed Wilson coefficients which refer to the operators contracting the flavour indices within the fermion bilinears or between the two different fermion bilinears, respectively. As an example, the operator  $\mathcal{O}_l = (\bar{l}_i \gamma_\mu l_j)(\bar{l}_k \gamma^\mu l_l)$  has two flavour-symmetric contractions

$$C_l \delta_{ij} \delta_{lk} \quad \text{and} \quad C'_l \delta_{ik} \delta_{jl}. \quad (4.2)$$

For the operator  $\mathcal{O}_{ee}$ , a Fierz identity implies a single independent coefficient  $C_{ee}$ . Limits on the primed and unprimed Wilson coefficients can generally be different. As an example,  $C'_l$  enters the shift of the Higgs vacuum expectation value to leave the input parameter  $G_F$  unchanged and is therefore tightly constrained through EWPO.  $C_l$ , on the other hand, is dominantly constrained through  $e^- e^+ \rightarrow l^- l^+$  observables and its limits are weaker than those on  $C'_l$ .

Note that even though all operators of the  $U(3)^5$  symmetric SMEFT are flavour conserving, flavour-violating effects still occur due to flavour violation in the SM. The RGE from the NP scale  $\Lambda$  down to the electroweak scale and below generates contributions to flavour-violating observables via the interplay between the flavour-violating SM interactions and the flavour-conserving NP vertices. Therefore, even the operators of the  $U(3)^5$  symmetric SMEFT can be constrained by flavour observables [127].

Six of the 47  $U(3)^5$ -symmetric operators are (purely bosonic and) CP odd and are best constrained through dedicated CP-sensitive observables and have negligible crosstalk with CP even operators [128]. Therefore, we set them aside in our analysis. We list the 41 CP even operators considered in our analysis in Table 2.2.

## 4.2 Experimental Input

In our analysis, we include data from EWPO, Higgs, top, low-energy parity violation experiments (PVE), lepton scattering, flavour, Drell-Yan as well as dijet+photon production. We list the corresponding observables and operator sets constrained in each dataset in the following. A graphical representation of operator sets contributing to the different observables is shown in Figure 4.1. We describe all the different datasets except dijets+ $\gamma$  in this section, while details about the computation of this specific observable are given in the next one.

### 4.2.1 Electroweak Precision Observables

We utilise a set of electroweak precision observables, including pseudo-measurements on the  $Z$  resonance [129], a combination of the  $W$  mass measurements at LEP [130], Tevatron [131] and ATLAS [132] and the LEP and Tevatron combination of the decay width of the  $W$  bo-

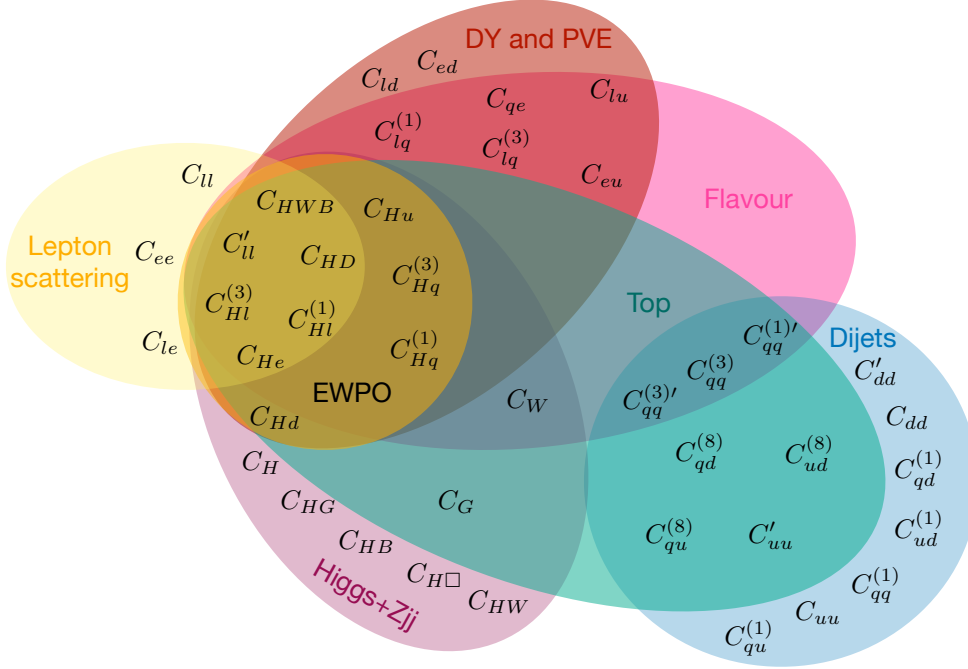


**Figure 4.1:** Venn diagram showing the operator sets contributing to the individual datasets at LO.

son [133]<sup>1</sup>

$$\Gamma_Z, \sigma_{\text{had}}^0, R_l^0, A_l, A_{FB}^l, R_c^0, A_c, A_{FB}^c, R_b^0, A_b, A_{FB}^{0,b}, m_W, \Gamma_W. \quad (4.3)$$

The subscript  $l$  in this list refers to an average over the lepton species. These measurements constrain the following operator set at leading order

$$\text{OS}_{\text{EWPO}} = \{C_{HWB}, C_{HD}, C_{Hl}^{(1)}, C_{Hl}^{(3)}, C_{Hq}^{(1)}, C_{Hq}^{(3)}, C_{Hu}, C_{Hd}, C_{He}, C_{ll}'\}. \quad (4.4)$$

### 4.2.2 Higgs and Electroweak Boson Observables

We include observables from the Higgs sector as included in [62]. These include Higgs signal-strength measurements for various production and decay channels, simplified template cross section (STXS) measurements and differential distributions. SMEFT predictions for the Higgs decays are based on [138]. For di-Higgs production, we include signal-strength measurements in the  $4b$ ,  $2b2\tau$  and  $2b2\gamma$  final states. Moreover, we consider the angular distribution  $\Delta\phi_{jj}$  in  $Zjj$  production, which is known to dominantly constrain the Wilson coefficient  $C_W$ . The full list of observables is given in Table 1. The set of operators contributing to Higgs observables and  $Zjj$  production is given by

$$\text{OS}_{\text{EWPO}} + \{C_W, C_G, C_{HB}, C_{HW}, C_{HG}, C_H, C_{H\Box}\}. \quad (4.5)$$

<sup>1</sup>It was pointed out in [134–137] that combinations of the measurements of  $W$ -boson mass and its decay width can be problematic as both results are partially based on the same datasets. We have explicitly checked that removing  $\Gamma_W$  from our dataset does not influence our limits beyond the 5% level. Moreover, it was suggested that LEP data should in principle not enter the combined measurement of the  $W$  boson mass due to its extraction from  $W^+W^-$  production, which makes it sensitive to modified triple-gauge couplings [136, 137]. However, given that the ATLAS and Tevatron measurements dominate the combination, we expect the impact on our fit to be small.

### 4.2.3 Top Observables

For the top sector, we reuse the datasets and corresponding predictions from fitmaker [69]. These include cross-section measurements, differential distributions and asymmetry observables for single-top,  $t\bar{t}$  and  $ttV$  production. The observables are listed in Tables 2-3. The set of operators contributing to top observables is given by

$$\text{OS}_{\text{EWPO}} + \{C_W, C_G, C_{qq}^{(1)'}, C_{qq}^{(3)}, C_{qq}^{(3)'}, C'_{uu}, C_{ud}^{(8)}, C_{qu}^{(8)}, C_{qd}^{(8)}\}. \quad (4.6)$$

### 4.2.4 Parity Violation Experiments and Lepton Scattering

With the aim of constraining semileptonic operators, we include data from atomic parity violation (APV) and parity violating electron scattering (PVES) experiments, which we collectively refer to as parity violation experiments (PVE). Specifically, we include the weak charge  $\mathcal{O}_W$  of  $^{133}\text{Cs}$  [139] and of the proton [140], deep inelastic scattering of polarised electrons as measured by the PVDIS experiment [141] and measurements of parity-violating scattering provided by SAMPLE [142].

As a constraint on purely leptonic operators, we use muon neutrino-electron scattering, the weak mixing angle measured in parity violating electron scattering [139],  $\tau$  polarisation measured in  $e^+e^- \rightarrow \tau^+\tau^-$  [143] as well as differential cross sections and asymmetries in  $e^+e^- \rightarrow l^+l^-$  [130, 143, 144]. The corresponding theory predictions are taken from [57, 145]. The set of operators entering our low-energy observables is given by

$$\text{OS}_{\text{EWPO}} + \{C_{lq}^{(1)}, C_{lq}^{(3)}, C_{ed}, C_{eu}, C_{ld}, C_{lu}, C_{qe}, C_{ll}, C_{ee}, C_{le}\}. \quad (4.7)$$

### 4.2.5 Drell-Yan Observables

Semileptonic operators can also be constrained in Drell-Yan lepton production. We use the HighPT [146] tool to obtain the theory predictions for differential distributions of the  $pp \rightarrow ee, \mu\mu, \tau\tau$  processes at leading order in the SMEFT. The corresponding experimental datasets are listed in Table 3. To avoid conflicts with the EFT validity range, we only use invariant mass bins up to an energy of 3 TeV. We describe the differential Drell-Yan cross sections by the following set of operators

$$\text{OS}_{\text{EWPO}}(\text{without } C_{HWB}, C_{HD}, C'_{ll}) + \{C_{lq}^{(1)}, C_{lq}^{(3)}, C_{ed}, C_{eu}, C_{ld}, C_{lu}, C_{qe}\}. \quad (4.8)$$

Note that currently shifts of the SM parameters as a result of the scheme choice are not taken into account in HighPT. Consequently, the Wilson coefficients  $C_{HWB}$ ,  $C'_{ll}$  and  $C_{HD}$ , which only contribute to the Drell-Yan dataset through these shifts, are not taken into account. Given that these coefficients are tightly constrained by EWPO, we expect the impact of the missing contributions to be subdominant.

### 4.2.6 Flavour Observables

We utilise the datasets and predictions as implemented in Flavio [36, 39, 147, 148] for flavour-sector observables. These include differential branching ratios of  $B$  mesons and Kaons, angular observables,  $B$ ,  $K$  and  $D$  meson mixing observables as well as the  $R_K$  and  $R_K^*$  ratios. A comprehensive list of the flavour observables included in our analysis is provided in Table 4<sup>2</sup>.

<sup>2</sup>We note the use of the up-aligned basis  $(u_L, V_{\text{CKM}} d_L)^T$  for the left-handed quark doublets in all our considerations about flavour. Nonetheless, the use of the down-aligned basis  $(V_{\text{CKM}}^+ u_L, d_L)^T$  leads to the

As these observables are defined at low energies, we study them in the so-called WET. We have already introduced the whole notation in the previous chapter. Starting from the SMEFT lagrangian, using the evolution matrix approach, we perform the running from the high scale ( $\mu = 4$  TeV) to the electroweak scale ( $\mu = M_Z$ ), where we match the SMEFT onto the LEFT at one loop, using `DsixTools` [36, 39, 44, 148, 149]. For the subsequent running from the electroweak (EW) scale to the bottom-quark mass scale in the LEFT, we use the `Wilson` package [43]. As a cross check, we have explicitly confirmed that we can reproduce the results presented in [150]. The SMEFT Wilson coefficients appearing in the theory predictions of flavour violating processes are

$$\mathcal{O}_{\text{SEWPO}}(\text{without } C_{Hd}) + \{C_W, C_{lq}^{(1)}, C_{lq}^{(3)}, C_{lu}, C_{eu}, C_{qe}, C_{qq}^{(1)'}, C_{qq}^{(3)}, C_{qq}^{(3)'}\}. \quad (4.9)$$

### 4.3 Dijets+ $\gamma$ Production

The set of observables discussed so far, though well established in the literature, is insufficient to fully constrain all the Wilson coefficients compatible with the imposed symmetry assumptions. In particular, within the four-quark operator sector, several coefficients remain either entirely unconstrained or only weakly bounded at the level of single-parameter fits. When multiple operators are considered simultaneously, this results in the appearance of flat directions. To address this limitation, this section focuses on the computation of a new observable specifically designed to probe four-quark operators, with emphasis on those involving down-type or right-handed quarks, which are only poorly constrained—or not constrained at all—by existing top and flavour data. A natural strategy in this context is to exploit dijet production at the LHC, which provides direct sensitivity to the four-quark operator parameter space. However, the high trigger thresholds for jets at the LHC restrict the accessible kinematic regime to dijet invariant masses in the multi-TeV range. In this high-energy domain, quadratic terms in the EFT expansion often dominate over linear contributions, potentially raising concerns regarding the validity of the EFT description [151]. A more suitable alternative is offered by the production of two jets in association with a photon [152], which allows one to access significantly lower dijet invariant-mass ranges,  $m_{jj} < 1.2$  TeV, thereby overcoming the issue and providing a powerful probe of the four-quark operator space.

Using a flat factor  $\epsilon_{\text{det}} = 0.28$  for the experimental detector efficiency, we can reproduce the ATLAS SM distribution within 10%. Using `SMEFTsim` [153], we have determined the SMEFT prediction for each bin of the differential cross section at LO in SMEFT. The obtained predictions are available as an ancillary file in [68] (flavour symmetric) and in [72] (flavour general).

It is worth noting that some of the considered four-quark operators,  $\mathcal{O}_{qd}^{(1)}$ ,  $\mathcal{O}_{qu}^{(1)}$ ,  $\mathcal{O}_{ud}^{(1)}$ , do not interfere with the dominant SM diagram, the  $t$ -channel exchange of a gluon. As a result, we expect the quadratic SMEFT contributions for these operators, which we generally neglect in our study, to be dominant with respect to their linear counterparts. To highlight this effect, we present the ratio for bounds from single-parameter fits based on linear SMEFT predictions only over bounds from linear+quadratic fits in Table 4.1. As anticipated, the limits on  $C_{qd}^{(1)}$ ,  $C_{qu}^{(1)}$ ,  $C_{ud}^{(1)}$  are tightened by more than a factor 2.5 in a quadratic fit. Since we will only underestimate the limits on these Wilson coefficients in our linear fit, we will

---

same results. For example, we consider the tree-level flavour changing neutral current induced by the operator  $\mathcal{O}_{qq}^{(1)'} = (\bar{q}_r \gamma_\mu q_s)(\bar{q}_s \gamma^\mu q_r)$  via the misalignment between the up- and down-type quarks when rotating to the mass basis: In the up-aligned basis we get  $(\bar{u}_l \gamma^\mu u_k)(V_{km}^* \bar{d}_m \gamma_\mu V_{ln} d_n)$ , while in the down-aligned basis we get the identical result  $(V_{ln} \bar{u}_l \gamma^\mu V_{km}^* u_k)(\bar{d}_m \gamma_\mu d_n)$ .

$C_{qq}^{(1)}$	$C_{qq}^{(1)prime}$	$C_{qq}^{(3)}$	$C_{qq}^{(3)prime}$	$C_{qd}^{(8)}$	$C_{qu}^{(8)}$	$C_{ud}^{(8)}$	$C_{dd}$
0.9	0.9	1.0	1.0	1.7	1.4	1.6	2.5
$C_{dd}^{prime}$	$C_{uu}$	$C_{uu}^{prime}$	$C_{qd}^{(1)}$	$C_{qu}^{(1)}$	$C_{ud}^{(1)}$	$C_G$	
2.2	0.9	0.9	5.9	3.9	2.6	1.4	

**Table 4.1:** Ratio of the 68% CL limits on the operators contributing to dijet+photon production at linear and quadratic order in SMEFT.

keep their linear contributions. The remaining operators are much more mildly influenced, typically by 10 – 20%, in a quadratic fit.

We neglect the clearly subdominant electroweak contributions to dijet production and describe the differential distributions by

$$\{C_G, C_{qd}^{(1)}, C_{qu}^{(1)}, C_{ud}^{(1)}, C_{qq}^{(1)}, C_{qq}^{(1)prime}, C_{qq}^{(3)}, C_{qq}^{(3)prime}, C_{uu}, C_{uu}^{prime}, C_{dd}, C_{dd}^{prime}, C_{ud}^{(8)}, C_{qu}^{(8)}, C_{qd}^{(8)}\}. \quad (4.10)$$

## 4.4 LO Results

For our global analyses, we obtain the limits on a Wilson coefficient while profiling over the remaining parameters as explained in 3.3.

We present our global analysis with SMEFT predictions at LO in Figure 4.2. Operators from the Higgs-EW sector as well as four-lepton operators, shown in the upper panel of the plot, are well constrained. All corresponding Wilson coefficients, except  $C_H$ , are constrained to a region within  $|C|/\Lambda^2 < 1/\text{TeV}^2$  at 95% CL. The four-fermion operators involving quark fields, shown in the lower panel of the plot, are generally more weakly constrained. The limits of two of the seven semileptonic operators as well as nine of the 14 four-quark operators exceed  $|C|/\Lambda^2 = 1/\text{TeV}^2$  (on at least one side). In particular,  $C_{qd}^{(1)}$ ,  $C_{ud}^{(1)}$ ,  $C_{qu}^{(1)}$ ,  $C_{dd}$  and  $C_{dd}^{prime}$  are essentially unconstrained, with limits on  $|C|/\Lambda^2$  greater than  $50/\text{TeV}^2$ . Nevertheless, it is interesting to note that the inclusion of these very weakly constrained operators does not invalidate the limits on the remaining Wilson coefficients.

All 41 Wilson coefficients included in our global fit are consistent with the SM within  $2\sigma$ . However, six Wilson coefficients exhibit deviations exceeding  $1.5\sigma$

$$\{C_{ll}, C_{ee}, C_{lu}, C_{lq}^{(1)}, C_{qq}^{(1)}, C_{qq}^{(3)}\}. \quad (4.11)$$

The shift in  $C_{ll}$  can be attributed mainly to a small deviation in the measurement of the differential cross-section of  $e^+e^- \rightarrow e^+e^-$ , while  $C_{ee}$  is affected by the measurement of the weak mixing angle in parity-violating electron scattering ( $g_{AV}^{ee}$ ). Several semileptonic operators exhibit deviations from the SM, with the largest shifts arising for  $C_{lu}$  and  $C_{lq}^{(1)}$ . These deviations are primarily induced by the Drell-Yan data, in particular with muons in the final state. In the four-quark sector,  $C_{qq}^{(3)}$  is dominantly shifted by single-top production data and the shift of  $C_{qq}^{(1)}$  is dominated by dijet data, which is the only observable constraining this operator at LO.

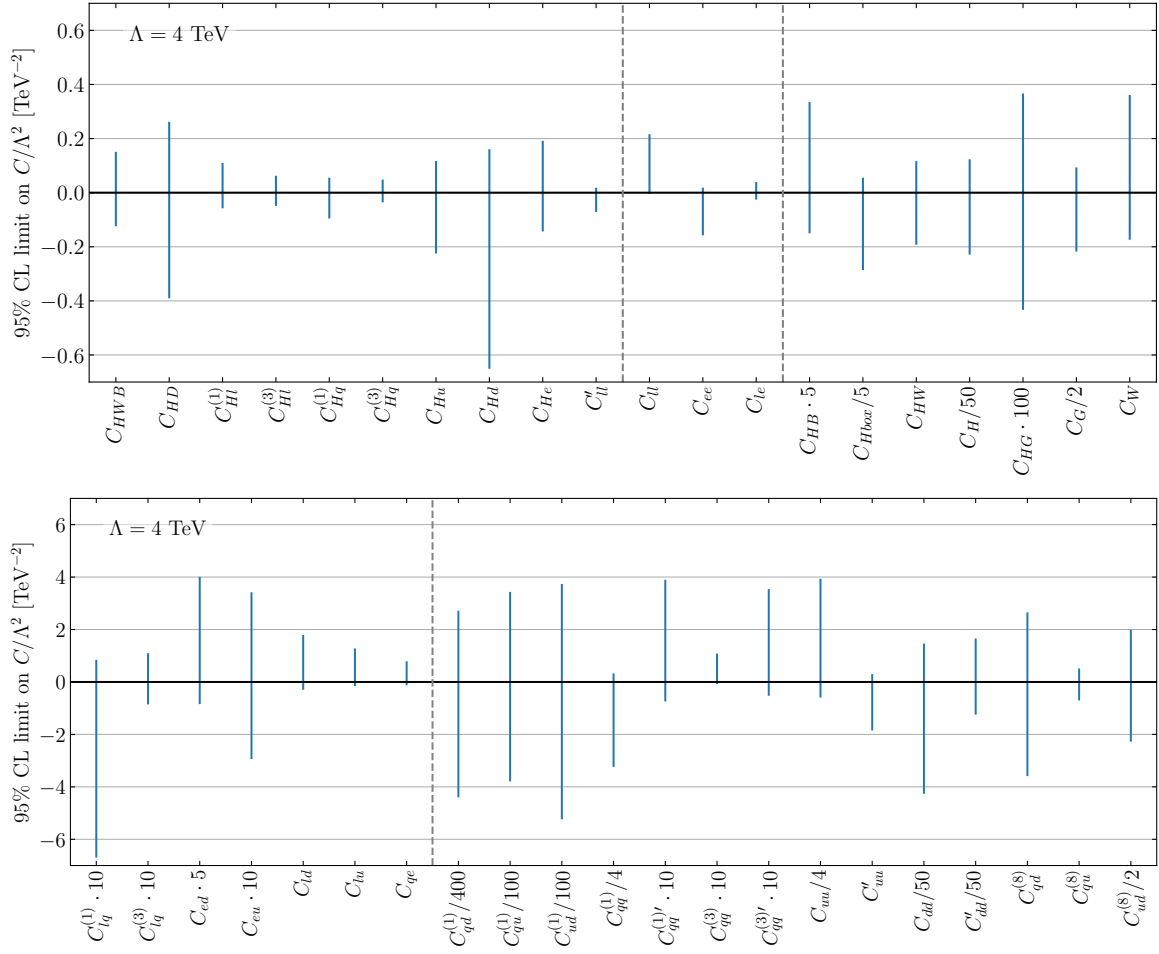


**Figure 4.2:** Limits on the Wilson coefficients in a global analysis using LO SMEFT predictions.



# Global Analysis with NLO Contributions

## Contents

<b>5.1</b>	<b>SMEFT Predictions at NLO . . . . .</b>	<b>43</b>
<b>5.2</b>	<b>Comparison Between LO and NLO Results . . . . .</b>	<b>44</b>
<b>5.3</b>	<b>Interplay and Correlations . . . . .</b>	<b>46</b>

As shown in the previous chapter, some four-quark operators within the minimal MFV set remain weakly constrained in a leading-order fit to our datasets. These operators contribute to a number of precisely measured observables at NLO. In this chapter, we perform a global analysis based on NLO predictions, where present. This includes NLO predictions for EWPO [93, 94] as well as partial NLO predictions for  $t\bar{t}$  production [95, 96] and Higgs decays to bottom quark pairs [97]. Note that not all observables are considered at NLO precision in our partial NLO global analysis. As a result, our analysis does not consider all degeneracies which might be present in the SMEFT predictions at NLO<sup>1</sup>. Nevertheless, the inclusion of EWPO at NLO precision serves as a good testcase to study the impact of the additional freedom in the Wilson coefficient space at NLO on the operators present already at LO.

## 5.1 SMEFT Predictions at NLO

### 5.1.1 EWPO

We include NLO predictions for EWPO from [93, 94], see also [124] for partial results in other EW input schemes. At NLO precision, EWPO are sensitive to 25 additional Wilson coefficients. Explicitly, the considered NLO EWPO predictions are sensitive to

$$\{C_{ll}, C_{ee}, C_{le}, C_{HB}, C_{H\Box}, C_{HW}, C_W, C_{lq}^{(1)}, C_{lq}^{(3)}, C_{ed}, C_{eu}, C_{ld}, C_{lu}, C_{qe}, C_{qd}^{(1)}, C_{qu}^{(1)}, C_{ud}^{(1)}, C_{qq}^{(1)}, C_{qq}^{(1)'}, C_{qq}^{(3)}, C_{qq}^{(3)'}, C_{uu}, C_{uu}', C_{dd}, C_{dd}'\}, \quad (5.1)$$

in addition to those listed in Equation (4.4).

<sup>1</sup>See e.g. [97] for an example of how the consideration of further NLO effects can spoil the loop sensitivity to the Higgs self-coupling.

### 5.1.2 Top

SMEFT predictions for top observables at NLO are provided by the SMEFfit collaboration [95, 96], which employs the  $\{G_F, M_W, M_Z\}$  input scheme. While this input scheme is different from the one utilised in our analysis, the impact of the electroweak input-scheme choice on top quark physics is expected to be small. We have explicitly checked that the LO predictions for  $m_{tt}$  differential distributions are very similar in the two input schemes. To improve the bounds on some four-quark operators, we update the predictions for the charge asymmetry as well as  $m_{tt}$  differential distributions to NLO precision as a proof-of-principle. These observables have been shown to have the largest constraining power for four-quark operators [96]. NLO predictions of the considered top quark production processes add sensitivity to the operators

$$\{C_{qd}^{(1)}, C_{qu}^{(1)}, C_{ud}^{(1)}, C_{qq}^{(1)}, C_{uu}\}. \quad (5.2)$$

### 5.1.3 Higgs

The dominant contributions of third generation four-quark operators to single-Higgs production and decay are known [97]. We include the NLO predictions for gluon fusion Higgs production,  $t\bar{t}h$  production and the loop-induced decays  $h \rightarrow gg, \gamma\gamma$ , which receive contributions from the operators

$$\{C_{qu}^{(1)}, C_{qq}^{(1)}, C_{qq}^{(3)}, C_{uu}, C_{qu}^{(8)}\}. \quad (5.3)$$

Specifically,  $C_{qu}^{(1)}, C_{uu}, C_{qu}^{(8)}$  contribute to  $t\bar{t}h$  production only, while the remaining operators affect all considered processes. While the constraining power of Higgs data for these operators, which appear at NLO only, is generally small, we find that in particular the bounds on  $C_{qu}^{(1)}$  tighten with the inclusion of these NLO effects.

Moreover, we include NLO contributions from  $C_H$  to total Higgs production and decay channels [154, 155]. However, this only marginally affects the results as the constraints on  $C_H$  are dominated by di-Higgs production.

## 5.2 Comparison Between LO and NLO Results

In Figure 5.1, we present a comparison of the global fit at LO with the one including partial NLO SMEFT predictions. The corresponding numerical fit results can be found in Table 5 in Appendix B. The bounds on most operators are only mildly influenced by the inclusion of NLO SMEFT predictions. However, in the four-quark sector the limits on the Wilson coefficients  $C_{qd}^{(1)}, C_{qu}^{(1)}, C_{ud}^{(1)}$  and, to a smaller extent,  $C_{uu}$  significantly tighten when improving the SMEFT predictions to NLO precision and are now below  $|C|/\Lambda^2 < 10/\text{TeV}^2$ . The Wilson coefficients  $C_{dd}$  and  $C'_{dd}$  remain the only ones exceeding this limit. On the other hand, the bounds on  $C_{Hq}^{(1)}$  are weakened by a factor 2.5 through its correlations with four-quark operators in EWPO, in particular with  $C_{qq}^{(1)}$  and  $C_{uu}$ . We show these correlations arising at NLO in Figure 5.2. At LO, there are no visible correlations between  $C_{Hq}^{(1)}$  and the four-quark operators as indicated by the blue contours. At NLO, shown in orange, a strong correlation with  $C_{qq}^{(1)}$  and an anti-correlation with  $C_{uu}$  are induced through the EWPO SMEFT predictions, weakening the limits on  $C_{Hq}^{(1)}$ .

All 41 Wilson coefficients remain consistent with the SM within  $2\sigma$  in the NLO fit. However, the number of Wilson coefficients exhibiting deviations exceeding  $1.5\sigma$  grows from

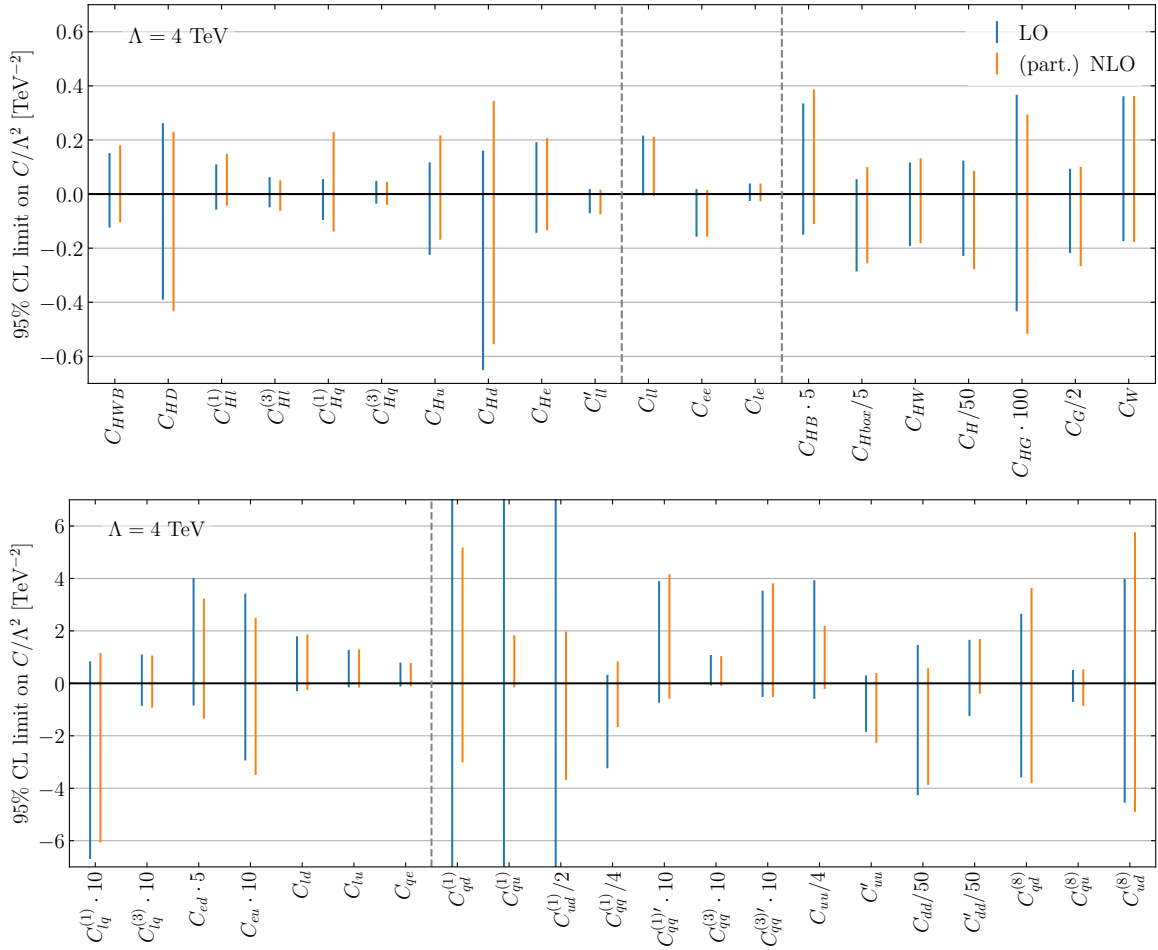


**Figure 5.1:** Comparison of the global analysis at LO with the one including partial NLO predictions.

six to nine

$$\{C_{ll}, C_{ee}, C_{lu}, C_{qq}^{(3)}, C_{ld}, C_{qu}^{(1)}, C_{qq}^{(1')}, C_{qq}^{(3')}, C_{uu}\}, \quad (5.4)$$

where we have greyed out the Wilson coefficients which already deviated from zero in the LO fit, see Equation (4.11). Two coefficients, which exhibit deviations  $\geq 1.5\sigma$  in the LO fit are shifted towards more SM-like values at NLO,  $C_{qq}^{(1)}$  and  $C_{lq}^{(1)}$ . For  $C_{qq}^{(1)}$ , this is due to its additional NLO contributions to EWPO, Higgs and top data. The shift of  $C_{lq}^{(1)}$  towards more SM-like values in the NLO fit is the result of EWPO data. On the other hand,  $C_{qu}^{(1)}$ , which at NLO is strongly constrained by Higgs data, deviates due to experimental deviations in  $t\bar{t}H$  production.  $C_{uu}$  experiences a shift away from zero in both the LO and NLO analyses, which is caused by the dijet dataset. However, the shift becomes more apparent at NLO, where the overall bounds on this parameter shrink as a result of stronger limits on other correlated four-quark operators. For  $C_{qq}^{(1)'}$ , which is dominantly affected by  $t\bar{t}V$ , and  $C_{qq}^{(3)'}$ , which is mainly shifted by both  $t\bar{t}V$  and dijet data, the change of the limits between the LO and NLO analysis is only marginal, the central values are shifted by 13% and 9%, respectively. The same is true for the semileptonic operator  $C_{ld}$ , for which the central value only changes by 8%.

We have again checked explicitly that when conducting a fit without the five most poorly

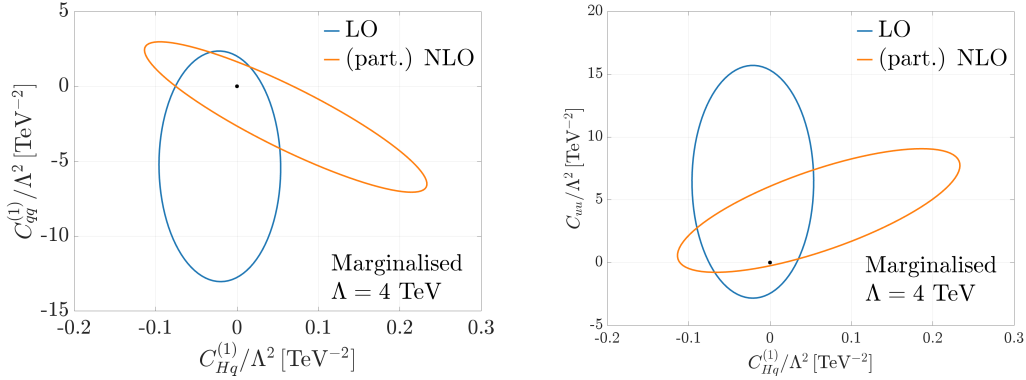


**Figure 5.2:** 95% CI limits in the LO and partial NLO analyses showing the correlations of  $C_{Hq}^{(1)}$  with  $C_{qq}^{(1)}$  (left) and  $C_{uu}^{(1)}$  (right).

constrained operators,  $C_{qd}^{(1)}$ ,  $C_{ud}^{(1)}$ ,  $C_{qu}^{(1)}$ ,  $C_{dd}$  and  $C'_{dd}$ , limits on the remaining operators exhibit no significant changes. The only noticeable effects are on four-quark operators for which the corresponding limits strengthen by up to 33% when removing the five least constrained operators from the fit. Moreover, the limit on  $C_G$  changes by 17% and the limit on  $C_{Hq}^{(1)}$ , which suffers from large correlations in the global analysis, receives a 35% correction. This highlights the robustness of the results even though some operators remain weakly limited given the current dataset.

In Figure 5.3 we present the ratio of the uncertainties on the Wilson coefficients in a global fit over the uncertainties in a one-parameter fit. This can be seen as a measure of the sensitivity of each operator on correlations with the remaining ones. As expected, we find that the bounds on many operators are significantly weakened in the global analysis. Limits on semileptonic operators and four-quark operators involving right-handed quark fields only, typically increase by more than a factor 20 in a global fit. For semileptonic operators, this is due to the Drell-Yan dataset imposing tight constraints at the one-parameter level, while only poorly disentangling the effects of different operators. Of those operators affecting EWPO at LO,  $C_{HWB}$  and  $C_{HD}$  have the largest degeneracies and the corresponding limits increase by factors 44 and 26, respectively, in a global fit. In the Higgs-gauge sector, only  $C_{HW}$  and  $C_{HB}$ , which have large correlations with  $C_{HWB}$  and  $C_{HD}$ , see also the correlation matrix in Figure 2, are significantly weakened in the global analysis by factors of 20 and 21, respectively. The operators whose limits are most stable under a global analysis are  $C_{le}$ ,  $C_H$ ,  $C_G$  and  $C_W$ . The corresponding limits change by less than 50 % in a global fit.

### 5.3 Interplay and Correlations

The datasets described previously described are sensitive to different, and often unique, directions in parameter space. The combination of different datasets hence plays a crucial role for the limits obtained in a global analysis. In this section, we will discuss the constraining power of the individual datasets as well as their interplay.

In Figure 5.4, we once again display the results of the comprehensive global analysis encompassing all 41 Wilson coefficients. In addition to the global analysis including all datasets, we use different colours to represent fits with the exclusion of a single dataset to highlight the relevance of the respective set. To ensure a better readability of the plot, we exclusively display bounds in cases where the removal of a dataset impacts the constrained

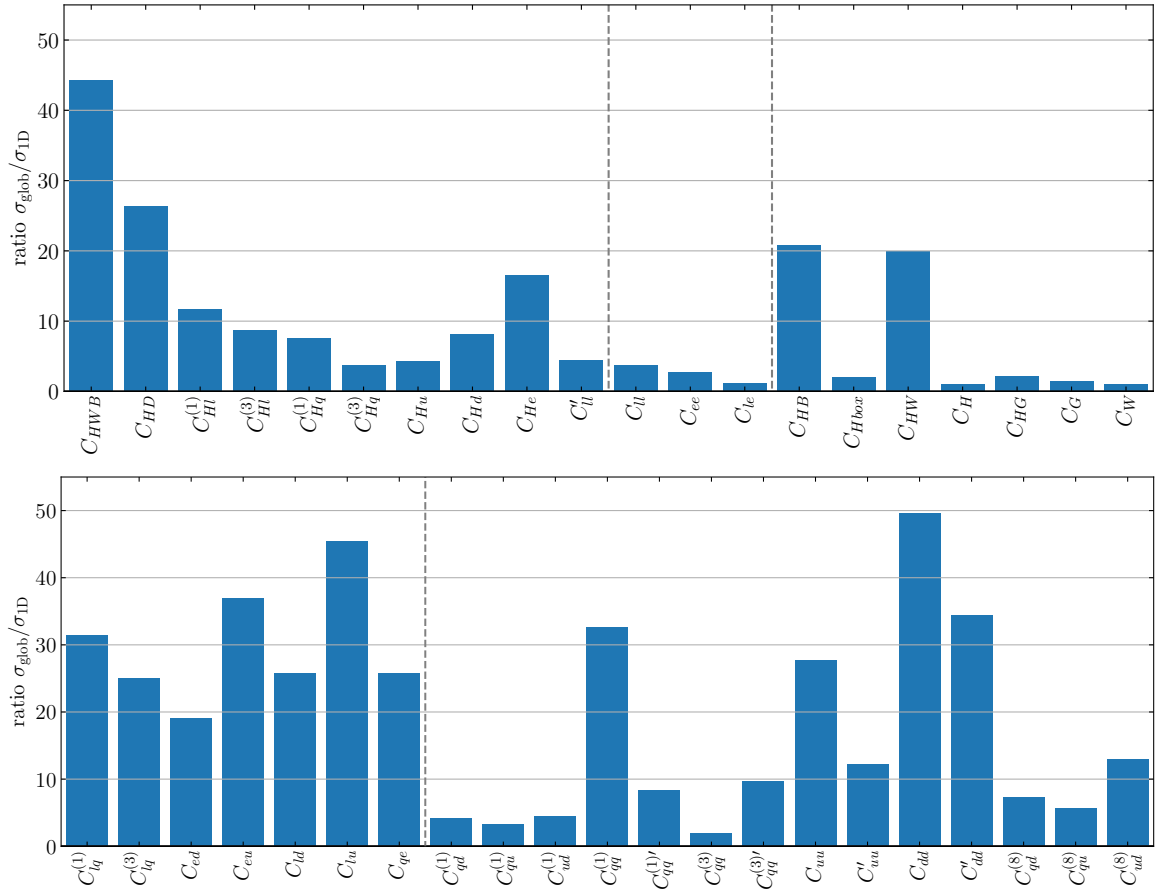


**Figure 5.3:** Ratio of the uncertainties on the Wilson coefficients in a global 41-parameter analysis over the uncertainties in a single-parameter analysis (both including partial NLO predictions). This can be interpreted as a measure of the relevance of correlations with the remaining Wilson coefficients in the analysis.

range by a minimum of 100 %. As expected, the ten operators contributing to EWPO at LO, displayed in the upper panel, are dominantly constrained by EWPO and Higgs physics, corresponding to the orange and green lines, respectively. However, we see that the other datasets, such as PVE (pink), top (red) and dijets (brown), are also crucial for constraining some of these operators. For  $C_{HI}^{(1)}$ , the relevance of the PVE dataset is a result of correlations with semileptonic operators and will be further explored in Subsection 5.3.1. For  $C_{Hd}$  and  $C_{Hq}^{(1)}$ , correlations in EWPO with four-quark operators ( $C_{Hq}^{(1)}$  with  $C_{qq}^{(1)}$ ,  $C_{uu}$  and  $C_{Hd}$  with the weakly constrained  $C_{dd}$ ) lead to relevant contributions from top and dijet observables.

Four-lepton operators are dominantly constrained in lepton-scattering experiments and EWPO. By constraining  $C'_{ll}$ , EWPO also play an important role in disentangling the correlations with  $C_{ll}$  present in lepton scattering.

Operators contributing to modified Higgs couplings, shown in the central panel, do not receive important contributions from any other sector.  $C_G$  and  $C_W$  are dominantly constrained in top physics and  $Zjj$  production (the latter is not shown as an individual dataset), respectively.

Semileptonic operators, also displayed in the central panel, are all dominantly constrained by PVE and Drell-Yan, except  $C_{lq}^{(3)}$  and  $C_{eu}$  which receive important contributions from the flavour sector as well as EWPO. We study the interplay of PVE and Drell-Yan further in

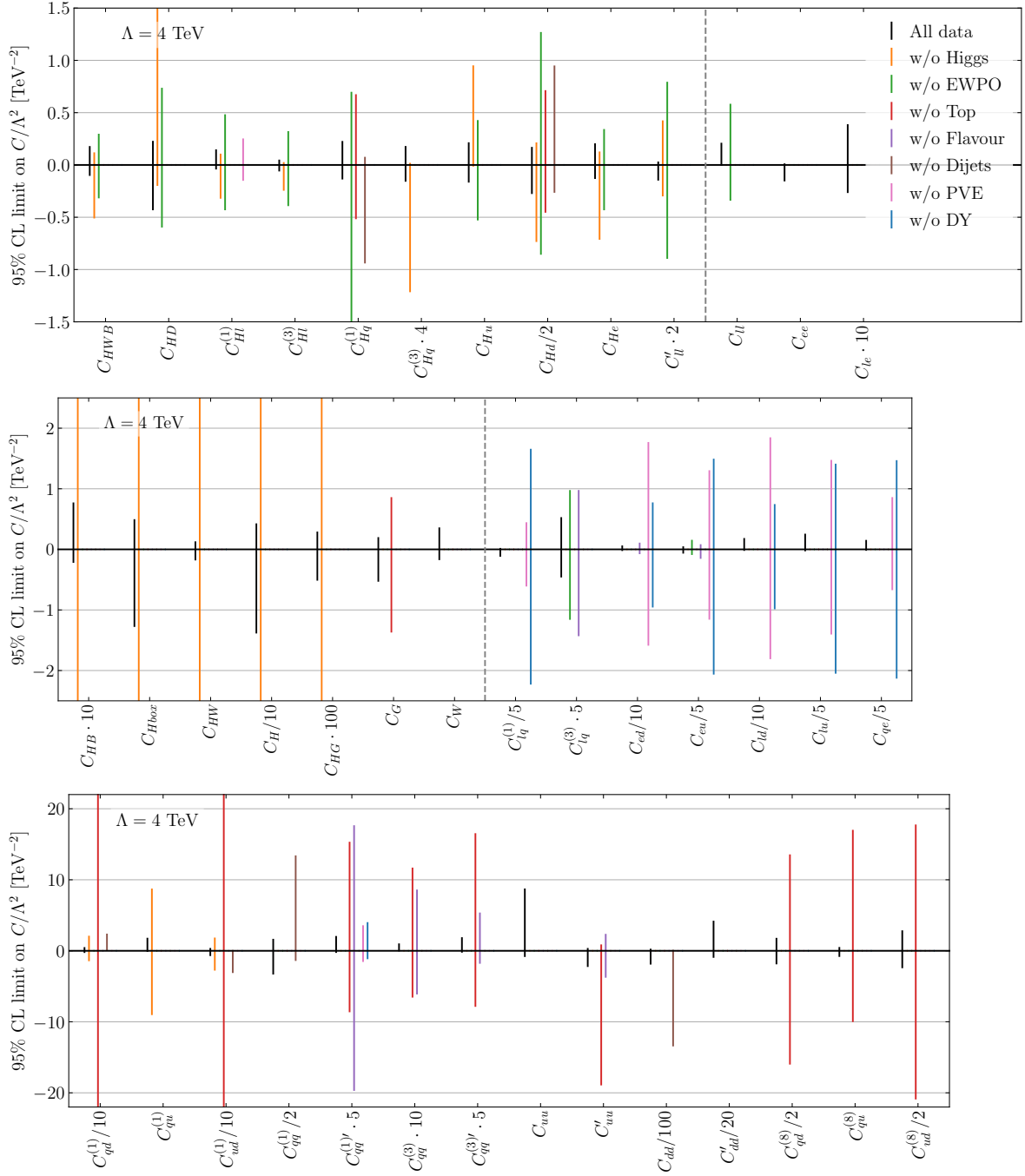


**Figure 5.4:** Global analysis including NLO predictions. Different colours correspond to analyses removing certain datasets to highlight their relevance. Note that some Wilson coefficients have been rescaled and that the y-axis range is different in the three plot panels.

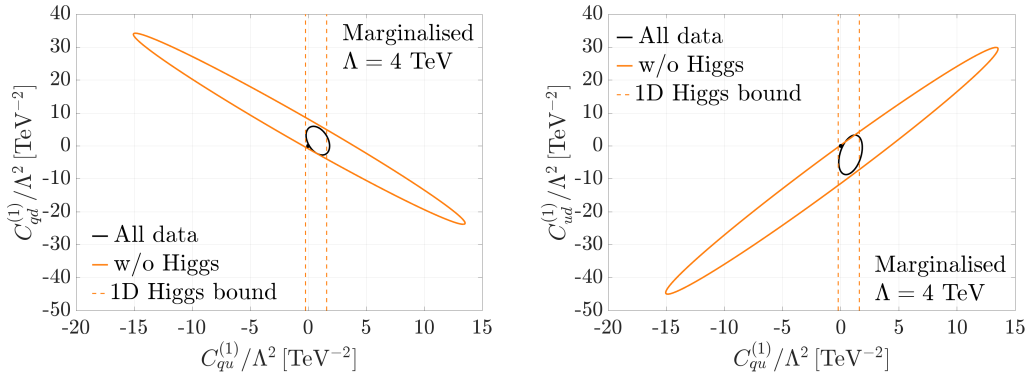


**Figure 5.5:** 95% CI limits with and without the inclusion of the Higgs dataset showing the impact of this dataset on  $C_{qd}^{(1)}$  (left) and  $C_{ud}^{(1)}$  (right) through lifting correlations with  $C_{qu}^{(1)}$ .

### Subsection 5.3.2.

Interestingly, four-quark operators, displayed in the lower panel, receive important constraints from all considered datasets except EWPO. For most operators the most dominant constraints result from Higgs, top, dijet and flavour data. Higgs physics plays an important role in setting the limits on  $C_{qd}^{(1)}$ ,  $C_{qu}^{(1)}$ ,  $C_{ud}^{(1)}$ , even though only  $C_{qu}^{(1)}$  is directly constrained in Higgs physics (through NLO  $t\bar{t}h$  production). The effect on the other two operators is the result of strong correlations with  $C_{qu}^{(1)}$  as shown in Figure 5.5. The orange contours correspond to a global analysis without Higgs data and show a strong correlation between the considered four-quark operators. Limits on  $C_{qu}^{(1)}$  from Higgs physics, indicated by the dashed lines, break this degeneracy. The combination of all datasets (black contours) therefore not only enhances the limits on  $C_{qu}^{(1)}$  but also influences the correlated coefficients  $C_{qd}^{(1)}$  and  $C_{ud}^{(1)}$ .

For  $C_{qd}^{(1)}$ ,  $C_{ud}^{(1)}$ ,  $C_{qq}^{(1)}$ ,  $C_{dd}$ , dijet data have a relevant impact for breaking degeneracies between operators and shifting the limits towards SM values. Without dijet data, deviations in  $t\bar{t}h$  production push the limits towards non-SM values. For  $C_{dd}'$ , which can only be very weakly constrained, the changes of the limits when removing the EWPO and dijet dataset are smaller than the chosen threshold of two (100%). Therefore, no dataset-specific additional limits are shown in the plot. Somewhat surprisingly, Drell-Yan and PVE influence the bounds on  $C_{qq}^{(1)'}.$  We further investigate this effect in Subsection 5.3.2.

### 5.3.1 EWPO and PVE Datasets

At LO, the operators contributing to the description of EWPO are tightly constrained. At NLO, the number of operators contributing to EWPO extends from ten to 35, hence adding a lot more freedom to the fit. The additional degrees of freedom need to be constrained by other datasets, otherwise the limits on the operators appearing at LO will be degraded. PVE plays an important role in constraining semileptonic operators and lifting degeneracies between these and the operators entering EWPO at LO. We illustrate two examples of the breaking of this degeneracy in Figure 5.6. The pink contours show large correlations between  $C_{HI}^{(1)}$  and  $C_{lu}$  (left panel) as well as  $C_{lq}^{(1)}$  (right panel) when PVE data are absent from the fit. By setting strong constraints on  $C_{lu}$  and  $C_{lq}^{(1)}$  and testing different directions in the  $C_{HI}^{(1)}$ – $C_{lu}/C_{lq}^{(1)}$  parameter space, PVE has an important impact on the global analyses bounds of  $C_{HI}^{(1)}$ , see Figure 5.4.

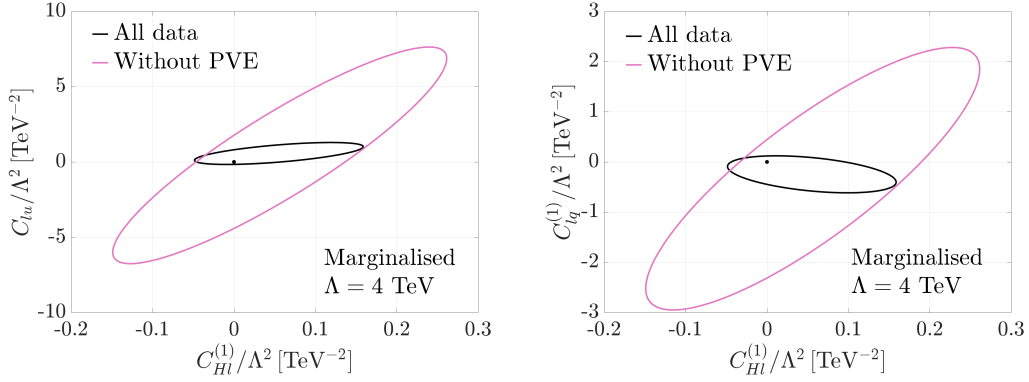


**Figure 5.6:** 95% CI limits with and without the inclusion of the PVE dataset showing the impact of this dataset on  $C_{Hl}^{(1)}$  through lifting correlations with  $C_{lu}$  and  $C_{lq}^{(1)}$ .

It was shown that the inclusion of  $\beta$ -decay observables and semileptonic meson decays [156, 157] can have an interesting interplay with EWPO. For a discussion about the impact of these observables see Appendix B of [68].

### 5.3.2 Drell-Yan, PVE and Flavour Datasets

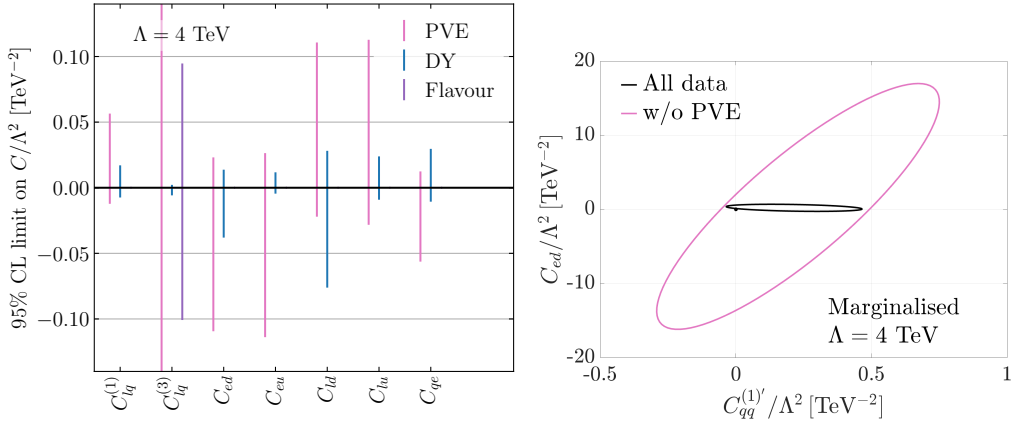


**Figure 5.7:** (Incomplete) list of single-parameter bounds at 95% CL on semileptonic operators (left). Note that for the flavour dataset we suppress the limits on all operators except  $C_{lq}^{(3)}$  because they are not competitive with PVE and Drell-Yan. 95% CI limits with and without the inclusion of the PVE dataset showing the impact of this dataset on  $C_{qq}^{(1)'}$  through lifting correlations with  $C_{ed}$  (right).

Drell-Yan and PVE data are both sensitive to semileptonic operators

$$\{C_{lq}^{(1)}, C_{lq}^{(3)}, C_{ed}, C_{eu}, C_{ld}, C_{lu}, C_{qe}\}. \quad (5.5)$$

We present single-parameter fit results for both datasets in Figure 5.7. For  $C_{lq}^{(3)}$ , we also show limits from the flavour dataset, which are competitive for this coefficient. Constraints from Drell-Yan dominate over those from PVE throughout the whole parameter space. Nevertheless, limits from PVE are of a similar order of magnitude and this dataset plays an important role in the global analysis through its ability to test different directions in parameter space compared to Drell-Yan. To highlight the complementarity of both searches, we present 2D-limit plots for  $C_{lu}$ -vs- $C_{qe}$  and  $C_{lq}^{(3)}$ -vs- $C_{eu}$  in Figure 5.8. In a two-parameter fit,

shown by the filled contours, we find that PVE (pink) and Drell-Yan (blue) probe almost orthogonal directions in parameter space for  $C_{qe}$  and  $C_{lu}$ . In Drell-Yan, these two Wilson coefficients appear with the same sign as they are both dominated by up-type quark contributions, which leads to an anti-correlation of  $C_{qe}$  and  $C_{lu}$ . Only exclusive down-type quark contributions,  $C_{ed}$  and  $C_{ld}$ , as well as the structurally distinct  $C_{lq}^{(3)}$  enter with an opposite sign for Drell-Yan. The PVE dataset is sensitive to axial couplings in the quark or lepton sector. As the operators corresponding to  $C_{qe}$  and  $C_{lu}$  involve quarks and leptons of different chiralities, all PVE observables will be sensitive to a negative relative combination of these two operators (whenever both operators appear), which results in a positive correlation of the Wilson coefficients. The complementarity between the PVE and Drell-Yan datasets also remains when marginalising over additional semileptonic Wilson coefficients. This is shown by the unfilled contours in the left panel of Figure 5.8. Comparing Figure 5.4, we find that PVE is particularly relevant for the semileptonic operators specifically involving down-type quarks since the corresponding measurements do not experience the same parton distribution function (PDF) suppression as Drell-Yan.

In the right panel of Figure 5.8, we show the two-parameter limits on  $C_{lq}^{(3)}$ -vs- $C_{eu}$  when marginalising over  $C_{lq}^{(1)}$ ,  $C_{lu}$  and  $C_{qe}$ . Again, Drell-Yan and PVE probe complementary directions in parameter space. In addition, flavour plays an important role by setting constraints on  $C_{lq}^{(3)}$ .

Even when combining all datasets, the limits on almost all semileptonic operators are weakened by a more than a factor 20 in the global analysis, see Figure 5.3. The Drell-Yan dataset delivers strong individual constraints on semileptonic operators. However, different bins and final states of the distributions only have a marginal impact on the relative importance of different Wilson coefficients of semileptonic operators. Therefore, this dataset is particularly affected by correlations. Therefore, in order to further improve bounds on semileptonic operators, it is relevant to add observables constraining different combinations of the corresponding Wilson coefficients.

The complementarity between low-energy Parity-Violating Electron Scattering (PVES) and LHC Run I Drell-Yan data in constraining semileptonic operators has already been studied in [158]. While this previous work is based on LHC Run I data up to 1.5 TeV, our analysis includes LHC Run II data up to an invariant-mass of 3 TeV.

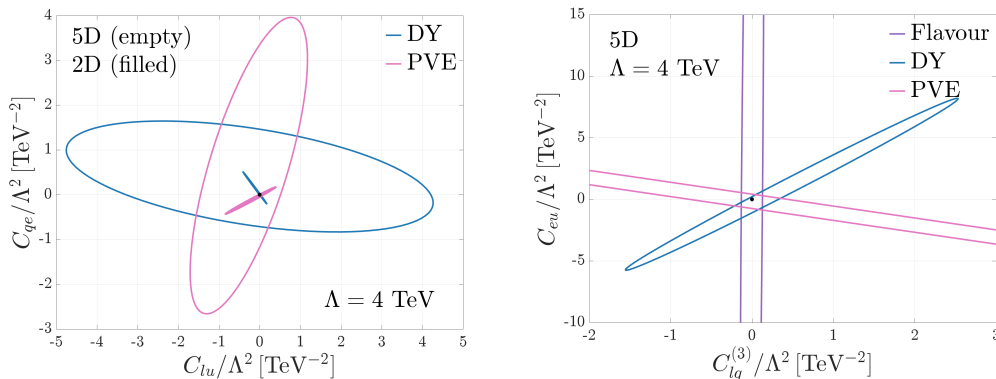


**Figure 5.8:** 95% CI contours on the two-dimensional parameter space of the semileptonic operators from PVE and Drell-Yan (and flavour). The 5D analyses are marginalised over the Wilson coefficients  $C_{lq}^{(1)}$ ,  $C_{lq}^{(3)}$  and  $C_{eu}$  (left) and  $C_{lq}^{(3)}$ ,  $C_{lu}$  and  $C_{qe}$  (right).

In addition to setting limits on semileptonic operators, we have observed in Figure 5.4

that the PVE and Drell-Yan datasets also affect bounds on the four-quark operator  $C_{qq}^{(1)'}$  even though they are not directly sensitive to this coefficient. To explain this feature, we report in the right panel of Figure 5.7 the 2D-limits on  $C_{qq}^{(1)'}$ -vs- $C_{ed}$ . In a global fit without PVE data, these two operators are correlated as shown by the pink contour. PVE sets a stringent constraint on  $C_{ed}$  which in turn improves the bounds on  $C_{qq}^{(1)'}$  significantly, see the black contour.

### 5.3.3 Top, Flavour and Dijet Datasets

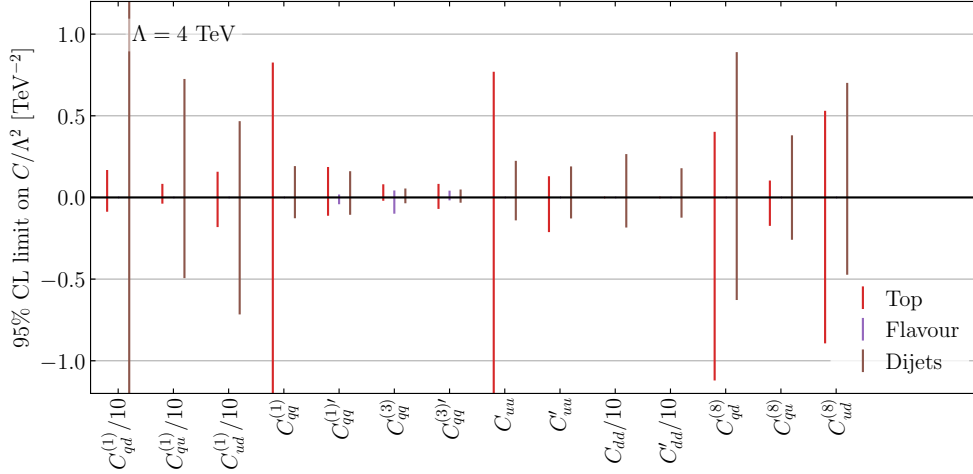


**Figure 5.9:** Single-operator bounds at 95% CL on the Wilson coefficients of the four-quark operators from different datasets.

Top, flavour and dijet data overlap in their sensitivity to four-quark operators. In the following, we will discuss in how far the bounds from these sectors are complementary in a global fit, focusing in particular on the interplay of top and flavour data.

We compare the one-parameter bounds on the relevant Wilson coefficients in Figure 5.9. At the single-parameter level, top (red) and dijet (brown) data are equally relevant for constraining four-quark operators. However, at the level of a global fit, limits from top physics typically dominate and dijet data is mainly relevant to set limits on operators which do not contribute to top physics such as those involving only down-type quarks, see Figure 5.4. The flavour dataset (purple) has a crucial impact on the bounds on  $C_{qq}^{(1)'}$  and  $C_{qq}^{(3)'}$  even in our  $U(3)^5$  symmetric scenario, setting the strongest one-parameter bounds on these operators and having a strong effect in the global analysis as well. For these two parameters, flavour data can only constrain the direction  $C_{qq}^{(1)'} - C_{qq}^{(3)'}$ , which contributes at tree-level to  $C_1$  and at one-loop to  $C_9$  and  $C_{10}$  of the WET. This can be explained by the fact that only structures with one up-type and one down-type quark bilinear  $(\bar{u}\gamma_\mu u)_L(\bar{d}\gamma^\mu d)_L$  with colour indices contracted within the brackets contribute to flavour observables, for which  $C_{qq}^{(1)'}$  and  $C_{qq}^{(3)'}$  have exactly opposite signs. On the other hand,  $t\bar{t}$  production receives contributions from both the above structure and from its equivalent with two up-type quark bilinears. The latter, to which  $C_{qq}^{(1)'}$  and  $C_{qq}^{(3)'}$  both contribute with the same sign, dominates due to the larger up-type PDFs. As a result,  $C_{qq}^{(1)'}$  and  $C_{qq}^{(3)'}$  have a positive relative sign in all considered  $t\bar{t}$  observables. We show the complementary behaviour of top and flavour data in Figure 5.10. The filled contours correspond to fitting  $C_{qq}^{(1)'}$  and  $C_{qq}^{(3)'}$  only, whereas the

empty contours have been obtained in a 14-parameter fit marginalising over the remaining twelve four-quark operators. We can see that while the limits are degraded in a global fit, as expected, the complementarity of the flavour and top datasets persists. Therefore, both datasets are essential in order to perform a global analysis including these two operators. See also [159] on resolving the flavour structure of the four-quark operators  $\mathcal{O}_{qq}^{(1)}$  and  $\mathcal{O}_{qq}^{(3)}$  including higher-order terms of the MFV expansion using similar datasets<sup>2</sup>.

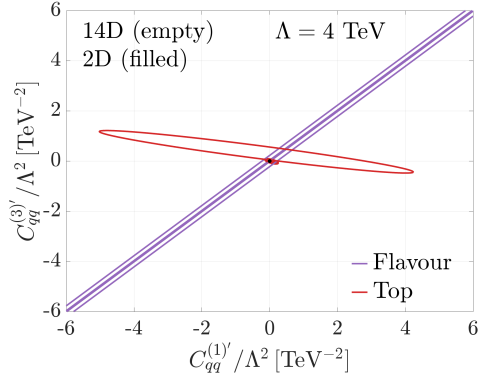


**Figure 5.10:** 95% CI contours of  $C_{qq}^{(1)'}$  vs  $C_{qq}^{(3)'}$  from flavour and top data. See text for details.

In our work, the flavour dataset mostly affects bounds on the operators of the four-quark sector. When going beyond our minimal MFV hypothesis, flavour data has been shown to play an important role for constraining higher-order terms in the MFV expansion of semileptonic and gauge-fermion operators [150, 160, 161].

<sup>2</sup>Our parameters  $C_{qq}^{(x)'}$  correspond to  $(\widetilde{aa})^{(x)}$  in their notation.



# RGE Improved Global Analysis

## Contents

---

<b>6.1</b>	<b>Inclusion of the RGE . . . . .</b>	<b>56</b>
<b>6.2</b>	<b>The Impact of RGE on the Global Analysis . . . . .</b>	<b>59</b>

---

While in the previous chapter we constructed the likelihood to fit all SMEFT coefficients under our symmetry assumptions and studied how the inclusion of NLO contributions affects the fit, in this chapter we will systematically incorporate the effects of the RGE. There are several motivations to include these effects. The main one is that the energy scale of the observables included in our fit ranges from below 1 GeV, as in the case of PVE, over the mass of the  $Z$  boson for EWPO, up to 2.3 TeV for kinematic distributions in DY and  $t\bar{t}$  production. In Figure 6.1, we show a graphical representation of the energy scales associated with the hundreds of observables included in our analysis. The majority of the energy scales associated with the datasets lies at the electroweak scale. Only 45 observables from dijets, DY and top correspond to energy scales greater than 1 TeV, 118 observables lie above the 500 GeV threshold. 45 observables from the flavour sector, PVE and lepton scattering have been measured at scales below 10 GeV.

As explained in Chapter 2, when these large scale separations are present, RGE improved perturbation theory is a necessity. With this inclusion, often neglected in the literature of SMEFT global analyses, one can perform a really consistent study of the combination of different datasets each one lying at a different energy scale, while providing bounds on a common scale.

Having the full RGE-improved fit also facilitates the connection to UV-complete models, which are defined at high energy scales. Any consistent study of such models requires the inclusion of RGE effects in order to evolve the predictions down to the low-energy scale where the experimental data reside.

Another fundamental aspect for which it is crucial to include RGE effects is that we do not have access to NLO computations for all the observables we have in our fit. Since RGE, contains the logarithms (related to the divergencies) of these loop corrections, it provides a first test of how the full inclusion of these NLO contributions could look like.

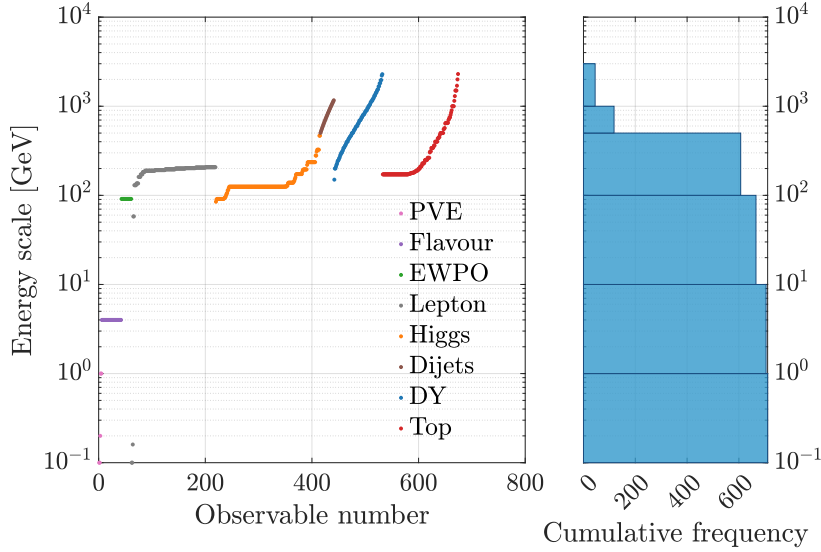


**Figure 6.1:** Energy scales corresponding to the observables included in our global analysis.

## 6.1 Inclusion of the RGE

The first practical modification we have to introduce is that since RGE is flavour dependent we need explicit flavour indices in all of our predictions. For this reason we need to introduce some changes in the dataset, like switching from the aforementioned flavour averaged EWPO observables to completely flavour general as reported in Table 4. Moreover, we reintroduce the flavour indices in Higgs and top observables that were suppressed for the fits described so far. In addition to our previous dataset, we incorporate observables from  $\beta$ -decay and semileptonic meson decays as a single pseudo-observable,  $\Delta_{\text{CKM}}$ , which represents the unitarity of the CKM matrix [156, 157, 162–166].

We showed that this pseudo-observable mainly exhibits sensitivity to  $C_{lq}^{(3)}$  in a global fit [68]. Furthermore, we also include kinematic distributions of LHC diboson measurements from ATLAS in the  $WZ$  [167] and  $WW$  [168] final states. The inclusion of the diboson datasets reduces the allowed Wilson coefficient ranges of the operators contributing to EWPO at LO by up to 23 %. The limits on the correlated Wilson coefficients CHB improves at a similar level.

In order to account for RGE effects, we need to assign a scale to each of our observables. As a baseline, we define the scale as the mass of the  $Z$  boson, the mass of the Higgs boson  $m_h$  and the mass of the top quark  $m_t$  in EWPO, Higgs and top-quark observables, respectively. In energy-dependent kinematic distributions, we use the invariant mass of the final state particles or the squared sum of a particle mass and its transverse momentum,  $\sqrt{m_i^2 + p_{T,i}^2}$ , as a scale measure. For bins in distributions, we use the lower edge of each bin as a measure of the scale of the process, as most distributions fall off quickly with enhanced energy. The scale assigned to each observable is explicitly listed in the last column of Tables 1, 2, 3, and 4 of Appendix A.

To perform the RG evolution, we employ the `DsixTools` package [36, 39, 44, 148, 149]. Resummed leading-log RGE effects are included via its evolution matrix approach which allows us to express the evolution of the Wilson coefficients from a high scale  $\Lambda$  to a lower

scale  $\mu$  as

$$C_i(\mu) = U_{ij}(\mu, \Lambda) C_j(\Lambda) \quad (6.1)$$

where  $U_{ij}$  denotes the evolution matrix. Following the discussion in [149], the RG equations governing the evolution of the SMEFT and LEFT Wilson coefficients can be expressed in compact matrix form as

$$\frac{dC_i^{(4)}(t)}{dt} = \frac{1}{16\pi^2} \gamma_{ij}^{(4)}(C_k^{(4)}, C_k^{(6)}) C_j^{(4)}(t), \quad (6.2)$$

$$\frac{dC_i^{(6)}(t)}{dt} = \frac{1}{16\pi^2} \gamma_{ij}^{(6)}(C_k^{(4)}) C_j^{(6)}(t), \quad (6.3)$$

where the indices  $i, j, k$  run over the set of EFT operators,  $t \equiv \ln \mu$  denotes the logarithmic renormalization scale, and  $\gamma$  represents the anomalous dimension matrix. The superscripts (4) and (6) refer to quantities associated with dimension-four and dimension-six operators, respectively. In this formulation, contributions from  $C_k^{(6)}$  to  $\gamma^{(6)}$  are neglected, as these would correspond to higher-order effects in the EFT expansion.

Since  $C_k^{(6)} \sim \mathcal{O}(1/\Lambda^2)$ , Equation (6.2) can be consistently truncated to

$$\frac{dC_i^{(4)}(t)}{dt} = \frac{1}{16\pi^2} \gamma_{ij}^{(4)}(C_k^{(4)}) C_j^{(4)}(t) + \mathcal{O}(1/\Lambda^2), \quad (6.4)$$

with  $\gamma_{ij}^{(4)}(C_k^{(4)}) \equiv \gamma_{ij}^{(4)}(C_k^{(4)}, 0)$ . These reduced equations coincide with the Standard Model RGEs, for which  $\gamma_{ij}^{(4)}$  is known. This smaller system can be solved numerically once for a given set of input parameters, resulting in a set of interpolating functions  $\hat{C}_k^{(4)}(t)$  such that

$$C_k^{(4)}(t) = \hat{C}_k^{(4)}(t) + \mathcal{O}(1/\Lambda^2). \quad (6.5)$$

Substituting this solution into Equation (6.3), we obtain

$$\frac{dC_i^{(6)}(t)}{dt} = \frac{1}{16\pi^2} \gamma_{ij}^{(6)}(\hat{C}_k^{(4)}) C_j^{(6)}(t) + \mathcal{O}(1/\Lambda^4) \equiv \hat{\gamma}_{ij}^{(6)}(t) C_j^{(6)}(t) + \mathcal{O}(1/\Lambda^4), \quad (6.6)$$

where  $\hat{\gamma}^{(6)}(t)$  is now an explicit function of  $t$  determined entirely by the precomputed  $\hat{C}_k^{(4)}(t)$ . Neglecting higher-order terms, Equation (6.6) is solved by

$$C_i^{(6)}(t) = U_{ij}^{(6)}(t, t_0) C_j^{(6)}(t_0), \quad (6.7)$$

where  $t_0 \equiv \ln \mu_0$  and  $\mu_0$  is the matching scale for the dimension-six Wilson coefficients. The evolution matrix  $U^{(6)}$  is given formally by

$$\begin{aligned} U^{(6)}(t, t_0) &= \mathcal{T} \exp \left[ \int_{t_0}^t \hat{\gamma}^{(6)}(\omega) d\omega \right] \\ &= \sum_{n=0}^{\infty} \int_{t_0}^t d\omega_n \int_{t_0}^{\omega_n} d\omega_{n-1} \cdots \int_{t_0}^{\omega_2} d\omega_1 \hat{\gamma}^{(6)}(\omega_1) \cdots \hat{\gamma}^{(6)}(\omega_n), \end{aligned} \quad (6.8)$$

where  $\mathcal{T}$  denotes  $t$ -ordering. In practice,  $U^{(6)}$  is most efficiently obtained by numerically solving Equation (6.6) for a set of linearly independent initial conditions for  $C_j^{(6)}(t_0)$ . Once computed for a fixed set of Standard Model inputs, the evolution matrix can be reused for

any set of dimension-six initial conditions, making the evaluation of Equation (6.7) computationally inexpensive.

As already pointed out, we choose a fixed value of  $\Lambda = 4$  TeV throughout our study. This value is approximately twice the scale of the highest-energy observable included in our fit to ensure the validity of the EFT approach. Note that at scales  $\mu < \Lambda$ , the set of Wilson coefficients included in our analysis is no longer constrained to those obeying a  $U(3)^5$  symmetry as flavour non-conserving interactions are still allowed within the SM. In other words, the initial conditions  $C(\Lambda) = 0$  can be violated along the RGE flow, leading to  $U(3)^5$  non-symmetric contributions to our observables at lower energy scales. This effect is particularly significant for the coefficient  $C_{uH}$ . To quantify it, we assume that all  $U(3)^5$ -symmetric coefficients are of order one at the high scale, while the flavour-violating ones are initially set to zero. As a result of RGE evolution,  $C_{uH}$  is of order one at the EW scale. In contrast, all other flavour-violating coefficients, generated only via the RGE evolution, reach at most the percent level. All of the Wilson coefficients induced through the RGE are dependent on the 41 coefficients defined at the NP scale. Therefore, they do not correspond to independent NP directions in our fit and cannot induce any flat directions.

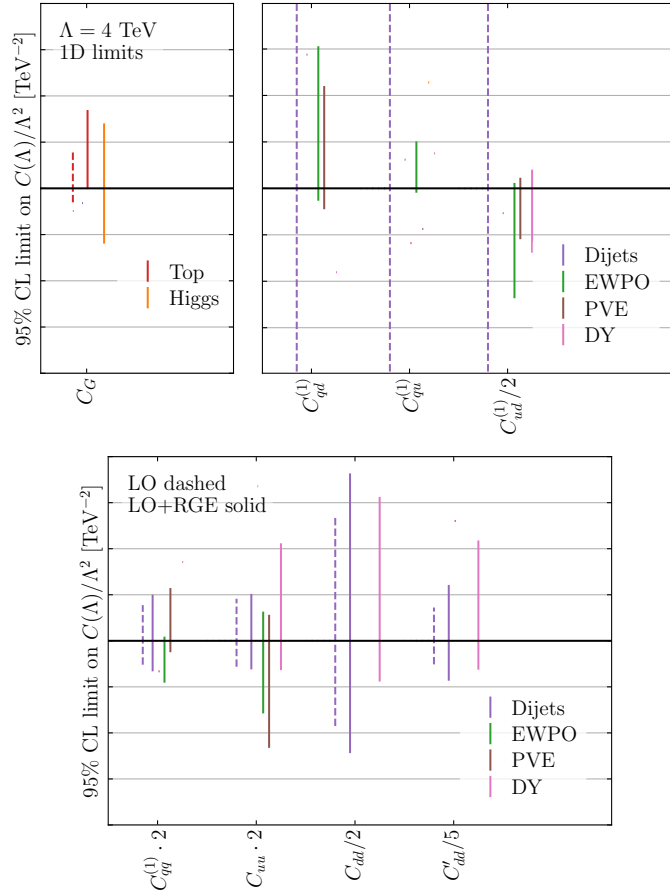


**Figure 6.2:** Single-parameter limits on the Wilson coefficients before (dashed) and after (solid) the inclusion of RGE effects from different datasets. We only display the strongest bound for the LO case and the LO+RGE bounds which are at most a factor two wider than the strongest bound in this setting. The different panels separate operators involving only gauge fields, four-quark operators with a suppressed interference in dijets+ $\gamma$  production and additional four-quark operators.

To assess the impact of RGE effects, we begin by examining single-parameter fits. The

inclusion of RGE mixing effects implies that operators defined at the high scale mix into operators defined at lower scales. Consequently, datasets that at LO do not constrain certain coefficients can provide significant constraints through RGE effects. These newly introduced constraints can be competitive or even stronger than those present before RGE effects are included, in cases where LO constraints are weak.

We present in Figure 6.2 the limits from single-parameter fits before (dashed lines) and after (solid lines) the inclusion of RGE effects for individual datasets. We show only the strongest bound for the LO case and the LO+RGE bounds that are at most a factor of two weaker than the strongest bound in this setting. For the coefficient  $C_G$ , the best constraints at LO and LO+RGE come from top quark processes. However, via mixing with the coefficient  $C_{HG}$ , the inclusion of RGE effects provides substantial additional constraints from Higgs data.

At LO, the only limits on the operators  $C_{qd}^{(1)}$ ,  $C_{qu}^{(1)}$ , and  $C_{ud}^{(1)}$  result from dijet+ $\gamma$  data. As the dijet production diagrams including the corresponding SMEFT operators and the dominant SM diagram do not interfere, the Wilson coefficients are poorly constrained at LO. When RGE effects are included, we observe additional limits from EWPO, PVE and DY on these coefficients. The mixing of  $C_{qd}^{(1)}$  and  $C_{ud}^{(1)}$  with the semileptonic operator  $C_{ed}$ , is responsible for the bounds from PVE and DY. Despite the fact that these mixing effects are suppressed by the electromagnetic coupling constant  $\alpha$ , they still lead to competitive constraints at the single-parameter fit level. This is a reflection of the fact that currently no dataset probes these coefficients well at LO. The constraints from EWPO result from the mixing of the considered four-quark operators with  $C_{Hu}$  and  $C_{Hd}$ , both of which are tightly constrained by EWPO.

The operator  $C_{qq}^{(1)}$  is dominantly constrained by dijet data at LO. This constraint remains relevant even when RGE effects are included, but after RGE, the most stringent bound comes from EWPO due to significant mixing with  $C_{Hq}^{(1)}$ . An additional constraint arises from PVE due to the mixing of  $C_{qq}^{(1)}$  and  $C_{qe}$ . The coefficient  $C_{uu}$  mixes with operator  $C_{Hu}$  and the semileptonic operators  $C_{eu}$  and  $C_{lu}$ , leading to additional bounds from EWPO, DY and PVE. Nevertheless, its dominant constraint still arises from dijet data. Finally, the operators  $C_{dd}$  and  $C'_{dd}$ , which at LO are constrained solely by dijet data, receive significant additional constraints from DY when mixing effects are included, even though the mixing of  $C_{dd}$  and  $C'_{dd}$  with semileptonic operators is suppressed by  $\alpha$ . For  $C_{dd}$ , DY even provides the strongest single-parameter constraint.

## 6.2 The Impact of RGE on the Global Analysis

We present now a global analysis based on RGE improved LO predictions.

In Figure 6.3, we show the 95% CL limits from a global fit on all 41 Wilson coefficients. We compare the bounds from the LO analysis (blue) and the RGE improved LO analysis (orange). We also show the limits from an RGE improved analysis based on partial NLO predictions (green). Overall, we find that the inclusion of RGE effects helps remove the (almost) flat directions present in the LO fit. Specifically, it significantly improves the bounds on  $C_{qd}^{(1)}$ ,  $C_{qu}^{(1)}$ ,  $C_{ud}^{(1)}$  and  $C_{dd}$ , which are only weakly constrained at LO. To quantify this statement, we present the results of a PCA following the steps explained in 3.3.

To estimate the uncertainty on the limits related to the choice of the scales outlined in Table 1, we varied these scales between twice and half of the central scale value. The corresponding variation in the bounds on the Wilson coefficients is shown in Figure 6.3 in a

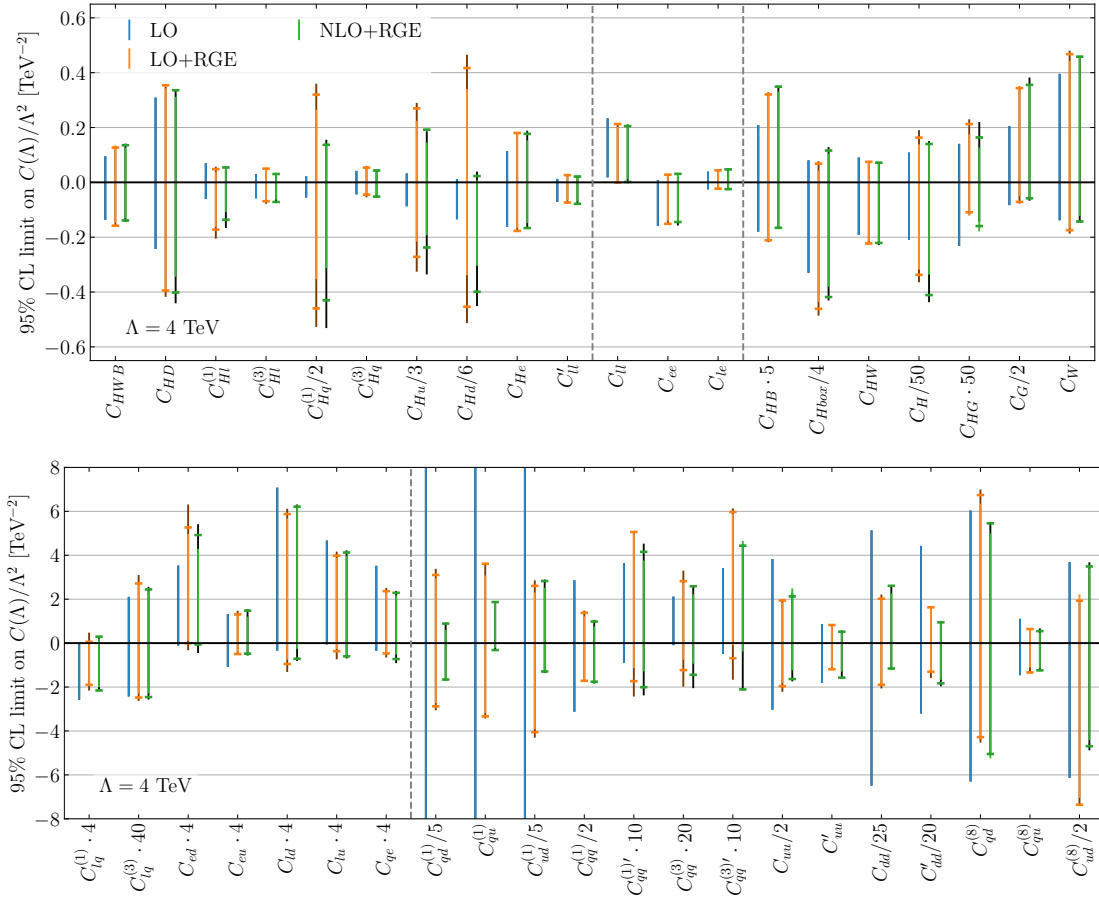


**Figure 6.3:** Comparison of the limits on the Wilson coefficients from a global fit purely based on LO predictions (LO), with those including RGE effects (LO+RGE) and including partial NLO predictions (NLO+RGE). The darker shading represents the scale uncertainty, estimated by varying the central scale to double or half of its value. The horizontal lines correspond to the limits at the central scale. Note that some Wilson coefficients have been scaled by appropriate factors on the  $x$  axis and that the  $y$  axis is different between the two panels.

darker shade. For most Wilson coefficients, the bounds change by less than 20% when the scale is varied, highlighting the robustness of the limits. However, for  $C_{Hq}^{(1)}$ ,  $C_{Hu}$ , and  $C_{Hd}$ , which are particularly sensitive to RGE effects, this uncertainty exceeds 20%. Additionally,  $C_H$  also deviates by more than 20%. The maximum change is observed for the coefficient  $C_{lq}^{(1)}$ , whose uncertainty increases by 35% when the scales are doubled. In the following, we discuss the main differences between the LO fit and RGE improved LO fit for different Wilson coefficient categories.

### 6.2.1 Operators Contributing to EWPO at LO

The global limits on  $C_{Hq}^{(1)}$ ,  $C_{Hu}$  and  $C_{Hd}$ , which contribute to modified  $Zq\bar{q}(h)$  couplings, increase by factors 10.1, 4.5 and 5.9, respectively. This is the result of significant correlations between the quark-gauge operators and four-quark operators induced by the RG evolution. For  $C_{Hq}^{(3)}$ , which also contributes to modified  $Wq\bar{q}'(h)$  interactions, correlations with four-quark operators are milder as a result of the additional constraints from  $W$  decay and  $Wh$  production. In the top left panel of Figure 6.4, we show the correlations of  $C_{Hq}^{(1)}$ ,  $C_{Hu}$  and  $C_{Hd}$  with selected four-quark operators after including RGE effects in the fit. As one can see,

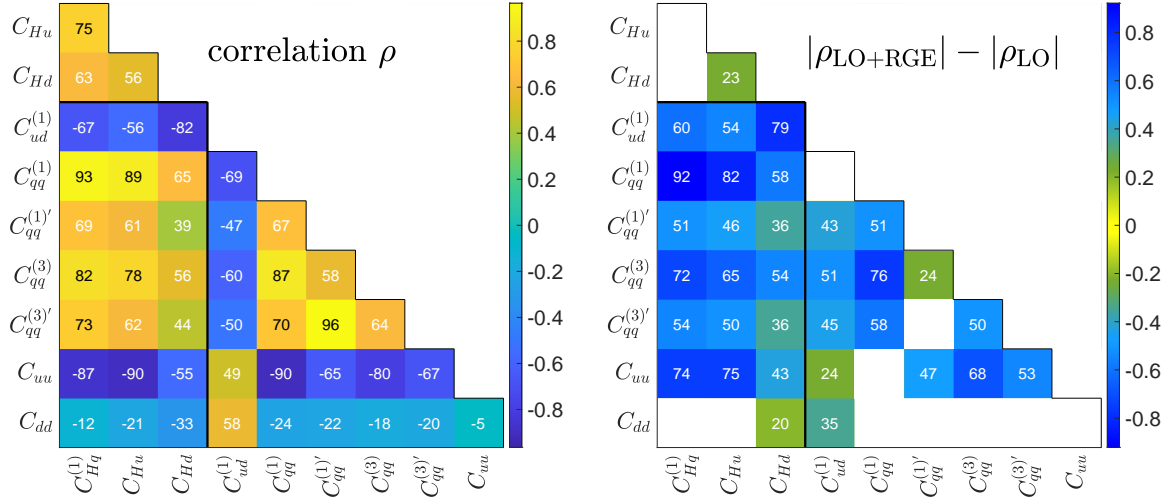


**Figure 6.4:** Left: Correlation  $\rho$  (in percent) between selected Wilson coefficients in the LO+RGE fit. Right: Difference between the absolute values of the correlations before and after the inclusion of RG evolution effects in the fit. Correlation changes below 20% have been omitted for better visibility of the dominant effects.

several correlations are above the 50% level. To highlight how much of these correlations is due to the RGE effects, in the top right panel of Figure 6.4, we show the difference between the absolute values between before and after including RGE effects in the fit. The absolute correlations of the operators  $C_{Hq}^{(1)}$ ,  $C_{Hu}$ , and  $C_{Hd}$  with  $C_{ud}^{(1)}$ ,  $C_{qq}^{(1)}$ ,  $C_{qq}^{(1) \prime}$ ,  $C_{qq}^{(3)}$ ,  $C_{qq}^{(3) \prime}$ , and  $C_{uu}$  all increase by at least 36%. The strongest increases for each gauge-quark coefficient are an increase by 92% between  $C_{Hq}^{(1)}$  and  $C_{qq}^{(1)}$ , 82% between  $C_{Hu}$  and  $C_{qq}^{(1)}$ , and 79% between  $C_{Hd}$  and  $C_{ud}^{(1)}$ . Evidently, the RGE improvement induces strong correlations between the gauge-quark operators and several four-quark operators<sup>1</sup>. We have explicitly checked that removing four-quark operators from the fit would reduce the changes of the limits on  $C_{Hq}^{(1)}$ ,  $C_{Hu}$ , and  $C_{Hd}$  in an RGE improved LO fit to the 10% level. Even only removing the four-quark operators  $\{C_{uu}, C_{dd}, C_{dd}^{\prime}, C_{qq}^{(1)}, C_{qq}^{(3)}\}$ , which are often excluded or constrained to specific directions in top-centered global analyses, already reduces the effect of the RGE improvement significantly, with limits still increasing by factors 2 – 3.

The Wilson coefficients of most other operators contributing to EWPO at LO are only mildly influenced by the RGE improvement. The bounds on  $C_{HD}$ ,  $C_{Hl}^{(1)}$  and  $C_{He}$  increase by 36%, 55% and 32%, respectively, as a result of increased correlations with various semilep-

<sup>1</sup>In our previous SMEFT fit based on partial NLO predictions [68], we noticed an increase of the limits on  $C_{Hq}^{(1)}$  by a factor two when including partial NLO EWPO predictions, while the limits on  $C_{Hu}$  and  $C_{Hd}$  only marginally changed. As the same diagrams contribute at NLO and in the RGE, this raises the question of why the correlation effects are stronger in the RGE improved fit than in the partial NLO fit. This is likely due to the fact that our NLO fit only includes partial NLO corrections. The lack of NLO predictions for  $Vh$  production leads to four-quark-operator-independent constraints on operators influencing quark-gauge interactions in the partial NLO fit. The (oversimplified) LO  $Zh$ -production prediction hence breaks degeneracies between the four-quark operators and  $C_{Hq}^{(1)}$ ,  $C_{Hu}$ ,  $C_{Hd}$ . For  $C_{Hq}^{(1)}$ , which has a reduced contribution to  $Zh$  production (compare to  $C_{Hu}$ ,  $C_{Hd}$  and  $C_{Hq}^{(3)}$ ) as a result of a cancellation between the contributions from up- and down-type quarks, this reduction of correlations with four-quark operators is less pronounced and we can already see its effect in the partial NLO fit. This highlights the relevance of further NLO SMEFT predictions, for instance for  $Zh$  production, which has recently been calculated for the production at lepton colliders [100].

tonic operators. Diagonal running effects generally only play a subdominant role for the operators contributing to EWPO at LO. Accounting only for diagonal running effects, the bounds on  $C_{HD}$ ,  $C_{Hl}^{(1)}$  and  $C_{He}$  would only increase by 16%, 13% and 1%, respectively.

### 6.2.2 Four-Lepton Operators

The four-lepton operators  $C_{ll}$ ,  $C_{ee}$ , and  $C_{le}$  are primarily constrained by lepton scattering processes at LO and exhibit minimal interplay with other datasets. Their RGE effects are suppressed by powers of  $\alpha$ . As expected, the limits on these coefficients remain largely unaffected by the inclusion of RGE effects, with global limits showing deviations of less than 7%. The bounds on  $C'_{ll}$ , which enters the SMEFT definition of the Higgs vacuum expectation value and thereby contributes to a larger set of observables, increases by 19% as a result of correlations.

### 6.2.3 Higgs Sector

The limits on most of the Wilson coefficients contributing mainly to Higgs physics do not significantly change after the inclusion of RGE effects. Increases and decreases of the limits in this sector are mostly dominated by diagonal running effects. For the coefficient  $C_{HG}$  the diagonal running contribution,  $C_{HG}(\Lambda) \approx 0.75 C_{HG}(m_H)^2$ , dominates the decrease of the bound on this coefficient by around 20%. Similarly, the bound on  $C_H$  weakens by around 75% dominantly as a result of its diagonal running,  $C_H(\Lambda) \approx 1.45 C_H(m_H)$ .

We also note some shifts of the RGE improved fit limits with respect to the LO fit. As an example, we discuss here the shift of  $C_G$  towards more non-SM like values, which is strongly correlated with the shift of  $C_{HG}$ . The shift of  $C_G$  in the RGE improved fit is rooted in multiple ( $< 2\sigma$ ) deviations in Run I  $t\bar{t}$  production and the fact that it mixes with an operator with a different kinematic structure at the experimentally relevant scale.  $t\bar{t}$  production is sensitive to modifications of the top-gluon coupling as induced by  $C_{uG}$ , which does not obey a  $U(3)^5$  symmetry at the high scale  $\Lambda$ , but which receives sizeable contributions from mixing with  $C_G$  at scales  $\mu < \Lambda$ .

CMS analysed Run I  $t\bar{t}$  data in a double differential distribution in the invariant mass  $m_{t\bar{t}}$  and rapidity  $y_{t\bar{t}}$  of the  $t\bar{t}$  system [169, 170]. In Figure 6.5, we show the measured  $m_{t\bar{t}}$  distribution relative to the SM value. For each bin in  $m_{t\bar{t}}$ , we show the four measurements in the different rapidity bins along with their symmetric error bars. As one can see, all four measurements in the first  $m_{t\bar{t}}$  bin lie systematically above the SM prediction, while they lie systematically below the SM prediction in all remaining bins. In the same plot, we also show the SMEFT predictions when turning on a single Wilson coefficient  $C_G$  (blue solid line) or a single Wilson coefficient  $C_{uG}$  (orange line) without including RGE effects. The values of the Wilson coefficients are chosen to match the RGE improved prediction from  $C_G(\Lambda) = 1$  at the scale of the first bin  $\mu = 340$  GeV,

$$\begin{aligned} C_G(340 \text{ GeV}) &= 0.78 C_G(4 \text{ TeV}), \\ C_{uG}(340 \text{ GeV}) &= -0.13 C_G(4 \text{ TeV}). \end{aligned} \tag{6.9}$$

<sup>2</sup>Note that we present  $C_i(\Lambda)$  as a function of its low scale definition  $C_i(\mu)$  here. The proportionality factor defined in this way corresponds more directly to the change of the limit between the LO fit, which sets constraints on  $C_i(\mu)$ , and the LO+RGE fit, which sets constraints on  $C_i(\Lambda)$ . If we presented  $C_i(\mu)$  as a function of  $C_i(\Lambda)$  instead, the limits would have an inverse proportionality.

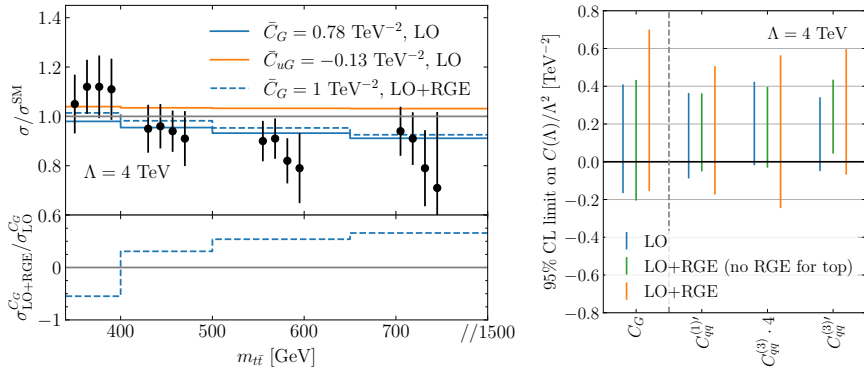


**Figure 6.5:** Left: SMEFT predictions for the  $m_{t\bar{t}}$  distribution in  $t\bar{t}$  production for the operators  $C_G$  and  $C_{uG}$ . We employ the notation  $\bar{C} = C/\Lambda^2$ . The reference values for  $\bar{C}_G$  and  $\bar{C}_{uG}$  refer to the RGE-induced contributions from  $\bar{C}_G(\Lambda) = 1 \text{ TeV}^{-1}$  at the scale  $\mu = 340 \text{ GeV}$ , see Equation (6.9). The datapoints refer to the CMS Run I measurements in a double differential  $m_{t\bar{t}} - y_{t\bar{t}}$  distribution [169, 170]. Right: Limits on selected operators excluding RGE effects in SMEFT predictions for top-quark observables.

Moreover, we show the distribution for  $C_G$  when running down to  $m_{t\bar{t}}$  from  $\Lambda = 4 \text{ TeV}$  (dashed blue line). Due to a sign difference between the two contributions from  $C_G(\Lambda)$  in the SMEFT prediction, they partially cancel each other and lead to a sign flip of the  $C_G(\mu)$  prediction of the low- $m_{t\bar{t}}$  bin of the  $m_{t\bar{t}}$  kinematic distributions. As a result, positive values of  $C_G$  are able to improve the agreement with the data throughout all measurements when RG effects are included, thereby shifting the  $C_G$  limits towards positive values.

To further highlight that the shift of  $C_G$  is dominated by top sector data, we show in Figure 6.5 (right) the limits from a global fit when excluding RGE effects in the top sector. As apparent from the plot, the limits on these two operators when excluding RGE effects in the top sector (green lines) match the limits from a fit excluding all RGE effects (blue lines) much more closely, and no shift is present.

Since both  $C_{uG}$  and  $C_G$  also enter the predictions of gluon-fusion Higgs production, they are correlated with  $C_{HG}$ <sup>33</sup>. The shift of  $C_G$  in turn leads to a shift of  $C_{HG}$ .

### 6.2.4 Semileptonic Operators

Semileptonic operators exhibit notable mixing effects with four-quark operators. The most significant impact on the limits is observed for the operator  $C_{ed}$ , whose bound increases by 45%. In particular, the operators  $C_{dd}$  and  $C'_{dd}$ , which are among the least constrained in the global fit, mix into  $C_{ed}$ . Figure 6.6 illustrates the 95% CL contours for  $C_{ed}$  and  $C_{dd}$ , marginalising over the remaining 39 parameters. When RGE effects are included (orange continuous line), the constraint on  $C_{ed}$  is weakened compared to the LO fit without RGE (blue line). However, when the RGE contributions are removed from the DY dataset (orange dashed line) the bound on  $C_{ed}$  shrinks back to the blue contour, showing the impact of RGE effects in DY. Notably, the correlation between  $C_{ed}$  and  $C_{dd}$  increases from  $-15\%$  to  $45\%$  in the global fit after the inclusion of RGE effects.

Other semileptonic operators are less affected by RGE effects. The bounds on  $C_{eu}$ ,  $C_{lq}^{(1)}$  and  $C_{qe}$  decrease by 25% due to additional constraints from EWPO after the RGE improvement, which significantly reduces the correlation between selected semileptonic operators. For instance, the correlation between  $C_{lq}^{(1)}$  and  $C_{ed}$  reduces by 79%. Meanwhile, the bounds of the remaining coefficients change by less than 15%.

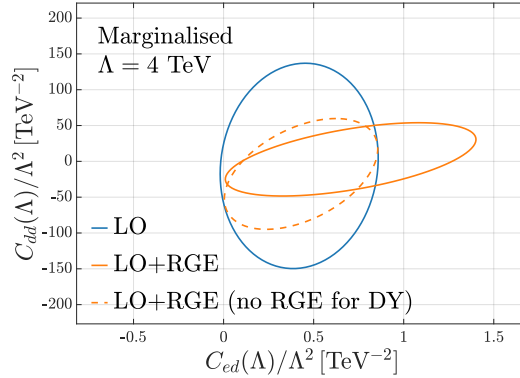


**Figure 6.6:** 95% CL limits on the Wilson coefficients  $C_{ed}$  and  $C_{dd}$  before and after the inclusion of RGE effects in a 2D plane.

### 6.2.5 Four-Quark Operators

The limits on individual four-quark operators significantly improve in the RG improved LO fit. As pointed out above, at LO, the Wilson coefficients  $C_{qd}^{(1)}$ ,  $C_{qu}^{(1)}$  and  $C_{ud}^{(1)}$  are only constrained by the dijets dataset. Since the corresponding operators do not interfere with the dominant SM diagram as a result of their colour structure, the bounds on these operators from an LO fit are weak, leaving (almost) blind directions in the fit. Through RGE effects, these operators are constrained in EWPO, PVE and DY, see also the single-parameter fit limits in Figure 6.2. The mixing of  $C_{qd}^{(1)}$ ,  $C_{qu}^{(1)}$  and  $C_{ud}^{(1)}$  generates sizeable contributions to  $C_{Hu}$ ,  $C_{Hd}$  and  $C_{qu}^{(1)}$ . While the strong crosstalk of these and other four-quark coefficients leads to weaker bounds on the coefficients entering EWPO at LO, as discussed above, bounds on the four-quark coefficients in turn improve. For DY and, subdominantly, PVE constraints, the dominant mixing effects are with the semileptonic operator  $C_{ed}$ . While limits from EWPO on  $C_{qd}^{(1)}$ ,  $C_{qu}^{(1)}$  and  $C_{ud}^{(1)}$  are stronger, they come with large correlations between these four-quark operators. The inclusion of DY data reduces this correlation. Interestingly, the limits on  $C_{qd}^{(1)}$ ,  $C_{qu}^{(1)}$ ,  $C_{ud}^{(1)}$  only show a weak dependence on the scale choice. Varying the scale by a factor of two results in 12 – 15% changes of the limits. This is a hint that the associated scale of the observables constraining these operators through RG effects are measured at the EW scale (EWPO) such that the effect of the scale variation is  $\log(2\mu_{EW}/\Lambda)/\log(\mu_{EW}/\Lambda) \approx 0.82 = 1 - 18\%$ .

Limits on  $C_{qq}^{(1)}$ ,  $C_{uu}$ ,  $C_{dd}$  and  $C'_{dd}$  improve by (40 – 70)%. As pointed out already in the discussion of single-parameter limits in 6.1, these coefficients receive additional constraints from DY, EWPO and PVE.

Limits on the coefficients  $C_{qq}^{(1)'}$ ,  $C_{qq}^{(3)}$ ,  $C_{qq}^{(3)'}$  weaken by (50 – 80)% in the RGE improved LO fit. RGE effects induce significant correlation increases between these four-quark operators, leading to broader bounds on the Wilson coefficients. These effects are dominated by RGE effects in the top sector, where these operators are tightly constrained, see right panel of Figure 6.5. Neglecting RGE effects for the top-sector observables, the limits (green lines) on these three Wilson coefficients are in close agreement with those of the LO fit (blue lines).

The bounds on  $C'_{uu}$  as well as on the octet four-quark operators change by less than 25%.

We additionally present here, a PCA that can be helpful to examine how the least constrained directions are influenced by the RGE improvement. As explained previously, the

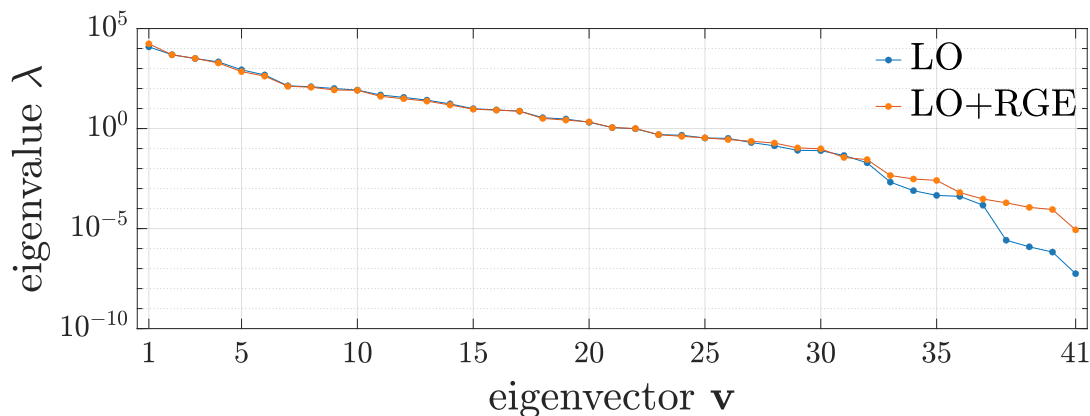


**Figure 6.7:** PCA analysis at LO (blue) and LO+RGE (orange). The eigenvalues of the Fisher matrix  $\lambda$  are shown for all the 41 eigenvectors  $\mathbf{v}$  in decreasing order.

eigenvalues  $\lambda_i$  of the Fisher matrix provide a measure of how good the directions spanned by the eigenvectors  $\mathbf{v}_i$  are constrained in the fit. If an eigenvector direction  $\mathbf{v}_i$  is unconstrained by the data, its corresponding Fisher matrix eigenvalue will be zero.

Figure 6.7 shows the eigenvalues of the Fisher matrix, associated with specific eigenvectors, plotted on a logarithmic scale and ordered from the most to the least constrained direction. The eigenvalues associated with the most constrained directions are very similar in the fits performed with and without RGE effects. On the other hand, the least constrained directions become significantly more constrained when RGE effects are included. In particular, we observe a notable reduction in the eigenvalues for the four least constrained directions. Among these, the least constrained direction differs by three orders of magnitude between the two fits, showing how the parameter space results more constrained when RGE is included.

As pointed out above, the limits on individual Wilson coefficients can also be reduced in the RGE improved fit. This mostly concerns the operators  $C_{Hu}$ ,  $C_{Hd}$  and  $C_{Hq}^{(1)}$ . The increase of the bounds on these coefficients can also be seen in the PCA, where the coefficients  $C_{Hu}$  and  $C_{Hd}$  contribute to the seventh least constrained direction in the LO+RGE fit, corresponding to an eigenvalue  $\lambda_{35} = 2.6 \times 10^{-3}$ . In contrast, in the fit without RGE effects, these same coefficients first appear in a direction associated with an eigenvalue  $\lambda_{24} = 4.7 \times 10^{-1}$ . This demonstrates that limits on these coefficients weaken when RGE effects are included.

We conclude this chapter by analysing how the combination of NLO contributions and RGE effects impacts the bounds. In particular, finite terms in NLO SMEFT predictions tame some of the correlations in the global fit appearing as a result of the RGE improvement. Formally, the inclusion of NLO SMEFT predictions requires the knowledge of two-loop RG equations. As these are currently only partially known [171–177], we employ the one-loop RGE as a proxy. In Figure 6.3, we present the limits from our RGE improved partial NLO fit (green). Deviations from the RGE improved LO fit can be observed mainly for those operators which are directly impacted by the NLO SMEFT predictions. Correlations between  $C_{Hq}^{(1)}$ ,  $C_{Hu}$ ,  $C_{Hd}$  and four-quark operators are reduced by NLO SMEFT predictions for EWPO which results in stronger constraints on these Wilson coefficients. The most significant change is observed in the correlation between  $C_{Hd}$  and  $C_{Hu}$ , which decreases by 55%. Moreover, correlations of  $C_{Hd}$  with multiple four-quark operators reduce by more than

30% . The correlation matrices for the RGE-improved fits at LO and NLO are presented in Appendix C. Limits on some four-quark operators contributing at NLO to  $t\bar{t}h$  ( $C_{qu}^{(1)}$ ) and  $t\bar{t}$  ( $C_{qd}^{(1)}, C_{ud}^{(1)}$ ) production are also reduced when including NLO predictions for these datasets. The allowed ranges of all other Wilson coefficients are changed by at most 24% ( $C_{HI}^{(3)}$ ).

## Conclusion of Part I

In Part I we have carried out the first comprehensive global analysis of the SMEFT under a  $U(3)^5$  flavour symmetry, within the framework of minimal flavour violation. Our study combines a remarkably wide set of experimental inputs, ranging from EWPO and Higgs measurements to top-quark, flavour, PVE, Drell–Yan, and dijet data, including the explicit computation of the SMEFT theory predictions for dijet+ $\gamma$  production. This combination allows us to fully explore the parameter space of the 41 independent dimension-six operators consistent with the assumed flavour symmetry and to remove potential flat directions that would otherwise remain unconstrained in more restricted analyses.

A key lesson from this study is the importance of datasets that may appear subdominant when a single parameter fit is considered. For example, while Drell–Yan data yield very strong single-parameter bounds, they suffer from degeneracies among semileptonic operators. When combined with PVE observables, which provide weaker individual limits, these degeneracies are efficiently resolved, leading to significantly stronger global constraints. Similarly, dijet+ $\gamma$  searches, by probing lower dijet invariant masses than inclusive dijet analyses, offer a powerful handle on four-quark operators while avoiding potential issues with EFT validity at very high energies. Additionally, even in a flavour-symmetric scenario like the one we work in, our analysis demonstrates that flavour observables must be included in a comprehensive fit, as they play a crucial role in constraining otherwise poorly tested directions of the Wilson-coefficient parameter space.

At leading order, we find that the majority of operators are already subject to strong limits, with 29 of them constrained to the level  $|C|/\Lambda^2 < 1/\text{TeV}^2$ . Nevertheless, some four-quark operators, in particular those involving right-handed down-type quarks, remain only weakly probed. These operators exhibit little impact on the global fit of the remaining Wilson coefficients, confirming that the structure of correlations between different operator sectors is relatively mild at LO. Still, their presence highlights the need for complementary observables capable of breaking degeneracies in the four-quark multi-parameter space. The inclusion of NLO SMEFT predictions and RGE effects substantially enriches the analysis. NLO corrections provide sensitivity to operators that contribute only marginally at LO, and introduce additional correlation patterns. RGE effects, in turn, connect observables across different scales, modifying bounds through both diagonal running and operator mixing. Four-fermion operators in particular profit from this interplay, as their mixing with semileptonic and bosonic operators leads to improved constraints. A notable example is provided by the four-down-quark coefficients  $C_{dd}$  and  $C'_{dd}$ , which, despite being poorly constrained at LO, become more tightly bounded once mixing with semileptonic operators is accounted

for. The robustness of these results is further confirmed by their weak dependence on the renormalisation scale choice. At the same time, correlations introduced by RGE effects can weaken certain bounds. This is especially visible for operators that modify the  $Zq\bar{q}(h)$  couplings, such as  $C_{Hq}^{(1)}$ ,  $C_{Hu}$  and  $C_{Hd}$ , where the interplay with four-quark operators leads to broader allowed parameter ranges. These results underscore the importance of including observables sensitive to four-quark interactions in global SMEFT fits, as they are essential to stabilise limits on these electroweak operators.

From a methodological perspective, our work demonstrates how the interplay of NLO corrections, RGE effects, and complementary datasets shapes the structure of global SMEFT fits. While NLO predictions increase the dimensionality of the relevant operator space for certain observables (e.g. EWPO), in practice the constraints from other datasets render the resulting additional degeneracies subdominant. This highlights that consistent progress in SMEFT precision requires not only higher-order theoretical predictions but also a careful balance and integration of all available experimental information. Looking ahead, several avenues for improvement remain open. A full implementation of NLO SMEFT predictions for all relevant observables would provide a clearer understanding of the role of finite terms and could tame some of the degeneracies induced by RGE effects. Finally, exploring more general flavour structures beyond the exact  $U(3)^5$  symmetry assumed here represents a natural and important next step, particularly within the broader MFV framework.

Overall, this study provides one of the most complete pictures to date of the current status of SMEFT constraints under flavour symmetry assumptions, and it lays the groundwork for future global fits with even higher precision and broader scope.

## Part II

# NLO Analysis of the $Q_1^q - Q_{7\gamma}$ Interference in $\bar{B} \rightarrow X_s \gamma$ at Subleading Power



# Introduction to $\bar{B} \rightarrow X_s \gamma$ at Subleading Power

## Contents

---

8.1	Motivations . . . . .	71
8.2	The Factorisation Formula . . . . .	74
8.3	The Known Functions at NLO: $H$ and $J^{(n)}$ . . . . .	75

---

## 8.1 Motivations

As discussed in Chapter 1, flavour-changing processes provide a highly sensitive probe of the SM. These transitions are strongly suppressed, making them ideal channels for uncovering potential signals of NP. Moreover, flavour observables play a crucial role in determining key SM parameters that are otherwise difficult to access. In particular, the inclusive penguin modes  $\bar{B} \rightarrow X_{s,d} \gamma$  and  $\bar{B} \rightarrow X_{s,d} \ell^+ \ell^-$  are theoretically very clean modes to indirectly search for NP (for reviews see [178–180]). Especially, the semi-leptonic  $\bar{B} \rightarrow X_s \ell^+ \ell^-$  modes have the potential to corroborate present tensions [181] in corresponding exclusive decays measured by LHCb (see [182] and references therein), but are affected by independent hadronic uncertainties. These inclusive penguin modes are golden modes for the Belle II experiment, but measurements of the decay mode  $\bar{B} \rightarrow X_{s,d} \ell^+ \ell^-$  might be also possible with the LHCb experiment, especially at high- $q^2$  [183–185]. The expected precision of the Belle II measurements [186] calls for a systematic reduction of the theoretical errors in the calculations of the decay rates, CP asymmetries and other observables.

Although these processes are mediated by weak interactions, the presence of strong interactions dramatically enhances the decay rates by approximately a factor of two and introduces significant theoretical challenges. Since quarks are confined within hadrons and the QCD coupling is large at hadronic scales, perturbative calculations alone are insufficient. However, the EFT framework provides powerful tools to disentangle high-energy (perturbative) and low-energy (non-perturbative) effects. While the former can be computed systematically, the latter are encoded in quantities such as form factors or shape functions, which can sometimes be estimated using methods like QCD sum rules or lattice QCD, but are not always reliably calculable. Together with residual perturbative uncertainties, these

non-perturbative effects limit the precision of theoretical predictions in both the SM and BSM scenarios.

In this thesis we focus on the decay  $\bar{B} \rightarrow X_s \gamma$ , but the same computations will be extremely useful also for the decay with the lepton pair in the final state. Substantial theoretical progress has been made in improving predictions for the branching ratio. Calculations begin in the WET where all heavy particles (above the  $b$ -quark mass  $m_b$ ) are integrated out. At leading order, the decay is governed by a single local operator,  $Q_{7\gamma}$ , involving a photon, a  $b$  quark, and an  $s$  quark.

Because  $m_b \gg \Lambda_{\text{QCD}}$ , it is possible to perform a  $1/m_b$  expansion using HQET. The leading contribution corresponds to the partonic decay, which can be calculated perturbatively. The branching ratio has now been computed up to next-to-next-to-leading order (NNLO) in renormalisation-group improved perturbation theory [187].

The experimental set up where the hadronic jet  $X_s$  has energy of order  $m_b$  but small invariant mass  $\sim m_b \Lambda_{\text{QCD}} \gg \Lambda_{\text{QCD}}$  is referred to us as the so-called endpoint region. In this regime, characterised by  $m_b - 2E_\gamma = \mathcal{O}(\Lambda_{\text{QCD}})$ , the local Operator Product Expansion (OPE) breaks down, and large logarithms emerge in the perturbative expansion. These must be resummed to maintain the validity of perturbation theory and SCET provides the appropriate framework for such resummation.

To further improve theoretical accuracy, one must include subleading-power corrections in the  $1/m_b$  expansion. A factorisation formula for the photon spectrum in the endpoint region is presented in [77] and reads

$$\begin{aligned} d\Gamma(\bar{B} \rightarrow X_s \gamma) &= \sum_{n=0}^{\infty} \frac{1}{m_b^n} \sum_i H_i^{(n)} J_i^{(n)} \otimes S_i^{(n)} \\ &+ \sum_{n=1}^{\infty} \frac{1}{m_b^n} \left[ \sum_i H_i^{(n)} J_i^{(n)} \otimes S_i^{(n)} \otimes \bar{J}_i^{(n)} \right. \\ &\left. + \sum_i H_i^{(n)} J_i^{(n)} \otimes S_i^{(n)} \otimes \bar{J}_i^{(n)} \otimes \bar{J}_i^{(n)} \right], \end{aligned} \quad (8.1)$$

where  $H$  stands for hard function,  $J$  and  $\bar{J}$  for jet functions and  $S$  for shape function. The first line describes the so-called direct contributions, while the second line contains the non-local, so-called resolved contributions. The latter appear only at order  $1/m_b$  in the heavy-quark expansion and are characterised by the fact that the photon is not directly connected to the electroweak vertex. In [188, 189], it was also shown that the support properties of the shape function imply that the resolved contributions (besides the  $Q_{8g} - Q_{8g}$  one) are almost cut independent when the photon energy cut is moved out of the endpoint region.

Starting from (8.1) and separating the contributions from different operators in the effective weak Hamiltonian, we write for the CP-averaged  $\bar{B} \rightarrow X_s \gamma$  photon-energy spectrum in the endpoint region [77]:

$$\begin{aligned} \frac{d\Gamma}{dE_\gamma} &= \frac{G_F^2 \alpha |V_{tb} V_{ts}^*|^2}{2\pi^4} \bar{m}_b^2(\mu) E_\gamma^3 \left[ |H_\gamma(\mu)|^2 \int_{-p_+}^{\bar{\Lambda}} d\omega m_b J(m_b(\omega + p_+), \mu) S(\omega, \mu) \right. \\ &\left. + \frac{1}{m_b} \sum_{i \leq j} \text{Re}[C_i^*(\mu) C_j(\mu)] F_{ij}(E_\gamma, \mu) + \dots \right], \end{aligned} \quad (8.2)$$

where  $p_+ \equiv m_b - 2E_\gamma$ ,  $\bar{\Lambda} = M_B - m_b$ , with  $M_B$  the B-meson mass,  $\bar{m}_b(\mu)$  is the running bottom quark mass in the  $\overline{\text{MS}}$ -scheme, and the terms of order  $1/m_b^2$  and higher have been

omitted. The different resolved contributions appearing in the second line of (8.2) have been extensively studied in [77, 190]. In this work we focus on the interference between the WET operators  $Q_1^q$  and  $Q_{7\gamma}$ , which is the most relevant numerically. In particular, the single resolved contribution at leading order in  $\alpha_s$ , for  $q = c$ , is given by

$$F_{17,c}(E_\gamma, \mu) = \frac{2}{3} (1 - \delta_u) \int_{-\infty}^{\bar{\Lambda}} d\omega \underbrace{\delta(\omega + p_+)}_{\text{LO } J^{(n)}} \times \underbrace{\text{Re} \int_{-\infty}^{\infty} \frac{d\omega_1}{\omega_1 + i\varepsilon} \left[ 1 - F\left(\frac{m_c^2 - i\varepsilon}{2E_\gamma \omega_1}\right) \right]}_{\text{LO } J^{(\bar{n})}} g_{17}(\omega, \omega_1, \mu), \quad (8.3)$$

where the CKM-suppressed parameter  $\delta_u$  is defined as

$$\delta_q = \frac{\text{Re} [\lambda_q C_1(\mu) (-\lambda_t^*) C_{7\gamma}^*(\mu)]}{|\lambda_t|^2 \text{Re} [C_1(\mu) C_{7\gamma}^*(\mu)]}, \quad \lambda_q = V_{qb} V_{qs}^*, \quad (8.4)$$

and we have introduced the subleading shape function  $g_{17}(\omega, \omega_1; \mu)$ . We have also introduced the penguin function given by:

$$F(x) = 4x \arctan^2 \left( \frac{1}{\sqrt{4x - 1}} \right). \quad (8.5)$$

In Equation (8.3), the LO  $n$ -jet function  $J^{(n)}$  reduces to a simple delta function, whereas the LO  $\bar{n}$ -jet function  $J^{(\bar{n})}$  is instead described by the penguin function.

It is worth mentioning that this resolved contribution was first calculated in a local expansion, which implies that the shape function effects were neglected [191–194]. It was shown that this leads to an underestimation of that resolved contribution in both penguin inclusive modes [77, 189]. A new theoretical input [195, 196], namely the derivation of the second moment of the non-perturbative subleading shape function  $g_{17}(\omega, \omega_1; \mu)$  in the resolved  $Q_1^c - Q_{7\gamma}$  contribution, reduced the corresponding uncertainty within the  $\bar{B} \rightarrow X_s \gamma$  decay rate. A more recent analysis, however, found a smaller reduction and additional uncertainties [197]: A clear underestimation of the charm-mass dependence and the missing uncertainty due to the  $1/m_b^2$  corrections in [196] were shown to be the reasons for this discrepancy [197].

The uncertainties associated with the resolved contributions remain among the largest in inclusive penguin modes. For the  $\bar{B} \rightarrow X_s \gamma$  decay, the resolved contribution arising from the interference of  $Q_1^c$  and  $Q_{7\gamma}$  has been estimated as  $(5.45 \pm 2.55)\%$  [188, 189], corresponding to a range of  $[2.9\%, 8.0\%]$ . Here, the Voloshin term of  $+3.3\%$  (using consistently LO Wilson coefficients), traditionally subtracted from the resolved contribution and computed via a local expansion [191–194], has been added back. In addition, a substantial scale ambiguity must be considered. At LO (including the Voloshin term), the scale of the hard functions, i.e. the Wilson coefficients, is not fixed. Shifting their scale from the hard scale to the hard-collinear scale results in an increase of the range of more than 40% in the final prediction [197]. Explicitly, the range gets changed to  $[4.2\%, 11.7\%]$ . The overall range including the scale ambiguity is then  $[2.9\%, 11.7\%]$ . Here the charm-mass dependence of the Voloshin term is not taken into account yet.

This pronounced scale ambiguity, together with the strong dependence on the charm-quark mass, provides a clear motivation for a systematic calculation of the  $\mathcal{O}(\alpha_s)$  radiative

corrections, to this resolved contribution, within RG-improved perturbation theory. Part II of this thesis is devoted precisely to this task. Within the framework of SCET, the NLO corrections can be computed explicitly for the different components of the factorisation formula. In particular, we aim to determine the NLO corrections to the hard function  $H^1$ , to both jet functions  $J^{(n)}$  and  $J^{(\bar{n})}$ , as well as the renormalisation-group evolution of the subleading shape function  $g_{17}$ .

## 8.2 The Factorisation Formula

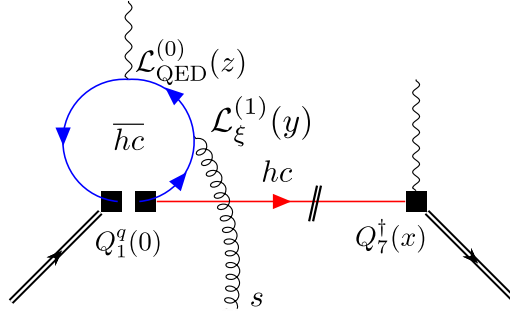


**Figure 8.1:** Schematic illustration of the factorisation theorem and the required Lagrangian insertions.

As discussed in Section 2.5, one of the main advantages of working within the SCET framework is the possibility to exploit factorisation.

The LO factorisation theorem was presented in [77]. In this section, we review the corresponding factorisation formula, which will serve as the starting point for computing the  $\mathcal{O}(\alpha_s)$  corrections. Our goal is to separate the contributions from the hard, hard-collinear, anti-hard-collinear, and soft modes in the  $Q_1^c$ - $Q_{7\gamma}$  interference term.

Figure 8.1 provides a schematic illustration of the factorisation mechanism. The anti-collinear field  $\mathcal{A}_{\perp, \bar{c}}$  is emitted from the anti-hard-collinear quark loop through a leading-power (in QED) Lagrangian insertion,  $\mathcal{L}_{\text{QED}}^{(0)}(z)$ . To compensate for the free transverse index  $\mu_\perp$  in the anti-hard-collinear jet function, a subleading insertion  $\mathcal{L}_\xi^{(1)}(y)$  is required. This insertion generates a soft shape function containing an additional soft gluon field. The red and blue lines in the figure represent the soft Wilson-line structures in the  $n^\mu$  and  $\bar{n}^\mu$  directions, respectively.

In Equation (8.3), we have already shown the different contributions to the factorisation formula at LO. In that case, the hard function reduces to a multiplicative constant. However, at NLO, non-trivial corrections will introduce a functional dependence on this term. Consequently, the factorisation theorem appropriate for including NLO effects reads

$$d\Gamma(\bar{B} \rightarrow X_s \gamma) \sim \int_0^1 du H(u; \mu) \int_{-\infty}^{\infty} \frac{d\omega_1}{\omega_1 + i0} J^{(\bar{n})}(u, \omega_1; \mu) \int_{-\infty}^{\bar{\Lambda}} d\omega J^{(n)}(\omega; \mu) g_{17}(\omega, \omega_1; \mu), \quad (8.6)$$

where the hard function  $H(u; \mu)$  is now convoluted over the variable  $u$ , which parameterises how the large energy  $2E_\gamma \approx m_b$  is shared between the quark and the antiquark in the loop depicted in Figure 8.1. This hard function, at NLO, is obtained by matching the WET operators onto SCET at  $\mathcal{O}(\alpha_s)$ , as will be discussed in Section 8.3.

<sup>1</sup>Note that in Equation (8.3) the LO hard function is simply a constant, whereas at NLO it becomes a non-trivial function that enters the convolution.

The function  $J^{(n)}(\omega; \mu)$  denotes the  $n$ -jet function. At LO, as shown in (8.3), it reduces to a  $\delta$ -function, while at NLO it acquires a less trivial form, which will also be presented in Section 8.3. The function  $g_{17}(\omega, \omega_1; \mu)$  is the only non-perturbative quantity in the expression, referred to as the shape function. Although it cannot be computed perturbatively, its RGE can be determined within perturbation theory; this will be the subject of Chapter 9. Finally, the  $\bar{n}$ -jet function  $J^{(\bar{n})}(u, \omega_1; \mu)$  can be extracted from the anti-hard-collinear momentum region of the partonic decay amplitude,

$$b(m_b v) \rightarrow s(E_X n) \gamma(E_\gamma \bar{n}) g\left(\frac{\omega_1}{2} n\right), \quad (8.7)$$

which we shall compute in detail in Chapter 10. Notice that for practical reasons we have taken out an explicit factor  $1/\omega_1$  which belongs to the jet function  $J^{(\bar{n})}$ .

The convolution structure of the factorisation formula can now be summarised as follows: the hard function  $H(u; \mu)$  is convoluted in  $u$  with the  $\bar{n}$ -jet function, while the shape function  $g_{17}(\omega, \omega_1; \mu)$  is convoluted with both jet functions, specifically with  $J^{(\bar{n})}(u, \omega_1; \mu)$  in the variable  $\omega_1$  and with  $J^{(n)}(\omega; \mu)$  in the variable  $\omega$ .

### 8.3 The Known Functions at NLO: $H$ and $J^{(n)}$

In this section, we review and recompute the functions that have been evaluated at NLO in the literature, namely the hard function and the  $n$ -jet function.

#### 8.3.1 The Hard Function at NLO

The hard matching functions required in our factorisation formula involve the matching of the operators  $Q_{7\gamma}$  and  $Q_1^q$  onto SCET. The hard function associated with  $Q_{7\gamma}$  was first computed in [198]. We recompute this function both to cross-check the results presented in that work and to explicitly provide the IR poles, which are essential for verifying the cancellation of singularities at the end of Part II. The Feynman diagrams contributing to the bare hard function are displayed in Figure 8.2.

In particular, we compute the  $\mathcal{O}(\alpha_s)$  corrections to the on-shell partonic matrix element  $b \rightarrow s\gamma$ , assuming the strange quark massless, while retaining the mass of the heavy bottom quark. The resulting expressions correspond to the hard matching coefficients in SCET.

The result for the bare hard function, which contains both UV and IR singularities, is given by

$$\langle Q_{7\gamma} \rangle_{\text{bare}}^{(1)} = -\frac{\alpha_s C_F}{4\pi} \left( \frac{1}{\varepsilon^2} + \frac{7}{2\varepsilon} + \frac{1}{\varepsilon} \log \frac{\mu^2}{m_b^2} + \frac{1}{2} \log^2 \frac{\mu^2}{m_b^2} + \frac{7}{2} \log \frac{\mu^2}{m_b^2} + 6 + \frac{\pi^2}{12} \right) \langle Q_{7\gamma} \rangle^{(0)}, \quad (8.8)$$

where the superscript (1) denotes the first order in  $\alpha_s$ . For later convenience, we explicitly provide the infrared (IR) singularities in  $\varepsilon$  after performing the UV renormalisation of (8.8). Upon subtracting the UV poles, we obtain:

$$H_7^{\text{poles}} = -\frac{\alpha_s C_F}{4\pi} \left( \frac{1}{\varepsilon^2} + \frac{5}{2\varepsilon} + \frac{1}{\varepsilon} \log \frac{\mu^2}{m_b^2} \right). \quad (8.9)$$

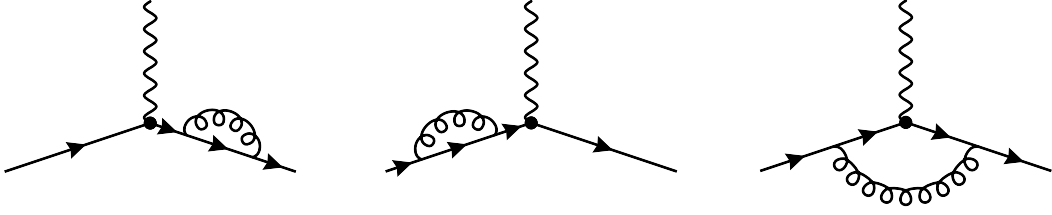


**Figure 8.2:** One-loop diagrams contributing to the the hard matching function for the operator  $Q_{7\gamma}$ . The outgoing strange quark is considered massless, while the  $b$ -quark has a mass  $m_b$ .

These singularities are expected to cancel against the UV poles of the jet functions. Finally, we quote the result for the finite terms from [198], including the IR free mixing contributions with  $Q_{8g}$  and  $Q_1^q$ , which is given by:

$$\begin{aligned}
H_\gamma(\mu) = & C_{7\gamma}(\mu) \left[ 1 + \frac{C_F \alpha_s(\mu)}{4\pi} \left( -2 \ln^2 \frac{m_b}{\mu} + 7 \ln \frac{m_b}{\mu} - 6 - \frac{\pi^2}{12} \right) \right] \\
& + C_{8g}(\mu) \frac{C_F \alpha_s(\mu)}{4\pi} \left( -\frac{8}{3} \ln \frac{m_b}{\mu} + \frac{11}{3} - \frac{2\pi^2}{9} + \frac{2\pi i}{3} \right) \\
& + C_1(\mu) \frac{C_F \alpha_s(\mu)}{4\pi} \left( \frac{104}{27} \ln \frac{m_b}{\mu} + g(z) + \varepsilon_{\text{CKM}} [g(0) - g(z)] \right), \quad (8.10)
\end{aligned}$$

where we defined the CKM dependent parameter as  $\varepsilon_{\text{CKM}} = -(V_{ub}V_{us}^*)/(V_{tb}V_{ts}^*)$ , the variable  $z = (m_q/m_b)^2$  and

$$\begin{aligned}
g(z) = & -\frac{833}{162} - \frac{20\pi i}{27} + \frac{8\pi^2}{9} z^{3/2} \\
& + \frac{2z}{9} \left[ 48 - 5\pi^2 - 36\zeta_3 + (30\pi - 2\pi^3)i + (36 - 9\pi^2 + 6\pi i) \ln z + (3 + 6\pi i) \ln^2 z + \ln^3 z \right] \\
& + \frac{2z^2}{9} \left[ 18 + 2\pi^2 - 2\pi^3 i + (12 - 6\pi^2) \ln z + 6\pi i \ln^2 z + \ln^3 z \right] \\
& + \frac{z^3}{27} \left[ -9 - 14\pi^2 + 112\pi i + (182 - 48\pi i) \ln z - 126 \ln^2 z \right] + \dots \quad (8.11)
\end{aligned}$$

are the first few terms in the expansion of the penguin function [199].

Similarly, we can compute the hard matching for the operator  $Q_1^q$ . The corresponding diagrams are given in Figure 8.3.

As in the previous case, we provide here the IR poles that will be needed in the following for the cancellation of singularities. The divergencies, after subtracting the UV poles, read:

$$H_1^{\text{poles}} = -\frac{\alpha_s}{4\pi} C_F \left[ \frac{1}{\varepsilon^2} + \frac{1}{\varepsilon} \left( \log \frac{\mu^2}{m_b^2} + \frac{5}{2} \right) \right] - \frac{\alpha_s}{4\pi} C_A \left[ \frac{1}{\varepsilon^2} + \frac{1}{\varepsilon} \left( \log \frac{\mu^2}{m_b^2 u(u-1)} + \frac{3}{2} \right) \right]. \quad (8.12)$$

Finally, the result for the renormalised finite pieces of the hard function, including the mixing with the operator  $Q_2^q$  are:

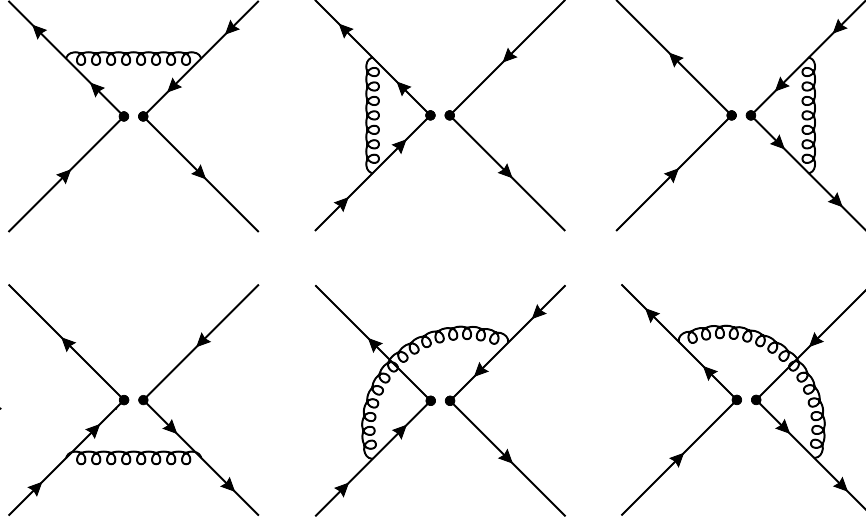


**Figure 8.3:** One-loop diagrams contributing to the the hard matching function for the operator  $Q_1^q$ . Self energy contributions are not shown. The outgoing strange quark is considered massless, while the incoming  $b$ -quark has a mass  $m_b$ .

$$\begin{aligned}
H_1^q(\mu) = & \left\{ -\frac{\alpha_s(\mu)}{4\pi} C_F \left[ \frac{1}{2} \log \frac{\mu^2}{m_b^2} \left( \log \frac{\mu^2}{m_b^2} + 17 \right) - 4\text{Li}_2(u) - \log^2(1-u) \right. \right. \\
& + \left. \left( \frac{2}{u} - 2\log(u) - 3 \right) \log(1-u) - \frac{\log(u)(3u + (1-u)\log(u) - 2)}{u-1} \right. \\
& \left. \left. + 4i\pi \tanh^{-1}(1-2u) + \frac{5\pi^2}{12} - 3i\pi + 29 \right] \right. \\
& - \frac{\alpha_s(\mu)}{4\pi} C_A \left[ - \left( \log \frac{\mu^2}{m_b^2} + \frac{1}{u} \right) \log(1-u) \right. \\
& + \frac{1}{12} \left( -6\log(-u)(2\log \frac{\mu^2}{m_b^2} - \log(-u)) + 6(\log \frac{\mu^2}{m_b^2} - 3) \log \frac{\mu^2}{m_b^2} - \pi^2 - 48 \right) \\
& \left. \left. + \text{Li}_2(u) + \log^2(1-u) \right] \right\} C_1(\mu) \\
& + \frac{\alpha_s(\mu)}{4\pi} \left\{ - \left( \log \frac{\mu^2}{m_b^2} + \frac{1}{u} \right) \log(1-u) \right. \\
& + \frac{1}{12} \left( -6\log(-u)(2\log \frac{\mu^2}{m_b^2} - \log(-u)) + 6(\log \frac{\mu^2}{m_b^2} - 3) \log \frac{\mu^2}{m_b^2} - \pi^2 - 48 \right) \\
& \left. \left. + \text{Li}_2(u) + \log^2(1-u) \right\} C_2(\mu).
\end{aligned} \tag{8.13}$$

We note that Equation (8.13) also contains contributions from evanescent terms [200], which are discussed in more detail in Appendix D.

### 8.3.2 The $n$ -Jet Function at NLO

The  $n$ -jet function  $J^{(n)}$  has been computed at NLO and NNLO in [201], and the result at N<sup>3</sup>LO was presented in [202]. In the following, we summarise the main aspects of the analysis in [201] and emphasise the relevant results. The jet function in SCET is defined as

$$\frac{\not{n}}{2} \bar{n} \cdot p \mathcal{J}(p^2, \mu) = \int d^4x e^{-ip \cdot x} \langle 0 | \text{T} \{ \chi_{hc}(0) \bar{\chi}_{hc}(x) \} | 0 \rangle, \quad (8.14)$$

where  $\chi_{hc}$  represents a gauge-invariant massless quark field after the decoupling transformation introduced in Chapter 2. After this transformation, the propagator can be rewritten in terms of the QCD quark fields as

$$\frac{\not{n}}{2} \bar{n} \cdot p \mathcal{J}(p^2, \mu) = \int d^4x e^{-ip \cdot x} \langle 0 | \text{T} \left\{ \frac{\not{n}\not{n}}{4} W^\dagger(0) \psi(0) \bar{\psi}(x) W(x) \frac{\not{n}\not{n}}{4} \right\} | 0 \rangle, \quad (8.15)$$

where the Wilson lines  $W(x)$  are defined in (2.31).

The jet function  $J^{(n)}$  appearing in the factorisation formula is then obtained from the contour integral

$$J^{(n)}\left(\ln \frac{Q^2}{\mu^2}, \mu\right) = \int_0^{Q^2} dp^2 j(p^2, \mu) = -\frac{1}{2\pi} \oint_{|p^2|=Q^2} dp^2 \mathcal{J}(p^2, \mu), \quad (8.16)$$

where  $j(p^2, \mu)$  denotes the discontinuity of the propagator:

$$j(p^2, \mu) = \frac{1}{\pi} \text{Im} \left[ i \mathcal{J}(p^2, \mu) \right] = \delta(p^2) + \mathcal{O}(\alpha_s). \quad (8.17)$$

The  $\mathcal{O}(\alpha_s)$  corrections are computed from the one-loop diagrams shown in Figure 8.4, giving [201]:

$$J^{(n)}\left(\ln \frac{Q^2}{\mu^2}, \mu\right) = 1 + \frac{\alpha_s}{4\pi} \left(\frac{Q^2}{\mu^2}\right)^{-\epsilon} C_F \left[ \frac{4}{\epsilon^2} + \frac{3}{\epsilon} + 7 - \pi^2 + \mathcal{O}(\epsilon) \right], \quad (8.18)$$

with  $\mu$  the renormalisation scale. The singularities in (8.18) arise from both UV and IR origins. The UV singularities are expected to cancel against the IR poles of the hard functions, while the IR singularities are expected to cancel against the UV poles of the soft function.

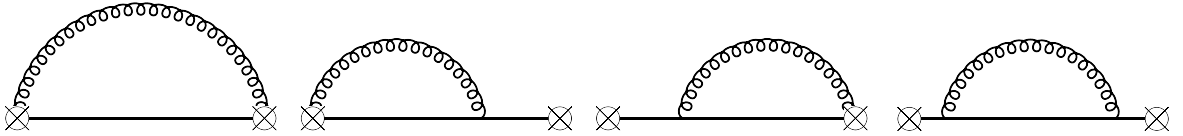


**Figure 8.4:** One-loop diagrams contributing to the  $n$ -jet function. Gluons emitted from the crossed circles originate from the Wilson lines.

# RGE of the Shape Function $g_{17}$

## Contents

<b>9.1</b>	<b>UV Singularities of <math>\mathcal{O}_{17}</math></b>	<b>80</b>
<b>9.2</b>	<b>Analytic Solution to the Renormalisation-Group Equation</b>	<b>91</b>
<b>9.3</b>	<b>The Exclusive Counterpart <math>\Phi_G</math></b>	<b>98</b>

The subleading shape-function  $g_{17}(\omega, \omega_1; \mu)$ , appearing in our factorisation formula (8.6) and introduced in [77], is the relevant soft function, that captures the non-perturbative low-energy QCD dynamics of this resolved contribution. The shape function is defined as the Fourier-transformed forward matrix element between two static  $\bar{B}$ -meson states,

$$g_{17}(\omega, \omega_1; \mu) = \frac{1}{2M_B} \int \frac{dr}{2\pi} e^{-i\omega_1 r} \int \frac{dt}{2\pi} e^{-i\omega t} \langle \bar{B}_v | \mathcal{O}_{17}(t, r) | \bar{B}_v \rangle, \quad (9.1)$$

of an operator in HQET,

$$\mathcal{O}_{17}(t, r) = (\bar{h}_v S_n)(tn) \not{n} (S_n^\dagger S_{\bar{n}})(0) i\gamma_\alpha^\perp \bar{n}_\beta (S_{\bar{n}}^\dagger g_s G_s^{\alpha\beta} S_{\bar{n}})(r\bar{n}) (S_{\bar{n}}^\dagger h_v)(0). \quad (9.2)$$

Where  $n^\mu$  and  $\bar{n}^\mu$  are the light-cone components of the SCET as defined in Section 2.5. Here, in particular,  $n^\mu$  is the light-like vector that points into the direction of the energetic  $s$ -quark (the collinear direction), and, the energetic photon has momentum in the opposite  $\bar{n}^\mu$  direction (the anti-collinear direction). Furthermore, the  $S_n$  are soft Wilson lines (defined in (2.32)) from the decoupling of the hard-collinear  $s$ -quark propagator, and correspondingly the  $S_{\bar{n}}$  arise from the decoupling of anti-hard-collinear propagators in the quark-loop, see Figure 9.1 and Figure 9.2. Importantly, the Wilson-lines in both light-cone directions combine to segments of finite length. In the following three sections we calculate the UV singularities of the operator  $\mathcal{O}_{17}(t, r)$  using standard HQET Feynman rules from time-ordered products in a  $B$ -meson forward matrix element. However, once  $\alpha_s$  corrections are considered, we have to implement the restricted cuts, because  $g_{17}$  is a soft function of a squared amplitude. We will address this task in the following. In particular, the calculation using time-ordered fields reveals an interesting and surprising feature: the anomalous dimension contains terms that are irrelevant in the factorisation theorem. We will also use this observation to simplify an amplitude-level soft function for the exclusive decay  $\bar{B}_{s,d} \rightarrow \gamma\gamma$ .

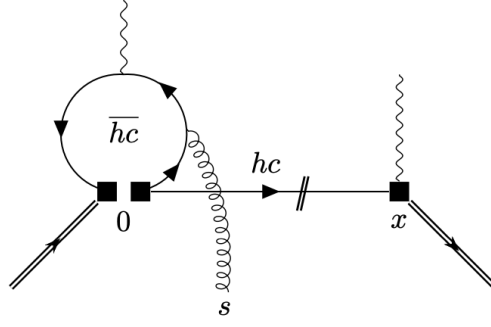


**Figure 9.1:** Leading-order contribution to the  $\bar{B} \rightarrow X_s \gamma$  decay rate from the  $Q_1^q - Q_{7\gamma}$  interference. Symmetric diagrams are not shown.

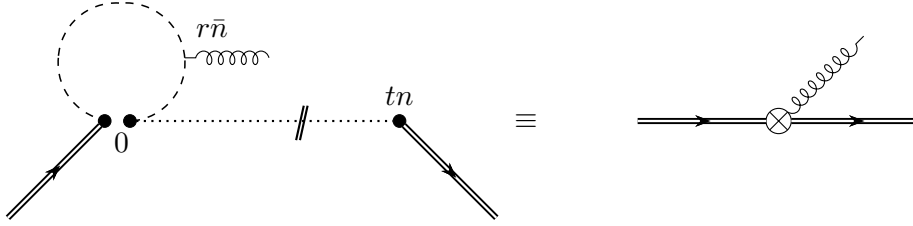


**Figure 9.2:** The left-hand side shows the non-local space-time structure of the soft fields and Wilson lines as they appear in the effective operator  $\mathcal{O}_{17}$  in (9.2). Here, dashed lines denote soft Wilson lines in the  $\bar{n}^\mu$  direction from the decoupling of anti-hard-collinear quark fields, and similarly the dotted line represents a soft Wilson line in the  $n^\mu$  direction. Throughout this paper, we simply represent the non-local field configuration through an effective vertex denoted by the  $\otimes$  symbol on the right-hand side of the equation. Note that at higher orders, more than one gluon can be emitted from the effective vertex due to the presence of the Wilson lines.

## 9.1 UV Singularities of $\mathcal{O}_{17}$

We compute UV singularities of the momentum-space operator

$$\tilde{\mathcal{O}}_{17}^{(\text{bare})}(\omega, \omega_1) = \int \frac{dr}{2\pi} e^{-i\omega_1 r} \int \frac{dt}{2\pi} e^{-i\omega t} \mathcal{O}_{17}^{(\text{bare})}(t, r) \quad (9.3)$$

at one-loop order, and extract its  $Z$ -factor in the  $\overline{\text{MS}}$ -scheme from

$$\tilde{\mathcal{O}}_{17}^{(\text{bare})}(\omega, \omega_1) = \int d\omega' \int d\omega'_1 Z_{17}^{-1}(\omega, \omega_1, \omega', \omega'_1; \mu) \tilde{\mathcal{O}}_{17}^{(\text{ren})}(\omega, \omega_1; \mu). \quad (9.4)$$

Despite the non-perturbative nature of the shape function  $g_{17}$ , the UV-singularities of the defining operator can safely be computed in perturbation theory using partonic external states. More specifically, in the following we compute one-loop corrections to the matrix element  $\langle \tilde{\mathcal{O}}_{17}^{(\text{bare})}(\omega, \omega') \rangle \equiv \langle h_v(k, s) g(k_g, \lambda) | \tilde{\mathcal{O}}_{17}^{(\text{bare})}(\omega, \omega') | h_v(k', s') \rangle$ . As a consequence of the space-time arguments of the fields in (9.2), it suffices at tree-level to set the residual heavy-quark momentum to  $k^\mu = \frac{1}{2}(nk)\bar{n}^\mu \equiv \frac{1}{2}k_+ \bar{n}^\mu$ , and similarly the gluon momentum to  $k_g^\mu = \frac{1}{2}(\bar{n}k_g)n^\mu \equiv \frac{1}{2}k_{g-} n^\mu$ . At  $\mathcal{O}(\alpha_s)$ , however, we keep the parton momenta slightly off-shell whenever necessary to regularize potential IR divergences in the loop integrals. Further, we perform the calculation with a “physical gluon”, i.e. its polarization vector  $\epsilon_\mu^a(k_g, \lambda)^*$  is chosen to be perpendicular to  $n^\mu$  and  $\bar{n}^\mu$ .

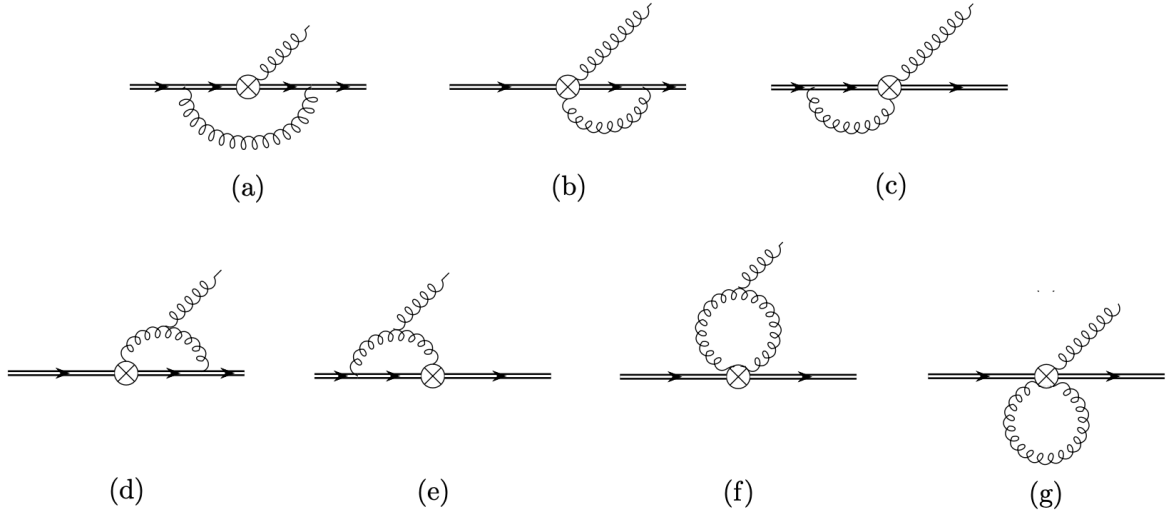


**Figure 9.3:** One-loop diagrams that contribute to the partonic matrix element  $\langle \tilde{\mathcal{O}}_{17} \rangle$ . The square denotes the insertion of the operator. Self-energy contributions are not shown.

At tree-level, the partonic matrix element follows from the Feynman rule

$$\begin{array}{c} l_1, \mu, a \\ \nearrow \\ k' \text{---} \otimes \text{---} k \end{array} = \delta(\omega - k_+) \delta(\omega_1 - \ell_{1-}) g_s t^a \not{n} (\bar{n}^\mu \not{\ell}_{1\perp} - \gamma_\perp^\mu \ell_{1-}), \quad (9.5)$$

and evaluates to

$$\langle \tilde{\mathcal{O}}_{17}^{(\text{bare})}(\omega, \omega_1) \rangle^{(0)} = -\omega_1 \delta(\omega_1 - k_{g-}) \delta(\omega - k_+) [\bar{h}_v \not{n} \not{A}_\perp h_v], \quad (9.6)$$

where now the objects in the square brackets represent on-shell spinors for the heavy quarks, and a polarization vector for the gluon,  $A_\mu = g_s \epsilon_\mu^a(k_g, \lambda) t^a$ . As depicted in Figure 9.2, the  $\otimes$  symbol used in (9.5) and in the following represents the non-local operator  $\mathcal{O}_{17}$ , where the non-localities along the different light-cones lead to the  $\delta$ -functions in the momentum-space Feynman rule. Due to the spin-symmetry of soft-gluon interactions with heavy-quark fields, the spinor product remains unchanged at the loop level. The prefactor  $(-\omega_1)$  arises from the derivatives in the gluon field-strength tensor.

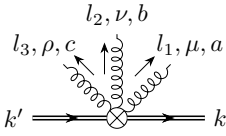
All one-loop graphs that contribute to the UV singularities in Feynman gauge are shown in Figure 9.3. We note that the external gluon does not couple directly to the heavy-quark line due to its perpendicular polarisation. Diagrams without the additional gluon in the final state vanish due to rotational symmetry, i.e.  $\mathcal{O}_{17}$  does not mix into operators with only two quark fields. Additionally, the gluon exchange between the two heavy-quark lines in diagram (a) is UV-finite. Evaluating the diagrams in Feynman gauge demands Feynman rules for up to three gluon emissions from the operator  $\mathcal{O}_{17}$ . They arise from the gluon field-strength tensor as well as from the various Wilson lines in (9.2). For the two-gluon emission Feynman rule one finds

$$\begin{array}{c} l_2, \nu, b \\ \nearrow \\ k' \text{---} \otimes \text{---} k \\ \nearrow \\ l_1, \mu, a \end{array} = -\delta(\omega - k_+) \delta(\omega_1 - \ell_{1-} - \ell_{2-}) g_s^2 i f^{abc} t^c \not{n} \gamma_\perp^\mu \bar{n}^\nu \quad (9.7)$$

$$\begin{aligned}
& + \delta(\omega_1 - \ell_{2-}) \frac{n^\mu}{\ell_{1+}} \left( \delta(\omega - k_+ - \ell_{1+}) - \delta(\omega - k_+) \right) g_s^2 t^a t^b \not{n} (\bar{n}^\nu \ell_{2\perp} - \gamma_\perp^\nu \ell_{2-}) \\
& - \delta(\omega - k_+) \frac{\bar{n}^\mu}{\ell_{1-}} \left( \delta(\omega_1 - \ell_{1-} - \ell_{2-}) - \delta(\omega_1 - \ell_{2-}) \right) g_s^2 i f^{abc} t^c \not{n} (\bar{n}^\nu \ell_{2\perp} - \gamma_\perp^\nu \ell_{2-}) \\
& + (l_1, \mu, a) \leftrightarrow (l_2, \nu, b).
\end{aligned}$$

Here the first line describes two gluons that are emitted from the field-strength tensor  $G_s^{\alpha\beta}$ , whereas the second and third line describe one gluon from  $G_s^{\alpha\beta}$  and one from the finite-length Wilson lines in the  $n^\mu$  and  $\bar{n}^\mu$  direction, respectively.

For diagram (g) we also need the three-gluon emission Feynman rule, which is a quite lengthy expression. However, most of the contractions vanish in Feynman gauge, or due to rotational symmetry, and here we only quote the relevant piece that gives a non-vanishing contraction in diagram (g):



$$\begin{aligned}
& \ni -\frac{n^\mu}{\ell_{1+}} \left( \delta(\omega - k_+ - \ell_{1+}) - \delta(\omega - k_+) \right) i g_s^3 f^{bcd} t^a t^d \not{n} \\
& \times \left[ \delta(\omega_1 - \ell_{2-} - \ell_{3-}) \gamma_\perp^\nu \bar{n}^\rho + \frac{\bar{n}^\nu}{\ell_{2-}} \left( \delta(\omega_1 - \ell_{2-} - \ell_{3-}) - \delta(\omega_1 - \ell_{3-}) \right) \left( \ell_{3\perp} \bar{n}^\rho - \gamma_\perp^\rho \ell_{3-} \right) \right] \\
& + \text{permutations}.
\end{aligned} \tag{9.8}$$

We regulate UV-divergences in dimensional regularization, i.e. by evaluating the loop integrals in  $d = 4 - 2\varepsilon$  space-time dimensions. After the integrations have been carried out, the respective expressions need to be expanded around  $\varepsilon = 0$  in the distribution sense. Besides the standard plus-distributions,

$$\int d\omega' [\dots]_+ f(\omega') \equiv \int d\omega' [\dots] (f(\omega') - f(\omega)), \tag{9.9}$$

one also needs the modified plus-distributions,

$$\int d\omega' [\dots]_{\oplus/\ominus} f(\omega') \equiv \int d\omega' [\dots] (f(\omega') - \theta(\pm\omega') f(\omega)), \tag{9.10}$$

which arise because the variables  $\omega$  and  $\omega_1$  can take both positive and negative values. It turns out to be convenient to define

$$\begin{aligned}
F^>(\omega, \omega') &= \left[ \frac{\omega \theta(\omega' - \omega)}{\omega' (\omega' - \omega)} \right]_+ + \left[ \frac{\theta(\omega - \omega')}{\omega - \omega'} \right]_\oplus, \\
F^<(\omega, \omega') &= \left[ \frac{\omega \theta(\omega - \omega')}{\omega' (\omega - \omega')} \right]_+ + \left[ \frac{\theta(\omega' - \omega)}{\omega' - \omega} \right]_\ominus, \\
G^>(\omega, \omega') &= (\omega + \omega') \left[ \frac{\theta(\omega' - \omega)}{\omega' (\omega' - \omega)} \right]_+ - i\pi \delta(\omega - \omega'), \\
G^<(\omega, \omega') &= (\omega + \omega') \left[ \frac{\theta(\omega - \omega')}{\omega' (\omega - \omega')} \right]_+ + i\pi \delta(\omega - \omega'),
\end{aligned} \tag{9.11}$$

as well as the linear combinations

$$H_\pm(\omega, \omega') = \theta(\pm\omega) F^{>(<)}(\omega, \omega') + \theta(\mp\omega) G^{<(>)}(\omega, \omega'), \tag{9.12}$$

which have been introduced in the study of QED corrections to the  $B$ -meson light-cone distribution amplitude in [203].

### 9.1.1 Abelian Contributions

In the Abelian limit, all soft Wilson lines in the  $\bar{n}$ -direction in (9.2) cancel. From the spin-symmetry of HQET, it follows that the UV singularities of  $\mathcal{O}_{17}$  proportional to the color factor  $C_F$  coincide with those of the leading shape function, computed e.g. in [204]. The contribution to the  $Z$ -factor, which arises from diagrams (b) and (c) in Figure 9.3 (recall that diagram (a) is UV-finite in Feynman gauge), reads

$$Z(\omega, \omega_1, \omega', \omega'_1; \mu) = \delta(\omega_1 - \omega'_1) \delta(\omega - \omega') \quad (9.13)$$

$$+ \frac{\alpha_s C_F}{4\pi} \delta(\omega_1 - \omega'_1) \left\{ \left( \frac{2}{\varepsilon^2} + \frac{4}{\varepsilon} \ln \frac{\mu}{\bar{\Lambda} - \omega} - \frac{2}{\varepsilon} \right) \delta(\omega - \omega') - \frac{4}{\varepsilon} \left[ \frac{\theta(\omega' - \omega)}{\omega' - \omega} \right]_+^{(\bar{\Lambda})} \right\} + \mathcal{O}(\alpha_s^2),$$

where  $\bar{\Lambda} = M_B - m_b$  is the difference of the  $B$ -meson mass and the  $b$ -quark pole mass. The superscript  $(\bar{\Lambda})$  on the plus-distribution indicates that the integral in  $\omega'$  is restricted to the interval  $(-\infty, \bar{\Lambda}]$ ,

$$\int_{-\infty}^{\bar{\Lambda}} d\omega' [\dots]_+ f(\omega') \equiv \int_{-\infty}^{\bar{\Lambda}} d\omega' [\dots] (f(\omega') - f(\omega)), \quad (9.14)$$

which is also the reason for the logarithmic dependence on  $\bar{\Lambda}$ .

In the following, we prefer to use an alternative representation that is independent of the IR parameter  $\bar{\Lambda}$ , but is equivalent to (9.13) when acting on a function supported on aforementioned interval. This expression is derived by computing diagrams (b) and (c) by means of the residue theorem. Since the computation of all diagrams follow a similar pattern we now perform this computation step by step to present the important features. We start by choosing  $\ell$  to be the loop momentum that flows out from the square vertex in diagram (b). The integral contributing to the  $Z$ -factor reads:

$$ig_s^2 C_F \tilde{\mu}^{2\varepsilon} \delta(\omega_1 - \omega'_1) \int \frac{d^D \ell}{(2\pi)^D} \frac{\delta(\omega - \omega' + \ell_+) - \delta(\omega - \omega')}{[v \cdot (k - \ell) + i0] (\ell^2 + i0) (\ell_+ + \Delta)}, \quad (9.15)$$

where  $\tilde{\mu}$  is the dimensional regularisation scale defined as in the  $\overline{\text{MS}}$  scheme by

$$\tilde{\mu}^{2\varepsilon} = (4\pi)^{-\varepsilon} e^{\gamma_E \varepsilon} \mu^{2\varepsilon},$$

with  $\gamma_E$  the Euler–Mascheroni constant. In addition, we introduced  $\Delta$ , with  $\text{Im } \Delta > 0$ , which is a shift in the Wilson-line propagator arising from off-shell lines in QCD diagrams, and regularizes infrared divergences from  $\ell_+ \rightarrow 0$  in the two individual terms.

We note that, because the Wilson lines are of finite length, the UV poles in  $\varepsilon$  in (9.20) are independent of  $\Delta$  in the limit  $\Delta \rightarrow 0$  once consistently expanded in the distribution sense.<sup>1</sup>

In order to compute the integral, we express the integration momentum in light-cone coordinates and rewrite the propagators in order to make manifest the poles in the  $\ell_-$  component:

<sup>1</sup>We note that in some cases the Wilson lines do not combine to finite segments, but instead extend to infinity. The UV poles of the operators then depend logarithmically on such a regulator, hence spoiling its renormalisation. In addition, the regulator-dependent contributions are also gauge-dependent [205]. An additional rearrangement needs to be performed to remove these contributions from “charges at infinity”, see e.g. [203, 205–208], thereby restoring gauge invariance and renormalisability.

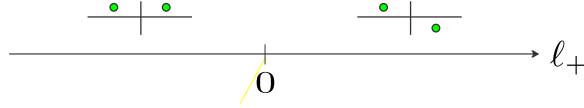


**Figure 9.4:** Location of poles related to the integral in (9.15). Green dots denote poles located in the upper or lower complex half-plane. The order of the denominators matches that in Equation (9.15).

$$-ig_s^2 C_F \tilde{\mu}^{2\varepsilon} \delta(\omega_1 - \omega'_1) \int \frac{dl_+ dl_- d\ell_\perp^{D-2}}{(2\pi)^D} \frac{\delta(\omega - \omega' + \ell_+) - \delta(\omega - \omega')}{\ell_+ [\ell_+ + \ell_- - \delta_k - i0] \left( \ell_- + \frac{\ell_\perp^2 + i0}{\ell_+} \right) (\ell_+ + \Delta)}, \quad (9.16)$$

where we defined  $\delta_k = -2v \cdot k$ , which is an off-shell IR regulator depending on the outgoing heavy-quark momentum  $k$ . We show in Figure 9.4 the location of the poles in dependence on the variable  $\ell_+$ . In particular, we see that the integral vanishes closing the contour in the lower complex plane for  $\ell_+ < 0$ . While picking up the residues in the  $\ell_-$ -component closing the contour in the lower plane for  $\ell_+ > 0$  we obtain

$$-2\pi^2 g_s^2 C_F \tilde{\mu}^{2\varepsilon} \delta(\omega_1 - \omega'_1) \int_0^\infty dl_+ \int \frac{d\ell_\perp^{D-2}}{(2\pi)^D} \frac{\delta(\omega - \omega' + \ell_+) - \delta(\omega - \omega')}{[\ell_+(\ell_+ - \delta_k) - \ell_\perp^2] (\ell_+ + \Delta)}. \quad (9.17)$$

To evaluate the integral in the perpendicular component, we perform the change of variable  $x = -k_\perp^2 > 0$ , leading to:

$$\int \frac{dk_\perp^{D-2}}{(2\pi)^{4-2\varepsilon}} \rightarrow \int_0^\infty dx \frac{x^{-\varepsilon}}{\Gamma(1-\varepsilon) 4^{2-\varepsilon} \pi^{3-\varepsilon}}. \quad (9.18)$$

Through this, we get:

$$-\frac{2g_s^2 C_F \tilde{\mu}^{2\varepsilon}}{\Gamma(1-\varepsilon)(4\pi)^{2-\varepsilon}} \delta(\omega_1 - \omega'_1) \int_0^\infty dl_+ \int_0^\infty dx \frac{x^{-\varepsilon}}{x + \ell_+(\ell_+ - \delta_k)} \frac{\delta(\omega - \omega' + \ell_+) - \delta(\omega - \omega')}{(\ell_+ + \Delta)}. \quad (9.19)$$

Finally, performing the integral over  $x$  and observing that we can drop the IR regulator  $\delta_k$ , since the limit  $\delta_k \rightarrow 0$  is IR finite, we obtain

$$\begin{aligned} & -\frac{\alpha_s C_F e^{\varepsilon\gamma_E} \mu^{2\varepsilon}}{2\pi} \delta(\omega_1 - \omega'_1) \Gamma(\varepsilon) \int_0^\infty dl_+ \ell_+^{-2\varepsilon} \frac{1}{\ell_+ + \Delta} \left( \delta(\omega - \omega' + \ell_+) - \delta(\omega - \omega') \right) \\ & = -\frac{\alpha_s C_F e^{\varepsilon\gamma_E}}{2\pi} \delta(\omega_1 - \omega'_1) \Gamma(\varepsilon) \left\{ \frac{\theta(\omega' - \omega)}{\omega' - \omega + \Delta} \left( \frac{\mu}{\omega' - \omega} \right)^{2\varepsilon} \right. \\ & \quad \left. - \delta(\omega - \omega') \Gamma(2\varepsilon) \Gamma(1 - 2\varepsilon) \left( \frac{\mu}{\Delta} \right)^{2\varepsilon} \right\}. \end{aligned} \quad (9.20)$$

The expansion of the second line of (9.20) in terms of (modified) plus-distributions has been discussed in detail in [203]. We report here all the required steps which are common to all the necessary expansions of this chapter.

We start assuming  $\omega > 0$ , and we rewrite the non-local term employing the standard plus-distribution defined as

$$\begin{aligned}
& \theta(\omega) \int_{-\infty}^{\infty} d\omega' \frac{\theta(\omega' - \omega)}{\omega' - \omega + \Delta} \left( \frac{\mu}{\omega' - \omega} \right)^{2\varepsilon} \phi(\omega') \\
&= \theta(\omega) \int_{-\infty}^{\infty} d\omega' \omega' \left[ \frac{\theta(\omega' - \omega)}{\omega'(\omega' - \omega + \Delta)} \right]_+ \phi(\omega') + \theta(\omega)\phi(\omega) \int_{\omega}^{\infty} d\omega' \frac{\omega}{\omega'(\omega' - \omega + \Delta)} + \mathcal{O}(\varepsilon) \\
&= \theta(\omega) \int_{-\infty}^{\infty} d\omega' \omega' \left[ \frac{\theta(\omega' - \omega)}{\omega'(\omega' - \omega)} \right]_+ \phi(\omega') - \theta(\omega)\phi(\omega) \ln \frac{\Delta}{\omega} + \mathcal{O}(\varepsilon, \Delta).
\end{aligned} \tag{9.22}$$

In the expansion above, we assumed that the test function  $\phi(\omega)$  behaves like  $1/\omega'$  up to logarithmic corrections. We therefore do not get any UV divergence in the  $\omega'$  integration. In the last line of (9.22), we also expanded the regulator  $\Delta$  in the plus-distribution, since it is IR finite for  $\Delta \rightarrow 0$ .

While for  $\omega > 0$ , the standard plus-distribution was sufficient, for  $\omega < 0$ , the non-local term  $\theta(\omega' - \omega)/(\omega' - \omega)$  needs to be regulated with a distribution for  $\omega' < 0$ , but not for  $\omega' > 0$ . We therefore employ the modified plus-distribution given in (9.10).

In particular, the  $\ominus$ -distribution is needed in order to regulate the  $1/(\omega' - \omega)$  pole for  $\omega < 0$  and  $\omega' < 0$ . Using the  $\ominus$ -distribution, we get

$$\begin{aligned}
& \theta(-\omega) \int_{-\infty}^{\infty} d\omega' \frac{\theta(\omega' - \omega)}{\omega' - \omega + \Delta} \left( \frac{\mu}{\omega' - \omega} \right)^{2\varepsilon} \phi(\omega') \\
&= \theta(-\omega) \int_{-\infty}^{\infty} d\omega' \left[ \frac{\theta(\omega' - \omega)}{\omega' - \omega + \Delta} \right]_{\ominus} \phi(\omega') + \theta(-\omega)\phi(\omega) \int_{\omega}^0 d\omega' \frac{1}{\omega' - \omega + \Delta} + \mathcal{O}(\varepsilon) \\
&= \theta(-\omega) \int_{-\infty}^{\infty} d\omega' \left[ \frac{\theta(\omega' - \omega)}{\omega' - \omega} \right]_{\ominus} \phi(\omega') - \theta(-\omega)\phi(\omega) \ln \frac{\Delta}{-\omega} + \mathcal{O}(\varepsilon, \Delta).
\end{aligned} \tag{9.23}$$

Finally, adding all the contributions, the off-shell regulator  $\Delta$  cancels and the result for the  $Z$ -factor related to the abelian contribution of diagram (b) reads

$$\begin{aligned}
& \frac{\alpha_s C_F}{2\pi} \delta(\omega_1 - \omega'_1) \left\{ \delta(\omega - \omega') \left( \frac{1}{2\varepsilon^2} + \frac{1}{2\varepsilon} \ln \frac{\mu^2}{\omega^2} \right) \right. \\
& \quad \left. - \frac{1}{\varepsilon} \theta(\omega) \left[ \frac{\theta(\omega' - \omega)}{\omega'(\omega' - \omega)} \right]_+ \omega' - \frac{1}{\varepsilon} \theta(-\omega) \left[ \frac{\theta(\omega' - \omega)}{\omega' - \omega} \right]_{\ominus} \right\}.
\end{aligned} \tag{9.24}$$

Diagram (c) yields the same result, and, after taking into account the divergent one-loop contribution from the heavy-quark wave-function renormalisation constant,<sup>2</sup>

$$Z_h^{(1)} - 1 = \frac{\alpha_s C_F}{2\pi\varepsilon}, \tag{9.25}$$

we obtain for the Abelian part of the  $Z$ -factor

$$\begin{aligned}
Z_{17}^{(1)}(\omega, \omega_1, \omega', \omega'_1; \mu) \Big|_{C_F} &= \frac{\alpha_s C_F}{4\pi} \delta(\omega_1 - \omega'_1) \left\{ \left( \frac{2}{\varepsilon^2} + \frac{2}{\varepsilon} \ln \frac{\mu^2}{\omega^2} - \frac{2}{\varepsilon} \right) \delta(\omega - \omega') \right. \\
& \quad \left. - \frac{4}{\varepsilon} \theta(\omega) \left[ \frac{\theta(\omega' - \omega)}{\omega'(\omega' - \omega)} \right]_+ \omega' - \frac{4}{\varepsilon} \theta(-\omega) \left[ \frac{\theta(\omega' - \omega)}{\omega' - \omega} \right]_{\ominus} \right\}.
\end{aligned} \tag{9.26}$$

<sup>2</sup>Note that this constant contributes to  $Z_{17}^{(1)}$  with a negative sign due to  $Z_h^{1/2} h_v^{\text{ren}} = h_v^{\text{bare}}$ .

Here the superscript (1) denotes that we work at  $\mathcal{O}(\alpha_s)$ . It is straightforward to see that this form is equivalent to (9.13) by employing the following identities

$$\begin{aligned}\theta(\omega) \left[ \frac{\theta(\omega' - \omega)}{\omega'(\omega' - \omega)} \right]_+ \omega' &= \theta(\omega) \left[ \frac{\theta(\omega' - \omega)}{\omega' - \omega} \right]_+^{(\bar{\Lambda})} + \theta(\omega) \delta(\omega - \omega') \ln \frac{\bar{\Lambda} - \omega}{\omega}, \\ \theta(-\omega) \left[ \frac{\theta(\omega' - \omega)}{\omega' - \omega} \right]_{\ominus} &= \theta(-\omega) \left[ \frac{\theta(\omega' - \omega)}{\omega' - \omega} \right]_+^{(\bar{\Lambda})} + \theta(-\omega) \delta(\omega - \omega') \ln \frac{\bar{\Lambda} - \omega}{-\omega},\end{aligned}\quad (9.27)$$

which hold if the test functions have support on the interval  $\{\omega, \omega'\} \in (-\infty, \bar{\Lambda}]$ . For the two expressions in (9.13) and (9.26) to be equivalent, it is crucial that only  $\theta$ -functions that enforce  $\omega' > \omega$  appear inside the plus distributions. This guarantees that a function with support  $\bar{\Lambda} > \omega'$  is mapped onto a function with support  $\bar{\Lambda} > \omega$ .

### 9.1.2 Non-Abelian Contributions

Next, we examine the non-Abelian contributions, which arise from all diagrams shown in Figure 9.3 except (a). For transparency, we separately discuss the contributions that arise from gluons emitted from the field-strength tensor, from the Wilson lines in the  $n^\mu$  direction or the  $\bar{n}^\mu$  direction. The contraction of Wilson lines in the two light-cone directions in diagram (g) is discussed on its own.

Setting all Wilson lines to unity leaves diagrams (d) and (e), as well as (b), (c), and (f), but using only the first line of the Feynman rule in (9.7) for the latter three. In this case, the UV poles of diagrams (d) and (b) cancel. Similarly, the contribution from diagram (c) is canceled by a piece from diagram (e), but a UV-divergent contribution from (e) remains. This piece can simply be expanded in the dimensional regulator  $\varepsilon$  without the need of introducing plus-type distributions. The contribution to the  $Z$ -factor reads

$$\frac{\alpha_s C_A}{8\pi\varepsilon} \delta(\omega - \omega') \frac{\omega_1}{(\omega'_1)^2} [\theta(\omega_1) \theta(\omega'_1 - \omega_1) - \theta(-\omega_1) \theta(\omega_1 - \omega'_1)]. \quad (9.28)$$

Lastly, the contribution from diagram (f) is purely local. Taking into account the symmetry factor 2, one finds

$$\frac{3\alpha_s C_A}{8\pi\varepsilon} \delta(\omega - \omega') \delta(\omega_1 - \omega'_1). \quad (9.29)$$

Next, we investigate diagrams (b), (c) and (f) using the second line of (9.7), as well as diagram (g) using only the first term in the second line of (9.8). These Feynman rules represent one gluon emitted from the finite-distance Wilson line in the  $n^\mu$  direction, and one or two gluons emitted from the field-strength tensor. The respective contribution from diagram (b) is proportional to  $C_F$  and already contained in (9.13), whereas the one from (c) is proportional to  $(C_F - C_A/2)$ , and therefore comes with the same integral (9.20). Diagram (g), which also needs to be divided by its symmetry factor 2, is canceled by a piece from diagram (f), and the remaining terms from (f) result again in the expression (9.28).

The Feynman rule that represents one gluon emitted from the Wilson line in the  $\bar{n}^\mu$  direction and one from the field-strength tensor is given by the third line of (9.7). Diagram (c) then contributes the following term to the  $Z$ -factor,

$$-\frac{\alpha_s C_A e^{\varepsilon\gamma_E} \mu^{2\varepsilon}}{4\pi} \delta(\omega - \omega') \Gamma(\varepsilon) \int_0^\infty d\ell_- \ell_-^{-2\varepsilon} \frac{1}{\ell_- - \bar{\Delta}} \left( \delta(\omega_1 - \omega'_1 + \ell_-) - \delta(\omega_1 - \omega'_1) \right)$$

$$= -\frac{\alpha_s C_A}{4\pi} \delta(\omega - \omega') \frac{1}{\varepsilon} \left\{ \frac{\theta(\omega'_1 - \omega_1)}{\omega'_1 - \omega_1 - \bar{\Delta}} - \delta(\omega_1 - \omega'_1) \left( \frac{1}{2\varepsilon} - \ln \frac{-\bar{\Delta}}{\mu} \right) \right\} + \mathcal{O}(\varepsilon^0). \quad (9.30)$$

Similar to (9.20), the quantity  $\bar{\Delta}$ , with  $\text{Im } \bar{\Delta} > 0$ , is an off-shell regulator for IR divergences, that can be set to zero after expanding in terms of plus-type distributions, which is analogous to (9.24). The UV-divergent piece of diagram (f) yields the integral

$$\begin{aligned} & -\frac{\alpha_s C_A}{4\pi} \delta(\omega - \omega') \frac{1}{\varepsilon} \int_0^{\omega'_1} \frac{d\ell_-}{\ell_- - \bar{\Delta}} \left( \delta(\omega_1 - \omega'_1 + \ell_-) - \delta(\omega_1 - \omega'_1) \right) \frac{(\omega'_1 - \ell_-)(2\omega'_1 - \ell_-)}{(\omega'_1)^2} \\ &= -\frac{\alpha_s C_A}{4\pi} \delta(\omega - \omega') \frac{1}{\varepsilon} \left\{ -\frac{\omega_1}{(\omega'_1)^2} [\theta(\omega_1)\theta(\omega'_1 - \omega_1) - \theta(-\omega_1)\theta(\omega_1 - \omega'_1)] \right. \\ & \quad \left. + \frac{2\omega_1[\theta(\omega_1)\theta(\omega'_1 - \omega_1) - \theta(-\omega_1)\theta(\omega_1 - \omega'_1)]}{\omega'_1(\omega'_1 - \omega_1 - \bar{\Delta})} + \delta(\omega_1 - \omega'_1) \left( \frac{5}{2} + 2 \ln \frac{\bar{\Delta}}{\bar{\Delta} - \omega_1} \right) \right\}. \end{aligned} \quad (9.31)$$

Compared to (9.24), the additional constraint  $\theta(\pm\omega_1)$  in the first term of the last line allows to expand this piece in standard plus-distributions, after which we can set  $\bar{\Delta} \rightarrow 0$ . Diagram (f) then results in

$$\begin{aligned} & -\frac{\alpha_s C_A}{4\pi} \delta(\omega - \omega') \frac{1}{\varepsilon} \left\{ -\frac{\omega_1}{(\omega'_1)^2} [\theta(\omega_1)\theta(\omega'_1 - \omega_1) - \theta(-\omega_1)\theta(\omega_1 - \omega'_1)] \right. \\ & \quad \left. + 2\theta(\omega_1)\omega_1 \left[ \frac{\theta(\omega'_1 - \omega_1)}{\omega'_1(\omega'_1 - \omega_1)} \right]_+ + 2\theta(-\omega_1)\omega_1 \left[ \frac{\theta(\omega_1 - \omega'_1)}{\omega'_1(\omega_1 - \omega'_1)} \right]_+ + \frac{5}{2} \delta(\omega_1 - \omega'_1) \right\}. \end{aligned} \quad (9.32)$$

The contribution from diagram (b) turns out to be more subtle. Carrying out the integration over the  $\ell_+$ -component is trivial due to the appearing  $\delta$ -function. Performing additionally the integration over the perpendicular components yields for the UV-divergent piece

$$\begin{aligned} & -\frac{\alpha_s C_A}{4\pi\varepsilon} \frac{1}{2\pi i} \int d\ell_- \frac{1}{\omega - \omega' + \ell_- + \delta} \frac{1}{\ell_- - \bar{\Delta}} \left( \delta(\omega_1 - \omega'_1 + \ell_-) - \delta(\omega_1 - \omega'_1) \right) \\ &= -\frac{\alpha_s C_A}{4\pi\varepsilon} \left( \frac{1}{2\pi i} \frac{1}{\omega - \omega' + \omega'_1 - \omega_1 + i0} \frac{1}{\omega'_1 - \omega_1 - i0} - \delta(\omega_1 - \omega'_1) \frac{1}{\omega - \omega' + i0} \right), \end{aligned} \quad (9.33)$$

with  $\delta = 2vk + i0$  an off-shellness for the residual momentum of the external heavy-quark line. However, note the important fact that no  $\theta$ -functions appear in this expression, and the only relevant piece of the IR regulators is their  $i0$  prescriptions that dictate how the pole is shifted to the complex plane. The equal sign in (9.33) has to be understood in that sense. In our convention, all IR regulators have a  $+i0$  prescription, which matches the Feynman propagators of the corresponding QCD diagrams. The second term in (9.33) can be further expressed in terms of the  $H_{\pm}$  distributions, defined in (9.11) and (9.12), via

$$\frac{1}{\omega - \omega' + i0} = H_+(\omega, \omega') - H_-(\omega, \omega') - 2\pi i \delta(\omega - \omega'). \quad (9.34)$$

For reasons that become clear later, we do not further manipulate the first term in (9.33) at this point.

The last missing contribution arises from diagram (g) using the second term in the second line of the Feynman rule in (9.8). This contribution describes the contraction of one gluon field from the Wilson line in the  $n^{\mu}$  direction with a gluon field from the  $\bar{n}^{\mu}$  Wilson line. The

gluon-field from the field-strength tensor is contracted with the external state. Note that, because the field-strength tensor is contracted with an  $\bar{n}_\beta$  in (9.1), there is no non-vanishing contraction of two gluons from  $G_s^{\alpha\beta}$  and one gluon from the  $\bar{n}^\mu$  Wilson line. After performing the integral over the perpendicular components one finds

$$\begin{aligned}
& \frac{\alpha_s C_A}{4\pi} \Gamma(\varepsilon) e^{\varepsilon\gamma_E} \mu^{2\varepsilon} \frac{1}{2\pi i} \int dl_+ \int dl_- (-l_+ l_- - i0)^{-\varepsilon} \\
& \quad \times \frac{1}{\ell_+ + \Delta} \left( \delta(\omega - \omega' - \ell_+) - \delta(\omega - \omega') \right) \frac{1}{\ell_- - \bar{\Delta}} \left( \delta(\omega_1 - \omega'_1 + \ell_-) - \delta(\omega_1 - \omega'_1) \right) \\
= & -\frac{\alpha_s C_A}{4\pi} \frac{1}{\varepsilon} \left\{ \frac{1}{2\pi i} \frac{1}{\omega' - \omega - i0} \frac{1}{\omega'_1 - \omega_1 - i0} - \left( \frac{1}{\varepsilon} + i\pi \right) \delta(\omega - \omega') \delta(\omega_1 - \omega'_1) \right. \\
& \quad + \delta(\omega_1 - \omega'_1) \left( \frac{\theta(\omega - \omega')}{\omega - \omega' + \Delta} + \delta(\omega - \omega') \ln \frac{\Delta}{\mu} \right) \\
& \quad \left. + \delta(\omega - \omega') \left( \frac{\theta(\omega_1 - \omega'_1)}{\omega_1 - \omega'_1 + \bar{\Delta}} + \delta(\omega_1 - \omega'_1) \ln \frac{\bar{\Delta}}{\mu} \right) \right\} + \mathcal{O}(\varepsilon^0). \tag{9.35}
\end{aligned}$$

The expression of the last two lines in terms of plus-type distributions reads

$$\begin{aligned}
& \frac{\theta(\omega - \omega')}{\omega - \omega' + \Delta} + \delta(\omega - \omega') \ln \frac{\Delta}{\mu} \\
= & \theta(\omega) \left[ \frac{\theta(\omega - \omega')}{\omega - \omega'} \right]_{\oplus} + \theta(-\omega) \left[ \frac{\theta(\omega - \omega')}{\omega'(\omega - \omega')} \right]_{+} \omega' - \frac{1}{2} \ln \frac{\mu^2}{\omega^2} \delta(\omega - \omega'), \tag{9.36}
\end{aligned}$$

whereas for the first term in (9.35) one could use the identity (9.34). However, we again prefer to not manipulate this term.

Summing up all pieces, and including the  $\mathcal{O}(\alpha_s)$  coupling and gluon-field renormalisation factors

$$Z_{g_s} \sqrt{Z_3} - 1 = -\frac{\alpha_s C_A}{4\pi\varepsilon} + \mathcal{O}(\alpha_s^2), \tag{9.37}$$

one finally obtains for the non-Abelian contributions to the  $Z$ -factor

$$\begin{aligned}
Z_{17}^{(1)}(\omega, \omega_1, \omega', \omega'_1; \mu) \Big|_{C_A} = & \frac{\alpha_s C_A}{4\pi} \delta(\omega - \omega') \left\{ \left( \frac{1}{\varepsilon^2} + \frac{1}{\varepsilon} \ln \frac{\mu^2}{\omega_1^2} \right) \delta(\omega_1 - \omega'_1) \right. \\
& \left. + \frac{2}{\varepsilon} \frac{\omega_1}{(\omega'_1)^2} [\theta(\omega_1) \theta(\omega'_1 - \omega_1) - \theta(-\omega_1) \theta(\omega_1 - \omega'_1)] - \frac{1}{\varepsilon} \text{Re } \mathbf{H}(\omega_1, \omega'_1) \right\} \\
& + \Delta Z_{17}(\omega, \omega_1, \omega', \omega'_1; \mu), \tag{9.38}
\end{aligned}$$

where we have defined  $\mathbf{H}(\omega_1, \omega'_1) = H_+(\omega_1, \omega'_1) + H_-(\omega_1, \omega'_1)$ . The quantity  $\Delta Z_{17}$  contains the terms which have non-trivial structures in both sets of arguments  $(\omega, \omega')$  and  $(\omega_1, \omega'_1)$  simultaneously,

$$\Delta Z_{17}(\omega, \omega_1, \omega', \omega'_1; \mu) = \frac{\alpha_s C_A}{4\pi\varepsilon} \frac{1}{2\pi i} \frac{1}{\omega'_1 - \omega_1 - i0} \left( \frac{1}{\omega' - \omega + \omega_1 - \omega'_1 - i0} - \frac{1}{\omega' - \omega - i0} \right). \tag{9.39}$$

Interestingly, besides these pieces the dependence on  $\omega$  in (9.38) is purely local, as the distributions exactly cancel in sum of all diagrams. The complete one-loop  $Z$ -factor of the operator  $\tilde{\mathcal{O}}_{17}$  is then given by

$$Z_{17} = \delta(\omega - \omega') \delta(\omega_1 - \omega'_1) + Z_{17}^{(1)} \Big|_{C_F} + Z_{17}^{(1)} \Big|_{C_A} + \mathcal{O}(\alpha_s^2), \tag{9.40}$$

where we have suppressed the arguments for brevity.

### 9.1.3 Cut Diagrams and the Relevance of $\Delta Z_{17}$

The appearance of structures like in (9.39) in the UV-poles of the soft HQET operator  $\mathcal{O}_{17}$  seems problematic. In the effective theory, the two collinear directions are decoupled, and each hard-collinear sector is described by a jet function that only depends either on  $\omega$  (the soft momentum component associated with the  $n^\mu$  direction) or  $\omega_1$  (the soft momentum component associated with the  $\bar{n}^\mu$  direction).

At  $\mathcal{O}(\alpha_s)$ , all divergences in  $\varepsilon$  must cancel in the sum of the hard, hard-collinear, anti-hard-collinear and soft loops, where the hard functions do not depend on the soft momenta. This would indicate that the  $Z$ -factor of the operator  $\mathcal{O}_{17}$  should be of the form

$$Z^{(1)}(\omega, \omega_1, \omega', \omega'_1; \mu) = \delta(\omega_1 - \omega'_1) Z_n^{(1)}(\omega, \omega'; \mu) + \delta(\omega - \omega') Z_{\bar{n}}^{(1)}(\omega_1, \omega'_1; \mu), \quad (9.41)$$

i.e. the dependence on the two light-cone momentum projections decouples. The terms in (9.39) obviously have a different form, and might suggest the presence of other long-range interactions between the two collinear sectors which superficially would violate soft-collinear factorisation. However, in the following we will argue that both terms in  $\Delta Z_{17}$  are irrelevant for the decay rate, thus, our results agree with factorisation in terms of hard, (anti)hard-collinear and soft modes. First, we show that  $\Delta Z_{17}$  vanishes in the convolution with the jet functions on the level of time-ordered products. Second, we derive that  $\Delta Z_{17}$  vanishes when the cut is taken into account using cutting rules.

Let us recall that the UV-singularities in (9.26) and (9.38) were calculated using standard Feynman rules from time-ordered products in a  $B$ -meson forward matrix element. In other words, we have not yet applied the necessary cuts that contribute to the  $\bar{B} \rightarrow X_s \gamma$  decay rate. In that case, we will now argue that the problematic terms (9.39) vanish when convoluted with the jet functions due to the location of singularities in the complex plane. A crucial property for this argument is that the terms in  $\Delta Z_{17}$  do not contain any integration constraints from  $\theta$ -functions, i.e. in any matrix element of  $\tilde{\mathcal{O}}_{17}$  all light-cone momenta are unrestricted, and hence integrated over the entire real axis in factorisation theorems.<sup>3</sup> Due to the directed energy flow, the relevant (time-ordered) jet functions for the forward matrix element have singularities or branch cuts only in the lower half-plane, i.e. they depend on  $\omega + i0$  and  $\omega_1 + i0$ , respectively. At leading order, for example, the jet function in the  $n^\mu$  direction is simply given by the inverse hard-collinear propagator  $\sim (\omega + i0)^{-1}$ , and the same is true for the jet function in the  $\bar{n}^\mu$  direction in the massless-quark limit  $m_u = 0$ . The convolution of  $\Delta Z_{17}$  with these jet functions can be performed with contour methods, and because the singularities of  $\Delta Z_{17}$  in (9.39) are located in the same half-plane, the convolution integrals vanish. Both terms in the expression (9.39) vanish upon integration in  $\omega$ , while the  $\omega_1$  integration would only eliminate the second term.

We will show explicitly, that  $\Delta Z_{17}$  is irrelevant for the cancellation of all  $1/\varepsilon$  singularities between hard, (anti)hard-collinear and soft loops at NLO.

An alternative point-of-view provides a discussion in position space [77]. The large energy in the  $n^\mu$  direction flows from left to right in the Feynman diagram in Figure 9.1. Hence, *after* convolution with the (time-ordered) jet functions, the heavy-quark field with position argument  $(tn)$  is evaluated at a later time than the one at space-time point 0. This is ensured

<sup>3</sup>We argue in Appendix A of [85], that imposing a restricted support with cut-offs leads to inconsistencies with the local limit of the operator.

by the relation

$$\int d\omega \frac{e^{-i\omega t}}{\omega + p_+ + i0} = -2\pi i e^{ip_+ t} \theta(t), \quad (9.42)$$

where  $p_+$  is the small component of the hard-collinear momentum. Indeed, the field  $\bar{h}_v(tn)$  appears to the left of  $h_v(0)$  in (9.2) such that the fields are correctly time-ordered. Contrarily, after a Fourier transform to position space, the terms in  $\Delta Z_{17}$  are non-zero only for  $t < 0$ , and thus do not contribute. It would be interesting to investigate the UV singularities of the operator directly in position space, as was done for the soft-quark function in  $gg \rightarrow h$  at next-to-leading power in [205].

Recall that the relevant integrals that contribute to the  $\bar{B} \rightarrow X_s \gamma$  decay rate contain cuts. In particular, at leading order, the  $n$ -jet function is given by the discontinuity of the hard-collinear  $s$ -quark propagator, whereas the  $\bar{n}$ -jet function is defined at the amplitude level and arises from the anti-hard-collinear momentum configuration in the quark-loop in Figure 9.1. While the potentially problematic terms vanish after convolution with the time-ordered propagators, they certainly do not when convoluted with the physically relevant  $n$ -jet function. However, it turns out that both terms in  $\Delta Z_{17}$  arise from soft gluons connecting the amplitude with the complex conjugate amplitude. Since taking the cut enforces  $t > 0$  from the positive-energy constraint, a definition of the shape function  $g_{17}(\omega, \omega_1; \mu)$  that contains the relevant cut-propagators would directly eliminate  $\Delta Z_{17}$ . In summary, the contribution  $\Delta Z_{17}$ , which is non-zero only for  $t < 0$ , is irrelevant in both cases, since either taking the cut or the convolution with the time-ordered jet function enforces  $t > 0$ .

As already mentioned above, the  $\bar{B} \rightarrow X_s \gamma$  decay rate cannot be expressed as the imaginary part of a  $B$ -meson forward matrix element of time-ordered operators because not all possible cuts also contribute to the  $b \rightarrow s \gamma$  decay. Thus, a precise prescription is needed how to implement the restricted cuts when radiative corrections to the process are taken into account. A path-integral method to evaluate such cut diagrams is given by the Keldysh formalism [209, 210], see also [211] for a concise summary. Here one introduces fields with a subscript “+” that belong to the amplitude and are evaluated with standard HQET Feynman rules from time-ordered products. On the other hand, fields with a subscript “−” belong to the complex conjugate amplitude and are evaluated with complex-conjugate Feynman rules from anti-time-ordered products. The Feynman rule for the contraction of two fields with different indices, i.e. a propagator that connects the amplitude with the complex conjugate amplitude, is evaluated using the on-shell condition:

$$\frac{i}{\ell^2 + i0} \rightarrow 2\pi\delta(\ell^2)\theta(\ell_0). \quad (9.43)$$

On a diagrammatic level, these rules precisely correspond to the cutting-rules explained in the beginning of this section. However, since the shape function  $g_{17}$  is defined by a hadronic matrix element, a non-perturbative definition at the level of the path integral is required. The soft operator (9.2) that defines the shape function  $g_{17}$  should, thus, be written as

$$\mathcal{O}_{17}(t, r) \rightarrow (\bar{h}_v S_n)_-(tn) \not{n} (S_n^\dagger S_{\bar{n}})_+(0) i\gamma_\alpha^\perp \bar{n}_\beta (S_{\bar{n}}^\dagger g_s G_s^{\alpha\beta} S_{\bar{n}})_+(r\bar{n}) (S_{\bar{n}}^\dagger h_v)_+(0). \quad (9.44)$$

This prescription does not affect the Feynman rules for the effective vertex provided in (9.5), (9.7), (9.8), but the use of cut propagators from (9.43) introduces some relevant differences in a few diagrams. Indeed, evaluating all diagrams in Figure 9.3 with these cutting rules leaves most of the previous results unchanged. In particular the Abelian part of the  $Z$ -factor, as

well as the sum of diagrams (a) and (c)-(f) remain unaffected. Notable differences are that the contribution (9.33) becomes UV-finite, and second, the expression in (9.35) becomes

$$-\frac{\alpha_s C_A}{4\pi} \frac{1}{\varepsilon} \left\{ -\frac{1}{\varepsilon} \delta(\omega - \omega') \delta(\omega_1 - \omega'_1) + \delta(\omega_1 - \omega'_1) \left( \frac{\theta(\omega' - \omega)}{\omega' - \omega - \Delta} + \delta(\omega - \omega') \ln \frac{-\Delta}{\mu} \right) + \delta(\omega - \omega') \left( \frac{\theta(\omega_1 - \omega'_1)}{\omega_1 - \omega'_1 + \bar{\Delta}} + \delta(\omega_1 - \omega'_1) \ln \frac{\bar{\Delta}}{\mu} \right) \right\} + \mathcal{O}(\varepsilon^0). \quad (9.45)$$

This is indeed the sum of (9.33) and (9.35) apart from the two terms in  $\Delta Z_{17}$ . In other words, one finds the same soft UV poles when computing time-ordered diagrams and dropping irrelevant terms that vanish after convolution with the jet functions, or by directly computing cut diagrams. The reason for this is likely the absence of imaginary parts in the non-vanishing soft contributions, as in that case the cuts in the respective diagrams for the decay rate only affect the  $s$ -quark propagator, which belongs to the  $n$ -jet function. The shape function  $g_{17}$  that appears in the factorisation theorem for the  $\bar{B} \rightarrow X_s \gamma$  decay rate, and is convoluted with the discontinuity of the  $n$ -jet function, is given by the operator (9.44) including the cuts through the Keldysh formalism.

As stated before, evaluating the matrix element with time-ordered products is relevant for the soft function that appears in the factorisation of the  $B$ -meson forward matrix element of time-ordered weak Hamiltonians, i.e. before the restricted cuts are taken. Interestingly, such irrelevant contributions also arise for soft functions defined at the amplitude level, for example in exclusive  $B$  decays. In this case indeed only ordinary (time-ordered) Feynman diagrams contribute. We will discuss an example from the literature [212] in greater detail in Section 9.3.1.

## 9.2 Analytic Solution to the Renormalisation-Group Equation

In this subsection we present an analytic solution to the RG equation for the subleading shape function  $g_{17}(\omega, \omega_1; \mu)$  as defined using time-ordered and anti-time-ordered fields in (9.44),

$$\frac{d}{d \ln \mu} g_{17}(\omega, \omega_1; \mu) = - \int d\omega' \int d\omega'_1 \gamma_{17}(\omega, \omega_1, \omega', \omega'_1; \mu) g_{17}(\omega', \omega'_1; \mu), \quad (9.46)$$

in momentum space. To do so, let us first recall that the anomalous dimension which governs the scale evolution of  $g_{17}(\omega, \omega_1; \mu)$  is defined as

$$\gamma_{17}(\omega, \omega_1, \omega', \omega'_1; \mu) = - \int d\hat{\omega} \int d\hat{\omega}_1 \frac{dZ_{17}(\omega, \omega_1, \hat{\omega}, \hat{\omega}_1; \mu)}{d \ln \mu} Z_{17}^{-1}(\hat{\omega}, \hat{\omega}_1, \omega', \omega'_1; \mu), \quad (9.47)$$

with the  $Z$ -factor from (9.26) and (9.38) without  $\Delta Z_{17}$ . At  $\mathcal{O}(\alpha_s)$ , we can decompose the anomalous dimension as a sum of two pieces, each of which is associated with only one of the two light-cone directions,

$$\gamma_{17}(\omega, \omega_1, \omega', \omega'_1; \mu) = \frac{\alpha_s}{\pi} \left\{ C_F \delta(\omega_1 - \omega'_1) \gamma_n(\omega, \omega'; \mu) + \frac{C_A}{2} \delta(\omega - \omega') \gamma_{\bar{n}}(\omega_1, \omega'_1; \mu) \right\}. \quad (9.48)$$

The Abelian part

$$\gamma_n(\omega, \omega'; \mu) = \left( \ln \frac{\mu^2}{\omega^2} - 1 \right) \delta(\omega - \omega') - 2\theta(\omega) \left[ \frac{\theta(\omega' - \omega)}{\omega'(\omega' - \omega)} \right]_+ \omega' - 2\theta(-\omega) \left[ \frac{\theta(\omega' - \omega)}{\omega' - \omega} \right]_{\ominus} \quad (9.49)$$

only acts on the soft variables associated with the collinear direction, and the non-Abelian part

$$\gamma_{\bar{n}}(\omega_1, \omega'_1; \mu) = \ln \frac{\mu^2}{\omega_1^2} \delta(\omega_1 - \omega'_1) - \text{Re} \mathbf{H}(\omega_1, \omega'_1) + \frac{2\omega_1}{(\omega'_1)^2} [\theta(\omega_1)\theta(\omega'_1 - \omega_1) - \theta(-\omega_1)\theta(\omega_1 - \omega'_1)] \quad (9.50)$$

only acts on the soft variables associated with the anti-collinear direction. Because the dependence on the two momentum variables  $\omega$  and  $\omega_1$  factorizes, the RG Equation (9.46) can be separated in two independent equations which we solve consecutively.

### 9.2.1 Abelian Part

Our strategy to solve the integro-differential evolution equation closely follows the discussion from [203]. The RG equation in the Abelian limit is identical to the one of the leading shape function. To introduce some notation and concepts for the following, we now re-derive its well-known solution [204].

To do so, we first divide the support of the shape function in the variable  $\omega$  into two branches,

$$g_{17}(\omega, \omega_1; \mu) = \theta(\omega)g_{17}^>(\omega, \omega_1; \mu) + \theta(-\omega)g_{17}^<(\omega, \omega_1; \mu), \quad (9.51)$$

after which we perform a Mellin transformation that translates the distributions into ordinary functions or derivatives in the conjugate variable [213–215]. The Mellin transform is defined separately for positive values of  $\omega$  via

$$\begin{aligned} \tilde{g}_{17}^>(\eta, \omega_1; \mu) &= \int_0^\infty \frac{d\omega}{\omega} \left(\frac{\mu}{\omega}\right)^\eta g_{17}^>(\omega, \omega_1; \mu), \\ g_{17}^>(\omega, \omega_1; \mu) &= \int_{c-i\infty}^{c+i\infty} \frac{d\eta}{2\pi i} \left(\frac{\mu}{\omega}\right)^{-\eta} \tilde{g}_{17}^>(\eta, \omega_1; \mu), \end{aligned} \quad (9.52)$$

and for negative  $\omega$  by

$$\begin{aligned} \tilde{g}_{17}^<(\eta, \omega_1; \mu) &= \int_0^\infty \frac{d\omega}{\omega} \left(\frac{\mu}{\omega}\right)^\eta g_{17}^<(-\omega, \omega_1; \mu), \\ g_{17}^<(-\omega, \omega_1; \mu) &= \int_{c-i\infty}^{c+i\infty} \frac{d\eta}{2\pi i} \left(\frac{\mu}{\omega}\right)^{-\eta} \tilde{g}_{17}^<(\eta, \omega_1; \mu). \end{aligned} \quad (9.53)$$

The expressions for the different types of distributions convoluted with pure powers in  $\omega$  are collected in Appendix B of [203], and we do not repeat them here. In Mellin space, the Abelian part of the evolution equation turns into the following coupled system of differential equations

$$\left(\frac{d}{d \ln \mu} - \eta\right) \tilde{g}_{17}^>(\eta, \omega_1; \mu) = \frac{\alpha_s C_F}{\pi} \left[-2H_{-1-\eta} - 2\partial_\eta + 1\right] \tilde{g}_{17}^>(\eta, \omega_1; \mu), \quad (9.54)$$

$$\begin{aligned} \left(\frac{d}{d \ln \mu} - \eta\right) \tilde{g}_{17}^<(\eta, \omega_1; \mu) &= \frac{\alpha_s C_F}{\pi} \left[-2H_\eta - 2\partial_\eta + 1\right] \tilde{g}_{17}^<(\eta, \omega_1; \mu) \\ &+ \frac{\alpha_s C_F}{\pi} 2\Gamma(-\eta)\Gamma(1+\eta)\tilde{g}_{17}^>(\eta, \omega_1; \mu), \end{aligned} \quad (9.55)$$

which hold for  $-1 < \text{Re}(\eta) < 0$ , and  $H_\eta$  is the Harmonic number function. This system can be diagonalized by choosing  $\tilde{g}_{17}^>(\eta, \omega_1; \mu)$  and the linear combination

$$\tilde{g}_{17}(\eta, \omega_1; \mu) \equiv \int_{-\infty}^{+\infty} \frac{d\omega}{-\omega - i0} \left(\frac{\mu}{-\omega - i0}\right)^\eta g_{17}(\omega, \omega_1; \mu) = \tilde{g}_{17}^<(\eta, \omega_1; \mu) - \tilde{g}_{17}^>(\eta, \omega_1; \mu)e^{i\pi\eta}, \quad (9.56)$$

as the two independent functions. The latter fulfills

$$\left(\frac{d}{d\ln\mu} - \eta\right) \tilde{g}_{17}(\eta, \omega_1; \mu) = \frac{\alpha_s C_F}{\pi} \left[-2H_\eta - 2\partial_\eta + 1\right] \tilde{g}_{17}(\eta, \omega_1; \mu), \quad (9.57)$$

which can be easily verified using the identity  $\Gamma(-\eta)\Gamma(1+\eta) = e^{i\pi\eta}(i\pi + H_\eta - H_{-1-\eta})$ . We note that the integral in (9.56) does not have an inverse transformation and should therefore not be considered as an integral transform.

Instead of solving (9.54) and (9.55), it is simpler to solve (9.54) and (9.57) and then use (9.56) to obtain  $\tilde{g}_{17}^{\lessgtr}(\eta, \omega_1; \mu)$ . The two solutions to the diagonal equations read

$$\tilde{g}_{17}^{\gtrless}(\eta, \omega_1; \mu) = e^{2V+2\gamma_E a} \left(\frac{\mu}{\mu_0}\right)^\eta \frac{\Gamma(-\eta)}{\Gamma(-\eta-2a)} \tilde{g}_{17}^{\gtrless}(\eta+2a, \omega_1; \mu_0), \quad (9.58)$$

$$\tilde{g}_{17}(\eta, \omega_1; \mu) = e^{2V+2\gamma_E a} \left(\frac{\mu}{\mu_0}\right)^\eta \frac{\Gamma(1+\eta+2a)}{\Gamma(1+\eta)} \tilde{g}_{17}(\eta+2a, \omega_1; \mu_0), \quad (9.59)$$

with the evolution factors

$$\begin{aligned} V(\mu, \mu_0) &= - \int_{\mu_0}^{\mu} \frac{d\mu'}{\mu'} \frac{\alpha_s(\mu') C_F}{\pi} \left[ \ln \frac{\mu'}{\mu_0} - \frac{1}{2} \right], \\ a(\mu, \mu_0) &= - \int_{\mu_0}^{\mu} \frac{d\mu'}{\mu'} \frac{\alpha_s(\mu') C_F}{\pi}, \end{aligned} \quad (9.60)$$

whose dependence on  $\mu$  and  $\mu_0$  has been omitted in (9.58) and (9.59) for brevity. Further, in the integrand we can identify the factor  $\gamma_{\text{cusp}} = \alpha_s C_F / \pi + \mathcal{O}(\alpha_s^2)$  with the leading term of the universal cusp anomalous dimension.

After performing the inverse transformations (9.52) and (9.53), one finds the momentum-space solution for the  $\omega > 0$  branch,

$$g_{17}^{\gtrless}(\omega, \omega_1; \mu) = \frac{e^{2V+2\gamma_E a}}{\Gamma(-2a)} \int_{\omega}^{\infty} \frac{d\omega'}{\omega' - \omega} \left(\frac{\mu_0}{\omega' - \omega}\right)^{2a} g_{17}^{\gtrless}(\omega', \omega_1; \mu_0), \quad (9.61)$$

and for the  $\omega < 0$  branch,

$$\begin{aligned} g_{17}^{\lessgtr}(\omega, \omega_1; \mu) &= \frac{e^{2V+2\gamma_E a}}{\Gamma(-2a)} \left[ \int_0^{\infty} \frac{d\omega'}{\omega' - \omega} \left(\frac{\mu_0}{\omega' - \omega}\right)^{2a} g_{17}^{\gtrless}(\omega', \omega_1; \mu_0) \right. \\ &\quad \left. + \int_{\omega}^0 \frac{d\omega'}{\omega' - \omega} \left(\frac{\mu_0}{\omega' - \omega}\right)^{2a} g_{17}^{\lessgtr}(\omega', \omega_1; \mu_0) \right]. \end{aligned} \quad (9.62)$$

Combining the two then simply yields

$$g_{17}(\omega, \omega_1; \mu) = \frac{e^{2V+2\gamma_E a}}{\Gamma(-2a)} \int_{\omega}^{\infty} \frac{d\omega'}{\omega' - \omega} \left(\frac{\mu_0}{\omega' - \omega}\right)^{2a} g_{17}(\omega', \omega_1; \mu_0). \quad (9.63)$$

This result trivially reproduces the one presented in [204] for the leading shape function, once a restricted support  $\omega' \in (-\infty, \bar{\Lambda}]$  is assumed for the initial condition  $g_{17}(\omega', \omega_1; \mu_0)$ . Recall that this is only consistent with renormalisation if we adopt the definition of  $g_{17}(\omega, \omega_1; \mu)$  in terms of time-ordered and anti-time-ordered fields in (9.44). From now on we will explicitly include the upper cut-off in  $\omega$ .

### 9.2.2 Non-Abelian Part

We now move on to the non-Abelian part of the evolution equation, and adopt the same procedure as discussed before. First, we perform a similar split into a positive-support and negative-support branch,

$$g_{17}(\omega, \omega_1; \mu) = \theta(\omega_1)g_{17}^>(\omega, \omega_1; \mu) + \theta(-\omega_1)g_{17}^<(\omega, \omega_1; \mu). \quad (9.64)$$

For compactness of the notation we use the same symbols as in (9.51). The variable to which the superscripts  $>$  and  $<$  refer is always clear from the context.

Transforming the distributions from (9.50) to Mellin space yields the differential equations

$$\begin{aligned} & \left( \frac{d}{d \ln \mu} - \eta_1 \right) \tilde{g}_{17}^>(\omega, \eta_1; \mu) \\ &= - \frac{\alpha_s C_A}{2\pi} \left\{ [H_{-1-\eta_1} + H_{\eta_1} + 2H_{1-\eta_1} + 2\partial_{\eta_1}] \tilde{g}_{17}^>(\omega, \eta_1; \mu) - \Gamma(-\eta_1)\Gamma(1+\eta_1) \tilde{g}_{17}^<(\omega, \eta_1; \mu) \right\}, \end{aligned} \quad (9.65)$$

and

$$\begin{aligned} & \left( \frac{d}{d \ln \mu} - \eta_1 \right) \tilde{g}_{17}^<(\omega, \eta_1; \mu) \\ &= - \frac{\alpha_s C_A}{2\pi} \left\{ [H_{-1-\eta_1} + H_{\eta_1} + 2H_{1-\eta_1} + 2\partial_{\eta_1}] \tilde{g}_{17}^<(\omega, \eta_1; \mu) - \Gamma(-\eta_1)\Gamma(1+\eta_1) \tilde{g}_{17}^>(\omega, \eta_1; \mu) \right\}, \end{aligned} \quad (9.66)$$

which again hold for  $-1 < \text{Re}(\eta_1) < 0$ , where  $\eta_1$  is the Mellin-space variable conjugate to  $\omega_1$ . Since this system is symmetric, it can be diagonalized by using the sum and difference  $\tilde{g}_{17}^\pm(\omega, \eta_1; \mu) \equiv \tilde{g}_{17}^>(\omega, \eta_1; \mu) \pm \tilde{g}_{17}^<(\omega, \eta_1; \mu)$  as independent functions. However, the equations become somewhat simpler if one uses the following two linear combinations,

$$\begin{aligned} \tilde{g}_{17}^{(A)}(\omega, \eta_1; \mu) &= \tilde{g}_{17}^>(\omega, \eta_1; \mu) e^{\frac{i\pi\eta_1}{2}} - \tilde{g}_{17}^<(\omega, \eta_1; \mu) e^{-\frac{i\pi\eta_1}{2}}, \\ \tilde{g}_{17}^{(B)}(\omega, \eta_1; \mu) &= \tilde{g}_{17}^<(\omega, \eta_1; \mu) e^{\frac{i\pi\eta_1}{2}} - \tilde{g}_{17}^>(\omega, \eta_1; \mu) e^{-\frac{i\pi\eta_1}{2}}. \end{aligned} \quad (9.67)$$

Interestingly, it then turns out that both functions fulfill the same diagonal RG equation,

$$\left( \frac{d}{d \ln \mu} - \eta_1 \right) \tilde{g}_{17}^{(A,B)}(\omega, \eta_1; \mu) = - \frac{\alpha_s C_A}{\pi} \left[ H_{\eta_1} + H_{1-\eta_1} + \partial_{\eta_1} \right] \tilde{g}_{17}^{(A,B)}(\omega, \eta_1; \mu), \quad (9.68)$$

which is solved by

$$\tilde{g}_{17}^{(A,B)}(\omega, \eta_1; \mu) = e^{V_1 + 2\gamma_E a_1} \left( \frac{\mu}{\mu_0} \right)^{\eta_1} \frac{\Gamma(2-\eta_1)\Gamma(1+\eta_1+a_1)}{\Gamma(2-\eta_1-a_1)\Gamma(1+\eta_1)} \tilde{g}_{17}^{(A,B)}(\omega, \eta_1 + a_1; \mu_0), \quad (9.69)$$

where now the evolution factors read

$$\begin{aligned} V_1(\mu, \mu_0) &= - \int_{\mu_0}^{\mu} \frac{d\mu'}{\mu'} \frac{\alpha_s(\mu') C_A}{\pi} \ln \frac{\mu'}{\mu_0}, \\ a_1(\mu, \mu_0) &= - \int_{\mu_0}^{\mu} \frac{d\mu'}{\mu'} \frac{\alpha_s(\mu') C_A}{\pi}. \end{aligned} \quad (9.70)$$

Solving (9.67) for the two branches  $\tilde{g}_{17}^{>,<}$  yields

$$\tilde{g}_{17}^{>,<}(\omega, \eta_1; \mu) = - e^{V_1 + 2\gamma_E a_1} \left( \frac{\mu}{\mu_0} \right)^{\eta_1} \frac{\Gamma(-\eta_1)\Gamma(2-\eta_1)\Gamma(1+\eta_1+a_1)}{\Gamma(2-\eta_1-a_1)} \left[ \quad (9.71)$$

$$\frac{1}{\pi} \sin \left( (\eta_1 + \frac{a_1}{2})\pi \right) \tilde{g}_{17}^{>,<}(\omega, \eta_1 + a_1; \mu) + \frac{1}{\pi} \sin \left( \frac{a_1\pi}{2} \right) \tilde{g}_{17}^{<,>}(\omega, \eta_1 + a_1; \mu) \Big].$$

After replacing the sine functions by gamma functions via the reflection formula, the inverse Mellin transform can be expressed in terms of Meijer-G functions, which are defined by the complex contour integral

$$G_{p,q}^{m,n} \left( \begin{matrix} \mathbf{a} \\ \mathbf{b} \end{matrix} \middle| z \right) = \int \frac{d\eta}{2\pi i} z^\eta \frac{\prod_{j=1}^m \Gamma(b_j - \eta) \prod_{j=1}^n \Gamma(1 - a_j + \eta)}{\prod_{j=m+1}^q \Gamma(1 - b_j + \eta) \prod_{j=n+1}^p \Gamma(a_j - \eta)} \quad (9.72)$$

for integer  $0 \leq m \leq q$  and  $0 \leq n \leq p$ , where  $\mathbf{a} = (a_1, \dots, a_p)$  and  $\mathbf{b} = (b_1, \dots, b_q)$ . Further details and properties of these functions are e.g. outlined in Appendix D of [203]. The resulting momentum-space solution reads

$$g_{17}(\omega, \omega_1; \mu) = \int \frac{d\omega'_1}{|\omega'_1|} U_{\bar{n}}^{(17)}(\omega_1, \omega'_1; \mu, \mu_0) g_{17}(\omega, \omega'_1; \mu_0), \quad (9.73)$$

with the evolution function

$$U_{\bar{n}}^{(17)}(\omega_1, \omega'_1; \mu, \mu_0) = -e^{V_1 + 2\gamma_E a_1} \left( \frac{\mu_0}{|\omega'_1|} \right)^{a_1} \left\{ \theta(\tau) G_{3,3}^{1,2} \left( \begin{matrix} -1, & 1, & a_1/2 \\ a_1 + 1, & a_1 - 1, & a_1/2 \end{matrix} \middle| \tau \right) \right. \\ \left. + \frac{1}{2\pi} \sin \left( \frac{a_1\pi}{2} \right) \theta(-\tau) \Gamma(1 + a_1) \Gamma(3 + a_1) (-\tau)^{1+a_1} {}_2F_1(1 + a_1, 3 + a_1, 3; \tau) \right\}, \quad (9.74)$$

where we defined the ratio  $\tau = \omega'_1/\omega_1$ .

The appearing Meijer-G function can be reduced to a hypergeometric function on the interval  $1 > \tau > -1$  via

$$G_{3,3}^{1,2} \left( \begin{matrix} -1, & 1, & a_1/2 \\ a_1 + 1, & a_1 - 1, & a_1/2 \end{matrix} \middle| \tau \right) \\ = \frac{1}{2\pi} \sin \left( \frac{a_1\pi}{2} \right) \Gamma(1 + a_1) \Gamma(3 + a_1) \tau^{1+a_1} {}_2F_1(1 + a_1, 3 + a_1, 3; \tau), \quad (9.75)$$

where the variable  $\tau$  is implicitly supplemented with an  $+i0$  prescription. From this identity it follows that the evolution function in (9.74) is continuous at  $\tau = 0$ .

### 9.2.3 Phenomenological Implications

To summarize, the solution to the RG equation takes the factorized form

$$g_{17}(\omega, \omega_1; \mu) = \int_{\omega}^{\bar{\Lambda}} \frac{d\omega'}{\omega' - \omega} U_{\bar{n}}^{(17)}(\omega, \omega'; \mu, \mu_0) \int_{-\infty}^{\infty} \frac{d\omega'_1}{|\omega'_1|} U_{\bar{n}}^{(17)}(\omega_1, \omega'_1; \mu, \mu_0) g_{17}(\omega', \omega'_1; \mu_0), \quad (9.76)$$

with the evolution function for the soft momenta associated with the  $n^\mu$  light-cone,

$$U_n^{(17)}(\omega, \omega'; \mu, \mu_0) = \frac{e^{2V + 2\gamma_E a}}{\Gamma(-2a)} \left( \frac{\mu_0}{\omega' - \omega} \right)^{2a}, \quad (9.77)$$

and the evolution function for the soft momenta associated with the  $\bar{n}^\mu$  light-cone given by (9.74). Below we will discuss some consequences of RG evolution relevant in phenomenological applications. A serious numerical estimate of the evolution effects, however, is left for future work.

The functional behavior of the shape function for  $\omega \rightarrow \bar{\Lambda}$  and  $\omega \rightarrow -\infty$  that follows from its  $\mathcal{O}(\alpha_s)$  anomalous dimension is known from the literature [204]. Assuming that the function at the low scale  $\mu_0$  falls off like  $\omega^{-\xi}$  for  $\omega \rightarrow -\infty$ , one finds that for  $\mu > \mu_0$  it falls off as  $\sim \omega^{-2a-\min(1,\xi)}$ , with  $a < 0$  [204]. For  $\omega \rightarrow \bar{\Lambda}$ , on the other hand, assuming that the shape function at the low scale vanishes as  $(\bar{\Lambda} - \omega)^\xi$ , at higher scales it vanishes as  $\sim (\bar{\Lambda} - \omega)^{-2a+\xi}$ . Inverse moments of the shape function converge at the scale  $\mu_0$  as long as  $\xi > 0$ , but typically one would assume  $\xi > 1$  such that the normalization integral, i.e. the local limit, exists. After evolution to the scale  $\mu$ , inverse moments then converge as long as  $2a > -1$ , which is true for realistic scales. It is well known that the normalization integral as well as positive moments, however, become divergent, because the RG evolution generates a radiative tail that falls off slower than  $1/\omega$  [204]. Given that the cut-propagators from the jet function impose a lower cut-off on  $\omega$ , convolution integrals in factorisation theorems converge for all practical purposes.

The asymptotic behavior of  $g_{17}(\omega, \omega_1; \mu)$  for  $\omega_1 \rightarrow \pm\infty$  is determined by the location of singularities of the Mellin-space solution (9.71). Assuming  $g_{17}(\omega, \omega_1 \rightarrow \pm\infty; \mu_0) \sim \omega_1^{-\xi_1}$ , its Mellin transform has a singularity at  $\eta_1 = -\xi_1$ . We deform the integration contour to enclose all poles and cuts on the left half-plane with respect to  $\text{Re}(\eta_1) = c$ , where  $-1 - a_1 < c < 0$ . The singularities of the initial condition with shifted argument at  $\eta_1 = -\xi_1 - a_1$ , as well as of the gamma function at  $\eta_1 = -1 - a_1$  lead to

$$g_{17}(\omega, \omega_1 \rightarrow \pm\infty; \mu) \sim \omega_1^{-a_1 - \min(1, \xi_1)}. \quad (9.78)$$

For the limit  $\omega_1 \rightarrow 0$ , the singularity from  $\Gamma(-\eta_1)$  determines that the function approaches a constant. After expanding the Mellin-space solutions (9.71) around  $\eta_1 = 0$ , one finds  $\tilde{g}_{17}^>(\omega, \eta_1; \mu) \simeq \tilde{g}_{17}^<(\omega, \eta_1; \mu)$ , and it follows that  $g_{17}(\omega, \omega_1; \mu)$  is continuous at  $\omega_1 = 0$ . This guarantees that principal-value integrals of the form

$$\int \frac{d\omega_1}{\omega_1 + i0} g_{17}(\omega, \omega_1; \mu) = \text{P} \int \frac{d\omega_1}{\omega_1} g_{17}(\omega, \omega_1; \mu) - i\pi g_{17}(\omega, 0; \mu) \quad (9.79)$$

are also well-defined. Hence, also the convolution integrals in  $\omega_1$  in factorisation theorems exist for all practical purposes.

Two important properties of the shape function  $g_{17}(\omega, \omega_1; \mu)$  were derived in [77]. First, the function is real-valued, i.e. does not carry any strong phases. Because the anomalous dimension in (9.48) itself is also real-valued, the function trivially does not develop strong phases through RG evolution. Second, the shape function obeys the identity

$$\int_{-\infty}^{\bar{\Lambda}} d\omega g_{17}(\omega, \omega_1; \mu_0) = \int_{-\infty}^{\bar{\Lambda}} d\omega g_{17}(\omega, -\omega_1; \mu_0), \quad (9.80)$$

which becomes ill-defined at scales  $\mu > \mu_0$  due to the radiative tail for large  $\omega$  discussed in the previous paragraph.

Nevertheless, the anomalous dimension associated with the  $\bar{n}^\mu$  sector (9.50) is anti-symmetric under the exchange  $\omega_1 \leftrightarrow -\omega_1$  and  $\omega'_1 \leftrightarrow -\omega'_1$ . As a consequence, a symmetric function in  $\omega_1$  remains symmetric under RG evolution. To see this, assume that at some initial scale  $g_{17}^<(\omega, \omega_1; \mu_0) = g_{17}^>(\omega, -\omega_1; \mu_0)$  holds, where the  $>$  and  $<$  signs refer to the variable  $\omega_1$ . In that case, the solution to the RG equation in the  $\bar{n}^\mu$  sector can be expressed as

$$g_{17}(\omega, \omega_1; \mu) = \int_0^\infty \frac{d\omega'_1}{\omega'_1} U_{\bar{n}}^{\text{sym}}(\omega_1, \omega'_1; \mu, \mu_0) g_{17}(\omega, \omega'_1; \mu_0), \quad (9.81)$$

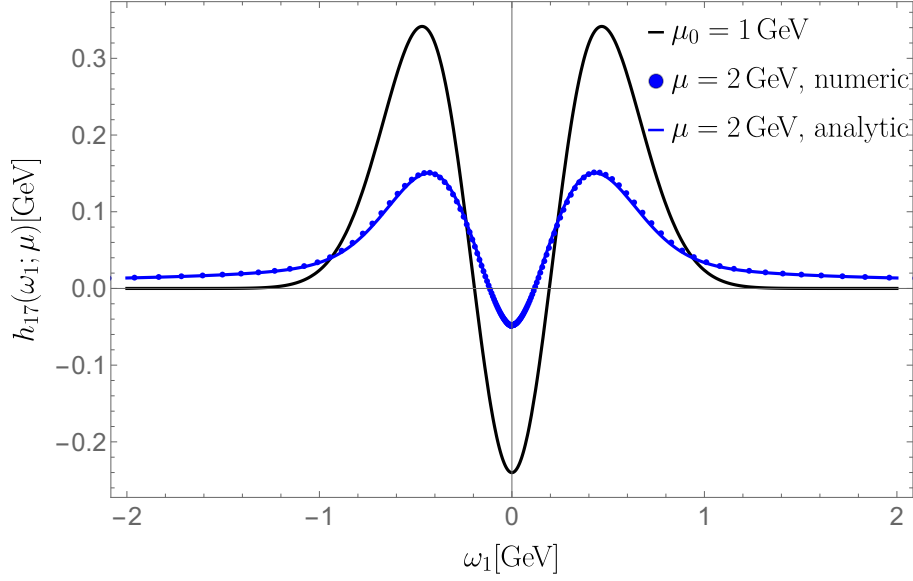


**Figure 9.5:** Scale evolution of the function  $h_{17}(\omega_1; \mu)$ , using the model (9.85) with  $n \leq 2$  Hermite polynomials at the low scale  $\mu_0 = 1$  GeV (black curve). The blue curve shows the analytic solution (9.84) for  $\mu = 2$  GeV, which is in good agreement with the numeric solution from discretisation of the momentum-space RG equation (blue dots). The latter is obtained using  $N = 600$  points that are logarithmically distributed on the intervals  $[-\Omega, -\varepsilon]$  and  $[\varepsilon, \Omega]$ , with  $\varepsilon = 10^{-9}$  GeV and  $\Omega = 10^3$  GeV. The strong coupling constant is evaluated with one-loop running and  $n_f = 4$  quark flavors, using  $\alpha_s(\mu_0) = 0.48$ . We emphasize that the blue curve only includes the non-Abelian piece (9.50) of the anomalous dimension.

with

$$U_n^{\text{sym}}(\omega_1, \omega'_1; \mu, \mu_0) = -e^{V_1 + 2\gamma_E a_1} \left(\frac{\mu_0}{\omega'_1}\right)^{a_1} \left\{ G_{3,3}^{1,2} \left( \begin{matrix} -1, & 1, & a_1/2 \\ a_1 + 1, & a_1 - 1, & a_1/2 \end{matrix} \middle| |\tau| \right) \right. \\ \left. + \frac{1}{2\pi} \sin\left(\frac{a_1\pi}{2}\right) \Gamma(1 + a_1) \Gamma(3 + a_1) |\tau|^{1+a_1} {}_2F_1(1 + a_1, 3 + a_1, 3; -|\tau|) \right\}. \quad (9.82)$$

Because the absolute value  $|\tau| = |\omega'_1/\omega_1|$  appears as an argument of the Meijer-G functions, it is easy to see that  $g_{17}^<(\omega, \omega_1; \mu) = g_{17}^>(\omega, -\omega_1; \mu)$  holds at any scale  $\mu$ .

We numerically test the derived solution of the RG equation using a simple model at the scale  $\mu_0 = 1$  GeV. We follow [77] and define

$$h_{17}(\omega_1, \mu_0) = \int_{-\Delta}^{\bar{\Lambda}} d\omega g_{17}(\omega, \omega_1; \mu_0), \quad (9.83)$$

with  $\Delta = m_b - 2E_0$  and  $E_0$  is the energy cut in the photon spectrum.

As the evolution in the Abelian limit coincides with the well-known scale evolution of the leading shape function, we restrict ourselves to the non-Abelian piece in the following, such that at the scale  $\mu > \mu_0$  one has<sup>4</sup>

$$h_{17}(\omega_1; \mu) = \int_{-\Delta}^{\bar{\Lambda}} d\omega g_{17}(\omega, \omega_1; \mu) = \int_{-\infty}^{\infty} \frac{d\omega'_1}{|\omega'_1|} U_n^{(17)}(\omega_1, \omega'_1; \mu, \mu_0) h_{17}(\omega_1; \mu_0). \quad (9.84)$$

<sup>4</sup>In general, including the Abelian part requires specifying a model for the shape function  $g_{17}(\omega, \omega_1; \mu_0)$  instead of its integral  $h_{17}(\omega_1; \mu_0)$ . For example, if one assumes at  $\mu_0$  a factorisation of the form

$$g_{17}(\omega, \omega_1; \mu_0) = \hat{f}(\omega; \mu_0) h_{17}(\omega_1; \mu_0),$$

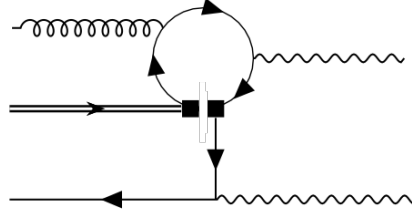


**Figure 9.6:** Leading order contribution from the operator  $Q_1^q$  to the exclusive double radiative  $\bar{B}_{d,s} \rightarrow \gamma\gamma$  decay.

We emphasize again, that a serious numerical analysis – including perturbative corrections to the jet and hard functions – will be presented elsewhere.

A specific model for the function  $h_{17}(\omega_1; \mu_0)$  has been introduced in [196], and expands the function in Hermite polynomials multiplied by a Gaussian of width  $\sigma$ ,

$$h_{17}(\omega_1; \mu_0) = \sum_n a_{2n} H_{2n} \left( \frac{\omega_1}{\sqrt{2}\sigma} \right) e^{-\frac{\omega_1^2}{2\sigma^2}}. \quad (9.85)$$

Here the sum runs only over even integers to ensure that  $h_{17}$  is an even function. In the following, we restrict ourselves to the first two terms  $n \in (0, 1)$ , in which case the coefficients  $a_0$  and  $a_2$  can be related to positive moments of the function  $h_{17}$  [196],

$$a_0 = \frac{\langle \omega_1^0 h_{17} \rangle}{\sqrt{2\pi}|\sigma|}, \quad a_2 = \frac{\langle \omega_1^2 h_{17} \rangle - \sigma^2 \langle \omega_1^0 h_{17} \rangle}{4\sqrt{2\pi}|\sigma|^3}. \quad (9.86)$$

As representative numerical values we use  $\langle \omega_1^0 h_{17} \rangle = 0.25 \text{ GeV}^2$ ,  $\langle \omega_1^2 h_{17} \rangle = 0.1 \text{ GeV}^4$ , and  $\sigma = 0.3 \text{ GeV}$ , which lie within the bounds quoted in [196]. Figure 9.5 shows this function at the two different scales  $\mu_0 = 1 \text{ GeV}$  and  $\mu = 2 \text{ GeV}$ , where the latter function is obtained analytically using the evolution function (9.82) for symmetric initial functions, and numerically by discretisation of the momentum-space RG equation (see caption of Figure 9.5 for more details). The appearing integrals can be performed analytically, using e.g. *Mathematica*, and result in a sum of several higher Meijer-G functions, which we do not quote here.

### 9.3 The Exclusive Counterpart $\Phi_G$

In this section, we analyse the soft function that has been introduced in [216] in the context of rare exclusive  $\bar{B}_{s,d} \rightarrow \gamma\gamma$  decays, cf. Fig 9.6, and whose renormalisation properties have recently been studied in [212]. It turns out that also in this case the analytic properties of the soft anomalous dimension allow one to considerably simplify scale evolution. Provided the soft function is convoluted with appropriate jet functions, logarithms between the soft and the hard-collinear scale can be resummed by solving a “reduced” RG equation.

with  $\int_{-\Delta}^{\bar{\Lambda}} d\omega \hat{f}(\omega; \mu_0) = 1$ , then the right-hand side of (9.84) is simply multiplied by the factor

$$c(\mu, \mu_0) = \int_{-\Delta}^{\bar{\Lambda}} d\omega \int_{\omega}^{\bar{\Lambda}} \frac{d\omega'}{\omega' - \omega} U_n^{(17)}(\omega, \omega'; \mu, \mu_0) \hat{f}(\omega; \mu_0).$$

The definition of the occurring soft function is rather similar to the one of  $g_{17}(\omega, \omega_1; \mu)$  in (9.1), and reads<sup>5</sup>

$$\mathcal{F}_B(\mu)\Phi_G(\omega, \omega_1; \mu) = \frac{1}{2M_B} \int \frac{dr}{2\pi} e^{i\omega_1 r} \int \frac{dt}{2\pi} e^{i\omega t} \langle 0 | \mathcal{O}_G(t, r) | \bar{B}_v \rangle, \quad (9.87)$$

with the scale-dependent static decay constant  $\mathcal{F}_B(\mu)$ , and the HQET operator

$$\mathcal{O}_G(t, r) = (\bar{q}_s S_n)(tn) \not{n} (S_n^\dagger S_{\bar{n}})(0) \gamma_\alpha^\perp \bar{n}_\beta \gamma_5 (S_{\bar{n}}^\dagger g_s G_s^{\alpha\beta} S_n)(r\bar{n}) (S_{\bar{n}}^\dagger h_v)(0). \quad (9.88)$$

The most important difference to the shape function  $g_{17}$  is that the soft function  $\Phi_G$  is defined at the amplitude level. Consequently, the soft quark-field  $q_s$  is a light-quark field,  $q = s, d$ , and the operator contains a  $\gamma_5$  Dirac matrix to ensure the correct parity. Furthermore, because all soft momenta are incoming, the signs of the exponentials are different from those in the definition of  $g_{17}$  in (9.1). As a consequence, the distributions  $H_\pm$  transform according to

$$\begin{aligned} H_+(-\omega, -\omega') &= H_-(\omega, \omega') + 2\pi i \theta(\omega) \delta(\omega - \omega'), \\ H_-(-\omega, -\omega') &= H_+(\omega, \omega') - 2\pi i \theta(-\omega) \delta(\omega - \omega'). \end{aligned} \quad (9.89)$$

### 9.3.1 Anomalous Dimension

The anomalous dimension of the operator  $\mathcal{O}_G$  was calculated in [212], and reads

$$\begin{aligned} \Gamma_G(\omega, \omega_1, \omega', \omega'_1; \mu) &= \frac{\alpha_s C_F}{\pi} \left[ \left( \ln \frac{\mu}{\omega - i0} - \frac{1}{2} \right) \delta(\omega - \omega') - H_+(\omega, \omega') \right] \delta(\omega_1 - \omega'_1) \\ &+ \frac{\alpha_s C_A}{\pi} \left[ \left( \ln \frac{\mu}{\omega_1 - i0} + \frac{i\pi}{2} \right) \delta(\omega_1 - \omega'_1) - H_+(\omega_1, \omega'_1) \right. \\ &\quad \left. + \frac{\omega_1}{(\omega'_1)^2} [\theta(\omega_1)\theta(\omega'_1 - \omega_1) - \theta(-\omega_1)\theta(\omega_1 - \omega'_1)] \right] \delta(\omega - \omega') \\ &+ \frac{\alpha_s}{\pi} \Delta\Gamma_G(\omega, \omega_1; \omega', \omega'_1; \mu), \end{aligned} \quad (9.90)$$

with

$$\Delta\Gamma_G = \frac{i}{4} \frac{C_A}{\pi} [\Delta H(\omega, \omega') - 2i\pi\delta(\omega - \omega')] [\Delta H(\omega_1, \omega'_1) - 2i\pi\delta(\omega_1 - \omega'_1)], \quad (9.91)$$

where we omitted the arguments of  $\Delta\Gamma_G$  on the left-hand side for brevity, and defined  $\Delta H \equiv H_+ - H_-$ . The Abelian contribution coincides with the well-known evolution kernel of the leading-twist  $B$ -meson light-cone distribution amplitude [217], or with its generalization to functions with support on the entire real axis [203], respectively. We note that the relation

$$\ln \frac{\mu}{\omega - i0} \delta(\omega - \omega') - H_+(\omega, \omega') = \frac{1}{2} \ln \frac{\mu^2}{\omega^2} \delta(\omega - \omega') - \text{Re} H_+(\omega, \omega') \quad (9.92)$$

implies that the Abelian part of the anomalous dimension is real-valued. The non-Abelian contributions can be extracted from the calculation of UV singularities presented in the

<sup>5</sup>We slightly changed the notation to be consistent with our definition of  $g_{17}$ . In particular, we use the soft-momentum variables  $(\omega, \omega_1)$  instead of  $(\omega_1, \omega_2)$  used in [212].

previous Section 9.1 via the transformations (9.89), and by taking into account that the contribution (9.33) from diagram (b) is UV-finite in the light-quark case.

The RG equation with the anomalous dimension (9.90) has been solved in [212]. Notably, the distribution  $H_-$  generates a non-vanishing support for negative values of the soft momentum variables [203]; a somewhat unfamiliar feature for amplitude-level soft functions. Using similar arguments as in the previous section, we will now argue that the analytic properties of the soft anomalous dimension and the jet functions allow one to solve a “reduced” RG equation that features two important simplifications:

- First, as factorisation in SCET would indicate, the dependence on the soft momenta  $(\omega, \omega_1)$  associated with the two light-cone directions  $n^\mu$  and  $\bar{n}^\mu$  decouples,
- and second, a positively-supported function at the low scale  $\mu_0$  does *not* acquire support for negative values at  $\mu > \mu_0$  in either of the two variables.

The latter property has the important consequence that no additional complex phases are generated through the convolution integrals in inverse moments. Furthermore, we then find that the asymptotic behavior for small arguments is consistent with the usual conformal spin of the soft fields. Using a specific example, these features are discussed in greater detail below.

The calculation of the anomalous dimension for an amplitude-level soft function proceeds via standard time-ordered Feynman diagrams that do not contain any cut propagators. However, given that (9.34) is equivalent to

$$\frac{1}{\omega - \omega' - i0} = H_+(\omega, \omega') - H_-(\omega, \omega'), \quad (9.93)$$

and the jet functions for the exclusive  $\bar{B}_{d,s} \rightarrow \gamma\gamma$  process have singularities or branch-cuts located in the upper half-plane (i.e. depend on  $\omega - i0$  and  $\omega_1 - i0$ , respectively), implies that we can identify the two distributions  $H_+(\omega, \omega') = H_-(\omega, \omega')$ .<sup>6</sup> For the special case of jet functions of the form  $\sim (\omega - i0)^q$  this has already been realised in [203]. Here we give an explanation for this observation, and generalize this statement to jet functions with similar analytic properties.

To give a more formal reasoning, it is important to note that distribution-valued objects are always defined on a function space with certain properties that are required e.g. for the convergence of integrals. This function space is typically defined in the primed variables  $(\omega', \omega'_1)$ , as these are the integration variables in the RG equation. However, as was also discussed in [203] in the context of these specific distributions, the soft function itself can be considered as a distribution-valued object in the variables  $(\omega, \omega_1)$ , see for example the fixed-order expressions for the  $B_c$ -meson light-cone distributions amplitude in the non-relativistic approximation in [218]. In this sense, the identity  $H_+ = H_-$  holds on a function space in  $(\omega, \omega_1)$  with two properties: First, all singularities and branch cuts of the test functions are located in the upper half-plane, and second, the functions are such that the residue theorem can be applied. The latter means that they should fall off fast enough for large  $(\omega, \omega_1)$ , and the integration domain should extend over the entire real axis. From dimensional arguments, and due to the directed flow of large energy, both of these properties are fulfilled by the relevant jet functions for the  $\bar{B}_{d,s} \rightarrow \gamma\gamma$  process. For example, the leading-order jet function in the  $n^\mu$  direction is simply given by the inverse hard-collinear propagator  $\sim (\omega - i0)^{-1}$ ,

<sup>6</sup>The  $i0$  prescriptions of the jet functions differ in inclusive and exclusive processes due to the different kinematics.

and similarly the jet function in the  $\bar{n}^\mu$  direction is given by  $(\omega_1 - i0)^{-1}$  at leading order and in the massless case  $m_u = 0$ .

We emphasize again that we have checked the cancellation of all singularities in  $1/\varepsilon$  between the different elements of the factorisation theorem at next-to-leading order and in the limit  $m_u = 0$ . The relevant two-loop  $\bar{n}$ -jet function is the same as for the inclusive  $\bar{B} \rightarrow X_s \gamma$  decay up to the different sign of the  $i0$  prescription.

To conclude this discussion let us stress that the anomalous dimension of a given operator is well-defined and unambiguous. Identifying  $H_+ = H_-$  is allowed whenever the soft operator is convoluted with the jet functions, and can hence simplify the resummation of logarithms between the soft and the hard-collinear scale. As soon as one is concerned about the soft function itself, however, it should be considered as a complex function with certain analytic properties, and one is not allowed to apply any simplifying identities.

Coming back to the anomalous dimension (9.90), we can now replace

$$\frac{\alpha_s}{\pi} \Delta \Gamma_G \rightarrow -\frac{\alpha_s C_A}{\pi} i\pi \delta(\omega - \omega') \delta(\omega_1 - \omega'_1), \quad (9.94)$$

which allows us to write

$$\Gamma_G(\omega, \omega_1, \omega', \omega'_1; \mu) = \frac{\alpha_s}{\pi} \left\{ C_F \delta(\omega_1 - \omega'_1) \Gamma_n(\omega, \omega'; \mu) + C_A \delta(\omega - \omega') \Gamma_{\bar{n}}(\omega_1, \omega'_1; \mu) \right\}, \quad (9.95)$$

as one would naively expect from factorisation in SCET. The individual  $\mathcal{O}(\alpha_s)$  anomalous dimensions in the two collinear sectors read

$$\Gamma_n(\omega, \omega'; \mu) = \frac{1}{2} \left( \ln \frac{\mu^2}{\omega^2} - 1 \right) \delta(\omega - \omega') - \text{Re} H_+(\omega, \omega'), \quad (9.96)$$

$$\begin{aligned} \Gamma_{\bar{n}}(\omega_1, \omega'_1; \mu) &= \frac{1}{2} \left( \ln \frac{\mu^2}{\omega_1^2} - i\pi \right) \delta(\omega_1 - \omega'_1) - \text{Re} H_+(\omega_1, \omega'_1) \\ &\quad + \frac{\omega_1}{(\omega'_1)^2} [\theta(\omega_1) \theta(\omega'_1 - \omega_1) - \theta(-\omega_1) \theta(\omega_1 - \omega'_1)], \end{aligned} \quad (9.97)$$

and again one can solve two separate RG equations related to the two variables  $\omega$  and  $\omega_1$ , respectively.

### 9.3.2 Solution to the “Reduced” RG Equation

The derivation of the solutions to these “reduced” RG equations for the Abelian and the non-Abelian part is very similar. In the following we present some details on the latter case, for which we follow the same procedure as in the previous section, but we quote the complete result for the evolution functions below. Performing the usual split into a positive-support and negative-support branch yields the Mellin-space equations

$$\begin{aligned} \left( \frac{d}{d \ln \mu} - \eta_1 \right) \tilde{\Phi}_G^>(\omega, \eta_1; \mu) &= \frac{\alpha_s C_A}{\pi} \left[ -H_{1-\eta_1} - H_{\eta_1} - \partial_{\eta_1} + \frac{i\pi}{2} \right] \tilde{\Phi}_G^>(\omega, \eta_1; \mu) \\ &\quad + \frac{\alpha_s C_A}{\pi} \Gamma(-\eta_1) \Gamma(1 + \eta_1) \tilde{\Phi}_G^<(\omega, \eta_1; \mu), \\ \left( \frac{d}{d \ln \mu} - \eta_1 \right) \tilde{\Phi}_G^<(\omega, \eta_1; \mu) &= \frac{\alpha_s C_A}{\pi} \left[ -H_{-1-\eta_1} - H_{1-\eta_1} - \partial_{\eta_1} + \frac{i\pi}{2} \right] \tilde{\Phi}_G^<(\omega, \eta_1; \mu), \end{aligned} \quad (9.98)$$

which again hold for  $-1 < \text{Re}(\eta_1) < 0$ . Notably, the equation for the negative-support branch is diagonal, because the anomalous dimension  $\Gamma_{\bar{n}}(\omega_1, \omega'_1; \mu)$  in (9.96) does not contain a respective mixing piece, which would arise for example from an  $H_-$  distribution. This implies that a function with no negative support at the scale  $\mu_0$  does *not* develop support for negative  $\omega_1$  through scale evolution, which can already be seen from (9.96) by noting that the distribution  $H_+$  reduces to the standard Lange-Neubert kernel [217],

$$H_+(\omega, \omega') \rightarrow F(\omega, \omega') = \omega \left[ \frac{\theta(\omega' - \omega)}{\omega'(\omega' - \omega)} \right]_+ + \left[ \frac{\theta(\omega - \omega')}{\omega - \omega'} \right]_+, \quad \text{for } \omega, \omega' > 0. \quad (9.99)$$

The solution for  $\tilde{\Phi}_G^<(\omega, \eta_1; \mu)$  can be obtained straightforwardly and reads

$$\tilde{\Phi}_G^<(\omega, \eta_1; \mu) = e^{V_G + 2\gamma_E a_1} \left( \frac{\mu}{\mu_0} \right)^{\eta_1} \frac{\Gamma(-\eta_1)\Gamma(2 - \eta_1)}{\Gamma(-\eta_1 - a_1)\Gamma(2 - \eta_1 - a_1)} \tilde{\Phi}_G^<(\omega, \eta_1 + a_1; \mu_0), \quad (9.100)$$

where  $a_1$  is defined in (9.70) and the evolution factor

$$V_G(\mu, \mu_0) = - \int_{\mu_0}^{\mu} \frac{d\mu'}{\mu'} \frac{\alpha_s(\mu') C_A}{\pi} \left[ \ln \frac{\mu'}{\mu_0} - \frac{i\pi}{2} \right], \quad (9.101)$$

differs from the definition of  $V_1$  in (9.70) due to the presence of the imaginary part  $-i\pi/2$  in the square brackets. The system (9.98) can be diagonalized using the following linear combination as the second independent function,

$$\tilde{\Phi}_G(\omega, \eta_1; \mu) \equiv \int_{-\infty}^{+\infty} \frac{d\omega_1}{\omega_1 - i0} \left( \frac{\mu}{\omega_1 - i0} \right)^{\eta_1} \Phi_G(\omega, \omega_1; \mu) = \tilde{\Phi}_G^>(\omega, \eta_1; \mu) - \tilde{\Phi}_G^<(\omega, \eta_1; \mu) e^{i\pi\eta_1}, \quad (9.102)$$

which is solved by

$$\tilde{\Phi}_G(\omega, \eta_1; \mu) = e^{V_G + 2\gamma_E a_1} \left( \frac{\mu}{\mu_0} \right)^{\eta_1} \frac{\Gamma(2 - \eta_1)\Gamma(1 + \eta_1 + a_1)}{\Gamma(1 + \eta_1)\Gamma(2 - \eta_1 - a_1)} \tilde{\Phi}_G(\omega, \eta_1 + a_1; \mu_0). \quad (9.103)$$

Performing the inverse Mellin transform, the momentum-space evolution functions can again be expressed in terms of Meijer-G functions. Including also the Abelian piece, the solution to the RG-equation for  $\Phi_G$  – restricted to the function space of relevant jet functions – then reads

$$\Phi_G(\omega, \omega_1; \mu) = \int \frac{d\omega'}{\omega'} \int \frac{d\omega'_1}{\omega'_1} U_n^{(G)}(\omega, \omega'; \mu, \mu_0) U_{\bar{n}}^{(G)}(\omega_1, \omega'_1; \mu, \mu_0) \Phi_G(\omega', \omega'_1; \mu_0). \quad (9.104)$$

The evolution functions are

$$U_n^{(G)}(\omega, \omega'; \mu, \mu_0) = -e^{V + 2\gamma_E a} \left( \frac{\mu_0}{\omega' - i0} \right)^a \left[ \theta(-\omega') e^{-i\pi a} G_{2,2}^{2,0} \left( \begin{matrix} -a, 1-a \\ 1, 0 \end{matrix} \middle| \frac{\omega}{\omega'} \right) - \theta(\omega) G_{2,2}^{1,1} \left( \begin{matrix} -a, 1-a \\ 1, 0 \end{matrix} \middle| \frac{\omega}{\omega'} \right) \right], \quad (9.105)$$

with  $V = V(\mu, \mu_0)$  and  $a = a(\mu, \mu_0)$  defined in (9.60), and

$$U_{\bar{n}}^{(G)}(\omega_1, \omega'_1; \mu, \mu_0) = -e^{V_G + 2\gamma_E a_1} \left( \frac{\mu_0}{\omega'_1 - i0} \right)^{a_1} \left[ \theta(-\omega'_1) e^{-i\pi a_1} G_{2,2}^{2,0} \left( \begin{matrix} -a_1, 2-a_1 \\ 2, 0 \end{matrix} \middle| \frac{\omega_1}{\omega'_1} \right) \right]$$

$$-\theta(\omega_1)G_{2,2}^{1,1}\left(\begin{matrix} -a_1, 2-a_1 \\ 2, 0 \end{matrix} \middle| \frac{\omega_1}{\omega'_1}\right)]. \quad (9.106)$$

Again, the Meijer-G functions can be reduced to hypergeometric functions in certain integration domains. For  $\omega/\omega' > -1$  the identity

$$G_{2,2}^{1,1}\left(\begin{matrix} -x, \alpha-x \\ \alpha, 0 \end{matrix} \middle| \frac{\omega}{\omega'}\right) = \frac{\Gamma(1+x+\alpha)}{\Gamma(-x)\Gamma(1+\alpha)} \left(\frac{\min(\omega, \omega')}{\max(\omega, \omega')}\right)^\alpha \left(\frac{\omega'}{\max(\omega, \omega')}\right)^{x+1-\alpha} \\ \times {}_2F_1\left(x+1, x+1+\alpha; \alpha+1; \frac{\min(\omega, \omega')}{\max(\omega, \omega')}\right) \quad (9.107)$$

holds, where an implicit  $+i0$  prescription is understood in the brackets of the first line. The second appearing Meier-G function vanishes for  $|\omega/\omega'| > 1$ ,

$$G_{2,2}^{2,0}\left(\begin{matrix} -x, \alpha-x \\ \alpha, 0 \end{matrix} \middle| \frac{\omega}{\omega'}\right) = 0. \quad (9.108)$$

### 9.3.3 Phenomenological Implications

We now consider the special case where  $\Phi_G(\omega, \omega_1, \mu_0) \sim \theta(\omega)\theta(\omega_1)$  at the low scale  $\mu_0$ . The solution to the “reduced” RG-equation then simplifies to

$$\Phi_G(\omega, \omega_1; \mu) = \theta(\omega)e^{V+2\gamma_E a} \int_0^\infty \frac{d\omega'}{\omega'} \left(\frac{\mu_0}{\omega'}\right)^a G_{2,2}^{1,1}\left(\begin{matrix} -a, 1-a \\ 1, 0 \end{matrix} \middle| \frac{\omega}{\omega'}\right) \\ \times \theta(\omega_1)e^{V_G+2\gamma_E a_1} \int_0^\infty \frac{d\omega'_1}{\omega'_1} \left(\frac{\mu_0}{\omega'_1}\right)^{a_1} G_{2,2}^{1,1}\left(\begin{matrix} -a_1, 2-a_1 \\ 2, 0 \end{matrix} \middle| \frac{\omega_1}{\omega'_1}\right) \Phi_G(\omega', \omega'_1; \mu_0), \quad (9.109)$$

and, since all variables are positive, we can substitute the Meijer-G functions using the identity (9.107).

The solution in the Abelian limit then corresponds to the well-known solution of the Lange-Neubert kernel for the leading-twist  $B$ -meson distribution amplitude [213], and takes a similar form for the non-Abelian piece, but with the parameter  $\alpha = 2$  in (9.107). This in particular implies that  $\Phi_G(\omega, \omega_1; \mu)$  falls off linearly in  $\omega$ , but quadratically  $\omega_1$  for small values,

$$\Phi_G(\omega, \omega_1; \mu) \sim \omega\omega_1^2, \quad \text{for small } \omega, \omega_1. \quad (9.110)$$

For large arguments, on the other hand, the function behaves as  $\sim \omega_1^{-a_1 - \min(1, \xi_1)}$  for  $\omega_1 \rightarrow \infty$ , and as  $\sim \omega^{-a - \min(1, \xi)}$  for  $\omega \rightarrow \infty$ , if the initial function falls off power-like with exponents  $\xi_1$  and  $\xi$ . Hence, convolution integrals in factorisation theorems again converge as long as the  $\mu$  is not chosen to be unphysically large. Interestingly, due to the factorisation of the two light-cone directions in (9.95), the asymptotic behavior for small momenta is consistent with the conformal spins of the light-quark and gluon fields [219] (see also [220]) that appear in the operator (9.88). Although this is merely an observation at this point, a connection between the conformal spin of the fields and the asymptotic behavior for such multi-light-cone soft functions would be important for studying the convergence of convolution integrals. As such soft functions will become relevant in a variety of inclusive and exclusive processes at next-to-leading power, a more rigorous understanding of this feature would be important.

As a concrete example, we study the same simple exponential model that was used in [212],

$$\Phi_G^{\text{exp}}(\omega, \omega_1, \mu_0) = \frac{\lambda_E^2 + \lambda_H^2}{6} \frac{\omega\omega_1^2}{\omega_0^5} e^{-\frac{\omega+\omega_1}{\omega_0}} \theta(\omega)\theta(\omega_1), \quad (9.111)$$

where the hadronic quantities  $\lambda_E$  and  $\lambda_H$  parametrize hadronic matrix elements of the chromo-electric and chromo-magnetic fields, respectively [221]. In particular, as the dependence on  $\omega$  and  $\omega_1$  factorizes, we can also express the function at the scale  $\mu > \mu_0$  as a product of functions that only depend on either one of the two variables. The integrals can easily be performed analytically, and result in

$$\begin{aligned} \Phi_G^{\text{exp}}(\omega, \omega_1, \mu) &= \theta(\omega) \frac{\lambda_E^2 + \lambda_H^2}{6\omega_0^2} \frac{\omega}{\omega_0} e^{V+2\gamma_E a} \left(\frac{\mu_0}{\omega_0}\right)^a \Gamma(2+a) {}_1F_1\left(2+a; 2; -\frac{\omega}{\omega_0}\right) \\ &\times \theta(\omega_1) \frac{\omega_1^2}{2\omega_0^2} e^{V_G+2\gamma_E a_1} \left(\frac{\mu_0}{\omega_0}\right)^{a_1} \Gamma(3+a_1) {}_1F_1\left(3+a_1; 3; -\frac{\omega_1}{\omega_0}\right). \end{aligned} \quad (9.112)$$

Importantly, inverse moments of the form

$$\int_{-\infty}^{+\infty} \frac{d\omega}{\omega - i0} \int_{-\infty}^{+\infty} \frac{d\omega_1}{\omega_1 - i0} \Phi_G(\omega, \omega_1; \mu) \quad (9.113)$$

are no longer integrated over the poles at  $\omega = 0$  or  $\omega_1 = 0$ , respectively. Thus, the convolution integrals do no longer give rise to complex phases. As a cross check of the “reduced” RG evolution, for which the integrations can be performed analytically, we have explicitly verified that the expression for the evolved function in (9.112) leads to the same double inverse moment as the result provided in [212] using the full anomalous dimension,

$$\begin{aligned} \int_0^\infty \frac{d\omega}{\omega} \int_0^\infty \frac{d\omega_1}{\omega_1} \Phi_G(\omega, \omega_1; \mu) &= \int_{-\infty}^{+\infty} \frac{d\omega}{\omega - i0} \int_{-\infty}^{+\infty} \frac{d\omega_1}{\omega_1 - i0} \Phi_G^{[212]}(\omega, \omega_1; \mu) \\ &= \frac{\lambda_E^2 + \lambda_H^2}{6\omega_0^2} e^{V_G+V+2\gamma_E(a_1+a)} \left(\frac{\mu_0}{\omega_0}\right)^{a_1+a} \Gamma(1+a_1)\Gamma(1+a). \end{aligned} \quad (9.114)$$

Lastly, we again verify our analytic solution numerically through discretisation of the momentum-space RG equation in Figure 9.7. To do so, we define a function  $\phi(\omega_1; \mu)$  that fulfills a RG equation with anomalous dimension

$$\frac{\alpha_s C_A}{\pi} \left( \frac{1}{2} \ln \frac{\mu^2}{\omega_1^2} \delta(\omega_1 - \omega'_1) - \text{Re} H_+(\omega_1, \omega'_1) + \frac{\omega_1}{(\omega'_1)^2} [\theta(\omega_1)\theta(\omega'_1 - \omega_1) - \theta(-\omega_1)\theta(\omega_1 - \omega'_1)] \right), \quad (9.115)$$

that corresponds to  $\Gamma_{\bar{n}}(\omega_1, \omega'_1; \mu)$  up to a local complex phase which can be factored out. We choose

$$\phi(\omega_1, \mu_0) = \theta(\omega_1) \frac{\omega_1^2}{\omega_0^2} e^{-\frac{\omega_1}{\omega_0}} \quad (9.116)$$

as an initial condition, such that its analytic expression at the scale  $\mu$  precisely results in the second line of (9.112), but with  $V_G$  replaced by its real part.

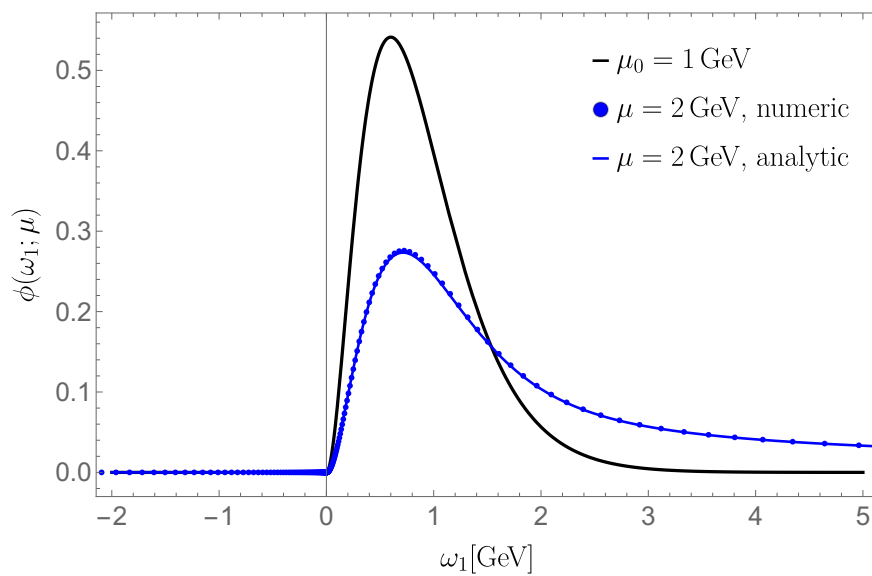


**Figure 9.7:** Scale evolution of the function  $\phi(\omega_1; \mu)$ , using the exponential model (9.116) with  $\omega_0 = 0.3$  GeV at the low scale  $\mu_0 = 1$  GeV (black curve). The blue curve shows the analytic solution for  $\mu = 2$  GeV, which again is in good agreement with the numeric solution from discretisation of the momentum-space RG equation (blue dots). Details on the discretisation and the strong coupling constant are explained in the caption of Figure 9.5.



# Chapter 10

## The $\bar{n}$ -Jet Function at NLO

### Contents

---

<b>10.1 The <math>\bar{n}</math>-Jet Function at One Loop . . . . .</b>	<b>107</b>
<b>10.2 The <math>\bar{n}</math>-Jet Function at Two Loops . . . . .</b>	<b>116</b>
<b>10.3 Full <math>u</math>-Dependence of the <math>\bar{n}</math>-Jet Function at NLO . . . . .</b>	<b>124</b>

---

In this chapter, we compute the  $\bar{n}$ -jet function that enters the factorisation formula (8.6) at NLO. We define this function via matching (see, e.g., the discussion in [222]) and can thus be extracted from the anti-hard-collinear momentum region of the partonic decay amplitude

$$b(m_b v) \rightarrow s(E_X n) \gamma(E_\gamma \bar{n}) g\left(\frac{\omega_1}{2} n\right), \quad (10.1)$$

induced by the operator  $Q_1^q$ . To this end, we evaluate the  $\mathcal{O}(\alpha_s)$  corrections to this amplitude, isolating the contribution from the anti-hard-collinear region. At LO, we provide results for both a massless up-quark ( $q = u$ ) and a massive charm-quark ( $q = c$ ) propagating in the loop, while for the NLO (two-loop) calculation we focus on the case where only a massless quark propagates in the loop, corresponding to the operator  $Q_1^u$  rather than the charm-quark contribution. A complete phenomenological analysis would require incorporating charm-quark mass effects, which we defer to future work. Nevertheless, since the  $m_c \rightarrow 0$  limit is smooth, the massless case already reproduces all the  $1/\epsilon$  divergences. This makes it sufficient for demonstrating the cancellation of poles among the four functions entering the factorisation formula, thereby providing a non-trivial cross-check of both the factorisation framework and the computations presented in Part II of this thesis.

### 10.1 The $\bar{n}$ -Jet Function at One Loop

The starting point of our analysis is the evaluation of the aforementioned  $b \rightarrow s\gamma g$  amplitude at leading order. Since the operator  $Q_1^q$  is a four-quark operator, the LO amplitude arises from a one-loop diagram, while the NLO correction corresponds to a two-loop contribution. A crucial observation, valid only at LO, is that this amplitude receives contributions exclusively from a single momentum region, specifically the anti-hard-collinear region. As a result, no additional expansion in momentum regions is necessary, and the diagram can be computed directly within this regime.

We first compute the contribution from a massless up quark, carrying electric charge  $Q_u$ , circulating in the loop. Subsequently, we include the effects of the charm-quark mass.

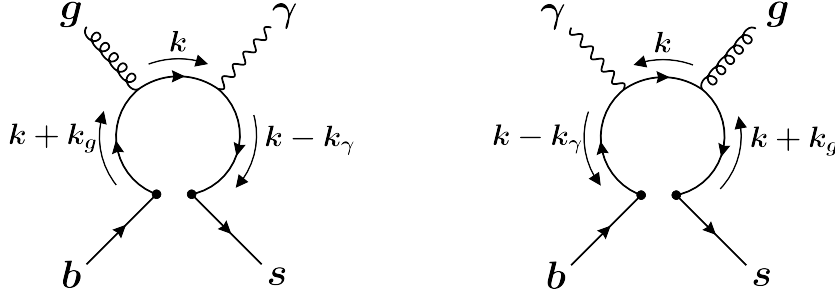


**Figure 10.1:** LO diagrams contributing to the  $b \rightarrow s\gamma g$  amplitude. The loop contains either a charm quark or an up quark. The two diagrams differ by the interchange of the gluon and photon emission vertices.

Moreover, in this section, we compute the dependence on the anti-hard collinear momentum fraction  $u$ , introduced in the factorisation formula (8.6), at one-loop both for the massless and massive case, presenting the basis for the two-loop computation.

More in general, this section does not only provide results for the LO amplitudes but lays out the computational framework and technical tools that will also be employed throughout the remainder of Part II to evaluate the two-loop amplitudes.

### 10.1.1 Massless Amplitude at LO

The diagrams contributing at leading order are shown in Figure 10.1. In the massless  $u$ -quark case, the corresponding amplitudes in dimensional regularisation, with  $D = 4 - 2\epsilon$ , are given for the first and second diagrams respectively by:

$$\begin{aligned} \mathcal{A}_{\text{LO}}^{(1),u}(b \rightarrow s\gamma g) &= \tilde{\mu}^{2\epsilon} \int \frac{d^D k}{(2\pi)^D} \bar{u}_{hc,L}^{(s)} \gamma^\mu i \frac{\not{k} - \not{k}_\gamma}{(k - k_\gamma)^2 + i0} i Q_u \not{\epsilon}_\perp^*(k_\gamma) i \frac{\not{k}}{k^2 + i0} \\ &\quad \times i g_s \not{\epsilon}_{s,\perp}^*(k_g) i \frac{\not{k} + \not{k}_g}{(k + k_g)^2 + i0} \gamma_\mu b_L, \end{aligned} \quad (10.2)$$

$$\begin{aligned} \mathcal{A}_{\text{LO}}^{(2),u}(b \rightarrow s\gamma g) &= -\tilde{\mu}^{2\epsilon} \int \frac{d^D k}{(2\pi)^D} \bar{u}_{hc,L}^{(s)} \gamma^\mu i \frac{\not{k} + \not{k}_g}{(k + k_g)^2 + i0} i g_s \not{\epsilon}_{s,\perp}^*(k_g) i \frac{\not{k}}{k^2 + i0} \\ &\quad \times i Q_u \not{\epsilon}_\perp^*(k_\gamma) i \frac{\not{k} - \not{k}_\gamma}{(k - k_\gamma)^2 + i0} \gamma_\mu b_L. \end{aligned} \quad (10.3)$$

Here,  $\bar{u}_{hc,L}^{(s)}$  and  $b_L$  are the spinors for the left-handed collinear strange quark and the bottom quark, respectively. The polarisation vectors  $\epsilon_\perp^*(k_\gamma)$  and  $\epsilon_{s,\perp}^*(k_g) = t^a \epsilon_{s,\perp}^{a*}(k_g)$  correspond to the photon and the soft gluon, respectively. Since both the photon and the gluon are on-shell, we assume their polarisations are transverse to  $n^\mu$  and  $\bar{n}^\mu$ . The gluon and photon momenta are given by  $k_g^\mu = \omega_1 \frac{\bar{n}^\mu}{2}$  and  $k_\gamma^\mu = E_\gamma \bar{n}^\mu$ , while the loop momentum can be decomposed as  $k^\mu = k_+ \frac{\bar{n}^\mu}{2} + k_- \frac{n^\mu}{2} + k_\perp^\mu$ . The dimensional regularisation scale is defined as in the  $\overline{\text{MS}}$  scheme as  $\tilde{\mu}^{2\epsilon} = (4\pi)^{-\epsilon} e^{\gamma_E \epsilon} \mu^{2\epsilon}$ , where  $\gamma_E$  is the Euler-Mascheroni constant.

Since the one-loop integrals are manageable, we illustrate various strategies to evaluate them, which will prove useful later in the two-loop calculations.

For the amplitudes in equations (10.2) and (10.3), we proceed by expanding the numerator in the anti-hard-collinear limit. Even though only one region contributes, as stated

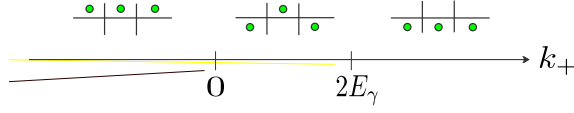


**Figure 10.2:** Location of poles related to the integral in (10.7). Green dots denote poles located in the upper or lower complex half-plane. The order of the denominators matches that in Equation (10.7).

previously, expanding the numerator helps simplify the expressions. The momentum scaling relevant for this region is:

$$\begin{aligned} k_g &\sim (\lambda^2, \lambda^2, \lambda^2) && \text{soft} \\ k_\gamma &\sim (\lambda^2, \lambda, 1) && \bar{h}c \\ k &\sim (\lambda^2, \lambda, 1) && \bar{h}c \end{aligned} \quad (10.4)$$

Retaining only the leading terms in the two amplitudes, we obtain:

$$\begin{aligned} \mathcal{A}_{\text{LO}}^u(b \rightarrow s\gamma g) &= \mathcal{A}_{\text{LO}}^{(1),u}(b \rightarrow s\gamma g) + \mathcal{A}_{\text{LO}}^{(2),u}(b \rightarrow s\gamma g) \\ &= i2(1 + \varepsilon)\tilde{\mu}^{2\varepsilon} g_s Q_u \bar{u}_{hc,L}^{(s)} \left[ \not{\epsilon}_\perp^*(k_\gamma), \not{\epsilon}_{s,\perp}^*(k_g) \right] \frac{\not{h}}{2} b_L I_{\text{LO}}^u, \end{aligned} \quad (10.5)$$

where  $I_{\text{LO}}^u$  is the scalar integral:

$$I_{\text{LO}}^u = \int \frac{d^D k}{(2\pi)^D} \frac{(k_+ - 2E_\gamma) \left( \frac{\varepsilon}{1-\varepsilon} k_\perp^2 - k_+ k_- \right) - \frac{k_+ k_\perp^2}{1-\varepsilon}}{(k^2 + i0) \left[ (k - k_\gamma)^2 + i0 \right] \left[ (k + k_g)^2 + i0 \right]}. \quad (10.6)$$

This integral is instructive for similar one-loop calculations and provides a basis for the two-loop case. We now show the full derivation.

The first step involves applying the residue theorem. To do this, we study the pole structure of the integrand. Expressing the integration measure in light-cone coordinates and expanding the denominators, we rewrite the integral as:

$$I_{\text{LO}}^u = \frac{1}{2} \int \frac{dk_+ dk_- dk_\perp^{D-2}}{(2\pi)^D} \frac{(k_+ - 2E_\gamma) \left( \frac{\varepsilon}{1-\varepsilon} k_\perp^2 - k_+ k_- \right) - \frac{k_+ k_\perp^2}{1-\varepsilon}}{k_+^2 (k_+ - 2E_\gamma) \left( k_- + \frac{k_\perp^2 + i0}{k_+} \right) \left( k_- + \frac{k_\perp^2 + i0}{k_+ - 2E_\gamma} \right) \left( k_- + \omega_1 + \frac{k_\perp^2 + i0}{k_+} \right)}. \quad (10.7)$$

We begin by evaluating the  $k_-$  integral. The location of the poles depends on the sign of  $k_+$  and whether  $k_+ < 2E_\gamma$  or  $k_+ > 2E_\gamma$ . Figure 10.2 shows which poles lie above or below the real axis for different values of  $k_+$ . We observe that the integrand vanishes for  $k_+ < 0$  and  $k_+ > 2E_\gamma$ , so only the range  $0 < k_+ < 2E_\gamma$  contributes.

We close the contour in the upper plane picking the residue corresponding to the second propagator and obtain:

$$I_{\text{LO}}^u = i\pi \int_0^{2E_\gamma} dk_+ \int \frac{dk_\perp^{D-2}}{(2\pi)^D} \frac{2 \frac{\varepsilon}{\varepsilon-1} E_\gamma (k_+ - 2E_\gamma) k_\perp^2}{(-2E_\gamma k_\perp^2) [-2E_\gamma k_\perp^2 + \omega_1 k_+ (k_+ - 2E_\gamma)]}. \quad (10.8)$$

To evaluate the perpendicular integral, we change variables to  $x = -k_\perp^2 > 0$ , leading to:

$$\int \frac{dk_\perp^{D-2}}{(2\pi)^{4-2\varepsilon}} \rightarrow \int_0^\infty dx \frac{x^{-\varepsilon}}{\Gamma(1-\varepsilon) 4^{2-\varepsilon} \pi^{3-\varepsilon}}. \quad (10.9)$$

We also rescale the variables as  $k = \frac{k_+}{2E_\gamma}$  and  $x' = \frac{x}{k(1-k)2E_\gamma} > 0$ , which gives a factorised expression that can be straightforwardly computed:

$$\begin{aligned} I_{\text{LO}}^u &= -\frac{i}{(4\pi)^{2-\varepsilon}} (2E_\gamma)^{1-\varepsilon} \frac{\varepsilon}{\Gamma(2-\varepsilon)} \int_0^1 dk k^{-\varepsilon} (1-k)^{1-\varepsilon} \int_0^\infty \frac{x^{-\varepsilon}}{x-\omega_1} \\ &= -\frac{i}{(4\pi)^{2-\varepsilon}} E_\gamma (-2E_\gamma \omega_1)^{-\varepsilon} \frac{\Gamma(1+\varepsilon)\Gamma(1-\varepsilon)^2}{(1-\varepsilon)\Gamma(2-2\varepsilon)}. \end{aligned} \quad (10.10)$$

Putting everything together, we find the final result for the massless one-loop amplitude:

$$\begin{aligned} \mathcal{A}_{\text{LO}}^u(b \rightarrow s\gamma g) &= \frac{g_s Q_u E_\gamma}{8\pi^2} \left( \frac{-2E_\gamma \omega_1}{\mu^2} \right)^{-\varepsilon} e^{\gamma_E \varepsilon} (1+\varepsilon) \frac{\Gamma(1+\varepsilon)\Gamma(1-\varepsilon)^2}{(1-\varepsilon)\Gamma(2-2\varepsilon)} \\ &\quad \times \bar{u}_{hc,L}^{(s)} \left[ \not{\epsilon}_\perp^*(k_\gamma), \not{\epsilon}_{s,\perp}^*(k_g) \right] \frac{\not{h}}{2} b_L. \end{aligned} \quad (10.11)$$

Note the commutator structure of the polarisation vectors, which arises from the exchange of photon and gluon in the two diagrams. This same structure is expected to appear in the two-loop calculation. Furthermore, as seen from Equation (10.10), the dependence on  $E_\gamma$  and  $\omega_1$  factorises completely. This holds generally and can be deduced from dimensional analysis of the initial loop integral. In particular, the expression includes the combination  $\left( \frac{-2E_\gamma \omega_1}{\mu^2} \right)^{-\varepsilon}$ , where the minus sign, also expected at NLO, ensures the correct imaginary part, which will prove crucial for the cancellation of poles at the end of Part II. Lastly, we note that the amplitude is finite at one loop and expanding in the dimensional regulator we get:

$$\mathcal{A}_{\text{LO}}^u(b \rightarrow s\gamma g) = \frac{g_s Q_u E_\gamma}{8\pi^2} \bar{u}_{hc,L}^{(s)} \left[ \not{\epsilon}_\perp^*(k_\gamma), \not{\epsilon}_{s,\perp}^*(k_g) \right] \frac{\not{h}}{2} b_L. \quad (10.12)$$

For illustration purpose we proceed evaluating again the same amplitude but using a more systematic and automatised method which can be used to tackle the computation at two loops in an easier way.

Loop amplitudes in quantum field theory involves integrals with complex numerator structures arising from gamma matrix contractions. The first step in simplifying such integrals is to reduce the Dirac structure appearing in the numerator. This is achieved by expressing all spinor and Lorentz structures in terms of a minimal basis of independent tensors or scalar products, using standard gamma matrix identities and, when appropriate, exploiting the equations of motion. We perform this first simplification of the Dirac structures using the Mathematica package `FeynCalc` [223–226] in its development version 10.1.0. Once the Dirac structure is reduced, the remaining loop integrals consist of scalar numerator terms over a set of propagators. These integrals can be systematically simplified using *integration-by-parts* (IBP) identities [227, 228], which relate different integrals through total derivative relations in dimensional regularisation. This method allows one to express all integrals in terms of a finite set of linearly independent integrals, known as master integrals (MIs). We perform the IBP reduction via the package `FIRE6` [229] supported also by the package `LiteRed` [230] for identifying additional symmetries. Once the full amplitude is expressed in terms of this minimal set of master integrals, one can proceed to evaluate them using techniques such as direct integration or using the differential equation method [231–234]. We adopt the first strategy now and illustrate the second one later in this section.

The amplitudes in (10.2) and (10.3) can be reduced using the aforementioned procedure to

$$\mathcal{A}_{\text{LO}}^u(b \rightarrow s\gamma g) = \tilde{\mu}^{2\varepsilon} i g_s Q_u E_\gamma \frac{2\varepsilon(\varepsilon+1)}{\varepsilon-1} G_{011}^A \bar{u}_{hc,L}^{(s)} \left[ \not{\epsilon}_\perp^*(k_\gamma), \not{\epsilon}_{s,\perp}^*(k_g) \right] \frac{\not{h}}{2} b_L, \quad (10.13)$$

where  $G_{011}^A$  is a master integral given by

$$G_{011}^A = \int \frac{d^D k}{(2\pi)^D} \frac{1}{\left[ (k+k_g)^2 + i0 \right] \left[ (k-k_\gamma)^2 + i0 \right]}, \quad (10.14)$$

related to the propagator topology  $A$  defined as

$$A = \left\{ \frac{1}{k^2 + i0}, \frac{1}{(k+k_g)^2 + i0}, \frac{1}{(k-k_\gamma)^2 + i0} \right\}, \quad (10.15)$$

with 0 and 1 representing powers of the propagators in the same order as in (10.15). The master integral is straightforward to compute and gives

$$G_{011}^A = i \frac{(-2E_\gamma \omega_1)^{-\varepsilon} \Gamma(1-\varepsilon)^2 \Gamma(\varepsilon)}{(4\pi)^{2-\varepsilon} \Gamma(2-2\varepsilon)}. \quad (10.16)$$

Substituting this result into (10.13) we reproduce the result we provided in (10.11).

Finally, for completeness and later convenience, we also give the result for the master integral

$$G_{111}^A = i \frac{(-2E_\gamma \omega_1)^{-1-\varepsilon} \Gamma(1-\varepsilon) \Gamma(\varepsilon) \Gamma(-\varepsilon)}{(4\pi)^{2-\varepsilon} \Gamma(1-2\varepsilon)}. \quad (10.17)$$

### 10.1.2 Massive Amplitude at LO

We now recompute the two diagrams shown in Figure 10.1, this time including the effects of a charm quark with electric charge  $Q_c$  in the loop. This introduces a non-zero mass  $m_c$  in the fermion propagators. The resulting one-loop amplitudes are given by:

$$\begin{aligned} \mathcal{A}_{\text{LO}}^{(1),c}(b \rightarrow s\gamma g) &= \tilde{\mu}^{2\varepsilon} \int \frac{d^D k}{(2\pi)^D} \bar{u}_{hc,L}^{(s)} \gamma^\mu i \frac{\not{k} - \not{k}_\gamma + m_c}{(k-k_\gamma)^2 - m_c^2 + i0} i Q_c \not{\epsilon}_\perp^*(k_\gamma) i \frac{\not{k} + m_c}{k^2 - m_c^2 + i0} \\ &\quad \times i g_s \not{\epsilon}_{s,\perp}^*(k_g) i \frac{\not{k} + \not{k}_g + m_c}{(k+k_g)^2 - m_c^2 + i0} \gamma_\mu b_L, \end{aligned} \quad (10.18)$$

$$\begin{aligned} \mathcal{A}_{\text{LO}}^{(2),c}(b \rightarrow s\gamma g) &= -\tilde{\mu}^{2\varepsilon} \int \frac{d^D k}{(2\pi)^D} \bar{u}_{hc,L}^{(s)} \gamma^\mu i \frac{\not{k} + \not{k}_g + m_c}{(k+k_g)^2 - m_c^2 + i0} i g_s \not{\epsilon}_{s,\perp}^*(k_g) i \frac{\not{k} + m_c}{k^2 - m_c^2 + i0} \\ &\quad \times i Q_c \not{\epsilon}_\perp^*(k_\gamma) i \frac{\not{k} - \not{k}_\gamma + m_c}{(k-k_\gamma)^2 - m_c^2 + i0} \gamma_\mu b_L. \end{aligned} \quad (10.19)$$

Simplifying the numerator and performing the IBP reduction, we obtain the total amplitude

$$\begin{aligned} \mathcal{A}_{\text{LO}}^c(b \rightarrow s\gamma g) &= i \tilde{\mu}^{2\varepsilon} g_s Q_c \bar{u}_{hc,L}^{(s)} \left[ E_\gamma \frac{1+\varepsilon}{\varepsilon-1} \left( \varepsilon G_{011}^{A,m_c} + 2m_c^2 G_{111}^{A,m_c} \right) \left[ \not{\epsilon}_\perp^*(k_\gamma), \not{\epsilon}_{s,\perp}^*(k_g) \right] \not{\eta} \right. \\ &\quad \left. + 2\varepsilon m_c \not{\epsilon}_\perp^*(k_\gamma) \cdot \not{\epsilon}_{s,\perp}^*(k_g) \left( 4E_\gamma \omega_1 G_{111}^{A,m_c} + 2G_{011}^{A,m_c} - E_\gamma \omega_1 G_{111}^{A,m_c} \not{\eta} \not{\eta} \right) \right. \\ &\quad \left. - 4\varepsilon m_c \left( E_\gamma \omega_1 G_{111}^{A,m_c} + G_{011}^{A,m_c} \right) \not{\epsilon}_{s,\perp}^*(k_g) \not{\epsilon}_\perp^*(k_\gamma) \right] b_L, \end{aligned} \quad (10.20)$$

where the master integrals  $G^{A,m_c}$  correspond to the topology with the same propagators as in (10.15), but, in this case, with an additional mass  $m_c$ . We recognise the same commutator structure as in the one-loop amplitude, along with additional Dirac structures. However, recalling the scalings  $E_\gamma \sim 1$ ,  $\omega_1 \sim \lambda^2$ , and  $m_c \sim \lambda$ , we note that these additional structures are subleading and can be neglected, yielding

$$\begin{aligned} \mathcal{A}_{\text{LO}}^c(b \rightarrow s\gamma g) &= i\tilde{\mu}^{2\varepsilon} g_s Q_c \bar{u}_{hc,L}^{(s)} \left[ \not{\epsilon}_\perp^*(k_\gamma), \not{\epsilon}_{s,\perp}^*(k_g) \right] \not{q} b_L \\ &\times E_\gamma \frac{1+\varepsilon}{\varepsilon-1} \left( \varepsilon G_{011}^{A,m_c} + 2m_c^2 G_{111}^{A,m_c} \right). \end{aligned} \quad (10.21)$$

The results for the two master integrals expanded in the dimensional regulator  $\varepsilon$  read:

$$\begin{aligned} G_{011}^{A,m_c} &= \frac{i}{16\pi^2} \left\{ \frac{1}{\varepsilon} + \log\left(\frac{4\pi}{m_c^2}\right) - \gamma_E + 2 \right. \\ &\quad \left. + \sqrt{1 - \frac{2m_c^2}{E_\gamma\omega_1}} \log\left[ 1 - \frac{E_\gamma\omega_1}{m_c^2} \left( 1 - \sqrt{1 - \frac{2m_c^2}{E_\gamma\omega_1}} \right) \right] + \mathcal{O}(\varepsilon) \right\}, \quad (10.22) \\ G_{111}^{A,m_c} &= \frac{i}{64\pi^2} \frac{\log^2\left[ 1 - \frac{E_\gamma\omega_1}{m_c^2} \left( 1 - \sqrt{1 - \frac{2m_c^2}{E_\gamma\omega_1}} \right) \right]}{E_\gamma\omega_1} + \mathcal{O}(\varepsilon). \end{aligned}$$

Substituting these master-integral results into (10.21) we obtain

$$\begin{aligned} \mathcal{A}_{\text{LO}}^c(b \rightarrow s\gamma g) &= \frac{g_s Q_c E_\gamma}{8\pi^2} \left\{ \frac{m_c^2}{2E_\gamma\omega_1} \log^2\left[ 1 - \frac{E_\gamma\omega_1}{m_c^2} \left( 1 - \sqrt{1 - \frac{2m_c^2}{E_\gamma\omega_1}} \right) \right] + 1 \right\} \\ &\times \bar{u}_{hc,L}^{(s)} \left[ \not{\epsilon}_\perp^*(k_\gamma), \not{\epsilon}_{s,\perp}^*(k_g) \right] \frac{\not{q}}{2} b_L. \end{aligned} \quad (10.23)$$

In the previous expression, the limit  $m_c \rightarrow 0$  is smooth, and we reproduce the massless result in (10.11). However, in the massive case, the dependence on the momentum variables  $E_\gamma$  and  $\omega_1$  is no longer a simple power law and cannot be inferred solely by dimensional analysis. Additionally, by restoring the  $i0$  prescription and applying logarithmic-trigonometric identities, we can rewrite the result in (10.23) as

$$\mathcal{A}_{\text{LO}}^c(b \rightarrow s\gamma g) = \frac{g_s Q_c E_\gamma}{8\pi^2} \left[ 1 - F\left(\frac{m_c^2 - i0}{2E_\gamma\omega_1}\right) \right] \bar{u}_{hc,L}^{(s)} \left[ \not{\epsilon}_\perp^*(k_\gamma), \not{\epsilon}_{s,\perp}^*(k_g) \right] \frac{\not{q}}{2} b_L, \quad (10.24)$$

where  $F(x) = 4x \arctan^2\left(\frac{1}{\sqrt{4x-1}}\right)$  is the well-known penguin function [77].

### 10.1.3 Massless $u$ -Dependent Amplitude at LO

Up to now, we have analysed the  $b \rightarrow s\gamma g$  amplitude without considering its dependence on the momentum fraction  $u$ . The variable  $u$  describes how the large energy  $2E_\gamma \approx m_b$  is split between the quark and anti-quark in the loop. It is defined as the anti-hard-collinear momentum fraction flowing out of the four-quark vertex, as illustrated in Figure 10.3. The momenta in Figure 10.3 are assigned consistently with those in Figure 10.1. In particular, on the left diagram we identify  $u = \frac{k_+}{2E_\gamma}$ , while on the right diagram we use the complementary fraction  $\bar{u} \equiv 1 - u = \frac{k_+}{2E_\gamma}$ .

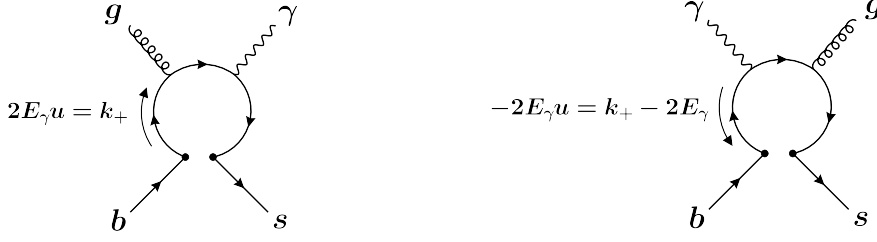


**Figure 10.3:** Schematic representation of the anti-hard-collinear momentum fraction  $u$ . The momentum assignments in both diagrams follow those of Figure 10.1.

The  $u$ -dependence is introduced by imposing these identifications via delta functions inside the amplitudes. We begin with the massless amplitudes, which read:

$$\begin{aligned} \mathcal{A}_{\text{LO}}^{(1),u}(u) &= \tilde{\mu}^{2\epsilon} \int \frac{d^D k}{(2\pi)^D} \bar{u}_{hc,L}^{(s)} \gamma^\mu i \frac{\not{k} - \not{k}_\gamma}{(k - k_\gamma)^2 + i0} i Q_u \not{\epsilon}_\perp^*(k_\gamma) i \frac{\not{k}}{k^2 + i0} \\ &\quad \times i g_s \not{\epsilon}_{s,\perp}^*(k_g) i \frac{\not{k} + \not{k}_g}{(k + k_g)^2 + i0} \gamma_\mu b_L \delta\left(u - \frac{k_+}{2E_\gamma}\right), \end{aligned} \quad (10.25)$$

$$\begin{aligned} \mathcal{A}_{\text{LO}}^{(2),u}(u) &= -\tilde{\mu}^{2\epsilon} \int \frac{d^D k}{(2\pi)^D} \bar{u}_{hc,L}^{(s)} \gamma^\mu i \frac{\not{k} + \not{k}_g}{(k + k_g)^2 + i0} i g_s \not{\epsilon}_{s,\perp}^*(k_g) i \frac{\not{k}}{k^2 + i0} \\ &\quad \times i Q_u \not{\epsilon}_\perp^*(k_\gamma) i \frac{\not{k} - \not{k}_\gamma}{(k - k_\gamma)^2 + i0} \gamma_\mu b_L \delta\left(\bar{u} - \frac{k_+}{2E_\gamma}\right). \end{aligned} \quad (10.26)$$

In particular, note that the amplitudes in (10.2) and (10.3) correspond to the integrals over  $u$  of the amplitudes in (10.25) and (10.26).

To employ the reduction techniques introduced earlier, we rewrite the delta function using the Sokhotski–Plemelj formula:

$$\frac{1}{x \pm i0} = \mathcal{P} \left( \frac{1}{x} \right) \mp i\pi \delta(x),$$

which allows us to express the delta function as a difference of linear propagators:

$$\delta\left(u - \frac{k_+}{2E_\gamma}\right) = \frac{2E_\gamma}{2\pi i} \left( \frac{1}{k_+ - 2E_\gamma u - i0} - \frac{1}{k_+ - 2E_\gamma u + i0} \right). \quad (10.27)$$

Performing the IBP reduction on the sum of the two amplitudes yields

$$\begin{aligned} \mathcal{A}_{\text{LO}}^u(u) &= -i \frac{g_s Q_u E_\gamma^2}{1 - \epsilon} \tilde{\mu}^{2\epsilon} \left[ f_{\text{LO}}^u(u) \bar{u}_{hc,L}^{(s)} \not{\epsilon}_\perp^*(k_\gamma) \not{\epsilon}_{s,\perp}^*(k_g) \not{n} b_L \right. \\ &\quad \left. - f_{\text{LO}}^u(\bar{u}) \bar{u}_{hc,L}^{(s)} \not{\epsilon}_{s,\perp}^*(k_g) \not{\epsilon}_\perp^*(k_\gamma) \not{n} b_L \right], \end{aligned} \quad (10.28)$$

where we defined

$$\begin{aligned} f_{\text{LO}}^u(u) &= G_{0111}^B(u) \left[ (4 - 2\epsilon)^2 \bar{u} - 2(4 - 2\epsilon)(u^2 - 5u + 5) + 4(u^2 - 5u + 5) \right] \\ &\quad - 4G_{1111}^B(u) (2 - 2\epsilon) E_\gamma \omega_1 u - 2G_{0111}^B(\bar{u}) u [(4 - 2\epsilon)\bar{u} - 2\epsilon - 2\bar{u}]. \end{aligned} \quad (10.29)$$

The master integrals involved correspond to the topology

$$B = \left\{ \frac{1}{k^2 + i0}, \frac{1}{(k + k_g)^2 + i0}, \frac{1}{(k - k_\gamma)^2 + i0}, \delta(k_+ - 2E_\gamma u(\bar{u})) \right\}, \quad (10.30)$$

where  $G_{abcd}^B(u)$  contains the delta function depending explicitly on  $u$ , while  $G_{abcd}^B(\bar{u})$  depends on  $\bar{u}$ . It should be noted that the notation adopted in (10.30) indicates that  $\delta(k_+ - 2E_\gamma u(\bar{u}))$  is to be interpreted as the difference between linear propagators, as defined in (10.27).

The two master integrals can be solved using the same method we employed to derive formula (10.11). However, here we present an alternative approach to determine their dependence: the differential equation method. As we have seen, in the massless case the dependence on  $E_\gamma$  and  $\omega_1$  is trivial, allowing us to write differential equations for the master integrals solely in terms of the variable  $u$ . Accordingly, we factor out the mass-dependent terms from our master integrals as

$$G_{1111}^B(u) = \frac{(-E_\gamma \omega_1)^{-\varepsilon}}{E_\gamma^2 \omega_1} g_{1111}^B(u), \quad G_{0111}^B(u) = \frac{(-E_\gamma \omega_1)^{-\varepsilon}}{E_\gamma} g_{0111}^B(u), \quad (10.31)$$

where the functions  $g_{1111}^B$  and  $g_{0111}^B$  are dimensionless and depend only on the variable  $u$ . Starting from this ansatz, we derive the differential equations using the package `LiteRed` in combination with `Fermatica` [235], obtaining

$$\frac{d}{du} \begin{pmatrix} g_{1111}^B(u) \\ g_{0111}^B(u) \end{pmatrix} = \begin{pmatrix} -\frac{2\varepsilon + 1}{u} & \frac{\varepsilon}{2u^2(1-u)} \\ 0 & \frac{\varepsilon(1-2u)}{(u-1)u} \end{pmatrix} \begin{pmatrix} g_{1111}^B(u) \\ g_{0111}^B(u) \end{pmatrix}.$$

This system admits a solution given by

$$\begin{aligned} g_{1111}^B(u) &= \left( \frac{c_1}{2} (1-u)^{-\varepsilon} u^{-\varepsilon-1} + c_2 u^{-2\varepsilon-1} \right) \theta(u, 1-u), \\ g_{0111}^B(u) &= c_1 (1-u)^{-\varepsilon} u^{-\varepsilon} \theta(u, 1-u), \end{aligned} \quad (10.32)$$

with  $\theta(u, 1-u)$ <sup>1</sup> being the two-dimensional Heaviside function enforcing  $0 < u < 1$ . The constants  $c_1$  and  $c_2$  depend on  $\varepsilon$ , and to determine them we use the results already known from (10.16) and (10.17), which correspond to the  $u$ -integrated versions of the master integrals we aim to compute. Specifically, the two conditions read

$$\int du G_{1111}^B(u) = G_{111}^A, \quad \int du G_{0111}^B(u) = G_{011}^A. \quad (10.33)$$

Solving the two equations and substituting the constants  $c_1$  and  $c_2$  into (10.32), we obtain the final expressions for the master integrals:

$$\begin{aligned} G_{1111}^B(u) &= \frac{i}{4(4\pi)^{2-\varepsilon}} \frac{(-2E_\gamma \omega_1)^{-\varepsilon}}{E_\gamma^2 \omega_1} \Gamma(\varepsilon) (1-u)^{-\varepsilon} u^{-1-\varepsilon} \theta(u, 1-u), \\ G_{0111}^B(u) &= \frac{i}{2(4\pi)^{2-\varepsilon}} \frac{(-2E_\gamma \omega_1)^{-\varepsilon}}{E_\gamma} \Gamma(\varepsilon) (1-u)^{-\varepsilon} u^{-\varepsilon} \theta(u, 1-u). \end{aligned} \quad (10.34)$$

<sup>1</sup>This support condition is imposed by the integral in  $k_+$ .

All the  $u$ -dependent master integrals have support on the interval  $(0, 1)$  as a consequence of the integration over the momentum  $k_+$ . Consequently, all  $u$ -dependent results presented below, both at one and two loops, share the same support. Finally, substituting these results into the total amplitude, we obtain

$$\begin{aligned} \mathcal{A}_{\text{LO}}^u(u) = & -\frac{g_s Q_u E_\gamma \left(\frac{-2E_\gamma \omega_1}{\mu^2}\right)^{-\epsilon}}{4\pi^2} e^{\gamma_E \epsilon} \frac{\Gamma(1+\epsilon)}{1-\epsilon} [u(1-u)]^{-\epsilon} \theta(u, 1-u) \\ & \times \bar{u}_{hc,L}^{(s)} \left[ \not{\epsilon}_{s,\perp}^*(k_g) \not{\epsilon}_\perp^*(k_\gamma) (1-u(1-\epsilon)) - \not{\epsilon}_\perp^*(k_\gamma) \not{\epsilon}_{s,\perp}^*(k_g) (u+(1-u)\epsilon) \right] \frac{\not{n}}{2} b_L. \end{aligned} \quad (10.35)$$

We observe that the  $u$ -dependence of the two Dirac structures differs, and that the amplitude is anti-symmetric under the replacement  $u \rightarrow \bar{u}$ . Integrating the above expression over the variable  $u$  reproduces the result in (10.11).

#### 10.1.4 Massive $u$ -Dependent Amplitude at LO

Finally, we compute the massive  $u$ -dependent one-loop amplitude. Following the same reasoning as in the previous subsection, this is achieved by inserting a delta function  $\delta\left(u - \frac{k_+}{2E_\gamma}\right)$  into (10.18) and a delta function  $\delta\left(\bar{u} - \frac{k_+}{2E_\gamma}\right)$  into (10.19).

Performing the IBP reduction again, as in the  $u$ -integrated massive case, new Dirac structures appear; however, they are all subleading and can be neglected. The resulting amplitude is lengthy and for sake of brevity we do not give it here. It depends on three master integrals, namely  $G_{0111}^{B,m_c}$ ,  $G_{1011}^{B,m_c}$ , and  $G_{1111}^{B,m_c}$ , associated with the topology  $B$  defined in (10.30) but with propagators of mass  $m_c$ . We compute these master integrals following the same procedure used to derive (10.11), obtaining

$$\begin{aligned} G_{0111}^{B,m_c}(u) &= \frac{i}{2(4\pi)^{2-\epsilon}} \Gamma(\epsilon) \frac{\left(m_c^2 - 2E_\gamma \omega_1 (1-u)u\right)^{-\epsilon}}{E_\gamma} \theta(u, 1-u), \\ G_{1011}^{B,m_c}(u) &= \frac{i}{2(4\pi)^{2-\epsilon}} \Gamma(\epsilon) \frac{m_c^{-2\epsilon}}{E_\gamma} \theta(u, 1-u), \\ G_{1111}^{B,m_c}(u) &= \frac{i}{4(4\pi)^{2-\epsilon}} \Gamma(\epsilon) \frac{\left[m_c^{-2\epsilon} - \left(m_c^2 - 2E_\gamma \omega_1 (1-u)u\right)^{-\epsilon}\right]}{E_\gamma^2 \omega_1 u} \theta(u, 1-u). \end{aligned} \quad (10.36)$$

These master integrals determine the final amplitude, which reads

$$\begin{aligned} \mathcal{A}_{\text{LO}}^c(u) = & -\frac{g_s Q_c}{(4\pi)^2 \omega_1} e^{\gamma_E \epsilon} \frac{\Gamma(\epsilon)}{\epsilon-1} \theta(u, 1-u) \times \left[ -2E_\gamma \omega_1 \epsilon \left(\frac{m_c^2 - 2E_\gamma \omega_1}{\mu^2}\right)^{-\epsilon} \right. \\ & \left. - \frac{m_c^2}{u(1-u)} \left(\frac{m_c^2}{\mu^2}\right)^{-\epsilon} \left(1 - \left(1 - \frac{2E_\gamma \omega_1}{m_c^2} (1-u)u\right)^{-\epsilon}\right) \right] \\ & \times \bar{\chi}_{hc,L}^{(s)} \left[ \not{\epsilon}_{s,\perp}^*(k_g) \not{\epsilon}_\perp^*(k_\gamma) (1-u(1-\epsilon)) - \not{\epsilon}_\perp^*(k_\gamma) \not{\epsilon}_{s,\perp}^*(k_g) (u+(1-u)\epsilon) \right] \not{n} b_L. \end{aligned} \quad (10.37)$$

We cross-check this result in two ways: integrating over  $u$  and expanding in  $\epsilon$  reproduces (10.23), while taking the limit  $m_c \rightarrow 0$  recovers (10.35).

## 10.2 The $\bar{n}$ -Jet Function at Two Loops

We now proceed to the computation of the  $b \rightarrow s\gamma g$  amplitude in the anti-hard collinear region at NLO in the coupling  $\alpha_s$ . This amounts to evaluating all gluon loop corrections to the LO diagrams shown in Figure 10.1. We show in Figure 10.4 the two-loop diagrams in which the gluon corrections connect distinct points within the quark loop, and in Figure 10.5 those where the gluon corrections connect the quark loop to the external  $b$  and  $s$  legs.

The reason for separating the diagrams into two categories is that, for those in Figure 10.4, only the anti-hard collinear region contributes. In contrast, for those in Figure 10.5, within our method-of-regions approach, it is necessary to expand the fermion propagator of the external legs, as we will show in the following.

For diagram (A) we show only one possible insertion of the self-energy correction; however, two additional insertions are also possible: one in the fermion line connecting the photon and the gluon, and one in the fermion line connecting the gluon to the 4-quark vertex. In addition, for diagrams (B), (C) and (D) the QCD correction to the gluon or photon vertex can be interchanged with the other emitted boson, while for diagrams (A) and (E) an additional one can be obtained by exchanging the gluon and photon emission vertices. For diagrams (G), (H), and (I), the gluon may alternatively be attached to the opposite external leg relative to the one shown. Finally, for each diagram in Figure 10.5 an additional one can be obtained by exchanging the gluon and photon emission vertices.

In the following, we will employ the IBP method, as outlined in the previous section, to compute all two-loop contributions. However, as a preliminary step, we present one complete calculation in detail. This serves two purposes: first, to illustrate the systematic approach used to compute the master integrals both in this section and the next; and second, to highlight the key features of the computation and its result.

We start with the diagrams of type (G.1) and (G.2), which comprise a total of eight diagrams when all possible gluon connections are included, together with the interchange of the external photon and gluon. Splitting these eight diagrams into two categories of four allows them to be combined in a convenient way, making the computation both simpler and more insightful. We focus in particular on the diagrams shown in Figure 10.6.

The amplitude for diagram (G.2a) is given by

$$\begin{aligned}
\mathcal{A}_{\text{NLO}}^{(\text{G.2a})}(b \rightarrow s\gamma g) &= \tilde{\mu}^{4\epsilon} \int \frac{d^D k}{(2\pi)^D} \int \frac{d^D l}{(2\pi)^D} \bar{u}_{hc,L}^{(s)} \gamma^\mu i \frac{\not{k} - \not{k}_\gamma}{(k - k_\gamma)^2 + i0} i Q_u \not{\epsilon}_\perp^*(k_\gamma) i \frac{\not{k}}{k^2 + i0} \\
&\quad \times i g_s \not{\epsilon}_{s,\perp}^*(k_g) i \frac{\not{k} + \not{k}_g}{(k + k_g)^2 + i0} i g_s t^a \gamma^\alpha i \frac{\not{k} + \not{k}_g + \not{l}}{(k + k_g + l)^2 + i0} \\
&\quad \times \gamma_\mu P_L i \frac{\not{k}_b + \not{l} - m_b}{(k_b + l)^2 - m_b^2 + i0} i g_s t^a \gamma_\alpha \frac{-i}{l^2 + i0} b_L,
\end{aligned} \tag{10.38}$$

where  $k_b$  is the incoming  $b$ -quark momentum. Owing to its connection to the external quark line, this integral is not restricted to the anti-hard collinear region. To isolate the region of

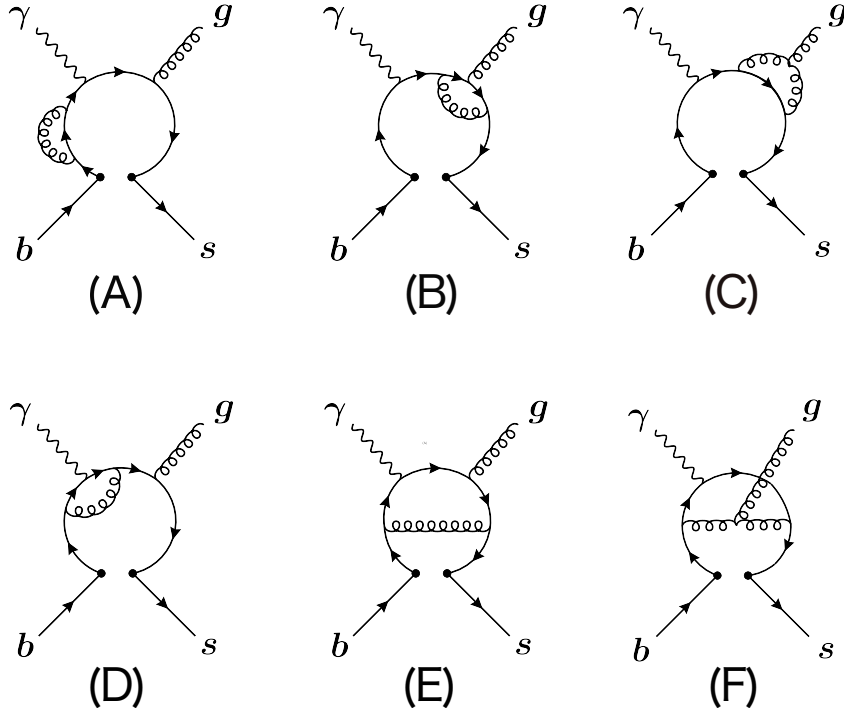


**Figure 10.4:** Two-loop diagrams contributing to the  $b \rightarrow s\gamma g$  amplitude. Only topologies without connections to the external  $b$  and  $s$  quark lines are shown. Diagram (A) displays one possible insertion of the self-energy correction, but two additional insertions are also possible. Furthermore, for diagrams (B), (C) and (D) the QCD correction to the gluon or photon vertex can be interchanged with the other emitted boson. For diagrams (A) and (E) an additional one can be obtained by exchanging the gluon and photon emission vertices.

interest, we expand the amplitude and obtain

$$\begin{aligned}
\mathcal{A}_{\text{NLO}}^{(\text{G.2a})}(b \rightarrow s\gamma g) &= 2g_s^3 Q_u C_F \tilde{\mu}^{4\epsilon} \int \frac{d^D k}{(2\pi)^D} \int \frac{d^D l}{(2\pi)^D} \bar{u}_{hc,L}^{(s)} \gamma^\mu \frac{\not{k} - \not{k}_\gamma}{(k - k_\gamma)^2 + i0} \not{\epsilon}_\perp^*(k_\gamma) \frac{\not{k}}{k^2 + i0} \\
&\quad \times \not{\epsilon}_{s,\perp}^*(k_g) \frac{\not{k}}{(k + k_g)^2 + i0} \gamma_\mu \frac{1}{(k + k_g + l)^2 + i0} \frac{1}{l^2 + i0} \frac{l_+ + k_+}{l_+ + i0} b_L,
\end{aligned} \tag{10.39}$$

where, in the second line, a linear propagator in the loop momentum  $l$  appears in the denominator.

Repeating the same procedure for diagram (G.2b), after the expansion we find

$$\begin{aligned}
\mathcal{A}_{\text{NLO}}^{(\text{G.2b})}(b \rightarrow s\gamma g) &= -2g_s^3 Q_u \left( C_F - \frac{1}{2} C_A \right) \tilde{\mu}^{4\epsilon} \int \frac{d^D k}{(2\pi)^D} \int \frac{d^D l}{(2\pi)^D} \bar{u}_{hc,L}^{(s)} \gamma^\mu \frac{\not{k} - \not{k}_\gamma}{(k - k_\gamma)^2 + i0} \\
&\quad \times \not{\epsilon}_\perp^*(k_\gamma) \frac{\not{k}}{k^2 + i0} \not{\epsilon}_{s,\perp}^*(k_g) \frac{\not{k}}{(k + k_g)^2 + i0} \gamma_\mu \frac{1}{(k + k_g + l)^2 + i0} \\
&\quad \times \frac{1}{l^2 + i0} \frac{l_+ + k_+}{l_+ + i0} b_L.
\end{aligned} \tag{10.40}$$

Summing the two amplitudes shows that the colour factor  $C_F$  cancels, leaving only  $C_A$ . This behaviour is common to all amplitudes in Figure 10.5. Expanding (G.1a) and (G.1b) and

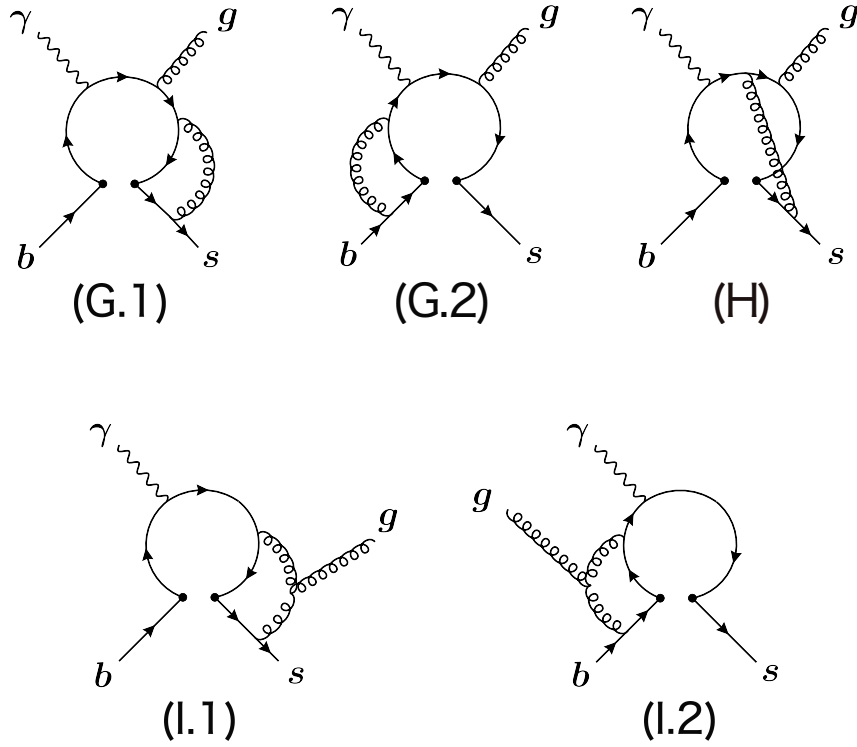


**Figure 10.5:** Two-loop diagrams contributing to the  $b \rightarrow s\gamma g$  amplitude, showing the connections to the external  $b$  and  $s$  quark lines. In each diagram, the gluon may alternatively be attached to the opposite external leg relative to the one shown. Moreover, for each diagram, an additional one is obtained by interchanging the gluon and photon emission vertices.

summing all contributions from Figure 10.6, we obtain

$$\mathcal{A}_{\text{NLO}}^{(10.6)}(b \rightarrow s\gamma g) = 2g_s^3 Q_u C_A (1 + \varepsilon) \tilde{\mu}^{4\varepsilon} \bar{u}_{hc,L}^{(s)} \left[ \not{\epsilon}_\perp^*(k_\gamma), \not{\epsilon}_{s,\perp}^*(k_g) \right] \frac{\not{n}}{2} b_L I_{\text{NLO}}^u, \quad (10.41)$$

with  $I_{\text{NLO}}^u$  defined as

$$I_{\text{NLO}}^u = \int \frac{d^D k}{(2\pi)^D} \int \frac{d^D l}{(2\pi)^D} \frac{k_+ + l_+}{(l_+ + i0)(l^2 + i0)[(k + k_g + l)^2 + i0]} \times \frac{(k_+ - 2E_\gamma) \left( \frac{\varepsilon}{1-\varepsilon} k_\perp^2 - k_+ k_- \right) - \frac{k_+ k_\perp^2}{1-\varepsilon}}{(k^2 + i0)[(k - k_\gamma)^2 + i0][(k + k_g)^2 + i0]}, \quad (10.42)$$

where the second line reproduces the expression encountered in the one-loop integral  $I_{\text{LO}}^u$ . The same strategy used at one loop to obtain (10.11) can be applied here, generalised to the two-loop case.

We first examine the singularities in  $k_-$  and  $l_-$ . To make them explicit, we rewrite (10.42)

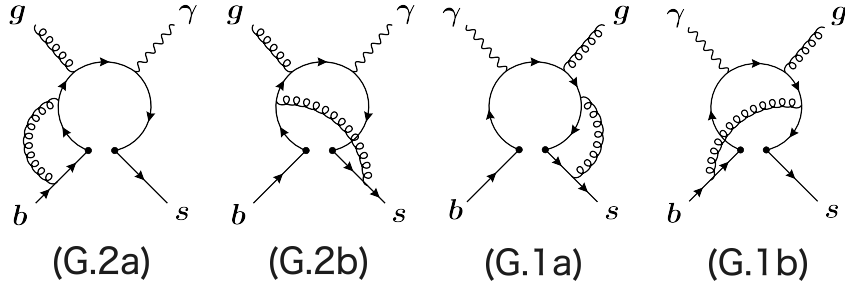


Figure 10.6: Subset of four diagrams of the kind (G.1) and (G.2).

as

$$\begin{aligned}
I_{\text{NLO}}^u &= -\frac{1}{4} \int \frac{dk_+ dk_- d^{D-2}k_\perp}{(2\pi)^D} \int \frac{dl_+ dl_- d^{D-2}l_\perp}{(2\pi)^D} \frac{1}{l_+^2 k_+^2 (k_+ - 2E_\gamma)} \\
&\quad \times \frac{1}{\left(l_- + \frac{l_\perp^2 + i0}{l_+}\right) \left(k_- - l_- + \omega_1 + \frac{(k_\perp + l_\perp)^2 + i0}{k_+ - l_+}\right)} \\
&\quad \times \frac{(k_+ - 2E_\gamma) \left(\frac{\varepsilon}{1-\varepsilon} k_\perp^2 - k_+ k_- \right) - \frac{k_+ k_\perp^2}{1-\varepsilon}}{\left(k_- + \frac{k_\perp^2 + i0}{k_+}\right) \left(k_- + \frac{k_\perp^2 + i0}{k_+ - 2E_\gamma}\right) \left(k_- + \omega_1 + \frac{k_\perp^2 + i0}{k_+}\right)}.
\end{aligned} \tag{10.43}$$

The pole locations are shown in Figure 10.7. The only non-vanishing contribution arises from the triangular region labelled (A).

Applying the residue theorem, we close the contour for  $l_-$  in the lower half-plane and for  $k_-$  in the upper half-plane. Completing the square in the transverse components we obtain:

$$\begin{aligned}
I_{\text{NLO}}^u &= -\pi^2 \frac{\varepsilon}{1-\varepsilon} \int_0^{2E_\gamma} dk_+ \int_0^{k_+} dl_+ \int \frac{d^{D-2}k_\perp}{(2\pi)^D} \int \frac{d^{D-2}l_\perp}{(2\pi)^D} \frac{1}{l_+^2 k_+} \\
&\quad \times \frac{1}{\left(\omega_1 + \frac{k_+}{l_+(k_+ - l_+)} \left(l_\perp - \frac{l_+}{k_+} k_\perp\right)^2 - \frac{2E_\gamma}{k_+(k_+ - 2E_\gamma)} k_\perp^2\right) \left(\omega_1 - \frac{2E_\gamma}{k_+(k_+ - 2E_\gamma)} k_\perp^2\right)}.
\end{aligned} \tag{10.44}$$

We now shift  $l_\perp \rightarrow l_\perp + \frac{l_+}{k_+} k_\perp$ , introduce  $x = -k_\perp^2 > 0$  and  $y = -l_\perp^2 > 0$ , and rescale  $y' = \frac{k_+}{l_+(k_+ - l_+)} y$  and  $x' = \frac{-2E_\gamma}{k_+(k_+ - l_+)} x$ . This yields

$$\begin{aligned}
I_{\text{NLO}}^u &= \frac{(2E_\gamma)^{\varepsilon-1} \varepsilon}{(4\pi)^{4-2\varepsilon} \Gamma(1-\varepsilon)^2 (\varepsilon-1)} \int_0^{2E_\gamma} dk_+ \int_0^{k_+} dl_+ \frac{l_+^{3-\varepsilon}}{k_+} [(2E_\gamma - k_+)(k_+ - l_+)]^{1-\varepsilon} \\
&\quad \times \int_0^\infty dx \int_0^\infty dy \frac{(x' y')^{-\varepsilon}}{(x' - \omega_1)(x' + y' - \omega_1)}.
\end{aligned} \tag{10.45}$$

Rescaling now also the momenta  $k_+$  and  $l_+$  according to  $l = \frac{l_+}{k_+}$  and  $k = \frac{k_+}{2E_\gamma}$ , we can write

$$\begin{aligned}
I_{\text{NLO}}^u &= \frac{(2E_\gamma)^{1-2\varepsilon} \varepsilon}{(4\pi)^{4-2\varepsilon} \Gamma(1-\varepsilon)^2 (\varepsilon-1)} \int_0^1 dk \frac{[k^2(1-k)]^{1-\varepsilon}}{k^2} \int_0^1 dl \frac{[l(1-l)]^{1-\varepsilon}}{l^2} \\
&\quad \times \int_0^\infty dx \int_0^\infty dy \frac{(x' y')^{-\varepsilon}}{(x' - \omega_1)(x' + y' - \omega_1)},
\end{aligned} \tag{10.46}$$

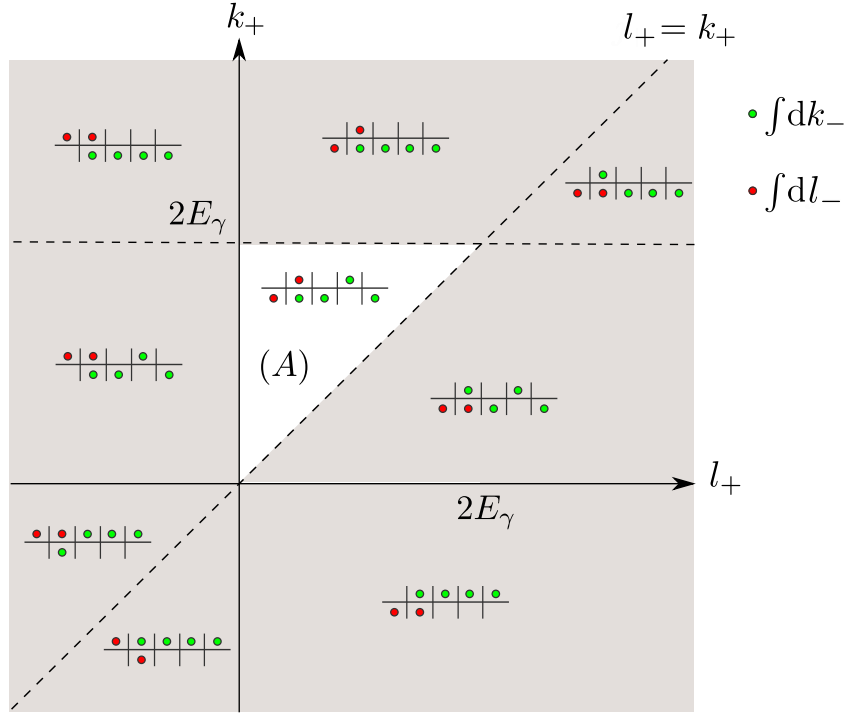


**Figure 10.7:** Location of poles related to the integral in (10.43). Colour dots denote poles located in the upper or lower complex half-plane. Green dots are related to the integral in  $k_-$ , while red dots to the integral in  $l_-$ . The order of the denominators matches that in Equation (10.43). Grey shading indicated the regions where the integral vanish.

which can be integrated and written in terms of Euler-Gamma functions as

$$I_{\text{NLO}}^u = \frac{2E_\gamma (-2E_\gamma \omega_1)^{-2\varepsilon}}{(4\pi)^{4-2\varepsilon}} \frac{\Gamma(1-2\varepsilon)\Gamma(2-\varepsilon)^2\Gamma(2\varepsilon)\Gamma(-\varepsilon)}{\Gamma(3-3\varepsilon)\Gamma(2-2\varepsilon)(\varepsilon-1)}. \quad (10.47)$$

Substituting into (10.41) gives

$$\begin{aligned} \mathcal{A}_{\text{NLO}}^{(10.6)}(b \rightarrow s\gamma g) &= \frac{3g_s\alpha_s Q_u C_A E_\gamma}{16\pi^3} \left(\frac{-2E_\gamma \omega_1}{\mu^2}\right)^{-2\varepsilon} \bar{u}_{hc,L}^{(s)} \left[ \not{\epsilon}_\perp^*(k_\gamma), \not{\epsilon}_{s,\perp}^*(k_g) \right] \frac{\not{p}}{2} b_L \\ &\times e^{2\gamma_E \varepsilon} \frac{(1+\varepsilon)\Gamma(2-\varepsilon)^2\Gamma(-\varepsilon)\Gamma(2\varepsilon-1)}{\Gamma(4-3\varepsilon)}. \end{aligned} \quad (10.48)$$

The structure closely parallels the one-loop result: the dependence on  $E_\gamma$  and  $\omega_1$  factorises following directly from dimensional analysis, additionally the same minus sign appears in  $\left(\frac{-2E_\gamma \omega_1}{\mu^2}\right)^{-2\varepsilon}$ . At two loops, however, both single and double  $1/\varepsilon$  poles emerge:

$$\begin{aligned} \mathcal{A}_{\text{NLO}}^{(10.6)}(b \rightarrow s\gamma g) &= \frac{g_s\alpha_s Q_u C_A E_\gamma}{16\pi^3} \bar{u}_{hc,L}^{(s)} \left[ \not{\epsilon}_\perp^*(k_\gamma), \not{\epsilon}_{s,\perp}^*(k_g) \right] \frac{\not{p}}{2} b_L \\ &\times \left( \frac{1}{4\varepsilon^2} + \frac{-4\log\left(\frac{-2E_\gamma \omega_1}{\mu^2}\right) + 13}{8\varepsilon} + \mathcal{O}(\varepsilon^0) \right). \end{aligned} \quad (10.49)$$

Applying the same method to the remaining diagrams in the (G.1) and (G.2) categories yields

$$\begin{aligned} \mathcal{A}_{\text{NLO}}^{(\text{G.1})+(\text{G.2})}(b \rightarrow s\gamma g) &= - \frac{12g_s\alpha_s Q_u C_A E_\gamma}{(4\pi)^3} \left( \frac{-2E_\gamma\omega_1}{\mu^2} \right)^{-2\varepsilon} \bar{u}_{hc,L}^{(s)} \left[ \not{\epsilon}_\perp^*(k_\gamma), \not{\epsilon}_{s,\perp}^*(k_g) \right] \frac{\not{n}}{2} b_L \\ &\times e^{2\gamma_E\varepsilon} \frac{(1+\varepsilon)\Gamma(2-\varepsilon)^2\Gamma(-\varepsilon)\Gamma(2\varepsilon)}{\Gamma(3-3\varepsilon)(2\varepsilon-1)(\varepsilon-1)}. \end{aligned} \quad (10.50)$$

Having presented step by step the main features of this computation, we now proceed to systematically reduce all NLO diagrams. The two-loop master integrals belong to a single topology, which we define as

$$C = \left\{ \frac{1}{l^2 + i0}, \frac{1}{k^2 + i0}, \frac{1}{(k+l)^2 + i0}, \frac{1}{(l-k_g)^2 + i0}, \frac{1}{(k-k_\gamma)^2 + i0}, \frac{1}{(k+l-k_\gamma-k_g)^2 + i0}, \frac{1}{k \cdot k_g + i0} \right\}. \quad (10.51)$$

We display in Table 10.1 the master integrals for each set of diagrams in Figure 10.5. Interestingly, no linear propagators appear. The amplitudes (G), (H), and (I) depend only on a single master integral, which can be computed with standard techniques and is given by

$$G_{0011100}^C = \frac{(-2E_\gamma\omega_1)^{1-2\varepsilon}}{(4\pi)^{4-2\varepsilon}} \frac{\Gamma(1-\varepsilon)^3\Gamma(2\varepsilon-1)}{\Gamma(3-3\varepsilon)}. \quad (10.52)$$

Diagrams	Master integrals
(G.1)+(G.2)	$G_{0011100}^C$
(H)	$G_{0011100}^C$
(I.1)+(I.2)	$G_{0011100}^C$

**Table 10.1:** Master integrals associated with the diagrams of Figure 10.5.

Using this result for the master integral, we obtain the amplitudes for the three combinations of diagrams listed in Table 10.1. In particular, besides reproducing the result in (10.50), we find for the other two amplitudes

$$\begin{aligned} \mathcal{A}_{\text{NLO}}^{(\text{H})}(b \rightarrow s\gamma g) &= - \frac{4g_s\alpha_s Q_u C_A E_\gamma}{(4\pi)^3} \left( \frac{-2E_\gamma\omega_1}{\mu^2} \right)^{-2\varepsilon} \bar{u}_{hc,L}^{(s)} \left[ \not{\epsilon}_\perp^*(k_\gamma), \not{\epsilon}_{s,\perp}^*(k_g) \right] \frac{\not{n}}{2} b_L \\ &\times e^{2\gamma_E\varepsilon} \frac{(1+\varepsilon)\Gamma(1-2\varepsilon)\Gamma(-\varepsilon)\Gamma(2-\varepsilon)^2\Gamma(2\varepsilon-1)}{\Gamma(3-3\varepsilon)\Gamma(2-2\varepsilon)(1-\varepsilon)}, \end{aligned} \quad (10.53)$$

$$\begin{aligned} \mathcal{A}_{\text{NLO}}^{(\text{I.1})+(\text{I.2})}(b \rightarrow s\gamma g) &= - \frac{12g_s\alpha_s Q_u C_A E_\gamma}{(4\pi)^3} \left( \frac{-2E_\gamma\omega_1}{\mu^2} \right)^{-2\varepsilon} \bar{u}_{hc,L}^{(s)} \left[ \not{\epsilon}_\perp^*(k_\gamma), \not{\epsilon}_{s,\perp}^*(k_g) \right] \frac{\not{n}}{2} b_L \\ &\times e^{2\gamma_E\varepsilon} \frac{(1+\varepsilon)(\varepsilon-2)\Gamma(2\varepsilon)\Gamma(1-2\varepsilon)\Gamma(2-\varepsilon)^2\Gamma(-\varepsilon)}{(2\varepsilon-1)\Gamma(2-2\varepsilon)\Gamma(4-3\varepsilon)}. \end{aligned} \quad (10.54)$$

Finally, summing all the diagrams of Figure 10.5, we obtain

$$\begin{aligned} \mathcal{A}_{\text{NLO}}^{(10.5)}(b \rightarrow s\gamma g) &= -\frac{3g_s\alpha_s Q_u C_A E_\gamma}{16\pi^3} \left(\frac{-2E_\gamma\omega_1}{\mu^2}\right)^{-2\varepsilon} \bar{u}_{hc,L}^{(s)} \left[ \not{\epsilon}_\perp^*(k_\gamma), \not{\epsilon}_{s,\perp}^*(k_g) \right] \frac{\not{h}}{2} b_L \\ &\times e^{2\gamma_E\varepsilon} \frac{(1+\varepsilon)(7\varepsilon-4)\Gamma(2\varepsilon)\Gamma(1-2\varepsilon)\Gamma(2-\varepsilon)^2\Gamma(-\varepsilon)}{(2\varepsilon-1)\Gamma(4-3\varepsilon)\Gamma(2-2\varepsilon)}. \end{aligned} \quad (10.55)$$

This result contains singularities in the dimensional regulator. Normalising to the one-loop result in (10.11) and expanding in  $\varepsilon$ , we find

$$\begin{aligned} \frac{\mathcal{A}_{\text{NLO}}^{(10.5)}(b \rightarrow s\gamma g)}{\mathcal{A}_{\text{LO}}^u(b \rightarrow s\gamma g)} &= \frac{\alpha_s}{4\pi} C_A \left[ \frac{2}{\varepsilon^2} + \frac{11}{2\varepsilon} - \frac{2}{\varepsilon} \log\left(-\frac{2E_\gamma\omega_1}{\mu^2}\right) \right. \\ &\quad \left. + \log^2\left(-\frac{2E_\gamma\omega_1}{\mu^2}\right) - \frac{11}{2} \log\left(-\frac{2E_\gamma\omega_1}{\mu^2}\right) - \frac{\pi^2}{6} + \frac{213}{12} + \mathcal{O}(\varepsilon) \right]. \end{aligned} \quad (10.56)$$

We now analyse the diagrams of Figure 10.4. In this case, no expansion is required, and we can compute them directly, as in the one-loop case. The master integrals associated with this set of diagrams are listed in Table 10.2. We have already computed the two-loop master integral  $G_{00111100}^C$  in (10.52) and the one-loop master integral  $G_{011}^A$  in (10.16), while the master integral  $G_{0111010}^C$  is given by

$$G_{0111010}^C = -\frac{(-2E_\gamma\omega_1)^{-2\varepsilon}}{(4\pi)^{4-2\varepsilon}} \frac{\Gamma(\varepsilon)\Gamma(2\varepsilon)\Gamma(1-2\varepsilon)\Gamma(1-\varepsilon)^2}{(1-2\varepsilon)\Gamma(2-3\varepsilon)}. \quad (10.57)$$

Finally, we compute the last master integral in an  $\varepsilon$ -expansion, obtaining

$$\begin{aligned} G_{11111110}^C &= -\frac{(-2E_\gamma\omega_1)^{-2-2\varepsilon}}{(4\pi)^{4-2\varepsilon}} \frac{1}{\Gamma(1-\varepsilon)^2} \left[ \frac{1}{\varepsilon^4} - \frac{5\pi^2}{6\varepsilon^2} - \frac{27\zeta(3)}{\varepsilon} - \frac{23\pi^4}{36} \right. \\ &\quad \left. + \varepsilon \left( 8\pi^2\zeta(3) - 117\zeta(5) \right) - \varepsilon^2 \left( \frac{19\pi^6}{315} - 267\zeta(3)^2 \right) \right. \\ &\quad \left. + \varepsilon^3 \left( \frac{109\pi^4\zeta(3)}{10} + 40\pi^2\zeta(5) + 6\zeta(7) \right) \right], \end{aligned} \quad (10.58)$$

in agreement with [236]. Using these expressions for the master integrals, we obtain the amplitudes corresponding to the diagrams in Figure 10.4. Their results are given by

$$\begin{aligned} \mathcal{A}_{\text{NLO}}^{(A)}(b \rightarrow s\gamma g) &= -\frac{4g_s\alpha_s Q_u C_F E_\gamma}{(4\pi)^3} \left(\frac{-2E_\gamma\omega_1}{\mu^2}\right)^{-2\varepsilon} e^{2\gamma_E\varepsilon} \bar{u}_{hc,L}^{(s)} \left[ \not{\epsilon}_\perp^*(k_\gamma), \not{\epsilon}_{s,\perp}^*(k_g) \right] \frac{\not{h}}{2} b_L \\ &\times \frac{(1+\varepsilon)\Gamma(1-\varepsilon)\Gamma(2\varepsilon) \left[ (3\varepsilon-3)\Gamma(1-\varepsilon)^2 - \varepsilon\Gamma(1-2\varepsilon)\Gamma(2-\varepsilon)\Gamma(\varepsilon) \right]}{(2\varepsilon-1)\Gamma(3-3\varepsilon)}, \end{aligned} \quad (10.59)$$

Diagrams	Master integrals
(A)	$G_{00111100}^C, G_{0111010}^C$
(B)	$G_{00111100}^C, G_{0111010}^C$
(C)	$G_{00111100}^C, G_{0111010}^C$
(D)	$G_{00111100}^C, G_{0111010}^C$
(E)	$G_{00111100}^C, G_{0111010}^C, \left(G_{011}^A\right)^2$
(F)	$G_{00111100}^C, G_{0111010}^C, G_{1111110}^C$

**Table 10.2:** Master integrals associated with the diagrams of Figure 10.4.

$$\begin{aligned}
\mathcal{A}_{\text{NLO}}^{(B)}(b \rightarrow s\gamma g) &= \frac{4g_s\alpha_s Q_u(C_A - 2C_F)E_\gamma}{(4\pi)^3} \left(\frac{-2E_\gamma\omega_1}{\mu^2}\right)^{-2\varepsilon} \bar{u}_{hc,L}^{(s)} \left[\not{\epsilon}_\perp^*(k_\gamma), \not{\epsilon}_{s,\perp}^*(k_g)\right] \frac{\not{h}}{2} b_L \\
&\times e^{2\gamma_E\varepsilon} \left[ (1+\varepsilon)\Gamma(1-2\varepsilon)\Gamma(1-\varepsilon)\Gamma(\varepsilon)\Gamma(2\varepsilon) - \Gamma(2-\varepsilon)\Gamma(-\varepsilon)\Gamma(2\varepsilon-1) \right] \\
&\times \frac{(1+\varepsilon)\Gamma(2-\varepsilon)}{(2\varepsilon-1)\Gamma(3-3\varepsilon)},
\end{aligned} \tag{10.60}$$

$$\begin{aligned}
\mathcal{A}_{\text{NLO}}^{(C)}(b \rightarrow s\gamma g) &= \frac{2g_s\alpha_s Q_u C_A E_\gamma}{(4\pi)^3} \left(\frac{-2E_\gamma\omega_1}{\mu^2}\right)^{-2\varepsilon} e^{2\gamma_E\varepsilon} \bar{u}_{hc,L}^{(s)} \left[\not{\epsilon}_\perp^*(k_\gamma), \not{\epsilon}_{s,\perp}^*(k_g)\right] \frac{\not{h}}{2} b_L \\
&\times \left[ (3\varepsilon-1)\Gamma(3-2\varepsilon)\Gamma(1-\varepsilon)\Gamma(\varepsilon) - 2(\varepsilon(2\varepsilon-5)+1)\Gamma(2-\varepsilon)\Gamma(-\varepsilon) \right] \\
&\times \frac{(1+\varepsilon)\Gamma(2-\varepsilon)\Gamma(1-2\varepsilon)\Gamma(2\varepsilon)}{\varepsilon(2\varepsilon-1)\Gamma(3-3\varepsilon)\Gamma(3-2\varepsilon)},
\end{aligned} \tag{10.61}$$

$$\begin{aligned}
\mathcal{A}_{\text{NLO}}^{(D)}(b \rightarrow s\gamma g) &= \frac{8g_s\alpha_s Q_u C_F E_\gamma}{(4\pi)^3} \left(\frac{-2E_\gamma\omega_1}{\mu^2}\right)^{-2\varepsilon} e^{2\gamma_E\varepsilon} \bar{u}_{hc,L}^{(s)} \left[\not{\epsilon}_\perp^*(k_\gamma), \not{\epsilon}_{s,\perp}^*(k_g)\right] \frac{\not{h}}{2} b_L \\
&\times \left[ (2\varepsilon^3 + \varepsilon^2 + \varepsilon - 1)\Gamma(1+\varepsilon)\Gamma(1-2\varepsilon) + (3\varepsilon^3 - \varepsilon^2 + 1)\Gamma(1-\varepsilon) \right] \\
&\times \frac{(1+\varepsilon)\Gamma(1-\varepsilon)^2\Gamma(2\varepsilon-1)}{\varepsilon(2\varepsilon-1)\Gamma(3-3\varepsilon)},
\end{aligned} \tag{10.62}$$

$$\begin{aligned}
\mathcal{A}_{\text{NLO}}^{(E)}(b \rightarrow s\gamma g) &= \frac{g_s\alpha_s Q_u(C_A - 2C_F)E_\gamma}{2(4\pi)^3} \left(\frac{-2E_\gamma\omega_1}{\mu^2}\right)^{-2\varepsilon} e^{2\gamma_E\varepsilon} \bar{u}_{hc,L}^{(s)} \left[\not{\epsilon}_\perp^*(k_\gamma), \not{\epsilon}_{s,\perp}^*(k_g)\right] \frac{\not{h}}{2} b_L \\
&\times \left[ \frac{4\varepsilon(4\varepsilon^3 + 10\varepsilon^2 - 11\varepsilon + 3)\Gamma(1-2\varepsilon)\Gamma(\varepsilon)\Gamma(2\varepsilon)}{(2\varepsilon-1)\Gamma(3-3\varepsilon)\Gamma(\varepsilon)} \right. \\
&\quad - \frac{4(6\varepsilon^5 - 11\varepsilon^4 + 42\varepsilon^3 - 52\varepsilon^2 + 25\varepsilon - 4)\Gamma(-\varepsilon)\Gamma(2\varepsilon-1)}{(2\varepsilon-1)\Gamma(3-3\varepsilon)\Gamma(\varepsilon)} \\
&\quad \left. - \frac{8(\varepsilon(\varepsilon(2\varepsilon+3)+3)-2)\Gamma(2-\varepsilon)^2\Gamma(\varepsilon)}{\Gamma(3-2\varepsilon)^2} \right] \times \frac{(1+\varepsilon)\Gamma(1-\varepsilon)^2\Gamma(\varepsilon)}{(1-\varepsilon)^2},
\end{aligned} \tag{10.63}$$

$$\begin{aligned} \mathcal{A}_{\text{NLO}}^{(\text{F})}(b \rightarrow s\gamma g) &= -\frac{g_s \alpha_s Q_u C_A E_\gamma}{(4\pi)^3} \left( \frac{-2E_\gamma \omega_1}{\mu^2} \right)^{-2\varepsilon} \bar{u}_{hc,L}^{(s)} \left[ \not{\epsilon}_\perp^*(k_\gamma), \not{\epsilon}_{s,\perp}^*(k_g) \right] \frac{\not{n}}{2} b_L \\ &\times \left[ \frac{1}{\varepsilon} \left( 1 + \frac{\pi^2}{6} \right) + \left( \zeta(3) + \frac{21}{2} + \frac{11}{12} \pi^2 \right) + \mathcal{O}(\varepsilon) \right]. \end{aligned} \quad (10.64)$$

Here, the last expression is expanded in the dimensional regulator  $\varepsilon$ , with terms of order higher than  $\varepsilon^0$  omitted. Finally, by summing all the diagrams of Figure 10.4, expanding in  $\varepsilon$ , and normalising to the one-loop result given in (10.11), we obtain

$$\frac{\mathcal{A}_{\text{NLO}}^{(10.4)}(b \rightarrow s\gamma g)}{\mathcal{A}_{\text{LO}}^u(b \rightarrow s\gamma g)} = \frac{\alpha_s}{4\pi} \left[ 4C_F - \left( \frac{1}{2} + \frac{\pi^2}{3} \right) C_A + \mathcal{O}(\varepsilon) \right]. \quad (10.65)$$

Interestingly, the sum of these diagrams does not exhibit  $1/\varepsilon$  poles; therefore, all divergences arise from formula (10.56). To conclude this section, we present the full result, normalised to the one-loop expression, obtained by summing all the diagrams of Figures 10.4 and 10.5:

$$\begin{aligned} \frac{\mathcal{A}_{\text{NLO}}^u(b \rightarrow s\gamma g)}{\mathcal{A}_{\text{LO}}^u(b \rightarrow s\gamma g)} &= \frac{\alpha_s}{4\pi} \left\{ \left[ \frac{2}{\varepsilon^2} + \frac{11}{2\varepsilon} - \frac{2}{\varepsilon} \log \left( -\frac{2E_\gamma \omega_1}{\mu^2} \right) \right. \right. \\ &\quad \left. \left. + \log^2 \left( -\frac{2E_\gamma \omega_1}{\mu^2} \right) - \frac{11}{2} \log \left( -\frac{2E_\gamma \omega_1}{\mu^2} \right) - \frac{\pi^2}{2} + \frac{69}{4} \right] C_A \right. \\ &\quad \left. + 4C_F + \mathcal{O}(\varepsilon) \right\}. \end{aligned} \quad (10.66)$$

### 10.3 Full $u$ -Dependence of the $\bar{n}$ -Jet Function at NLO

We now examine the dependence of the two-loop  $\bar{n}$ -jet function on the antihard-collinear momentum fraction  $u$ . As illustrated in Figure 10.3 for the one-loop case, this dependence is introduced by inserting a delta function that enforces  $u = \frac{k_+}{2E_\gamma}$  (or  $\bar{u} = \frac{k_+}{2E_\gamma}$ ) in the diagrams presented in Figures 10.4 and 10.5. The insertion of the delta function alters the structure of the calculation, as it increases both the number and complexity of the required master integrals, thereby making the computation more demanding. As in the previous case, we begin with the diagrams shown in Figure 10.5, which are comparatively simpler to evaluate. The amplitudes are once again reduced to master integrals, but in this case the integrals explicitly depend on the inserted delta function. For these diagrams, however, a single topology suffices to express all the necessary master integrals. This topology is defined as follows:

$$\begin{aligned} D &= \left\{ \frac{1}{l^2 + i0}, \frac{1}{(l+k_g)^2 + i0}, \frac{1}{(k+k_g)^2 + i0}, \frac{1}{(l-k_\gamma)^2 + i0}, \frac{1}{(k-l)^2 + i0}, \right. \\ &\quad \left. \frac{1}{(k-k_\gamma)^2 + i0}, \frac{1}{k^2 + i0}, \frac{1}{n \cdot l + i0}, \delta(k_+ - 2E_\gamma u(\bar{u})) \right\}. \end{aligned} \quad (10.67)$$

We remind that the notation adopted in (10.67) indicates that  $\delta(k_+ - 2E_\gamma u(\bar{u}))$  is to be interpreted as the difference between linear propagators, as defined in (10.27).

Diagrams	Master integrals
(G.1)+(G.2)	$G_{010011001}^D(u), G_{010011001}^D(\bar{u}), G_{010011101}^D(u), G_{010011101}^D(\bar{u})$
(H)	$G_{010011001}^D(u), G_{010011001}^D(\bar{u}), G_{010011101}^D(u), G_{010011101}^D(\bar{u})$
(I.1)+(I.2)	$G_{010011001}^D(u), G_{010011001}^D(\bar{u}), G_{010011101}^D(u), G_{010011101}^D(\bar{u})$

**Table 10.3:**  $u$ -dependent master integrals corresponding to the diagrams in Figure 10.5.

Table 10.3 lists the master integrals required for evaluating the diagrams shown in Figure 10.5. We compute the master integrals listed in Table 10.1 retaining their full  $\varepsilon$ -dependence, following the same procedure used to obtain (10.47). The results are given by:

$$G_{010011001}^D(u) = -\frac{\omega_1(-2E_\gamma\omega_1)^{-2\varepsilon}}{(4\pi)^{4-2\varepsilon}} u^{1-2\varepsilon}(1-u)^{-\varepsilon} \frac{\Gamma(1-\varepsilon)^2\Gamma(2\varepsilon-1)}{\Gamma(2-2\varepsilon)} \theta(u, 1-u), \quad (10.68)$$

$$G_{010011101}^D(u) = -\frac{1}{2} \frac{(-2E_\gamma\omega_1)^{-2\varepsilon}}{(4\pi)^{4-2\varepsilon} E_\gamma} u^{-2\varepsilon}(1-u)^{-\varepsilon} \frac{\Gamma(1-\varepsilon)\Gamma(-\varepsilon)\Gamma(2\varepsilon)}{\Gamma(2-2\varepsilon)} \theta(u, 1-u). \quad (10.69)$$

By substituting these master integrals into the reduced amplitudes, we obtain the final results for the diagrams shown in Figure 10.5. As observed already in the one-loop case, the two Dirac structures exhibit different  $u$ -dependence: one is proportional to a function of  $u$ , while the other is proportional to the same function evaluated at  $\bar{u} = 1-u$ . Furthermore, as in the  $u$ -integrated case, the colour factor  $C_F$  cancels in the sum of the diagrams, leaving only a dependence on  $C_A$ . Consequently, for a generic diagram (d) in Figure 10.5, all results take the following form:

$$\begin{aligned} \mathcal{A}_{\text{NLO}}^{(d)}(u) = & \frac{g_s\alpha_s Q_u C_A E_\gamma}{(4\pi)^3} \left( \frac{-2E_\gamma\omega_1}{\mu^2} \right)^{-2\varepsilon} \bar{u}_{hc,L}^{(s)} \left[ f_d(u) \not{\epsilon}_{s,\perp}^*(k_g) \not{\epsilon}_\perp^*(k_\gamma) \right. \\ & \left. - f_d(\bar{u}) \not{\epsilon}_\perp^*(k_\gamma) \not{\epsilon}_{s,\perp}^*(k_g) \right] \not{p} b_L, \end{aligned} \quad (10.70)$$

where the  $u$ -dependent functions  $f_d(u)$  have support on the interval  $(0, 1)$ , since all the master integrals are restricted to this range. In particular, for the sum of diagrams (G.1) and (G.2), the  $u$ -dependent function takes the form

$$\begin{aligned} f_G(u) = & -\frac{3(1-u)}{\varepsilon^2} + \frac{1}{\varepsilon} \left[ 2u^2 \tanh^{-1}(1-2u) + 5u + (5-6u) \log(1-u) \right. \\ & \left. + (4-3u) \log(u) - 8 \right] + \mathcal{O}(\varepsilon^0), \end{aligned} \quad (10.71)$$

in the case of diagram (H), the function reads

$$\begin{aligned} f_H(u) = & \frac{1-u}{\varepsilon^2} + \frac{1}{\varepsilon} \left[ u^2 \log\left(\frac{1}{u} - 1\right) - 3u - \log(1-u) + (3u-2) \log(u) + 4 \right] \\ & + \mathcal{O}(\varepsilon^0), \end{aligned} \quad (10.72)$$

while for the sum of diagrams (I.1) and (I.2):

$$f_1(u) = -\frac{2(1-u)}{\varepsilon^2} - \frac{1}{\varepsilon} \left[ (u^2 \log\left(\frac{1}{u} - 1\right) - 5u + (u-2) \log(1-u) + (5u-4) \log(u) + 7 \right] + \mathcal{O}(\varepsilon^0). \quad (10.73)$$

For the sake of brevity, we have provided in the main text only the  $1/\varepsilon$  poles, while the finite terms are listed in Appendix E. The results presented above can be cross-checked by integrating over the variable  $u$  in the interval  $(0, 1)$ . Performing this integral reproduces the results obtained in the previous section in (10.50), (10.53) and (10.54).

We now turn to the study of the diagrams shown in Figure 10.4. In order to compute diagram (F), it is necessary to introduce an additional topology:

$$E = \left\{ \frac{1}{l^2 + i0}, \frac{1}{k^2 + i0}, \frac{1}{(l - k_g)^2 + i0}, \frac{1}{(k - l)^2 + i0}, \frac{1}{(k - l - k_\gamma)^2 + i0}, \right. \\ \left. \frac{1}{(k - k_g - k_\gamma)^2 + i0}, \frac{1}{k_g \cdot k + i0}, \frac{1}{n \cdot l + i0}, \delta(k_+ - 2E_\gamma u(\bar{u})) \right\}. \quad (10.74)$$

The master integrals required to evaluate all amplitudes are listed in Table 10.4.

Interestingly, some of the master integrals are derivatives of other master integrals. In Table 10.4, we denote these integrals as  $(G_{abcde\bar{f}ghi}^{D,E}(u))'$ , where the derivative is taken with respect to the variable  $u$  (or  $\bar{u}$ ) indicated in the brackets. These derivatives arise due to the presence of squared linear propagators. In particular, in the amplitudes they always appear in pairs:

$$\mathcal{A} \sim \left( \frac{1}{k_+ - 2E_\gamma u + i0} \right)^2 - \left( \frac{1}{k_+ - 2E_\gamma u - i0} \right)^2. \quad (10.75)$$

Using the Sokhotski–Plemelj identity for the derivative of the delta function,

$$\frac{1}{(x + i0)^2} - \frac{1}{(x - i0)^2} = -2i\pi\delta'(x), \quad (10.76)$$

we can write

$$\mathcal{A} \sim \delta'(k_+ - 2E_\gamma u). \quad (10.77)$$

Finally, since the only dependence on the variable  $u$  appears in the delta function, these master integrals with a derivative delta are simply the derivatives of the corresponding integrals with a standard delta function.

Most of the master integrals can be computed with full  $\varepsilon$ -dependence, yielding:

$$G_{101011001}^D(u) = -\frac{1}{2} \frac{(-2E_\gamma\omega_1)^{-2\varepsilon}}{(4\pi)^{4-2\varepsilon} E_\gamma} u^{-2\varepsilon} (1-u)^{-\varepsilon} \frac{\Gamma(\varepsilon)\Gamma(1-\varepsilon)\Gamma(2\varepsilon)}{1-2\varepsilon} \theta(u, 1-u), \quad (10.78)$$

$$G_{101110001}^D(u) = -\frac{1}{2} \frac{(-2E_\gamma\omega_1)^{-2\varepsilon}}{(4\pi)^{4-2\varepsilon} E_\gamma} u^{-1-\varepsilon} (1-u)^{1-2\varepsilon} \frac{\Gamma(-\varepsilon)\Gamma(1-\varepsilon)\Gamma(2\varepsilon)}{\Gamma(2-2\varepsilon)} \\ \times {}_2F_1\left(1, 1-\varepsilon, 2-2\varepsilon; \frac{u-1}{u}\right) \theta(u, 1-u), \quad (10.79)$$

Diagrams	Master integrals
(A)	$G_{010011001}^D(u), G_{010011001}^D(\bar{u}), G_{010011101}^D(u), G_{010011101}^D(\bar{u}),$ $G_{101011001}^D(u), G_{101011001}^D(\bar{u}), (G_{101011001}^D(u))', (G_{101011001}^D(\bar{u}))'$
(B)	$G_{010011001}^D(u), G_{010011001}^D(\bar{u}), G_{010011101}^D(u), G_{010011101}^D(\bar{u}),$ $G_{101011001}^D(u), G_{101011001}^D(\bar{u}), (G_{101011001}^D(u))', (G_{101011001}^D(\bar{u}))'$
(C)	$G_{010011001}^D(u), G_{010011001}^D(\bar{u}), G_{010011101}^D(u), G_{010011101}^D(\bar{u}),$ $G_{101011001}^D(u), G_{101011001}^D(\bar{u}), (G_{101011001}^D(u))', (G_{101011001}^D(\bar{u}))'$
(D)	$G_{010011001}^D(u), G_{010011001}^D(\bar{u}), G_{101011001}^D(u), G_{101011001}^D(\bar{u}),$ $G_{101110001}^D(u), G_{101110001}^D(\bar{u}), (G_{101110001}^D(u))', (G_{101110001}^D(\bar{u}))'$
(E)	$G_{010011001}^D(u), G_{010011001}^D(\bar{u}), G_{011101001}^D(u), G_{011101001}^D(\bar{u}),$ $G_{101011001}^D(u), G_{101011001}^D(\bar{u}), (G_{101011001}^D(u))', (G_{101011001}^D(\bar{u}))',$ $G_{101110001}^D(u), G_{101110001}^D(\bar{u}), (G_{101110001}^D(u))', (G_{101110001}^D(\bar{u}))',$ $G_{010111001}^D(u), G_{010111001}^D(\bar{u}), G_{011110001}^D(u), G_{011110001}^D(\bar{u}),$ $G_{111111001}^D(u), G_{111111001}^D(\bar{u}), (G_{111111001}^D(u))', (G_{111111001}^D(\bar{u}))',$ $G_{111121001}^D(u), G_{111121001}^D(\bar{u})$
(F)	$G_{010011001}^D(u), G_{010011001}^D(\bar{u}), G_{101011001}^D(u), G_{101011001}^D(\bar{u}),$ $(G_{101011001}^D(u))', (G_{101011001}^D(\bar{u}))', G_{101110001}^D(u), G_{101110001}^D(\bar{u}),$ $(G_{101110001}^D(u))', (G_{101110001}^D(\bar{u}))', G_{111111001}^E(u), (G_{111111001}^E(u))'$ $G_{111121001}^E(u)$

**Table 10.4:**  $u$ -dependent master integrals corresponding to the diagrams in Figure 10.4.

$$G_{011101001}^D(u) = G_{011}^A G_{0111}^B(u), \quad (10.80)$$

$$G_{010111001}^D(u) = \frac{1}{4} \frac{(-2E_\gamma \omega_1)^{-2\varepsilon}}{(4\pi)^{4-2\varepsilon} E_\gamma} u^{1-2\varepsilon} (1-u)^{-\varepsilon} \frac{\Gamma(1-\varepsilon)\Gamma(-\varepsilon)\Gamma(1+2\varepsilon)}{\varepsilon\Gamma(2-2\varepsilon)} \times {}_2F_1(1, 1-\varepsilon, 2-2\varepsilon; u) \theta(u, 1-u), \quad (10.81)$$

$$G_{011110001}^D(u) = \frac{1}{2} \frac{(-2E_\gamma \omega_1)^{-2\varepsilon}}{(4\pi)^{4-2\varepsilon} E_\gamma} u^{-1-\varepsilon} (1-u)^{1-2\varepsilon} \frac{\Gamma(-\varepsilon)\Gamma(1-\varepsilon)\Gamma(2\varepsilon)}{\Gamma(2-2\varepsilon)} \times {}_2F_1\left(1, 1-\varepsilon, 2-2\varepsilon; \frac{u-1}{u}\right) \theta(u, 1-u). \quad (10.82)$$

While the previous master integrals are sufficient to compute diagrams (A)–(D), evaluating diagrams (E) and (F) requires additional master integrals, as indicated in Table 10.4. These remaining integrals are particularly challenging and cannot be computed analytically with full  $\varepsilon$ -dependence. For these cases, we employ the differential equation method presented

in 10.1.3. In particular, we outline here the main steps to evaluate the master integrals related to diagram (F), namely:  $G_{111111001}^E(u)$ ,  $(G_{111111001}^E(u))'$ , and  $G_{111121001}^E(u)$ . The first step, as in the one-loop  $u$ -dependent amplitude, is to derive the system of differential equations. Since the dependence on  $\omega_1$  and  $E_\gamma$  can be trivially inferred from dimensional analysis, as discussed above, we focus solely on the dependence on the variable  $u$ . We choose the following vector of independent master integrals:

$$v(u) = \left( G_{110011001}^E(u), G_{100111001}^E(u), G_{100101001}^E(u), G_{011110001}^E(u), G_{011101001}^E(u), \right. \\ \left. G_{011010001}^E(u), G_{211111001}^E(u), G_{121111001}^E(u), G_{111111001}^E(u) \right)^T. \quad (10.83)$$

In particular, while we directly require  $G_{111111001}^E(u)$ , the integrals  $(G_{111111001}^E(u))'$  and  $G_{111121001}^E(u)$  can be derived via IBP identities once the results for  $G_{121111001}^E(u)$  and  $G_{211111001}^E(u)$  are known, respectively<sup>2</sup>.

The differential equation for this set of master integrals then takes the form

$$v'(u) = A(u, \varepsilon)v(u), \quad (10.84)$$

with the matrix  $A(u, \varepsilon)$  given in Appendix F along with several additional details and explicit expressions for this computation. While in the one-loop case we could solve the equation directly, here it is not possible to find an analytic solution at all orders in  $\varepsilon$ . However, we employ the Mathematica package `CANONICA` [237] to find a rational transformation that changes the basis of master integrals such that the differential equation is in canonical form [238, 239], namely,

$$v'_c(u) = \varepsilon A_c(u)v_c(u), \quad (10.85)$$

where now the matrix does not depend on the dimensional regulator  $\varepsilon$  and is explicitly provided in Appendix F. This system can now be solved order by order in  $\varepsilon$  in terms of iterated integrals, such as multiple polylogarithms [240].

The solution can be expressed in fully analytic form once the integration constants are fixed. In our case, we can determine all constants related to the first six master integrals contained in  $v(u)$ , since we computed them in full  $\varepsilon$ -dependence. For the last three master integrals, we adopt a procedure analogous to that used in the one-loop example. In particular, the results of diagrams (E) and (F), once integrated over  $u$ , must reproduce the same results obtained in the previous section in (10.63) and (10.64). Imposing these conditions allows us to fix all the integration constants needed to complete the computation. The results for these master integrals are provided in Appendix F and have been cross-checked numerically using the package `AMFlow` [241].

Utilising these master integrals, we can now compute the amplitudes for diagrams (A)–(F). Similarly to (10.70), we can write for diagrams (A) and (D):

$$\mathcal{A}_{\text{NLO}}^{(A),(D)}(u) = \frac{g_s \alpha_s Q_u C_F E_\gamma}{(4\pi)^3} \left( \frac{-2E_\gamma \omega_1}{\mu^2} \right)^{-2\varepsilon} \bar{u}_{hc,L}^{(s)} \left[ f_{A,D}(u) \not{\epsilon}_{s,\perp}^*(k_g) \not{\epsilon}_\perp^*(k_\gamma) \right. \\ \left. - f_{A,D}(\bar{u}) \not{\epsilon}_\perp^*(k_\gamma) \not{\epsilon}_{s,\perp}^*(k_g) \right] \not{q} b_L, \quad (10.86)$$

<sup>2</sup>Clearly,  $(G_{111111001}^E(u))'$  can also be obtained simply by differentiating  $G_{111111001}^E(u)$  with respect to  $u$ .

for diagrams (B) and (E)

$$\begin{aligned} \mathcal{A}_{\text{NLO}}^{(\text{B}),(\text{E})}(u) = & \frac{g_s \alpha_s Q_u (C_F - 1/2 C_A) E_\gamma}{(4\pi)^3} \left( \frac{-2E_\gamma \omega_1}{\mu^2} \right)^{-2\varepsilon} \bar{u}_{hc,L}^{(s)} \left[ f_{\text{B,E}}(u) \not{\epsilon}_{s,\perp}^*(k_g) \not{\epsilon}_\perp^*(k_\gamma) \right. \\ & \left. - f_{\text{B,E}}(\bar{u}) \not{\epsilon}_\perp^*(k_\gamma) \not{\epsilon}_{s,\perp}^*(k_g) \right] \not{b}_L, \end{aligned} \quad (10.87)$$

and finally for diagrams (C) and (F)

$$\begin{aligned} \mathcal{A}_{\text{NLO}}^{(\text{C}),(\text{F})}(u) = & \frac{g_s \alpha_s Q_u C_A E_\gamma}{(4\pi)^3} \left( \frac{-2E_\gamma \omega_1}{\mu^2} \right)^{-2\varepsilon} \bar{u}_{hc,L}^{(s)} \left[ f_{\text{C,F}}(u) \not{\epsilon}_{s,\perp}^*(k_g) \not{\epsilon}_\perp^*(k_\gamma) \right. \\ & \left. - f_{\text{C,F}}(\bar{u}) \not{\epsilon}_\perp^*(k_\gamma) \not{\epsilon}_{s,\perp}^*(k_g) \right] \not{b}_L. \end{aligned} \quad (10.88)$$

The corresponding  $u$ -dependent functions are given by

$$f_{\text{A}}(u) = \frac{1}{\varepsilon} (1-u) \left[ 4 - u \log \left( \frac{1}{u} - 1 \right) \right] + \mathcal{O}(\varepsilon^0), \quad (10.89)$$

$$f_{\text{B}}(u) = \frac{1}{\varepsilon} (1-u) u \log \left( \frac{1}{u} - 1 \right) + \mathcal{O}(\varepsilon^0), \quad (10.90)$$

$$f_{\text{C}}(u) = \frac{1}{\varepsilon} (1-u) \left( 3u \tanh^{-1}(1-2u) - \frac{\pi^2}{6} - 2 \right) + \mathcal{O}(\varepsilon^0), \quad (10.91)$$

$$f_{\text{D}}(u) = -\frac{1}{\varepsilon} u \left( 2u \tanh^{-1}(1-2u) - \log[(1-u)u^3] \right) + \mathcal{O}(\varepsilon^0), \quad (10.92)$$

$$f_{\text{E}}(u) = -\frac{2}{\varepsilon} (1-u) \left( u \tanh^{-1}(1-2u) + 1 \right) + \mathcal{O}(\varepsilon^0), \quad (10.93)$$

$$f_{\text{F}}(u) = -\frac{1}{6\varepsilon} \left[ (u-1)(\pi^2 - 9u \log(1-u)) + 3u(3u+1) \log(u) \right] + \mathcal{O}(\varepsilon^0), \quad (10.94)$$

where, once again, the finite terms are provided in Appendix E. Integrating over the variable  $u$  reproduces the results of the previous section. In particular, it is noteworthy that the  $1/\varepsilon$  poles of the sum of diagrams in Figure 10.4 do not cancel when the  $u$ -dependence is retained, but only after performing the integration over  $u$ .

Finally, summing all contributions, we obtain

$$\begin{aligned} \mathcal{A}_{\text{NLO}}^u(u) = & \frac{g_s \alpha_s Q_u E_\gamma}{(4\pi)^3} \left( \frac{-2E_\gamma \omega_1}{\mu^2} \right)^{-2\varepsilon} \bar{u}_{hc,L}^{(s)} \left[ f_{\text{NLO}}^u(u) \not{\epsilon}_{s,\perp}^*(k_g) \not{\epsilon}_\perp^*(k_\gamma) \right. \\ & \left. - f_{\text{NLO}}^u(\bar{u}) \not{\epsilon}_\perp^*(k_\gamma) \not{\epsilon}_{s,\perp}^*(k_g) \right] \not{b}_L, \end{aligned} \quad (10.95)$$

where the  $u$ -dependent function reads

$$\begin{aligned}
f_{\text{NLO}}^u(u) = & -\frac{C_A}{\varepsilon^2} 4\bar{u} \\
& + \frac{2}{\varepsilon} \left\{ \frac{C_A}{2} \left[ 2(u^2 \tanh^{-1}(\bar{u} - u) + 4u - 6) + (6 - 7u) \log(\bar{u}u) \right] \right. \\
& \quad \left. + C_F \left[ \bar{u} + 2u \log(u) \right] \right\} \\
& - 3C_A \left\{ 8u \text{Li}_2(u) - u \left( 43 + \frac{4}{3}\pi^2 \right) + \log(\bar{u}) [19u - 25 + 16\bar{u} \log(u)] \right. \\
& \quad - \log(u) [(u + 5)(3u - 2) \log(u) + (36 - 33u)] - 12u^2 \tanh^{-1}(\bar{u} - u) \\
& \quad \left. - \bar{u}(3u - 10) \log^2(\bar{u}) + 67 \right\} \\
& + 6C_F \left\{ 8u \text{Li}_2(u) - \frac{4}{3}u(6 + \pi^2) + 6\bar{u} \log(\bar{u}) - 2u \log(u) [3 \log(u) - 8] + 10 \right\} \\
& + \mathcal{O}(\varepsilon).
\end{aligned} \tag{10.96}$$

# Cancellation of Singularities among the NLO-Improved Functions

After computing the  $\mathcal{O}(\alpha_s)$  corrections to all functions entering the factorisation formula (8.6), we now demonstrate that all singularities cancel in their sum. This provides both an important cross-check of the correctness of our computations and a non-trivial test of the entire factorisation framework.

As already discussed in Subsection 9.1.3, the mixing contribution  $\Delta Z_{17}$ , which could potentially spoil factorisation, vanishes once convoluted with the jet functions. As an additional consistency check, we show in this chapter that the corresponding poles are not required to achieve complete pole cancellation.

We start from the factorisation formula (8.6), omitting prefactors that are irrelevant for the present discussion:

$$d\Gamma(\bar{B} \rightarrow X_s \gamma) \sim \int_0^1 du H(u; \mu) \int_{-\infty}^{\infty} \frac{d\omega_1}{\omega_1 + i0} J^{(\bar{n})}(u, \omega_1; \mu) \int_{-\infty}^{\bar{\Lambda}} d\omega J^{(n)}(\omega; \mu) g_{17}(\omega, \omega_1; \mu). \quad (11.1)$$

To establish pole cancellation at NLO, we consider one function at  $\mathcal{O}(\alpha_s)$  at a time, keeping all others at LO. Particular care must be taken with the convolution structure: the hard function  $H(u; \mu)$  is convoluted in  $u$  with the  $\bar{n}$ -jet function, while  $g_{17}(\omega, \omega_1; \mu)$  is convoluted with both jet functions, namely with  $J^{(\bar{n})}(u, \omega_1; \mu)$  in the variable  $\omega_1$  and with  $J^{(n)}(\omega; \mu)$  in the variable  $\omega$ . Since  $H(u) = 1 + \mathcal{O}(\alpha_s)$  in (11.1), it suffices to compute the  $u$ -integral of the NLO bare  $\bar{n}$ -jet function  $J^{(\bar{n})}(u, \omega_1; \mu)$  in order to explicitly verify the pole cancellation at this order, as we shall see shortly.

Let us begin with the hard function at NLO. After UV renormalisation, the IR poles are given in Equations (8.9) and (8.12). Their sum reads

$$\begin{aligned} H_{\text{poles}}(u; \mu) &= H_1^{\text{poles}} + H_7^{\text{poles}} \\ &= -\frac{\alpha_s C_F}{4\pi} \left( \frac{2}{\varepsilon^2} + \frac{5}{\varepsilon} + \frac{2}{\varepsilon} \log \frac{\mu^2}{p_-^2} \right) - \frac{\alpha_s C_A}{4\pi} \left[ \frac{1}{\varepsilon^2} + \frac{1}{\varepsilon} \left( \log \frac{\mu^2}{p_-^2 u(u-1)} + \frac{3}{2} \right) \right], \end{aligned} \quad (11.2)$$

where we imposed the kinematic condition  $p_- = m_b$ . Considering the poles of the hard

function at  $\mathcal{O}(\alpha_s)$  while keeping the other functions at LO (superscript (0)), we obtain

$$\int_0^1 du H_{\text{poles}}(u; \mu) \int_{-\infty}^{\infty} \frac{d\omega_1}{\omega_1 + i0} J^{(\bar{n}), (0)}(u, \omega_1; \mu) \int_{-\infty}^{\bar{\Lambda}} d\omega J^{(n), (0)}(\omega; \mu) g_{17}^{(0)}(\omega, \omega_1; \mu), \quad (11.3)$$

where  $J^{(\bar{n}), (0)}(u, \omega_1; \mu)$  is the one-loop  $u$ -dependent  $\bar{n}$ -jet function from Equation (10.35),  $J^{(n), (0)}(\omega; \mu) = \delta(\omega + p_+)$ , and  $g_{17}^{(0)}(\omega, \omega_1; \mu)$  is the tree-level subleading shape function. Performing the  $u$ -integral yields

$$\begin{aligned} & -\frac{\alpha_s}{4\pi} \int_{-\infty}^{\infty} \frac{d\omega_1}{\omega_1 + i0} J^{(\bar{n}), (0)}(\omega_1; \mu) \int_{-\infty}^{\bar{\Lambda}} d\omega J^{(n), (0)}(\omega; \mu) g_{17}^{(0)}(\omega, \omega_1; \mu) \\ & \times \left\{ C_F \left[ \frac{2}{\varepsilon^2} + \frac{1}{\varepsilon} \left( 5 + 2 \log \frac{\mu^2}{p_-^2} \right) \right] + C_A \left[ \frac{1}{\varepsilon^2} + \frac{1}{\varepsilon} \left( \log \frac{\mu^2}{p_-^2} + \frac{7}{2} + i\pi \right) \right] \right\}, \end{aligned} \quad (11.4)$$

where  $J^{(\bar{n}), (0)}(\omega_1; \mu)$  denotes the  $u$ -integrated one-loop  $\bar{n}$ -jet function given in (10.11). We emphasise that all poles in (11.4) are IR in origin and must cancel against the UV poles of the jet functions.

Next, we consider the  $n$ -jet function at NLO. Its poles, obtained from Equation (8.18), read

$$J_{\text{poles}}^{(n)}(\omega; \mu) = \frac{\alpha_s}{4\pi} C_F \left[ \frac{4}{\varepsilon^2} + \frac{1}{\varepsilon} \left( 3 - 4 \log \frac{-p_-(\omega + p_+) - i0}{\mu^2} \right) \right], \quad (11.5)$$

where we used the kinematic relation  $Q^2 = -p_-(p_+ + \omega)$ . Substituting this into the factorisation formula gives

$$\begin{aligned} & \frac{\alpha_s}{4\pi} \int_{-\infty}^{\infty} \frac{d\omega_1}{\omega_1 + i0} J^{(\bar{n}), (0)}(\omega_1; \mu) \int_{-\infty}^{\bar{\Lambda}} d\omega J^{(n), (0)}(\omega; \mu) g_{17}^{(0)}(\omega, \omega_1; \mu) \\ & \times \left\{ C_F \left[ \frac{4}{\varepsilon^2} + \frac{1}{\varepsilon} \left( 3 - 4 \log \frac{-p_-(\omega + p_+) - i0}{\mu^2} \right) \right] \right\}. \end{aligned} \quad (11.6)$$

Similarly, the poles of the two-loop  $\bar{n}$ -jet function, given in Equation (10.95), lead to a trivial  $u$ -integral when the hard function is at LO. In this case we obtain

$$\begin{aligned} & \frac{\alpha_s}{4\pi} \int_{-\infty}^{\infty} \frac{d\omega_1}{\omega_1 + i0} J^{(\bar{n}), (0)}(\omega_1; \mu) \int_{-\infty}^{\bar{\Lambda}} d\omega J^{(n), (0)}(\omega; \mu) g_{17}^{(0)}(\omega, \omega_1; \mu) \\ & \times \left\{ C_A \left[ \frac{2}{\varepsilon^2} + \frac{1}{\varepsilon} \left( \frac{11}{2} + 2 \log \frac{-\mu^2}{2E_\gamma \omega_1} \right) \right] \right\}. \end{aligned} \quad (11.7)$$

The remaining contribution involves the UV poles of the shape function  $g_{17}$ , which cancel the IR poles of the jet functions. These poles are given in Equations (9.26) and (9.38) for the abelian and non-abelian terms, respectively. To perform the convolution between the poles of  $g_{17}$  and the jet functions, we make use of the following distributional identities:

$$\begin{aligned} & \int_{-\infty}^{\infty} d\omega_1 \frac{1}{\omega_1 + i0} \int_{-\infty}^{\infty} d\omega'_1 \left( \frac{\omega_1}{\omega_1'^2} \right) [\theta(\omega_1)\theta(\omega'_1 - \omega_1) - \theta(-\omega_1)\theta(\omega_1 - \omega'_1)] f(\omega'_1) \\ & = \int_{-\infty}^{+\infty} d\omega_1 \frac{1}{\omega_1 + i0} f(\omega_1), \end{aligned} \quad (11.8)$$

$$\int_{-\infty}^{\infty} d\omega_1 \frac{1}{\omega_1 + i0} \int_{-\infty}^{\infty} d\omega'_1 H_+(\omega_1, \omega'_1) f(\omega'_1) = \int_{-\infty}^{\infty} d\omega_1 \frac{1}{\omega_1 + i0} (2i\pi\theta(-\omega_1)) f(\omega_1), \quad (11.9)$$

and

$$\int_{-\infty}^{\bar{\Lambda}} d\omega \frac{1}{\omega + p_+ + i0} \int_{-\infty}^{\bar{\Lambda}} d\omega' \left[ \frac{\theta(\omega' - \omega)}{\omega' - \omega} \right]_+ f(\omega') = \int_{-\infty}^{\bar{\Lambda}} d\omega \frac{1}{\omega + p_+ + i0} \log \frac{-p_+ - \omega}{\bar{\Lambda} - \omega} f(\omega). \quad (11.10)$$

Applying these identities to the  $Z$ -factors in Equations (9.26) and (9.38), we obtain for the UV poles of  $g_{17}$ :

$$\begin{aligned} & -\frac{\alpha_s}{4\pi} \int_{-\infty}^{\infty} \frac{d\omega_1}{\omega_1 + i0} J^{(\bar{n}), (0)}(\omega_1; \mu) \int_{-\infty}^{\bar{\Lambda}} d\omega J^{(n), (0)}(\omega; \mu) g_{17}^{(0)}(\omega, \omega_1; \mu) \\ & \times \left\{ C_F \left[ \frac{2}{\epsilon^2} - \frac{1}{\epsilon} \left( 2 + 2 \log \frac{(p_+ + \omega)^2}{\mu^2} \right) \right] + C_A \left[ \frac{1}{\epsilon^2} + \frac{1}{\epsilon} \left( 2 + \log \frac{\mu^2}{\omega_1^2} + i\pi - 2\pi i\theta(-\omega_1) \right) \right] \right\}. \end{aligned} \quad (11.11)$$

Finally, summing the contributions in (11.4), (11.6), (11.7), and (11.11), we find that they cancel exactly, thus proving that all the  $1/\epsilon$  poles vanish in the sum of the four contributions.



# Chapter 12

## Conclusion of Part II

In Part II, we incorporated  $\mathcal{O}(\alpha_s)$  radiative corrections to the resolved-photon contribution from the  $Q_1^q - Q_{7\gamma}$  interference in  $\bar{B} \rightarrow X_s \gamma$ . These corrections are expected to reduce the sizeable scale ambiguity and charm-mass dependence of the leading-order result, which currently represent one of the dominant sources of theoretical uncertainty.

Based on the factorisation formula for this resolved contribution, we have rederived and reviewed the known results for the hard and  $n$ -jet functions. The central achievements of this part of the thesis concern two technically demanding ingredients: the computation of the two-loop  $\bar{n}$ -jet function and the renormalisation of the subleading shape function  $g_{17}(\omega, \omega_1; \mu)$ .

The shape function  $g_{17}$  encodes non-perturbative soft dynamics in the resolved-photon contribution. We showed that its operator definition must be refined to distinguish fields in the amplitude and its conjugate, which can be achieved using the Keldysh formalism. With this definition, the anomalous dimension of  $g_{17}$  decomposes into two terms, each depending only on a single light-cone momentum variable,  $\omega$  or  $\omega_1$ . Consequently, the RG equation factorises into two simpler equations, for which we provided analytic momentum-space solutions and a qualitative discussion of their phenomenological implications.

Motivated by these insights, we extended the analysis to a related amplitude-level soft function  $\Phi_G(\omega, \omega_1; \mu)$ , relevant for exclusive  $\bar{B}_{d,s} \rightarrow \gamma\gamma$  decays. We confirmed recent results for its anomalous dimension and showed that, despite the presence of seemingly factorisation-violating terms, their effect vanishes after convolution with jet functions due to analytic properties of the integrands. This allows for a “reduced” RG equation, whose structure closely resembles the Lange–Neubert kernel in both momentum variables, considerably simplifying the resummation of large logarithms.

Additionally, we computed the NLO (two-loop) corrections to the massless (up-quark)  $\bar{n}$ -jet function in two different forms: first in the integrated form, where the anti-hard-collinear momentum fraction  $u$  is already integrated, and second in full  $u$ -dependence, where the explicit dependence on  $u$  is retained. The second case is technically more demanding, as it requires handling two-loop integrals involving delta functions depending on one light-cone component of the loop momentum.

We systematically derived all the necessary master integrals and evaluated them using different methods, chosen according to the level of complexity of the individual integrals. Relying on the smooth limit  $m_c \rightarrow 0$ , the correct singularity structure of the function is fixed. By explicitly extracting all  $1/\epsilon$  poles, we verified that the divergences cancel when the four contributing functions are combined. This cancellation represents a non-trivial and

important cross check of the internal consistency of the factorisation theorem at NLO and of the presented computations.

For the outlook, the only remaining step toward a complete NLO analysis of the  $Q_1^c - Q_{7\gamma}$  interference is the inclusion of charm-mass effects in the finite parts of the  $\bar{n}$ -jet function. This technically challenging task is left for future work.

# Epilogue

The research presented in this thesis has explored two complementary frontiers in the study of physics beyond the Standard Model, connected through the unifying language of Effective Field Theories. The guiding motivation, outlined in the Preface, was to demonstrate how higher-order corrections and renormalisation group evolution constitute indispensable ingredients both for the consistent interpretation of high-energy precision data and for the reliable prediction of low-energy flavour observables. In the first part, we carried out a comprehensive global analysis of the SMEFT under a  $U(3)^5$  flavour symmetry. This study established one of the most complete and systematic assessments of dimension-six operators in the literature, combining a broad spectrum of observables with refined theoretical predictions. By incorporating NLO corrections and RGE effects, we highlighted how constraints on Wilson coefficients are significantly reshaped, revealing both strengthened bounds in certain directions and new correlations that demand careful treatment. The methodological lesson is clear: robust SMEFT analyses must be global in scope, balanced across diverse experimental inputs, and systematically improved with higher-order effects. In this sense, the work sets the stage for future fits of even greater breadth and precision, and for extensions to more general flavour structures.

In the second part, attention turned to the low-energy regime, where the inclusive  $\bar{B} \rightarrow X_s \gamma$  decay provides a fertile ground to test the Standard Model at high precision. By advancing the NLO analysis of the  $Q_1^q - Q_{7\gamma}$  interference, this thesis contributed key missing elements: the renormalisation of the subleading shape function, the factorisation of its RG evolution, and the computation of a technically challenging two-loop jet function. These achievements not only improve the theoretical uncertainties in an observable central to flavour physics, but also shed light on crucial technical details related to the internal consistency of the factorisation framework itself. While a complete treatment of charm-mass effects remains open, the results obtained here provide a firm foundation for the next step.

Taken together, both approaches underscore a common message: only through the consistent inclusion of NLO corrections and RGE effects can EFTs fulfil their promise as precision tools, bridging energy scales and connecting theory to experiment. Looking forward, the path opened by this thesis is twofold. On the high-energy side, extending global SMEFT analyses to full NLO coverage and more general flavour scenarios will be essential for extracting maximal information from upcoming collider and precision measurements. On the low-energy side, completing the NLO treatment of the  $\bar{B} \rightarrow X_s \gamma$  decay and extending similar methods to related processes will enhance the sensitivity of flavour observables to physics beyond the Standard Model. In both domains, the interplay between improved theory and new data will remain the key driver of progress.

In conclusion, this thesis has aimed to contribute to the ongoing effort of sharpening the theoretical tools with which we probe the Standard Model and its possible extensions. By advancing precision in both SMEFT global analyses and SCET-based flavour observables, it reinforces the view that the quest for new physics is not confined to a single energy scale, but rather unfolds across the entire spectrum of experimental opportunities united by the effective field theory framework.

# Appendices



## A Observables

We list the observables included in our analysis in Tables 1-4. Table 1 lists observables from Higgs physics, LHC diboson and  $Zjj$  production, Tables 2 and 3 list observables from the top sector as well as Drell-Yan and dijet+photon data, and Table 4 lists observables from EWPO, PVE, lepton scattering and flavour.

**Table 1:** Higgs and electroweak observables included in the fit.

Observables		no. of measurements	scale(s)	References
<b>Higgs Data</b>		159		
7 and 8 TeV	ATLAS & CMS combination	20	$M_H$	Table 8 of Ref. [242]
	ATLAS & CMS combination $\mu(h \rightarrow \mu\mu)$	1	$M_H$	Table 13 of Ref. [242]
Run-I data	ATLAS $\mu(h \rightarrow Z\gamma)$	1	$M_H$	Figure 1 of Ref. [243]
13 TeV ATLAS Run-II data	$\mu(h \rightarrow Z\gamma)$ at 139 fb <sup>-1</sup>	1	$M_H$	[244]
	$\mu(h \rightarrow \mu\mu)$ at 139 fb <sup>-1</sup>	1	$M_H$	[245]
	$\mu(h \rightarrow \tau\tau)$ at 139 fb <sup>-1</sup>	4	$M_H$	Figure 14 of Ref. [246]
	$\mu(h \rightarrow bb)$ in VBF and $ttH$ at 139 fb <sup>-1</sup>	1+1	$M_H$	[247, 248]
	STXS $h \rightarrow \gamma\gamma/ZZ/b\bar{b}$ at 139 fb <sup>-1</sup>	42	$\sqrt{M_H^2 + (p_T^H)^2}$	Figures 1 and 2 of Ref. [249]
	STXS $h \rightarrow WW$ in ggF, VBF at 139 fb <sup>-1</sup>	11	$\sqrt{M_H^2 + (p_T^H)^2}$	Figures 12 and 14 of Ref. [250]
	di-Higgs $\mu_{HH}^{bb\bar{b}\bar{b}}, \mu_{HH}^{bb\tau\bar{\tau}}, \mu_{HH}^{bb\gamma\gamma}$	3	$M_H$	[251-253]
13 TeV CMS Run-II data	$\mu(h \rightarrow b\bar{b})$ in $Vh$ at 35.9/41.5 fb <sup>-1</sup>	2	$M_H$	Table 4 of Ref. [254]
	$\mu(h \rightarrow WW)$ in ggF at 137 fb <sup>-1</sup>	1	$M_H$	[255]
	$\mu(h \rightarrow \mu\mu)$ at 137 fb <sup>-1</sup>	4	$M_H$	Figure 11 of Ref. [256]
	$\mu(h \rightarrow \tau\tau/WW)$ in $t\bar{t}h$ at 137 fb <sup>-1</sup>	3	$M_H$	Figure 14 of Ref. [257]
	STXS $h \rightarrow WW$ at 137 fb <sup>-1</sup> in $Vh$	4	$\sqrt{M_H^2 + (p_T^H)^2}$	Table 9 of Ref. [258]
	STXS $h \rightarrow \tau\tau$ at 137 fb <sup>-1</sup>	11	$\sqrt{M_H^2 + (p_T^H)^2}$	Figures 11/12 of Ref. [259]
	STXS $h \rightarrow \gamma\gamma$ at 137 fb <sup>-1</sup>	27	$\sqrt{M_H^2 + (p_T^H)^2}$	Table 13 and Figure 21 of Ref. [260]
	STXS $h \rightarrow ZZ$ at 137 fb <sup>-1</sup>	18	$\sqrt{M_H^2 + (p_T^H)^2}$	Table 6 and Figure 15 of Ref. [261]
	di-Higgs $\mu_{HH}^{bb\bar{b}\bar{b}}, \mu_{HH}^{bb\tau\bar{\tau}}, \mu_{HH}^{bb\gamma\gamma}$	3	$M_H$	[262-264]
ATLAS $Zjj$ 13 TeV $\Delta\phi_{jj}$ at 139 fb <sup>-1</sup>		12	$M_Z$	Figure 7(d) of Ref. [265]
ATLAS $WZ$ 13 TeV $p_T^Z$ at 36.1 fb <sup>-1</sup>		7	$\sqrt{M_Z^2 + (p_T^Z)^2}$	Figure 4(a) of Ref. [167]
ATLAS $WW$ 13 TeV $p_T^{\ell, \text{lead}}$ at 36.1 fb <sup>-1</sup>		14	$\sqrt{M_W^2 + (p_T^{\ell, \text{lead}})^2}$	Figure 7(a) of Ref. [168]

**Table 2:** Top physics observables from Tevatron and LHC Run I included in the fit.

Observables		no. of meas.	scale(s)	References
<b>Top Data from Tevatron and LHC Run I</b>		82		
Tevatron	forward-backward asymmetry $A_{FB}(m_{t\bar{t}})$ for $t\bar{t}$ production	4	$\max(m_t, m_{t\bar{t}})$	[266]
ATLAS & CMS	charge asymmetry $A_C(m_{t\bar{t}})$ for $t\bar{t}$ production in the $\ell$ +jets channel	6	$\max(m_t, m_{t\bar{t}})$	[267]
	$W$ -boson helicity fractions in top decay	3	$m_t$	[268]
ATLAS	charge asymmetry $A_C(m_{t\bar{t}})$ for $t\bar{t}$ production in the dilepton channel	1	$m_t$	[269]
	$\sigma_{t\bar{t}W}, \sigma_{t\bar{t}Z}$	2	$m_t$	[270]
	$\frac{d\sigma}{dp_t^T}, \frac{d\sigma}{d y_{t\bar{t}} }$ for $t$ -channel single-top production	4 + 5	$\sqrt{m_t^2 + (p_T^t)^2}, m_t$	[271]
	$\sigma_{tW}$ in the single lepton channel	1	$m_t$	[272]
	$\sigma_{tW}$ in the dilepton channel	1	$m_t$	[273]
	$s$ -channel single-top cross section	1	$m_t$	[274]
	$\frac{d\sigma}{dm_{t\bar{t}}}$ for $t\bar{t}$ production in the dilepton channel	6	$m_{t\bar{t}}$	[275]
	$\frac{d\sigma}{dp_t^T}$ for $t\bar{t}$ production in the $\ell$ +jets channel	8	$\sqrt{m_t^2 + (p_T^t)^2}$	[276]
CMS	$\sigma_{t\bar{t}\gamma}$ in the $\ell$ + jets channel	1	$m_t$	[277]
	charge asymmetry $A_C(m_{t\bar{t}})$ for $t\bar{t}$ production in the dilepton channel	3	$\max(m_t, m_{t\bar{t}})$	[278]
	$\sigma_{t\bar{t}W}, \sigma_{t\bar{t}Z}$	2	$m_t$	[277]
	$\sigma_{t\bar{t}\gamma}$ in the $\ell$ + jets channel.	1	$m_t$	[279]
	$s$ -channel single-top cross section	1	$m_t$	[280]
	$\frac{d\sigma}{dp_T^{t+\bar{t}}}$ of $t$ -channel single-top production	6	$\sqrt{m_t^2 + (p_T^t)^2}$	[281]
	$t$ -channel single-top and anti-top cross sections $R_t$	1	$m_t$	[282]
	$\sigma_{tW}$	1	$m_t$	[283]
	$\frac{d\sigma}{dm_{t\bar{t}}d y_{t\bar{t}} }$ for $t\bar{t}$ production in the dilepton channel	16	$m_{t\bar{t}}$	[169, 170]
	$\frac{d\sigma}{dp_t^T}$ for $t\bar{t}$ production in the $\ell$ +jets channel	8	$\sqrt{m_t^2 + (p_T^t)^2}$	[284, 285]

**Table 3:** Top physics observables from LHC Run II as well as data from Drell-Yan and dijet+photon production included in the analysis.

Observables		no. of meas.	scale(s)	References
<b>Top Data from LHC Run II</b>		55		
ATLAS	$\sigma_{tW}$	1	$m_t$	[286]
	$\sigma_{tZ}$	1	$m_t$	[287]
	$\sigma_{t+\bar{t}}$ , $R_t$ for $t$ -channel single-top and anti-top cross sections	1+1	$m_t$	[288]
	charge asymmetry $A_C(m_{t\bar{t}})$ for $t\bar{t}$ production	5	$\max(m_t, m_{t\bar{t}})$	[289]
	$\sigma_{t\bar{t}W}$ , $\sigma_{t\bar{t}Z}$	2	$m_t$	[290]
	$\frac{d\sigma}{dp_T^\gamma}$ for $t\bar{t}\gamma$ production	11	$\sqrt{m_t^2 + (p_T^\gamma)^2}$	[291]
CMS	$\sigma_{tW}$	1	$m_t$	[292]
	$\sigma_{tZ}$ in the $Z \rightarrow \ell^+\ell^-$ channel	1	$m_t$	[293]
	$\frac{d\sigma}{dp_T^{t+\bar{t}}}$ and $R_t(p_T^{t+\bar{t}})$ for $t$ -channel single-top quark production	5 + 5	$\sqrt{m_t^2 + (p_T^Z)^2}$	[294]
	$\frac{d\sigma}{dm_{t\bar{t}}}$ for $t\bar{t}$ production in the dilepton channel	6	$m_{t\bar{t}}$	[295]
	$\frac{d\sigma}{dm_{t\bar{t}}}$ for $t\bar{t}$ production in the $\ell$ +jets channel	15	$m_{t\bar{t}}$	[296]
	$\sigma_{t\bar{t}W}$	1	$m_t$	[297]
	$\frac{d\sigma}{dp_T^Z}$ for $t\bar{t}Z$ production	4	$\sqrt{m_t^2 + (p_T^Z)^2}$	[298]
<b>Drell-Yan</b>		109		
13 TeV	CMS $e^+e^-$ , $m_{ee}$	61 (up to 3 TeV)	$m_{ee}$	Figure 2 of [299]
	CMS $\mu^+\mu^-$ , $m_{\mu\mu}$	34 (up to 3 TeV)	$m_{\mu\mu}$	Figure 2 of [299]
	ATLAS $\tau^+\tau^-$ , $m_T^{\text{tot}}$	14 (up to 3 TeV)	$m_T^{\text{tot}}$	Figure 1 of [300]
<b>Dijets+photon</b>		26		
13 TeV	ATLAS $\frac{dN_{\text{ext}}}{dm_{jj}}$ for $pp \rightarrow jj\gamma + X$	26 (from 500 GeV)	$m_{jj}$	Figure 1 of [152]

**Table 4:** EWPO, PVE, lepton scattering and flavour observables included in the fit. For a summary of the experimental input values of the EWPO observables used, see also Tab. 3 of [93]. \* For scales below 5 GeV, we only include the LEFT RGE up to this scale. We explicitly checked that the evolution below 5 GeV is almost negligible when compared with the evolution between  $\Lambda$  and  $m_b$ .

Observables		no. of measurements	scale(s)	References
<b>Electroweak Precision Observables (EWPO)</b>		19	$M_Z$	[129]
<b>PVE and lepton scattering</b>		163		
PVE	$Q_W^{\text{Cs}}$	1	0.1 GeV*	[139]
	$Q_W^{\text{p}}$	1	0.1 GeV*	[140]
	$A_{1,2}^{\text{PVDIS}}$	2	1 GeV*	[141]
	SAMPLE	1	0.2 GeV*	[142]
lepton scattering	$\nu_\mu \nu_\mu ee$	2	0.1 GeV*	[139]
	$P_\tau, A_P$	2	58 GeV	[143]
	$g_{AV}^{ee}$ in $e^- e^- \rightarrow e^- e^-$	1	0.16 GeV*	[139]
	$A_{\text{FB}}^{\mu\tau}$ in $e^+ e^- \rightarrow l^+ l^-$	24	$\sqrt{s}_{\text{LEP}}$	[130, 144]
	$\sigma_{\mu,\tau}$ in $e^+ e^- \rightarrow l^+ l^-$	24	$\sqrt{s}_{\text{LEP}}$	[130, 144]
	$\frac{d\sigma(ee)}{d\cos\theta}$ in $e^+ e^- \rightarrow l^+ l^-$	105	$\sqrt{s}_{\text{LEP}}$	[130, 144]
<b>Flavour</b>		37		
Differential BR( $B \rightarrow K\mu\mu$ ) (from 14 GeV)		3		[301]
Differential BR( $B \rightarrow K^*\mu\mu$ ) (from 14 GeV)		3	$m_b$	[302]
Differential BR( $\Lambda_b \rightarrow \Lambda\mu\mu$ ) (from 15 GeV)		1		[303]
BR( $B \rightarrow X_s\mu\mu, \mu\mu, X_s\gamma, K^*\gamma, K^{(*)}\bar{\nu}\nu$ )		5	$m_b$	[304–308]
BR( $B_s \rightarrow \mu\mu, \phi\gamma$ )		2	$m_b$	[305, 309]
BR( $K^+ \rightarrow \mu^+\nu_\mu$ )		1	$m_c^*$	[310]
$R_K$ and $R_K^*$		4	$m_b^*$	[311]
B meson mixing		2	$m_b$	[312]
K meson mixing		1	$m_c^*$	[313]
D meson mixing		8	$m_c^*$	[312]
Angular observables in $B \rightarrow K^*\mu\mu$ and $\Lambda_b \rightarrow \Lambda\mu\mu$ (from 15 GeV)		16	$m_b$	[303, 314]
$\Delta_{\text{CKM}}$		1	$M_Z$	[156, 157]



coefficient	LO SMEFT predictions		partial NLO SMEFT predictions	
	single 95%CL limit	global 95%CL limit	single 95%CL limit	global 95%CL limit
$C_{HWB}$	[-0.004, 0.002]	[-0.12, 0.15]	[-0.004, 0.002]	[-0.1, 0.18]
$C_{HD}$	[-0.022, 0.003]	[-0.39, 0.26]	[-0.022, 0.003]	[-0.43, 0.23]
$C_{Hl}^{(1)}$	[-0.006, 0.011]	[-0.06, 0.11]	[-0.006, 0.011]	[-0.04, 0.15]
$C_{Hl}^{(3)}$	[-0.01, 0.003]	[-0.049, 0.063]	[-0.01, 0.003]	[-0.062, 0.051]
$C_{Hq}^{(1)}$	[-0.035, 0.014]	[-0.096, 0.055]	[-0.035, 0.014]	[-0.14, 0.23]
$C_{Hq}^{(3)}$	[-0.01, 0.013]	[-0.036, 0.048]	[-0.01, 0.013]	[-0.04, 0.045]
$C_{Hu}$	[-0.048, 0.04]	[-0.22, 0.12]	[-0.048, 0.04]	[-0.17, 0.22]
$C_{Hd}$	[-0.094, 0.016]	[-0.65, 0.16]	[-0.094, 0.016]	[-0.56, 0.34]
$C_{He}$	[-0.012, 0.009]	[-0.14, 0.19]	[-0.012, 0.009]	[-0.13, 0.21]
$C_{Hl}$	[-0.004, 0.017]	[-0.071, 0.018]	[-0.004, 0.017]	[-0.075, 0.016]
$C_{ll}$	[-0.011, 0.048]	[-0.0, 0.22]	[-0.011, 0.048]	[-0.01, 0.21]
$C_{ee}$	[-0.022, 0.04]	[-0.16, 0.02]	[-0.022, 0.04]	[-0.16, 0.01]
$C_{le}$	[-0.028, 0.027]	[-0.026, 0.039]	[-0.028, 0.027]	[-0.027, 0.039]
$C_{HB}$	[-0.003, 0.002]	[-0.03, 0.067]	[-0.003, 0.002]	[-0.022, 0.077]
$C_{H\Box}$	[-1.0, -0.2]	[-1.4, 0.3]	[-1.0, -0.2]	[-1.3, 0.5]
$C_{HW}$	[-0.009, 0.007]	[-0.19, 0.12]	[-0.009, 0.007]	[-0.18, 0.13]
$C_H$	[-9.5, 7.7]	[-11, 6]	[-9.5, 7.7]	[-13, 4]
$C_{HG}$	[-0.004, -0.0]	[-0.004, 0.004]	[-0.004, -0.0]	[-0.005, 0.003]
$C_G$	[-0.36, 0.16]	[-0.44, 0.19]	[-0.36, 0.16]	[-0.53, 0.2]
$C_W$	[-0.17, 0.36]	[-0.17, 0.36]	[-0.19, 0.34]	[-0.18, 0.36]
$C_{lq}^{(1)}$	[-0.005, 0.018]	[-0.67, 0.08]	[-0.004, 0.019]	[-0.61, 0.12]
$C_{lq}^{(3)}$	[-0.006, 0.002]	[-0.09, 0.11]	[-0.006, 0.002]	[-0.09, 0.11]
$C_{ed}$	[-0.04, 0.008]	[-0.17, 0.8]	[-0.04, 0.008]	[-0.27, 0.65]
$C_{eu}$	[-0.005, 0.011]	[-0.29, 0.34]	[-0.005, 0.011]	[-0.35, 0.25]
$C_{ld}$	[-0.039, 0.043]	[-0.3, 1.8]	[-0.039, 0.043]	[-0.2, 1.9]
$C_{lu}$	[-0.007, 0.025]	[-0.2, 1.3]	[-0.008, 0.024]	[-0.2, 1.3]
$C_{qe}$	[-0.016, 0.019]	[-0.13, 0.79]	[-0.016, 0.019]	[-0.12, 0.78]
$C_{qd}^{(1)}$	[-34, 23]	[-1760, 1090]	[-0.3, 1.7]	[-3.0, 5.2]
$C_{qu}^{(1)}$	[-4.9, 7.3]	[-380, 340]	[0.0, 0.6]	[-0.2, 1.8]
$C_{ud}^{(1)}$	[-7.2, 4.7]	[-520, 370]	[-1.8, 0.7]	[-7.4, 3.9]
$C_{qq}^{(1)}$	[-0.13, 0.19]	[-12, 1]	[-0.15, 0.16]	[-6.7, 3.4]
$C_{qq}^{(1)'} $	[-0.039, 0.018]	[-0.07, 0.39]	[-0.039, 0.018]	[-0.06, 0.42]
$C_{qq}^{(3)}$	[-0.021, 0.04]	[-0.01, 0.11]	[-0.021, 0.04]	[-0.01, 0.1]
$C_{qq}^{(3)'} $	[-0.017, 0.029]	[-0.05, 0.35]	[-0.017, 0.029]	[-0.05, 0.38]
$C_{uu}$	[-0.14, 0.22]	[-2, 15]	[-0.18, 0.17]	[-0.9, 8.8]
$C_{uu}'$	[-0.15, 0.07]	[-1.8, 0.3]	[-0.15, 0.07]	[-2.3, 0.4]
$C_{dd}$	[-1.8, 2.7]	[-210, 70]	[-1.9, 2.6]	[-190, 30]
$C_{dd}'$	[-1.2, 1.8]	[-62, 82]	[-1.2, 1.8]	[-19, 84]
$C_{qd}^{(8)}$	[-0.8, 0.21]	[-3.6, 2.7]	[-0.8, 0.21]	[-3.8, 3.6]
$C_{qu}^{(8)}$	[-0.18, 0.06]	[-0.7, 0.51]	[-0.18, 0.06]	[-0.86, 0.53]
$C_{ud}^{(8)}$	[-0.59, 0.23]	[-4.6, 4.0]	[-0.59, 0.23]	[-4.9, 5.8]

**Table 5:** Numerical results of the single-parameter and global analyses using purely LO or partial NLO SMEFT predictions. Fit results which do not change between the two setups have been greyed out.

## C Numerical Results for Chapter 6

We present the correlation matrix of our global fits based on RGE improved LO and NLO SMEFT predictions in Figures 2 and 3 respectively. Numerical values for the results of the global fits based on LO, RGE improved LO and RGE improved NLO SMEFT predictions can be found in Table 6.

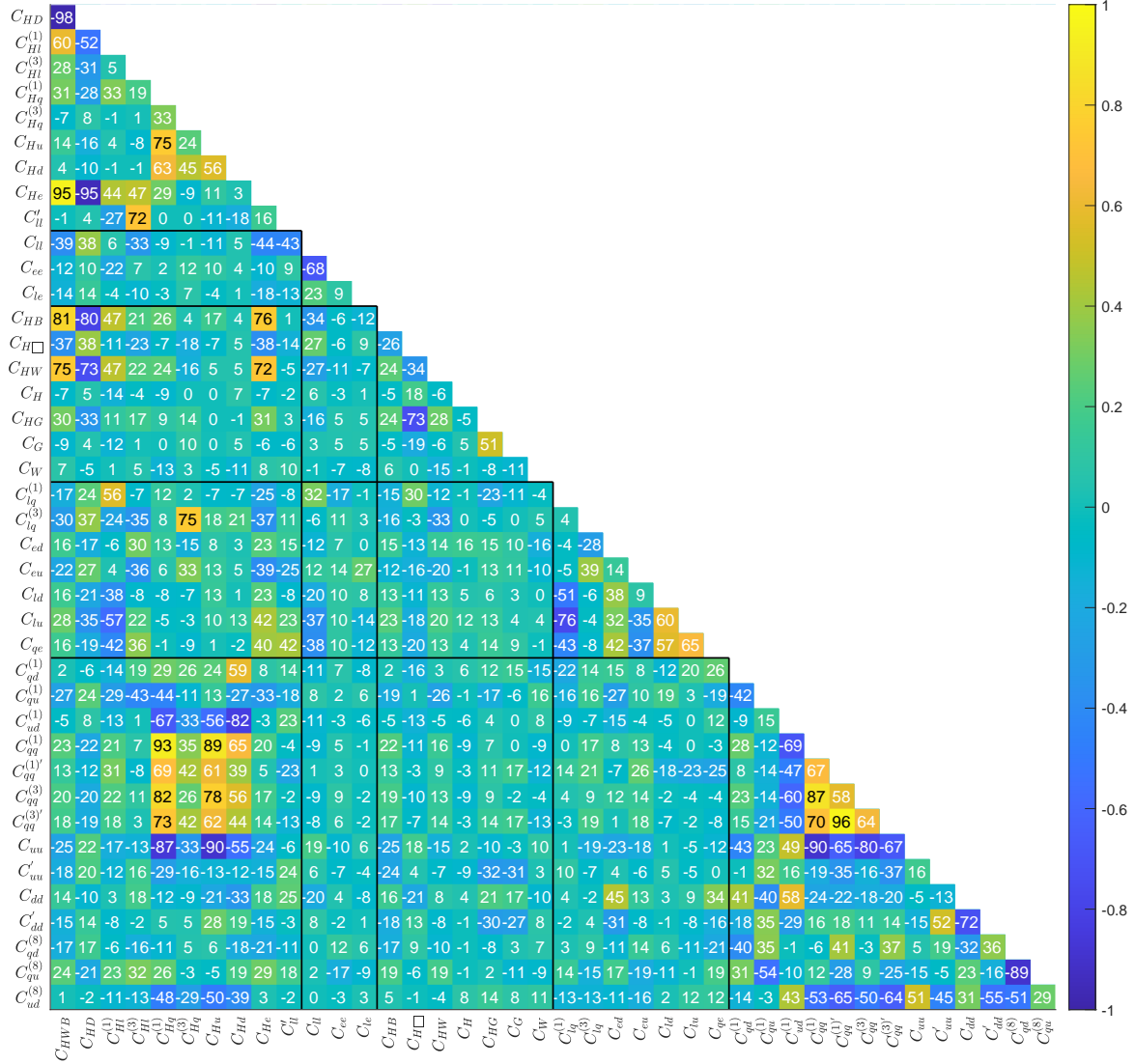


**Figure 2:** Correlation matrix of the LO global analysis including RGE effects. The numbers in the matrix correspond to the correlations in percent.



coefficient	global 95%CL limits on $C(\Lambda)/\Lambda^2$ [TeV $^{-2}$ ]		
	LO	LO+RGE	NLO+RGE
$C_{HWB}$	[-0.14, 0.09]	[-0.16, 0.13]	[-0.14, 0.14]
$C_{HD}$	[-0.24, 0.31]	[-0.39, 0.35]	[-0.4, 0.34]
$C_{HI}^{(1)}$	[-0.06, 0.069]	[-0.16, 0.04]	[-0.14, 0.05]
$C_{HI}^{(3)}$	[-0.058, 0.03]	[-0.069, 0.05]	[-0.072, 0.031]
$C_{Hq}^{(1)}$	[-0.11, 0.04]	[-0.92, 0.64]	[-0.8, 0.34]
$C_{Hq}^{(3)}$	[-0.044, 0.042]	[-0.045, 0.054]	[-0.052, 0.043]
$C_{Hu}$	[-0.26, 0.1]	[-0.82, 0.81]	[-0.71, 0.58]
$C_{Hd}$	[-0.81, 0.07]	[-2.7, 2.5]	[-2.4, 0.1]
$C_{He}$	[-0.16, 0.11]	[-0.18, 0.18]	[-0.17, 0.18]
$C'_{ll}$	[-0.072, 0.013]	[-0.074, 0.026]	[-0.078, 0.021]
$C_{ll}$	[0.02, 0.23]	[-0.0, 0.22]	[0.0, 0.21]
$C_{ee}$	[-0.16, 0.01]	[-0.15, 0.03]	[-0.14, 0.03]
$C_{le}$	[-0.025, 0.039]	[-0.023, 0.044]	[-0.025, 0.047]
$C_{HB}$	[-0.036, 0.042]	[-0.042, 0.064]	[-0.033, 0.07]
$C_{H\Box}$	[-1.3, 0.3]	[-1.7, 0.2]	[-1.7, 0.5]
$C_{HW}$	[-0.19, 0.09]	[-0.22, 0.08]	[-0.22, 0.07]
$C_H$	[-10, 5]	[-18, 9]	[-20, 7]
$C_{HG}$	[-0.005, 0.003]	[-0.002, 0.003]	[-0.003, 0.003]
$C_G$	[-0.17, 0.41]	[-0.16, 0.7]	[-0.12, 0.71]
$C_W$	[-0.14, 0.4]	[-0.19, 0.48]	[-0.14, 0.46]
$C_{lq}^{(1)}$	[-0.64, -0.01]	[-0.47, 0.02]	[-0.54, 0.07]
$C_{lq}^{(3)}$	[-0.061, 0.053]	[-0.062, 0.068]	[-0.064, 0.064]
$C_{ed}$	[-0.03, 0.88]	[-0.0, 1.3]	[-0.0, 1.2]
$C_{eu}$	[-0.27, 0.33]	[-0.12, 0.33]	[-0.12, 0.37]
$C_{ld}$	[-0.1, 1.8]	[-0.2, 1.4]	[-0.2, 1.6]
$C_{lu}$	[-0.0, 1.2]	[-0.07, 0.97]	[-0.2, 1.1]
$C_{qe}$	[-0.09, 0.88]	[-0.12, 0.59]	[-0.18, 0.57]
$C_{qd}^{(1)}$	[-730, 670]	[-13, 14]	[-8.3, 4.4]
$C_{qu}^{(1)}$	[-140, 130]	[-3.2, 3.7]	[-0.3, 1.9]
$C_{ud}^{(1)}$	[-170, 220]	[-21, 14]	[-6, 14]
$C_{qq}^{(1)}$	[-6.2, 5.7]	[-3.4, 2.8]	[-3.5, 2.0]
$C_{qq}^{(1)'} $	[-0.09, 0.36]	[-0.17, 0.51]	[-0.24, 0.45]
$C_{qq}^{(3)}$	[-0.0, 0.11]	[-0.06, 0.14]	[-0.07, 0.13]
$C_{qq}^{(3)'} $	[-0.05, 0.34]	[-0.07, 0.6]	[-0.13, 0.52]
$C_{uu}$	[-6.1, 7.7]	[-3.9, 3.9]	[-3.3, 4.3]
$C'_{uu}$	[-1.8, 0.9]	[-1.2, 0.8]	[-1.6, 0.5]
$C_{dd}$	[-160, 130]	[-47, 50]	[-28, 65]
$C'_{dd}$	[-63, 88]	[-26, 32]	[-36, 18]
$C_{qd}^{(8)}$	[-6.3, 6.0]	[-4.5, 7.0]	[-5.0, 5.5]
$C_{qu}^{(8)}$	[-1.5, 1.1]	[-1.3, 0.6]	[-1.2, 0.5]
$C_{ud}^{(8)}$	[-12, 7]	[-14, 3]	[-9.8, 7.4]

**Table 6:** Numerical results of the global analyses based on LO, RGE improved LO and RGE improved NLO SMEFT predictions. The Wilson coefficients are defined at the scale  $\Lambda = 4$  TeV.

## D Evanescent Operators in the BBL Basis

In higher-order calculations within the effective weak Hamiltonian, one encounters not only the physical four-fermion operators but also so-called evanescent operators. These operators vanish identically in strictly four dimensions, but in  $d = 4 - 2\epsilon$  dimensions they are non-trivial and play a crucial role in the renormalisation procedure [315].

In the standard Buchalla–Buras–Lautenbacher (BBL) basis [316], the two current–current operators relevant for  $\Delta S = 1$  processes are defined as

$$Q_1^q = (\bar{s}_\alpha \gamma_\mu P_L q_\beta)(\bar{q}_\beta \gamma^\mu P_L d_\alpha), \quad (1)$$

$$Q_2^q = (\bar{s}_\alpha \gamma_\mu P_L q_\alpha)(\bar{q}_\beta \gamma^\mu P_L d_\beta), \quad (2)$$

where  $\alpha, \beta$  denote color indices.

When performing loop calculations in  $d$  dimensions, Dirac structures involving strings of more than one  $\gamma$ -matrix contraction appear. In four dimensions, these can be reduced by Fierz identities to linear combinations of the physical operators  $Q_1^q$  and  $Q_2^q$ . However, in  $d \neq 4$ , the reduction produces extra terms proportional to  $\epsilon$  that must be consistently accounted for. This motivates the introduction of the evanescent operators:

$$E_1 = (\bar{s}_\alpha \gamma_\mu \gamma_\nu \gamma_\rho P_L q_\beta)(\bar{q}_\beta \gamma^\mu \gamma^\nu \gamma^\rho P_L d_\alpha) - (16 + 4\epsilon) Q_1^q, \quad (3)$$

$$E_2 = (\bar{s}_\alpha \gamma_\mu \gamma_\nu \gamma_\rho P_L q_\alpha)(\bar{q}_\beta \gamma^\mu \gamma^\nu \gamma^\rho P_L d_\beta) - (16 + 4\epsilon) Q_2^q, \quad (4)$$

where the coefficients are chosen such that  $E_{1,2}$  vanish identically for  $d = 4$ .

Although the matrix elements of  $E_i$  vanish in the four-dimensional physical theory, their presence in the operator basis is indispensable at intermediate stages. In particular:

- They absorb divergences generated in loop diagrams that cannot be renormalised by the physical operators alone.
- They mix with the physical operators under renormalisation, contributing with finite terms to the anomalous dimension matrix beyond the NLO.
- Their definition is scheme-dependent; different choices of evanescent operators correspond to different renormalisation schemes. Consistency requires that these choices are fixed once and maintained throughout the calculation.

At the end of the renormalisation procedure, one projects back onto the physical subspace by discarding the evanescent operators. However, the finite contributions they generated in the mixing must be kept. This ensures that the anomalous dimension matrices and Wilson coefficients are correctly defined and consistent with the chosen renormalisation scheme [317, 318].

Our result for the hard function written in Equation (8.13) includes in the finite pieces these contributions, in particular their result reads

$$H_1^{\text{evanescent}} = 3(C_A - 4C_F). \quad (5)$$

## E Results for the Finite Terms of the $u$ -Dependent $\bar{n}$ -Jet Function

In this appendix, we present the finite-term results for all diagrams shown in Figures 10.4 and 10.5, including their explicit dependence on the momentum fraction  $u$ . The results for each diagram read<sup>1</sup>:

$$f_A^0(u) = - \left[ 6u + 3(u-1)(\log(1-u) + \log(u)) \left( u \tanh^{-1}(1-2u) - 2 \right) - 10 \right], \quad (6)$$

$$f_B^0(u) = \frac{1}{6}(u-1) \left[ 9u \log \left( \frac{1}{u} - 1 \right) \log[(1-u)u] + 4(\pi^2 - 6) \right], \quad (7)$$

$$\begin{aligned} f_C^0(u) = \frac{1}{12} & \left[ 12(u-1)\zeta(3) - 4\pi^2 u + 72u - 9(u-1)u \log^2(1-u) \right. \\ & + 2 \left( -2\pi^2 u + 6u + \pi^2 + 12 \right) \log(1-u) \\ & + \log(u) \left( -2\pi^2(u-2) - 84u + 9(u-1)u \log(u) + 48 \right) \\ & + 4u \left( \left( \pi^2 - 18 \right) u + 18(u-1) \log[(1-u)u] \right) \tanh^{-1}(1-2u) \\ & \left. + 2\pi^2 - 96 \right], \quad (8) \end{aligned}$$

$$\begin{aligned} f_D^0(u) = \frac{1}{2} & \left[ 3(u-1)u \log^2(1-u) - 8(2u + u \log(u) - 2) \log(1-u) \right. \\ & \left. + 4(-3u + \log(u) + 3) - 3u \log(u)((u+3) \log(u) - 8) \right], \quad (9) \end{aligned}$$

$$\begin{aligned} f_E^0(u) = -\frac{1}{6} & \left[ -48u \operatorname{Li}_2(u) + 3u \left( 3(u-1) \log^2(1-u) - 8(\log(u) - 1) \log(1-u) \right. \right. \\ & \left. + \log(u)(4 - 3(u-1) \log(u)) \right) + 4 \left( 3(\pi^2 - 4)u - 6 \log[(1-u)u] \right. \\ & \left. \left. - \pi^2 + 15 \right) \right], \quad (10) \end{aligned}$$

$$\begin{aligned} f_F^0(u) = -\frac{1}{12} & \left[ \log(u) \left( -2\pi^2(u^2 + u - 2) + 6u(6u + 7) - 9u(3u + 1) \log(u) \right) \right. \\ & + 12(u-1)\zeta(3) - 6u + \pi^2(4u - 6) + 27(u-1)u \log^2(1-u) \\ & \left. + 2 \left( (u-1) \left( \pi^2(u-1) - 9(2u+3) \right) - 12u \log(u) \right) \log(1-u) + 6 \right], \quad (11) \end{aligned}$$

<sup>1</sup>Here, the superscript 0 denotes the  $\mathcal{O}(\varepsilon^0)$  term of the functions, while the  $1/\varepsilon$  poles are given in the main text.

$$\begin{aligned}
f_G^0(u) = \frac{1}{2} & \left[ \log(u) \left( 3 \left( u^2 + u - 2 \right) \log(u) - 4(u - 5) \right) + 12u^2 \tanh^{-1}(1 - 2u) \right. \\
& + 8(3u - 5) - 3(u - 3)(u - 1) \log^2(1 - u) \\
& \left. + \pi(\pi(u - 1)) + 2 \log(1 - u)(-13u + 6(u - 1) \log(u) + 14) \right], \tag{12}
\end{aligned}$$

$$\begin{aligned}
f_H^0(u) = \frac{1}{6} & \left[ \left( -9u^2 + 6u + 3 \right) \log^2(1 - u) + 18u^2 \log \left( \frac{1}{u} - 1 \right) - \left( 48 + \pi^2 \right) u \right. \\
& - 6 \log(1 - u)(u + 2(u - 1) \log(u) + 4) \\
& \left. + 3 \log(u)(4(5u - 4) + (u - 1)(3u - 4) \log(u)) + \pi^2 + 72 \right], \tag{13}
\end{aligned}$$

$$\begin{aligned}
f_I^0(u) = \frac{1}{6} & \left[ 6 \log \left( \frac{1}{u} - 1 \right) \left( 4 \log(1 - u) - 3u^2 \right) + 3(u - 2)(3u + 5) \log^2(1 - u) \right. \\
& + 6(4u \log(u) + 7) \log(1 - u) + 2(39u + \pi(\pi(u - 1))) - 60 \\
& \left. - 3 \log(u)(30u + (u - 1)(3u - 8) \log(u) - 28) \right]. \tag{14}
\end{aligned}$$

## F Details and Results for the Computation of Master Integrals

In this appendix we provide the explicit details of the computation presented in Section 10.3 for the computation of the master integrals of topology  $E$  in the cases where the differential equation method is required. Additionally, at the end, we also give the analogous results for topology  $D$ .

The system of differential equations associated to topology  $E$  discussed in Section 10.3 takes the form

$$v'(u) = A(u, \varepsilon) v(u), \tag{15}$$

where the matrix  $A(u, \varepsilon)$  is expanded in terms of its rows as follows:

$$\begin{aligned}
A_1 &= \left( \frac{\varepsilon - 3\varepsilon u}{(u - 1)u}, 0, 0, 0, 0, 0, 0, 0, 0 \right) \\
A_2 &= \left( 0, -\frac{2\varepsilon}{u - 1}, \frac{(1 - 2\varepsilon)^2}{2\varepsilon(u - 1)u}, 0, 0, 0, 0, 0, 0 \right) \\
A_3 &= \left( 0, 0, \frac{1 - 2\varepsilon}{u} - \frac{\varepsilon}{u - 1}, 0, 0, 0, 0, 0, 0 \right) \\
A_4 &= \left( 0, 0, 0, -\frac{2\varepsilon}{u}, 0, \frac{4\varepsilon^2 - 4\varepsilon + 1}{2\varepsilon u - 2\varepsilon u^2}, 0, 0, 0 \right) \\
A_5 &= \left( 0, 0, 0, 0, \frac{\varepsilon(2 - 3u)}{(u - 1)u}, 0, 0, 0, 0 \right) \\
A_6 &= \left( 0, 0, 0, 0, 0, \frac{-3\varepsilon u + \varepsilon + u}{(u - 1)u}, 0, 0, 0 \right)
\end{aligned}$$

$$\begin{aligned}
A_7 = & \left( \frac{4\varepsilon^2 - 1}{4(u-1)^4}, -\frac{\varepsilon(2\varepsilon + 1)}{4(u-1)^4}, \right. \\
& \frac{(1-2\varepsilon)^2(2\varepsilon+1)(\varepsilon^2(u(3(u-2)u+8)-4) + 2\varepsilon(3u-2)((u-1)u+1) + u^3)}{8\varepsilon(\varepsilon+1)^2(u-1)^4u^4}, \\
& \frac{\varepsilon(-2\varepsilon+u-2)}{4(u-1)^2u^3}, \frac{(4\varepsilon^2-1)(2\varepsilon-u+2)}{4(\varepsilon+1)(u-1)^2u^3}, \\
& \left. -\frac{(1-2\varepsilon)^2(2\varepsilon-u+2)(\varepsilon(3u-1)+u-1)}{8\varepsilon(\varepsilon+1)(u-1)^4u^3}, \right. \\
& \frac{4\varepsilon+3}{1-u}, -\frac{(2\varepsilon+1)(2u-1)}{(u-1)^2}, \left. -\frac{(2\varepsilon+1)^2}{(u-1)^2} \right) \\
A_8 = & \left( -\frac{(2\varepsilon-1)(3(\varepsilon+1)u+2\varepsilon+1)}{4(u-1)^3u^2}, \frac{\varepsilon(\varepsilon(2u+3)+3u+1)}{4(u-1)^3u^2}, \right. \\
& \left. -\frac{(1-2\varepsilon)^2((2\varepsilon+3)(3\varepsilon+1)u^3 + (\varepsilon-1)^2u^2 + 2\varepsilon(\varepsilon+1)u - 2\varepsilon(2\varepsilon+1))}{8\varepsilon(\varepsilon+1)(u-1)^3u^5}, \right. \\
& \frac{\varepsilon(2\varepsilon u + \varepsilon + u + 1)}{4(u-1)u^4}, -\frac{(4\varepsilon^2-1)(u+1)}{4(u-1)u^4}, \frac{(1-2\varepsilon)^2(u+1)(\varepsilon(2u-1)+u-1)}{8\varepsilon(u-1)^3u^4}, \\
& \left. \frac{\varepsilon+1}{u^2}, \frac{\varepsilon(5-2u)-u+3}{(u-1)u}, \frac{(2\varepsilon+1)(\varepsilon(u+2)+u+1)}{(u-1)u^2} \right) \\
A_9 = & \left( \frac{2\varepsilon-1}{2(u-1)^3}, -\frac{\varepsilon}{2(u-1)^3}, \frac{(1-2\varepsilon)^2(\varepsilon(u(u+2)-2)+u^2)}{4\varepsilon(\varepsilon+1)(u-1)^3u^3}, -\frac{\varepsilon}{2(u-1)u^2}, \right. \\
& \left. \frac{2\varepsilon-1}{2(u-1)u^2}, -\frac{(1-2\varepsilon)^2}{4\varepsilon(u-1)^2u^2}, 0, -\frac{2}{u-1}, \frac{4\varepsilon+2}{1-u} \right).
\end{aligned}$$

The previous system can be reduced to  $\varepsilon$ -form via a rational transformation as outlined in Section 10.3. In particular, after performing the transformation the system takes the form

$$v'_c(u) = \varepsilon A_c(u) v_c(u), \quad (16)$$

where the rows of the matrix  $A_c(u)$  are given by

$$\begin{aligned}
A_{c1} &= \left( \frac{1-3u}{(-1+u)u}, 0, 0, 0, 0, 0, 0, 0 \right) \\
A_{c2} &= \left( 0, -\frac{2}{-1+u}, \frac{1}{2(-1+u)}, 0, 0, 0, 0, 0 \right) \\
A_{c3} &= \left( 0, 0, \frac{2-3u}{(-1+u)u}, 0, 0, 0, 0, 0 \right) \\
A_{c4} &= \left( 0, 0, 0, -\frac{2}{u}, 0, -\frac{1}{2u}, 0, 0 \right) \\
A_{c5} &= \left( 0, 0, 0, 0, \frac{2-3u}{(-1+u)u}, 0, 0, 0 \right) \\
A_{c6} &= \left( 0, 0, 0, 0, 0, \frac{1-3u}{(-1+u)u}, 0, 0 \right)
\end{aligned}$$

$$\begin{aligned}
A_{c7} &= \left( 0, 0, -\frac{268721103959}{2281391819976u}, 0, \frac{115166187411}{380231969996u}, 0, \frac{2+4u}{u-u^2}, \frac{2+4u}{u-u^2}, -\frac{2(7+2u)}{(-1+u)u} \right) \\
A_{c8} &= \left( \frac{422276020507}{3422087729964u}, \frac{191943645685}{6844175459928u}, \frac{38388729137}{2281391819976u}, \frac{38388729137}{760463939992u}, \right. \\
&\quad \left. \frac{38388729137}{380231969996u}, \frac{115166187411}{1520927879984u}, \frac{1}{(-1+u)u}, \frac{1-3u}{(-1+u)u}, \frac{2+u}{(-1+u)u} \right) \\
A_{c9} &= \left( -\frac{38388729137(-7+u)}{6844175459928(-1+u)u}, -\frac{38388729137(1+5u)}{6844175459928(-1+u)u}, \frac{38388729137}{1140695909988u}, \right. \\
&\quad -\frac{38388729137}{760463939992u}, -\frac{38388729137}{380231969996u}, 0, \frac{1}{(-1+u)u}, \frac{1+u}{(-1+u)u}, \\
&\quad \left. -\frac{3(-2+u)}{(-1+u)u} \right).
\end{aligned}$$

The system in  $\varepsilon$ -form can now be solved order by order in the dimensional regulator and the solutions rotated back to get the final results for our master integrals. The analytic expressions for the master integrals of topology  $E$  that are not reported in the main text are given below:

$$G_{111111001}^E(u) = -\frac{\omega_1}{(4\pi)^{4-2\varepsilon}} e^{-2\varepsilon\gamma_E} (-2E_\gamma\omega_1)^{-3-2\varepsilon} g_{111111001}^E(u)\theta(u, 1-u), \quad (17)$$

with

$$\begin{aligned}
g_{111111001}^E(u) &= \frac{1}{\varepsilon^3\bar{u}u} - \frac{2\log(u\bar{u})}{\varepsilon^2\bar{u}u} + \frac{6\log^2(\bar{u}) + 6\log^2(u) + 9\log(u)\log(\bar{u}) - \pi^2}{3\varepsilon\bar{u}u} \\
&\quad - \frac{4088246098173952\pi^4 c_1 + 6218974120194 [\text{Li}_3(\bar{u}) + \text{Li}_3(u)]}{2072991373398\bar{u}u} \\
&\quad - \frac{4145982746796 \text{Li}_2(u) \tanh^{-1}(\bar{u}-u)}{2072991373398\bar{u}u} \\
&\quad - \frac{345498562233 (8\log^3(\bar{u}) + 8\log^3(u) + 21\log(u)\log^2(\bar{u}))}{2072991373398\bar{u}u} \\
&\quad + \frac{345498562233 (5(\pi^2 - 3\log^2(u))\log(\bar{u}) + 4\pi^2\log(u))}{2072991373398\bar{u}u} \\
&\quad - \frac{31478757892340\zeta(3) + 3762095455426\pi^2 - 36919447038852}{2072991373398\bar{u}u} \\
&\quad - \frac{136 (38388729137(3 + 2\delta_E)\delta_E - 49358620614)\delta_E}{2072991373398\bar{u}u} \\
&\quad - \frac{7524190910852\pi^2\delta_E}{2072991373398\bar{u}u} + \mathcal{O}(\varepsilon),
\end{aligned}$$

and

$$G_{111121001}^E(u) = -\frac{\omega_1}{(4\pi)^{4-2\varepsilon}} e^{-2\varepsilon\gamma_E} (-2E_\gamma\omega_1)^{-4-2\varepsilon} g_{111121001}^E(u)\theta(u, 1-u), \quad (18)$$

with

$$\begin{aligned}
g_{111121001}^E(u) &= \frac{1}{\varepsilon^3 \bar{u}^2} - \frac{2(\log(u\bar{u}) - 1)}{\varepsilon^2 \bar{u}^2 u} + \frac{6u \log^2(\bar{u}) - (9u - 9u \log(u) + 3) \log(\bar{u})}{3\varepsilon \bar{u}^2 u^2} \\
&+ \frac{u6(\log(u) - 2) \log(u) - \pi^2 - 15}{3\varepsilon \bar{u}^2 u^2} \\
&- \frac{2044123049086976\pi^4 c_1 + 2572044852179\pi^2 - 21569210579523}{1036495686699\bar{u}^2 u} \\
&- \frac{68(38388729137(3 + 2\delta_E)\delta_E - 49358620614) + 3762095455426\pi^2}{1036495686699\bar{u}^2 u} \delta_E \\
&- \frac{76777458274 \left( 81u(\text{Li}_3(\bar{u}) + \text{Li}_3(u)) + 410u\zeta(3) \right)}{2072991373398\bar{u}^2 u^2} \\
&+ \frac{8291965493592u^2 \tanh^{-1}(\bar{u} - u)}{2072991373398\bar{u}^2 u^2} \\
&- \frac{76777458274 \left( 54 \text{Li}_2(u)(-u + u \tanh^{-1}(\bar{u} - u) + 1) \right)}{2072991373398\bar{u}^2 u^2} \\
&+ \frac{345498562233 \left( -8u \log^3(\bar{u}) + 3(5u - 7u \log(u) + 3) \log^2(\bar{u}) \right)}{2072991373398\bar{u}^2 u^2} \\
&+ \frac{345498562233 \left( ((54 + 5\pi^2)u + 3u(12 - 5 \log(u))) \log(u) - 6 \right) \log(\bar{u})}{2072991373398\bar{u}^2 u^2} \\
&+ \frac{345498562233 \left( 4u \log(u)(-2(\log(u) - 3) \log(u) + \pi^2 + 12) \right)}{2072991373398\bar{u}^2 u^2} \\
&+ \mathcal{O}(\varepsilon),
\end{aligned}$$

where we defined the constant  $\delta_E = \gamma_E - \log(2\pi)$ .

Finally, we also report here the results for the master integrals of topology  $D$  that are not listed in the main text:

$$G_{111111001}^D(u) = -\frac{\omega_1}{(4\pi)^{4-2\varepsilon}} e^{-2\varepsilon\gamma_E} (-2E_\gamma \omega_1)^{-3-2\varepsilon} g_{111111001}^D(u) \theta(u, 1-u), \quad (19)$$

with

$$\begin{aligned}
g_{111111001}^D(u) &= \frac{1}{2\varepsilon^3 u} - \frac{\log(u)}{\varepsilon^2 u} \\
&+ \frac{4 \text{Li}_2(\bar{u}) - 2 \log^2(\bar{u}) + 4 \log^2(u) + 4 \log(u) \log(\bar{u}) + \pi^2}{4\varepsilon u} \\
&+ \frac{38607298560\pi^4 c_2 + 37702440 \text{Li}_3(\bar{u}) + 30161952 \text{Li}_3(u)}{7540488u} \\
&- \frac{22621464 \text{Li}_2(\bar{u}) \log(\bar{u}) - 1256748 \left( 3 \log^3(\bar{u}) - 4 \log^3(u) \right)}{7540488u} \\
&- \frac{1256748 \left( 3 \log(u) \log^2(\bar{u}) + 2\pi^2 \log(\bar{u}) + 5\pi^2 \log(u) \right)}{7540488u} \\
&- \frac{128020384\zeta(3) - 80871561\pi^2 - 593186592}{7540488u}
\end{aligned}$$

$$+ \mathcal{O}(\varepsilon),$$

and

$$G_{111121001}^D(u) = -\frac{\omega_1}{(4\pi)^{4-2\varepsilon}} e^{-2\varepsilon\gamma_E} (-2E_\gamma\omega_1)^{-4-2\varepsilon} g_{111121001}^D(u)\theta(u, 1-u), \quad (20)$$

with

$$\begin{aligned} g_{111121001}^D(u) = & \frac{1}{2\varepsilon^3 u^2} - \frac{\log(u) - 1}{\varepsilon^2 u^2} \\ & + \frac{\text{Li}_2(\bar{u}) + 3\bar{u}^{-1} - 1/2 \log^2(\bar{u}) + \log(u) \log(\bar{u})}{\varepsilon u^2} \\ & + \frac{(\log(u) - 2) \log(u) + \pi^2/4 + 1}{\varepsilon u^2} \\ & + \frac{45\pi^2 (857939968\pi^2 c_2 + 1880929) + 37702440 \text{Li}_3(\bar{u})}{7540488u^2} \\ & + \frac{30161952 \text{Li}_3(u) - 128020384\zeta(3)}{7540488u^2} \\ & + \frac{1256748 (3 \log^3(\bar{u}) - 3(\log(u) + 2) \log^2(\bar{u}))}{7540488u^2} \\ & + \frac{1256748 \log(u) (-5\pi^2 - 4(\log(u) - 3) \log(u))}{7540488u^2} \\ & - \frac{585646104u - 30161952u \log(u) + 60323904 \log(u) - 578105616}{7540488u^2 \bar{u}} \\ & + \frac{2513496 (\pi^2 u - 6u + 6\bar{u} \log(u) - \pi^2 - 12) \log(\bar{u})}{7540488u^2 \bar{u}} \\ & - \frac{\text{Li}_2(\bar{u})(3 \log(\bar{u}) - 2)}{u^2} \\ & + \mathcal{O}(\varepsilon). \end{aligned}$$

While for the computations presented in this thesis the explicit values of  $c_1$  and  $c_2$  are not required, for completeness we report their numerical values:

$$c_1 = 0.000175055, \quad c_2 = -0.000327445. \quad (21)$$

Finally, as a last remark, in order to reproduce the results shown in the main text one also needs the  $\mathcal{O}(\varepsilon)$  terms. However, due to the complexity of these expressions we refrain from reporting them here; they will instead be provided separately as a Mathematica ancillary file in an upcoming publication.

# List of Figures

4.1	Venn diagram showing the operator sets contributing to the individual datasets at LO. . . . .	37
4.2	Limits on the Wilson coefficients in a global analysis using LO SMEFT predictions. . . . .	41
5.1	Comparison of the global analysis at LO with the one including partial NLO predictions. . . . .	45
5.2	95% CI limits in the LO and partial NLO analyses showing the correlations of $C_{Hq}^{(1)}$ with $C_{qq}^{(1)}$ (left) and $C_{uu}$ (right). . . . .	46
5.3	Ratio of the uncertainties on the Wilson coefficients in a global 41-parameter analysis over the uncertainties in a single-parameter analysis (both including partial NLO predictions). This can be interpreted as a measure of the relevance of correlations with the remaining Wilson coefficients in the analysis. . . . .	47
5.4	Global analysis including NLO predictions. Different colours correspond to analyses removing certain datasets to highlight their relevance. Note that some Wilson coefficients have been rescaled and that the y-axis range is different in the three plot panels. . . . .	48
5.5	95% CI limits with and without the inclusion of the Higgs dataset showing the impact of this dataset on $C_{qd}^{(1)}$ (left) and $C_{ud}^{(1)}$ (right) through lifting correlations with $C_{qu}^{(1)}$ . . . . .	49
5.6	95% CI limits with and without the inclusion of the PVE dataset showing the impact of this dataset on $C_{HI}^{(1)}$ through lifting correlations with $C_{lu}$ and $C_{lq}^{(1)}$ . . . . .	50
5.7	(Incomplete) list of single-parameter bounds at 95% CL on semileptonic operators (left). Note that for the flavour dataset we suppress the limits on all operators except $C_{lq}^{(3)}$ because they are not competitive with PVE and Drell-Yan. 95% CI limits with and without the inclusion of the PVE dataset showing the impact of this dataset on $C_{qq}^{(1)'} $ through lifting correlations with $C_{ed}$ (right). . . . .	50
5.8	95% CI contours on the two-dimensional parameter space of the semileptonic operators from PVE and Drell-Yan (and flavour). The 5D analyses are marginalised over the Wilson coefficients $C_{lq}^{(1)}$ , $C_{lq}^{(3)}$ and $C_{eu}$ (left) and $C_{lq}^{(1)}$ , $C_{lu}$ and $C_{qe}$ (right). . . . .	51
5.9	Single-operator bounds at 95% CL on the Wilson coefficients of the four-quark operators from different datasets. . . . .	52

5.10	95% CI contours of $C_{qq}^{(1)'} vs C_{qq}^{(3)'}$ from flavour and top data. See text for details. . . . .	53
6.1	Energy scales corresponding to the observables included in our global analysis.	56
6.2	Single-parameter limits on the Wilson coefficients before (dashed) and after (solid) the inclusion of RGE effects from different datasets. We only display the strongest bound for the LO case and the LO+RGE bounds which are at most a factor two wider than the strongest bound in this setting. The different panels separate operators involving only gauge fields, four-quark operators with a suppressed interference in dijets+ $\gamma$ production and additional four-quark operators. . . . .	58
6.3	Comparison of the limits on the Wilson coefficients from a global fit purely based on LO predictions (LO), with those including RGE effects (LO+RGE) and including partial NLO predictions (NLO+RGE). The darker shading represents the scale uncertainty, estimated by varying the central scale to double or half of its value. The horizontal lines correspond to the limits at the central scale. Note that some Wilson coefficients have been scaled by appropriate factors on the $x$ axis and that the $y$ axis is different between the two panels.	60
6.4	Left: Correlation $\rho$ (in percent) between selected Wilson coefficients in the LO+RGE fit. Right: Difference between the absolute values of the correlations before and after the inclusion of RG evolution effects in the fit. Correlation changes below 20% have been omitted for better visibility of the dominant effects. . . . .	61
6.5	Left: SMEFT predictions for the $m_{t\bar{t}}$ distribution in $t\bar{t}$ production for the operators $C_G$ and $C_{uG}$ . We employ the notation $\bar{C} = C/\Lambda^2$ . The reference values for $\bar{C}_G$ and $\bar{C}_{uG}$ refer to the RGE-induced contributions from $\bar{C}_G(\Lambda) = 1 \text{ TeV}^{-1}$ at the scale $\mu = 340 \text{ GeV}$ , see Equation (6.9). The data-points refer to the CMS Run I measurements in a double differential $m_{t\bar{t}} - y_{t\bar{t}}$ distribution [169, 170]. Right: Limits on selected operators excluding RGE effects in SMEFT predictions for top-quark observables. . . . .	63
6.6	95% CL limits on the Wilson coefficients $C_{ed}$ and $C_{dd}$ before and after the inclusion of RGE effects in a 2D plane. . . . .	64
6.7	PCA analysis at LO (blue) and LO+RGE (orange). The eigenvalues of the Fisher matrix $\lambda$ are shown for all the 41 eigenvectors $\mathbf{v}$ in decreasing order. . . . .	65
8.1	Schematic illustration of the factorisation theorem and the required Lagrangian insertions. . . . .	74
8.2	One-loop diagrams contributing to the the hard matching function for the operator $Q_{7\gamma}$ . The outgoing strange quark is considered massless, while the $b$ -quark has a mass $m_b$ . . . . .	76
8.3	One-loop diagrams contributing to the the hard matching function for the operator $Q_1^q$ . Self energy contributions are not shown. The outgoing strange quark is considered massless, while the incoming $b$ -quark has a mass $m_b$ . . . . .	77
8.4	One-loop diagrams contributing to the $n$ -jet function. Gluons emitted from the crossed circles originate from the Wilson lines. . . . .	78
9.1	Leading-order contribution to the $\bar{B} \rightarrow X_s \gamma$ decay rate from the $Q_1^q - Q_{7\gamma}$ interference. Symmetric diagrams are not shown. . . . .	80

- 
- 9.2 The left-hand side shows the non-local space-time structure of the soft fields and Wilson lines as they appear in the effective operator  $\mathcal{O}_{17}$  in (9.2). Here, dashed lines denote soft Wilson lines in the  $\bar{n}^\mu$  direction from the decoupling of anti-hard-collinear quark fields, and similarly the dotted line represents a soft Wilson line in the  $n^\mu$  direction. Throughout this paper, we simply represent the non-local field configuration through an effective vertex denoted by the  $\otimes$  symbol on the right-hand side of the equation. Note that at higher orders, more than one gluon can be emitted from the effective vertex due to the presence of the Wilson lines. . . . . 80
- 9.3 One-loop diagrams that contribute to the partonic matrix element  $\langle \tilde{\mathcal{O}}_{17} \rangle$ . The square denotes the insertion of the operator. Self-energy contributions are not shown. . . . . 81
- 9.4 Location of poles related to the integral in (9.15). Green dots denote poles located in the upper or lower complex half-plane. The order of the denominators matches that in Equation (9.15). . . . . 84
- 9.5 Scale evolution of the function  $h_{17}(\omega_1; \mu)$ , using the model (9.85) with  $n \leq 2$  Hermite polynomials at the low scale  $\mu_0 = 1$  GeV (black curve). The blue curve shows the analytic solution (9.84) for  $\mu = 2$  GeV, which is in good agreement with the numeric solution from discretisation of the momentum-space RG equation (blue dots). The latter is obtained using  $N = 600$  points that are logarithmically distributed on the intervals  $[-\Omega, -\varepsilon]$  and  $[\varepsilon, \Omega]$ , with  $\varepsilon = 10^{-9}$  GeV and  $\Omega = 10^3$  GeV. The strong coupling constant is evaluated with one-loop running and  $n_f = 4$  quark flavors, using  $\alpha_s(\mu_0) = 0.48$ . We emphasize that the blue curve only includes the non-Abelian piece (9.50) of the anomalous dimension. . . . . 97
- 9.6 Leading order contribution from the operator  $Q_1^q$  to the exclusive double radiative  $\bar{B}_{d,s} \rightarrow \gamma\gamma$  decay. . . . . 98
- 9.7 Scale evolution of the function  $\phi(\omega_1; \mu)$ , using the exponential model (9.116) with  $\omega_0 = 0.3$  GeV at the low scale  $\mu_0 = 1$  GeV (black curve). The blue curve shows the analytic solution for  $\mu = 2$  GeV, which again is in good agreement with the numeric solution from discretisation of the momentum-space RG equation (blue dots). Details on the discretisation and the strong coupling constant are explained in the caption of Figure 9.5. . . . . 105
- 10.1 LO diagrams contributing to the  $b \rightarrow s\gamma g$  amplitude. The loop contains either a charm quark or an up quark. The two diagrams differ by the interchange of the gluon and photon emission vertices. . . . . 108
- 10.2 Location of poles related to the integral in (10.7). Green dots denote poles located in the upper or lower complex half-plane. The order of the denominators matches that in Equation (10.7). . . . . 109
- 10.3 Schematic representation of the anti-hard-collinear momentum fraction  $u$ . The momentum assignments in both diagrams follow those of Figure 10.1. . . 113

10.4	Two-loop diagrams contributing to the $b \rightarrow s\gamma g$ amplitude. Only topologies without connections to the external $b$ and $s$ quark lines are shown. Diagram (A) displays one possible insertion of the self-energy correction, but two additional insertions are also possible. Furthermore, for diagrams (B), (C) and (D) the QCD correction to the gluon or photon vertex can be interchanged with the other emitted boson. For diagrams (A) and (E) an additional one can be obtained by exchanging the gluon and photon emission vertices. . . .	117
10.5	Two-loop diagrams contributing to the $b \rightarrow s\gamma g$ amplitude, showing the connections to the external $b$ and $s$ quark lines. In each diagram, the gluon may alternatively be attached to the opposite external leg relative to the one shown. Moreover, for each diagram, an additional one is obtained by interchanging the gluon and photon emission vertices. . . . .	118
10.6	Subset of four diagrams of the kind (G.1) and (G.2). . . . .	119
10.7	Location of poles related to the integral in (10.43). Colour dots denote poles located in the upper or lower complex half-plane. Green dots are related to the integral in $k_-$ , while red dots to the integral in $l_-$ . The order of the denominators matches that in Equation (10.43). Grey shading indicated the regions where the integral vanish. . . . .	120
1	Correlation matrix of the global analysis including partial NLO SMEFT predictions. The numbers in the matrix correspond to the correlations in percent.	145
2	Correlation matrix of the LO global analysis including RGE effects. The numbers in the matrix correspond to the correlations in percent. . . . .	147
3	Correlation matrix of the NLO global analysis including RGE effects. The numbers in the matrix correspond to the correlations in percent. . . . .	148

# List of Tables

2.1	List of common dimension-six operators in the WET, relevant for flavour-changing processes. Color indices $\alpha, \beta$ are shown where relevant, $T^a$ denotes the $SU(3)$ generators, $\sigma_{\mu\nu} = \frac{i}{2}[\gamma_\mu, \gamma_\nu]$ is the antisymmetric combination of Dirac matrices, and $P_{L(R)} = (1 \mp \gamma_5)/2$ are the left-handed and right-handed chirality projectors. . . . .	14
2.2	Flavour symmetric and CP even dimension-six SMEFT operators in the Warsaw basis. . . . .	18
4.1	Ratio of the 68% CL limits on the operators contributing to dijet+photon production at linear and quadratic order in SMEFT. . . . .	40
10.1	Master integrals associated with the diagrams of Figure 10.5. . . . .	121
10.2	Master integrals associated with the diagrams of Figure 10.4. . . . .	123
10.3	$u$ -dependent master integrals corresponding to the diagrams in Figure 10.5. . . . .	125
10.4	$u$ -dependent master integrals corresponding to the diagrams in Figure 10.4. . . . .	127
1	Higgs and electroweak observables included in the fit. . . . .	141
2	Top physics observables from Tevatron and LHC Run I included in the fit. . . . .	142
3	Top physics observables from LHC Run II as well as data from Drell-Yan and dijet+photon production included in the analysis. . . . .	143
4	EWPO, PVE, lepton scattering and flavour observables included in the fit. For a summary of the experimental input values of the EWPO observables used, see also Tab. 3 of [93]. * For scales below 5 GeV, we only include the LEFT RGE up to this scale. We explicitly checked that the evolution below 5 GeV is almost negligible when compared with the evolution between $\Lambda$ and $m_b$ . . . . .	144
5	Numerical results of the single-parameter and global analyses using purely LO or partial NLO SMEFT predictions. Fit results which do not change between the two setups have been greyed out. . . . .	146
6	Numerical results of the global analyses based on LO, RGE improved LO and RGE improved NLO SMEFT predictions. The Wilson coefficients are defined at the scale $\Lambda = 4$ TeV. . . . .	149



# Bibliography

- [1] S. L. Glashow, *Partial Symmetries of Weak Interactions*, *Nucl. Phys.* **22** (1961) 579–588.
- [2] S. Weinberg, *A Model of Leptons*, *Phys. Rev. Lett.* **19** (1967) 1264–1266.
- [3] A. Salam, *Weak and Electromagnetic Interactions*, *Conf. Proc. C* **680519** (1968) 367–377.
- [4] F. Englert and R. Brout, *Broken Symmetry and the Mass of Gauge Vector Mesons*, *Phys. Rev. Lett.* **13** (1964) 321–323.
- [5] P. W. Higgs, *Broken Symmetries and the Masses of Gauge Bosons*, *Phys. Rev. Lett.* **13** (1964) 508–509.
- [6] ATLAS collaboration, G. Aad et al., *Observation of a new particle in the search for the Standard Model Higgs boson with the ATLAS detector at the LHC*, *Phys. Lett. B* **716** (2012) 1–29, [[1207.7214](#)].
- [7] CMS collaboration, S. Chatrchyan et al., *Observation of a New Boson at a Mass of 125 GeV with the CMS Experiment at the LHC*, *Phys. Lett. B* **716** (2012) 30–61, [[1207.7235](#)].
- [8] P. Fayet and S. Ferrara, *Supersymmetry*, *Phys. Rept.* **32** (1977) 249–334.
- [9] Baez, J.C. and Huerta, J., *The Algebra of Grand Unified Theories*, *arXiv* (2010) , [[0904.1556](#)].
- [10] Liu, Y.-X., *Introduction to Extra Dimensions and Thick Braneworlds*, *arXiv* (2017) , [[1707.08541](#)].
- [11] B. Bellazzini, C. Csáki and J. Serra, *Composite Higgses*, *Eur. Phys. J. C* **74** (2014) 2766, [[1401.2457](#)].
- [12] E. Abdalla and A. Marins, *The Dark Sector Cosmology*, *Int. J. Mod. Phys. D* **29** (2020) 2030014, [[2010.08528](#)].
- [13] Dienes, K.R., Dudas, E. and Gherghetta, T., *Light Neutrinos without Heavy Mass Scales: A Higher-Dimensional Seesaw Mechanism*, *arXiv* (1998) , [[hep-ph/9811428](#)].
- [14] Akhmedov, E.Kh., Branco, G.C. and Rebelo, M.N., *Seesaw mechanism and structure of neutrino mass matrix*, *arXiv* (1999) , [[hep-ph/9911364](#)].

- [15] N. Cabibbo, *Unitary Symmetry and Leptonic Decays*, *Phys. Rev. Lett.* **10** (1963) 531–533.
- [16] M. Kobayashi and T. Maskawa, *CP Violation in the Renormalizable Theory of Weak Interaction*, *Prog. Theor. Phys.* **49** (1973) 652–657.
- [17] L. Wolfenstein, *Parametrization of the kobayashi–maskawa matrix*, *Phys. Rev. Lett.* **51** (1983) 629–631.
- [18] S. Glashow, J. Iliopoulos and L. Maiani, *Weak interactions with lepton–hadron symmetry*, *Phys. Rev. D* **2** (1970) 1285–1292.
- [19] R. Placakyte, *Parton distribution functions*, *arXiv* (2011) , [[1111.5452](#)].
- [20] T. Kinoshita, *Mass singularities of feynman amplitudes*, *J. Math. Phys.* **3** (1962) 650–677.
- [21] T. Lee and M. Nauenberg, *Degenerate systems and mass singularities*, *Phys. Rev.* **133** (1964) B1549–B1562.
- [22] S. Frixione, P. Nason and C. Oleari, *Matching nlo qcd computations with parton shower simulations: the powheg method*, *JHEP* **2007** (2007) 070.
- [23] S. Frixione and B. R. Webber, *Matching nlo qcd computations and parton shower simulations*, *JHEP* **2002** (2002) 029, [[hep-ph/0204244](#)].
- [24] M. Cacciari, G. P. Salam and G. Soyez, *The anti- $k_t$  jet clustering algorithm*, *JHEP* **04** (2008) 063, [[0802.1189](#)].
- [25] S. Bentvelsen and I. Meyer, *The cambridge jet algorithm: features and applications*, *arXiv* (1998) , [[hep-ph/9803322](#)].
- [26] R. Atkin, *Review of jet reconstruction algorithms*, *J. Phys. Conf. Ser.* **645** (2015) 012008.
- [27] T. Sjöstrand, *The pythia event generator: Past, present and future*, *arXiv* (2019) , [[1907.09874](#)].
- [28] S. Gieseke, *The new monte carlo event generator herwig++*, *arXiv* (2004) , [[hep-ph/0408034](#)].
- [29] E. Bothmann, S. Höche, F. Krauss, S. Schumann et al., *Event generation with sherpa 2.2*, *arXiv* (2019) , [[1905.09127](#)].
- [30] J. Alwall et al., *The automated computation of tree-level and next-to-leading order differential cross sections, and their matching to parton shower simulations*, *JHEP* **07** (2014) 079, [[1405.0301](#)].
- [31] A. V. Manohar, *Introduction to Effective Field Theories*, *PoS TASI2016* (2018) 001, [[1804.05863](#)].
- [32] B. Grzadkowski, M. Iskrzynski, M. Misiak and J. Rosiek, *Dimension-Six Terms in the Standard Model Lagrangian*, *JHEP* **10** (2010) 085, [[1008.4884](#)].

- 
- [33] J. Aebischer, M. Fael, C. Greub and J. Virto, *B Physics Beyond the Standard Model at One Loop: Complete Renormalization Group Evolution below the Electroweak Scale*, *JHEP* **09** (2017) 158, [[1704.06639](#)].
- [34] E. Fermi, *Tentativo di una teoria delle  $\beta$ -radiazioni*, *Zeitschrift für Physik* **88** (1934) 161–177.
- [35] R. D. C. Miller and B. H. J. McKellar, *Effective field theory and weak non-leptonic interactions*, *Phys. Rep.* **106** (1984) 169–292.
- [36] E. E. Jenkins, A. V. Manohar and P. Stoffer, *Low-Energy Effective Field Theory below the Electroweak Scale: Operators and Matching*, *JHEP* **03** (2018) 016, [[1709.04486](#)].
- [37] F. J. Gilman and M. B. Wise, *Effective hamiltonian for  $\delta s = 1$  weak nonleptonic decays in the six-quark model*, *Phys. Rev. D* **20** (1979) 2392–2400.
- [38] M. Ciuchini, E. Franco, G. Martinelli and L. Reina, *The  $\delta s = 1$  effective hamiltonian including next-to-leading order qcd and qed corrections*, *Nucl. Phys. B* **415** (1994) 403–462, [[hep-ph/9304257](#)].
- [39] W. Dekens and P. Stoffer, *Low-energy effective field theory below the electroweak scale: matching at one loop*, *JHEP* **10** (2019) 197, [[1908.05295](#)].
- [40] A. Buras, *Gauge Theory of Weak Decays*. Cambridge University Press, 6, 2020, [10.1017/9781139524100](#).
- [41] J. Aebischer, M. Fael, C. Greub and J. Virto, *B physics Beyond the Standard Model at One Loop: Complete Renormalization Group Evolution below the Electroweak Scale*, *JHEP* **09** (2017) 158, [[1704.06639](#)].
- [42] L. Naterop and P. Stoffer, *Low-energy effective field theory below the electroweak scale: one-loop renormalization in the 't hooft-veltman scheme*, *Journal of High Energy Physics* **2024** (2024) .
- [43] J. Aebischer, J. Kumar and D. M. Straub, *Wilson: a Python package for the running and matching of Wilson coefficients above and below the electroweak scale*, *Eur. Phys. J. C* **78** (2018) 1026, [[1804.05033](#)].
- [44] A. Celis, J. Fuentes-Martin, A. Vicente and J. Virto, *DsixTools: The Standard Model Effective Field Theory Toolkit*, *Eur. Phys. J. C* **77** (2017) 405, [[1704.04504](#)].
- [45] P. Gambino and U. Haisch, *Electroweak effects in radiative B decays*, *JHEP* **09** (2000) 001, [[hep-ph/0007259](#)].
- [46] M. Misiak and M. Steinhauser, *Three loop matching of the dipole operators for  $b \rightarrow s\gamma$  and  $b \rightarrow sg$* , *Nucl. Phys. B* **683** (2004) 277–305, [[hep-ph/0401041](#)].
- [47] T. Hermann, M. Misiak and M. Steinhauser, *Three-loop QCD corrections to  $B_s \rightarrow \mu^+ \mu^-$* , *JHEP* **12** (2013) 097, [[1311.1347](#)].
- [48] W. Buchmüller and D. Wyler, *Effective lagrangian analysis of new interactions and flavor conservation*, *Nucl. Phys. B* **268** (1986) 621–653.
- [49] I. Brivio and M. Trott, *The standard model as an effective field theory*, *Phys. Rept.* **793** (2019) 1–98, [[1706.08945](#)].

- [50] T. Appelquist and J. Carazzone, *Infrared singularities and massive fields*, *Phys. Rev. D* **11** (1975) 2856–2861.
- [51] A. M. Galda, M. Neubert and S. Renner, *ALP — SMEFT interference*, *JHEP* **06** (2021) 135, [[2105.01078](#)].
- [52] J. Talbert, *The geometric  $\nu$ SMEFT: operators and connections*, *JHEP* **01** (2023) 069, [[2208.11139](#)].
- [53] E. E. Jenkins, A. V. Manohar and M. Trott, *Renormalization group evolution of the standard model dimension six operators i: Formalism and lambda dependence*, *JHEP* **10** (2013) 087, [[1308.2627](#)].
- [54] E. E. Jenkins, A. V. Manohar and M. Trott, *Renormalization group evolution of the standard model dimension six operators ii: Yukawa dependence*, *JHEP* **01** (2014) 035, [[1310.4838](#)].
- [55] R. Alonso, E. E. Jenkins, A. V. Manohar and M. Trott, *Renormalization group evolution of the standard model dimension six operators iii: Gauge coupling dependence and phenomenology*, *JHEP* **04** (2014) 159, [[1312.2014](#)].
- [56] D. A. Faroughy, G. Isidori, F. Wilsch and K. Yamamoto, *Flavour symmetries in the SMEFT*, *JHEP* **08** (2020) 166, [[2005.05366](#)].
- [57] A. Falkowski, M. González-Alonso and K. Mimouni, *Compilation of low-energy constraints on 4-fermion operators in the SMEFT*, *JHEP* **08** (2017) 123, [[1706.03783](#)].
- [58] A. Biekötter, T. Corbett and T. Plehn, *The Gauge-Higgs Legacy of the LHC Run II*, *SciPost Phys.* **6** (2019) 064, [[1812.07587](#)].
- [59] S. Kraml, T. Q. Loc, D. T. Nhung and L. D. Ninh, *Constraining new physics from Higgs measurements with Lilith: update to LHC Run 2 results*, *SciPost Phys.* **7** (2019) 052, [[1908.03952](#)].
- [60] S. Dawson, S. Homiller and S. D. Lane, *Putting standard model EFT fits to work*, *Phys. Rev. D* **102** (2020) 055012, [[2007.01296](#)].
- [61] E. d. S. Almeida, A. Alves, O. J. P. Éboli and M. C. Gonzalez-Garcia, *Electroweak legacy of the LHC run II*, *Phys. Rev. D* **105** (2022) 013006, [[2108.04828](#)].
- [62] Anisha, S. Das Bakshi, S. Banerjee, A. Biekötter, J. Chakraborty, S. Kumar Patra et al., *Effective limits on single scalar extensions in the light of recent LHC data*, *Phys. Rev. D* **107** (2023) 055028, [[2111.05876](#)].
- [63] A. Buckley, C. Englert, J. Ferrando, D. J. Miller, L. Moore, M. Russell et al., *Constraining top quark effective theory in the LHC Run II era*, *JHEP* **04** (2016) 015, [[1512.03360](#)].
- [64] D. Barducci et al., *Interpreting top-quark LHC measurements in the standard-model effective field theory*, [1802.07237](#).
- [65] I. Brivio, S. Bruggisser, F. Maltoni, R. Moutafis, T. Plehn, E. Vryonidou et al., *O new physics, where art thou? A global search in the top sector*, *JHEP* **02** (2020) 131, [[1910.03606](#)].

- 
- [66] S. Bißmann, J. Erdmann, C. Grunwald, G. Hiller and K. Kröniger, *Constraining top-quark couplings combining top-quark and  $\mathbf{B}$  decay observables*, *Eur. Phys. J. C* **80** (2020) 136, [[1909.13632](#)].
- [67] G. Durieux, A. Irlles, V. Miralles, A. Peñuelas, R. Pöschl, M. Perelló et al., *The electro-weak couplings of the top and bottom quarks — Global fit and future prospects*, *JHEP* **12** (2019) 98, [[1907.10619](#)].
- [68] R. Bartocci, A. Biekötter and T. Hurth, *A global analysis of the SMEFT under the minimal MFV assumption*, *JHEP* **05** (2024) 074, [[2311.04963](#)].
- [69] J. Ellis, M. Madigan, K. Mimasu, V. Sanz and T. You, *Top, Higgs, Diboson and Electroweak Fit to the Standard Model Effective Field Theory*, *JHEP* **04** (2021) 279, [[2012.02779](#)].
- [70] SMEFT collaboration, J. J. Ethier, G. Magni, F. Maltoni, L. Mantani, E. R. Nocera, J. Rojo et al., *Combined SMEFT interpretation of Higgs, diboson, and top quark data from the LHC*, *JHEP* **11** (2021) 089, [[2105.00006](#)].
- [71] F. Garosi, D. Marzocca, A. Rodriguez-Sanchez and A. Stanzione, *Indirect constraints on top quark operators from a global SMEFT analysis*, [2310.00047](#).
- [72] R. Bartocci, A. Biekötter and T. Hurth, *Renormalisation group evolution effects on global SMEFT analyses*, *JHEP* **05** (2025) 203, [[2412.09674](#)].
- [73] H. Georgi, *Heavy quark effective theory*, *Phys. Lett. B* (1990) .
- [74] M. Neubert, *Heavy quark symmetry*, *Phys. Rept.* **245** (1994) 259–396, [[hep-ph/9306320](#)].
- [75] A. G. Grozin, *Introduction to the heavy quark effective theory*, *arXiv* (1999) , [[hep-ph/9908366](#)].
- [76] D. Kenway, R. *The isgur-wise function*, *Nucl. Phys. Proc. Suppl.* **34** (1994) 153–158, [[hep-lat/9312021](#)].
- [77] M. Benzke, S. J. Lee, M. Neubert and G. Paz, *Factorization at Subleading Power and Irreducible Uncertainties in  $\bar{B} \rightarrow X_s \gamma$  Decay*, *JHEP* **08** (2010) 099, [[1003.5012](#)].
- [78] C. Bauer, S. Fleming and M. Luke, *Summing sudakov logarithms in  $b\bar{b}x_s\gamma$  in effective field theory*, *Phys. Rev. D* **63** (2000) 014006, [[hep-ph/0005275](#)].
- [79] T. Becher, A. Broggio and A. Ferroglia, *Introduction to soft-collinear effective theory*, *arXiv* (2014) , [[1410.1892](#)].
- [80] M. Beneke and V. A. Smirnov, *Asymptotic expansion of Feynman integrals near threshold*, *Nucl. Phys. B* **522** (1998) 321–344, [[hep-ph/9711391](#)].
- [81] A. M. Polyakov, *Gauge fields as rings of glue*, *Nucl. Phys. B* **164** (1980) 171–188.
- [82] P. Korchemsky, G. and V. Radyushkin, A. *Renormalization of the wilson loops beyond the leading order*, *Nucl. Phys. B* **283** (1987) 342–364.
- [83] V. V. Sudakov, *Vertex parts at very high-energies in quantum electrodynamics*, *Sov. Phys. JETP* **3** (1956) 65–76.

- [84] C. W. Bauer, D. Pirjol and I. W. Stewart, *Soft collinear factorization in effective field theory*, *Phys. Rev. D* **65** (2002) 054022, [[hep-ph/0109045](#)].
- [85] R. Bartocci, P. Böer and T. Hurth, *Renormalisation group evolution of the shape function  $g_{17}$  in  $\bar{B} \rightarrow X_s \gamma$  and  $\bar{B} \rightarrow X_s \ell^+ \ell^-$  at subleading power*, *JHEP* **04** (2025) 066, [[2411.16634](#)].
- [86] R. Bartocci, P. Böer and T. Hurth, *NLO analysis of the subleading-power  $Q_1 - Q_{7\gamma}$  interference in  $\bar{B} \rightarrow X_s \gamma$  at large photon energies*, 10, 2025, [[2510.18811](#)].
- [87] J. de Blas, J. C. Criado, M. Perez-Victoria and J. Santiago, *Effective description of general extensions of the Standard Model: the complete tree-level dictionary*, *JHEP* **03** (2018) 109, [[1711.10391](#)].
- [88] M. Trott, *Methodology for theory uncertainties in the standard model effective field theory*, *Phys. Rev. D* **104** (2021) 095023, [[2106.13794](#)].
- [89] T. Giani, G. Magni and J. Rojo, *SMEFiT: a flexible toolbox for global interpretations of particle physics data with effective field theories*, *Eur. Phys. J. C* **83** (2023) 393, [[2302.06660](#)].
- [90] N. Elmer, M. Madigan, T. Plehn and N. Schmal, *Staying on Top of SMEFT-Likelihood Analyses*, *SciPost Phys.* **18** (2025) 108, [[2312.12502](#)].
- [91] J. De Blas et al., *HEPfit: a code for the combination of indirect and direct constraints on high energy physics models*, *Eur. Phys. J. C* **80** (2020) 456, [[1910.14012](#)].
- [92] P. Stangl, *smelli – the SMEFT Likelihood*, *PoS TOOLS2020* (2021) 035, [[2012.12211](#)].
- [93] S. Dawson and P. P. Giardino, *Electroweak and QCD corrections to Z and W pole observables in the standard model EFT*, *Phys. Rev. D* **101** (2020) 013001, [[1909.02000](#)].
- [94] S. Dawson and P. P. Giardino, *Flavorful electroweak precision observables in the Standard Model effective field theory*, *Phys. Rev. D* **105** (2022) 073006, [[2201.09887](#)].
- [95] N. P. Hartland, F. Maltoni, E. R. Nocera, J. Rojo, E. Slade, E. Vryonidou et al., *A Monte Carlo global analysis of the Standard Model Effective Field Theory: the top quark sector*, *JHEP* **04** (2019) 100, [[1901.05965](#)].
- [96] Z. Kassabov, M. Madigan, L. Mantani, J. Moore, M. Morales Alvarado, J. Rojo et al., *The top quark legacy of the LHC Run II for PDF and SMEFT analyses*, *JHEP* **05** (2023) 205, [[2303.06159](#)].
- [97] L. Alasfar, J. de Blas and R. Gröber, *Higgs probes of top quark contact interactions and their interplay with the Higgs self-coupling*, *JHEP* **05** (2022) 111, [[2202.02333](#)].
- [98] M. Bonetti, R. V. Harlander, D. Korneev, M.-M. Long, K. Melnikov, R. Röntsch et al., *WH production at the LHC within SMEFT at next-to-next-to-leading order QCD*, *Phys. Rev. D* **112** (2025) 034033, [[2502.12846](#)].
- [99] S. Dawson, M. Forsslund and P. P. Giardino, *NLO SMEFT electroweak corrections to Higgs boson decays to four leptons in the narrow width approximation*, *Phys. Rev. D* **111** (2025) 015016, [[2411.08952](#)].

- 
- [100] K. Asteriadis, S. Dawson, P. P. Giardino and R. Szafron,  $e^+e^- \rightarrow ZH$  process in the SMEFT beyond leading order, *JHEP* **02** (2025) 162, [[2409.11466](#)].
- [101] R. Bartocci, *Global analysis of the  $U(3)^5$  symmetric SMEFT*, in *58th Rencontres de Moriond on Electroweak Interactions and Unified Theories*, 5, 2024, [2405.10101](#).
- [102] M. Battaglia, M. Grazzini, M. Spira and M. Wiesemann, *Sensitivity to BSM effects in the Higgs  $p_T$  spectrum within SMEFT*, *JHEP* **11** (2021) 173, [[2109.02987](#)].
- [103] R. Aoude, F. Maltoni, O. Mattelaer, C. Severi and E. Vryonidou, *Renormalisation group effects on SMEFT interpretations of LHC data*, *JHEP* **09** (2023) 191, [[2212.05067](#)].
- [104] S. Di Noi and R. Gröber, *Renormalisation group running effects in  $pp \rightarrow t\bar{t}h$  in the Standard Model Effective Field Theory*, *Eur. Phys. J. C* **84** (2024) 403, [[2312.11327](#)].
- [105] S. Di Noi, R. Gröber and M. K. Mandal, *Two-loop running effects in Higgs physics in Standard Model Effective Field Theory*, *JHEP* **12** (2025) 220, [[2408.03252](#)].
- [106] G. Heinrich and J. Lang, *Renormalisation group effects in SMEFT for di-Higgs production*, *SciPost Phys.* **18** (2025) 113, [[2409.19578](#)].
- [107] F. Maltoni, G. Ventura and E. Vryonidou, *Impact of SMEFT renormalisation group running on Higgs production at the LHC*, *JHEP* **12** (2024) 183, [[2406.06670](#)].
- [108] K. Asteriadis, S. Dawson, P. P. Giardino and R. Szafron, *Impact of Next-to-Leading-Order Weak Standard-Model-Effective-Field-Theory Corrections in  $e+e-\rightarrow ZH$* , *Phys. Rev. Lett.* **133** (2024) 231801, [[2406.03557](#)].
- [109] J. ter Hoeve, L. Mantani, J. Rojo, A. N. Rossia and E. Vryonidou, *Connecting scales: RGE effects in the SMEFT at the LHC and future colliders*, *JHEP* **06** (2025) 125, [[2502.20453](#)].
- [110] R. Bartocci, *Impact of NLO contributions and RGE effects on SMEFT global analyses*, *PoS DISCRETE2024* (2025) 094.
- [111] J. Skilling, *Nested sampling for general bayesian computation*, .
- [112] C. Andrieu and J. Thoms, *A tutorial on adaptive mcmc*, *Statistics and computing* **18** (2008) 343–373.
- [113] C. Degrande and H.-L. Li, *Impact of dimension-8 SMEFT operators on diboson productions*, *JHEP* **06** (2023) 149, [[2303.10493](#)].
- [114] J. Ellis, K. Mimasu and F. Zampedri, *Dimension-8 SMEFT analysis of minimal scalar field extensions of the Standard Model*, *JHEP* **10** (2023) 051, [[2304.06663](#)].
- [115] S. Alioli et al., *Theoretical developments in the SMEFT at dimension-8 and beyond*, in *Snowmass 2021*, 3, 2022, [2203.06771](#).
- [116] T. Corbett, A. Helset, A. Martin and M. Trott, *EWPD in the SMEFT to dimension eight*, *JHEP* **06** (2021) 076, [[2102.02819](#)].

- [117] T. Corbett, J. Desai, O. J. P. Éboli, M. C. Gonzalez-Garcia, M. Martines and P. Reimitz, *Impact of dimension-eight SMEFT operators in the electroweak precision observables and triple gauge couplings analysis in universal SMEFT*, *Phys. Rev. D* **107** (2023) 115013, [[2304.03305](#)].
- [118] T. Corbett, J. Desai, O. J. P. Eboli, M. C. Gonzalez-Garcia, M. Martines and P. Reimitz, *Drell-Yan production in universal theories beyond dimension-six SMEFT*, *Phys. Rev. D* **112** (2025) 013009, [[2503.19962](#)].
- [119] S. Dawson, M. Forsslund and M. Schnubel, *SMEFT matching to  $Z'$  models at dimension eight*, *Phys. Rev. D* **110** (2024) 015002, [[2404.01375](#)].
- [120] E. Celada, T. Giani, J. ter Hoeve, L. Mantani, J. Rojo, A. N. Rossia et al., *Mapping the SMEFT at high-energy colliders: from LEP and the (HL-)LHC to the FCC-ee*, *JHEP* **09** (2024) 091, [[2404.12809](#)].
- [121] S. Bißmann, C. Grunwald, G. Hiller and K. Kröninger, *Top and Beauty synergies in SMEFT-fits at present and future colliders*, *JHEP* **06** (2021) 010, [[2012.10456](#)].
- [122] J. de Blas, Y. Du, C. Grojean, J. Gu, V. Miralles, M. E. Peskin et al., *Global SMEFT Fits at Future Colliders*, in *Snowmass 2021*, 6, 2022, [2206.08326](#).
- [123] I. Brivio and M. Trott, *The Standard Model as an Effective Field Theory*, *Phys. Rept.* **793** (2019) 1–98, [[1706.08945](#)].
- [124] A. Biekötter, B. D. Pecjak, D. J. Scott and T. Smith, *Electroweak input schemes and universal corrections in SMEFT*, *JHEP* **07** (2023) 115, [[2305.03763](#)].
- [125] L. Calibbi and G. Signorelli, *Charged Lepton Flavour Violation: An Experimental and Theoretical Introduction*, *Riv. Nuovo Cim.* **41** (2018) 71–174, [[1709.00294](#)].
- [126] L. Silvestrini and M. Valli, *Model-independent Bounds on the Standard Model Effective Theory from Flavour Physics*, *Phys. Lett. B* **799** (2019) 135062, [[1812.10913](#)].
- [127] T. Hurth, S. Renner and W. Shepherd, *Matching for FCNC effects in the flavour-symmetric SMEFT*, *JHEP* **06** (2019) 029, [[1903.00500](#)].
- [128] F. Ferreira, B. Fuks, V. Sanz and D. Sengupta, *Probing CP-violating Higgs and gauge-boson couplings in the Standard Model effective field theory*, *Eur. Phys. J. C* **77** (2017) 675, [[1612.01808](#)].
- [129] ALEPH, DELPHI, L3, OPAL, SLD, LEP ELECTROWEAK WORKING GROUP, SLD ELECTROWEAK GROUP, SLD HEAVY FLAVOUR GROUP collaboration, S. Schael et al., *Precision electroweak measurements on the Z resonance*, *Phys. Rept.* **427** (2006) 257–454, [[hep-ex/0509008](#)].
- [130] ALEPH, DELPHI, L3, OPAL, LEP ELECTROWEAK collaboration, S. Schael et al., *Electroweak Measurements in Electron-Positron Collisions at W-Boson-Pair Energies at LEP*, *Phys. Rept.* **532** (2013) 119–244, [[1302.3415](#)].
- [131] CDF, D0 collaboration, T. E. W. Group, *2012 Update of the Combination of CDF and D0 Results for the Mass of the W Boson*, [1204.0042](#).

- 
- [132] ATLAS collaboration, M. Aaboud et al., *Measurement of the  $W$ -boson mass in  $pp$  collisions at  $\sqrt{s} = 7$  TeV with the ATLAS detector*, *Eur. Phys. J. C* **78** (2018) 110, [[1701.07240](#)].
- [133] PARTICLE DATA GROUP collaboration, P. A. Zyla et al., *Review of Particle Physics*, *PTEP* **2020** (2020) 083C01.
- [134] L. Berthier and M. Trott, *Consistent constraints on the Standard Model Effective Field Theory*, *JHEP* **02** (2016) 069, [[1508.05060](#)].
- [135] L. Berthier and M. Trott, *Towards consistent Electroweak Precision Data constraints in the SMEFT*, *JHEP* **05** (2015) 024, [[1502.02570](#)].
- [136] M. Bjørn and M. Trott, *Interpreting  $W$  mass measurements in the SMEFT*, *Phys. Lett. B* **762** (2016) 426–431, [[1606.06502](#)].
- [137] L. Berthier, M. Bjørn and M. Trott, *Incorporating doubly resonant  $W^\pm$  data in a global fit of SMEFT parameters to lift flat directions*, *JHEP* **09** (2016) 157, [[1606.06693](#)].
- [138] I. Brivio, T. Corbett and M. Trott, *The Higgs width in the SMEFT*, *JHEP* **10** (2019) 056, [[1906.06949](#)].
- [139] PARTICLE DATA GROUP collaboration, C. Patrignani et al., *Review of Particle Physics*, *Chin. Phys. C* **40** (2016) 100001.
- [140] QWEAK collaboration, D. Androic et al., *First Determination of the Weak Charge of the Proton*, *Phys. Rev. Lett.* **111** (2013) 141803, [[1307.5275](#)].
- [141] PVDIS collaboration, D. Wang et al., *Measurement of parity violation in electron–quark scattering*, *Nature* **506** (2014) 67–70.
- [142] E. J. Beise, M. L. Pitt and D. T. Spayde, *The SAMPLE experiment and weak nucleon structure*, *Prog. Part. Nucl. Phys.* **54** (2005) 289–350, [[nucl-ex/0412054](#)].
- [143] VENUS collaboration, H. Hanai et al., *Measurement of tau polarization in  $e^+e^-$  annihilation at  $s^{*(1/2)} = 58$ -GeV*, *Phys. Lett. B* **403** (1997) 155–162, [[hep-ex/9703003](#)].
- [144] LEP, ALEPH, DELPHI, L3, OPAL, LEP ELECTROWEAK WORKING GROUP, SLD ELECTROWEAK GROUP, SLD HEAVY FLAVOR GROUP collaboration, t. S. Electroweak, *A Combination of preliminary electroweak measurements and constraints on the standard model*, [hep-ex/0312023](#).
- [145] A. Falkowski and K. Mimouni, *Model independent constraints on four-lepton operators*, *JHEP* **02** (2016) 086, [[1511.07434](#)].
- [146] L. Allwicher, D. A. Faroughy, F. Jaffredo, O. Sumensari and F. Wilsch, *HighPT: A tool for high- $p_T$  Drell-Yan tails beyond the standard model*, *Comput. Phys. Commun.* **289** (2023) 108749, [[2207.10756](#)].
- [147] D. M. Straub, *flavio: a Python package for flavour and precision phenomenology in the Standard Model and beyond*, [1810.08132](#).

- [148] E. E. Jenkins, A. V. Manohar and P. Stoffer, *Low-Energy Effective Field Theory below the Electroweak Scale: Anomalous Dimensions*, *JHEP* **01** (2018) 084, [[1711.05270](#)].
- [149] J. Fuentes-Martin, P. Ruiz-Femenia, A. Vicente and J. Virto, *DsixTools 2.0: The Effective Field Theory Toolkit*, *Eur. Phys. J. C* **81** (2021) 167, [[2010.16341](#)].
- [150] R. Aoude, T. Hurth, S. Renner and W. Shepherd, *The impact of flavour data on global fits of the MFV SMEFT*, *JHEP* **12** (2020) 113, [[2003.05432](#)].
- [151] E. Keilmann and W. Shepherd, *Dijets at Tevatron Cannot Constrain SMEFT Four-Quark Operators*, *JHEP* **09** (2019) 086, [[1907.13160](#)].
- [152] ATLAS collaboration, M. Aaboud et al., *Search for low-mass resonances decaying into two jets and produced in association with a photon using pp collisions at  $\sqrt{s} = 13$  TeV with the ATLAS detector*, *Phys. Lett. B* **795** (2019) 56–75, [[1901.10917](#)].
- [153] I. Brivio, *SMEFTsim 3.0 — a practical guide*, *JHEP* **04** (2021) 073, [[2012.11343](#)].
- [154] G. Degrassi, P. P. Giardino, F. Maltoni and D. Pagani, *Probing the Higgs self coupling via single Higgs production at the LHC*, *JHEP* **12** (2016) 080, [[1607.04251](#)].
- [155] G. Degrassi and M. Vitti, *The effect of an anomalous Higgs trilinear self-coupling on the  $h \rightarrow \gamma Z$  decay*, *Eur. Phys. J. C* **80** (2020) 307, [[1912.06429](#)].
- [156] M. González-Alonso and J. Martin Camalich, *Global Effective-Field-Theory analysis of New-Physics effects in (semi)leptonic kaon decays*, *JHEP* **12** (2016) 052, [[1605.07114](#)].
- [157] A. Falkowski, M. González-Alonso and O. Naviliat-Cuncic, *Comprehensive analysis of beta decays within and beyond the Standard Model*, *JHEP* **04** (2021) 126, [[2010.13797](#)].
- [158] R. Boughezal, F. Petriello and D. Wiegand, *Disentangling Standard Model EFT operators with future low-energy parity-violating electron scattering experiments*, *Phys. Rev. D* **104** (2021) 016005, [[2104.03979](#)].
- [159] S. Bruggisser, D. van Dyk and S. Westhoff, *Resolving the flavor structure in the MFV-SMEFT*, *JHEP* **02** (2023) 225, [[2212.02532](#)].
- [160] S. Bruggisser, R. Schäfer, D. van Dyk and S. Westhoff, *The Flavor of UV Physics*, *JHEP* **05** (2021) 257, [[2101.07273](#)].
- [161] C. Grunwald, G. Hiller, K. Kröniger and L. Nollen, *More Synergies from Beauty, Top, Z and Drell-Yan Measurements in SMEFT*, [2304.12837](#).
- [162] M. Kirk, *Cabibbo anomaly versus electroweak precision tests: An exploration of extensions of the Standard Model*, *Phys. Rev. D* **103** (2021) 035004, [[2008.03261](#)].
- [163] V. Cirigliano, W. Dekens, J. de Vries, E. Mereghetti and T. Tong, *Beta-decay implications for the W-boson mass anomaly*, *Phys. Rev. D* **106** (2022) 075001, [[2204.08440](#)].
- [164] A. Crivellin, M. Kirk, T. Kitahara and F. Mescia, *Global fit of modified quark couplings to EW gauge bosons and vector-like quarks in light of the Cabibbo angle anomaly*, *JHEP* **03** (2023) 234, [[2212.06862](#)].

- 
- [165] M. Thomas Arun, K. Deka and T. Srivastava, *Constraining SMEFT BSM scenarios with EWPO and  $\Delta_{CKM}$* , [2301.09273](#).
- [166] V. Cirigliano, W. Dekens, J. de Vries, E. Mereghetti and T. Tong, *Anomalies in global SMEFT analyses: a case study of first-row CKM unitarity*, [2311.00021](#).
- [167] ATLAS collaboration, M. Aaboud et al., *Measurement of  $W^\pm Z$  production cross sections and gauge boson polarisation in pp collisions at  $\sqrt{s} = 13$  TeV with the ATLAS detector*, *Eur. Phys. J. C* **79** (2019) 535, [[1902.05759](#)].
- [168] ATLAS collaboration, M. Aaboud et al., *Measurement of fiducial and differential  $W^+W^-$  production cross-sections at  $\sqrt{s} = 13$  TeV with the ATLAS detector*, *Eur. Phys. J. C* **79** (2019) 884, [[1905.04242](#)].
- [169] CMS collaboration, A. M. Sirunyan et al., *Measurement of double-differential cross sections for top quark pair production in pp collisions at  $\sqrt{s} = 8$  TeV and impact on parton distribution functions*, *Eur. Phys. J. C* **77** (2017) 459, [[1703.01630](#)].
- [170] CMS collaboration, S. Chatrchyan et al., *Measurement of the  $t\bar{t}$  production cross section in the dilepton channel in pp collisions at  $\sqrt{s} = 8$  TeV*, *JHEP* **02** (2014) 024, [[1312.7582](#)].
- [171] R. Alonso, E. E. Jenkins, A. V. Manohar and M. Trott, *Complete one-loop renormalisation of the higgs effective field theory*, *Phys. Lett. B* **754** (2016) 335–342, [[1512.03433](#)].
- [172] Z. Bern, L. J. Dixon et al., *Anomalous dimensions via on-shell methods: non-renormalizable theories and higher loops*, *Phys. Rev. Lett.* **125** (2020) 131603, [[2006.08695](#)].
- [173] X. Jin et al., *Unitarity method for two-loop eft anomalous dimensions*, *JHEP* **10** (2020) 123.
- [174] E. E. Jenkins, A. V. Manohar and P. Stoffer, *The geometric universal one-loop effective action*, *JHEP* **11** (2023) 045, [[2311.04173](#)].
- [175] J. Fuentes-Martín, J. König, A. E. Pagès and F. W. Thomsen, *A proof of concept for matchete: automated matching between efts*, *Eur. Phys. J. C* **83** (2023) 662, [[2212.04510](#)].
- [176] S. Di Noi and L. Silvestrini, *Rgesolver: a c++ library for renormalization group evolution in smeft*, *Eur. Phys. J. C* **84** (2024) 34, [[2403.01234](#)].
- [177] A. Ibarra, N. Leister and D. Zhang, *Complete two-loop matching of lepton-number violating operators in the type-ii seesaw model*, *JHEP* **05** (2024) 123, [[2411.08011](#)].
- [178] T. Hurth, *Present status of inclusive rare B decays*, *Rev. Mod. Phys.* **75** (2003) 1159–1199, [[hep-ph/0212304](#)].
- [179] T. Hurth and M. Nakao, *Radiative and Electroweak Penguin Decays of B Mesons*, *Ann. Rev. Nucl. Part. Sci.* **60** (2010) 645–677, [[1005.1224](#)].
- [180] T. Hurth and F. Mahmoudi, *Colloquium: New physics search with flavor in the LHC era*, *Rev. Mod. Phys.* **85** (2013) 795, [[1211.6453](#)].

- [181] T. Huber, T. Hurth, J. Jenkins, E. Lunghi, Q. Qin and K. K. Vos, *Phenomenology of inclusive  $\bar{B} \rightarrow X_s \ell^+ \ell^-$  for the Belle II era*, *JHEP* **10** (2020) 088, [[2007.04191](#)].
- [182] T. Hurth, F. Mahmoudi and S. Neshatpour, *B anomalies in the post  $R_{K^{(*)}}$  era*, *Phys. Rev. D* **108** (2023) 115037, [[2310.05585](#)].
- [183] Y. Amhis and P. Owen, *Isospin extrapolation as a method to study inclusive  $\bar{B} \rightarrow X_s \ell^+ \ell^-$  decays*, *Eur. Phys. J. C* **82** (2022) 371, [[2106.15943](#)].
- [184] G. Isidori, Z. Polonsky and A. Tinari, *Semi-inclusive  $b \rightarrow s \bar{\ell} \ell$  transitions at high  $q^2$* , *Phys. Rev. D* **108** (2023) 093008, [[2305.03076](#)].
- [185] T. Huber, T. Hurth, J. Jenkins, E. Lunghi, Q. Qin and K. K. Vos, *Inclusive  $\bar{B} \rightarrow X_s \ell^+ \ell^-$  at the LHC: theory predictions and new-physics reach*, [2404.03517](#).
- [186] BELLE-II collaboration, W. Altmannshofer et al., *The Belle II Physics Book*, *PTEP* **2019** (2019) 123C01, [[1808.10567](#)].
- [187] M. Misiak et al., *Updated NNLO QCD predictions for the weak radiative B-meson decays*, *Phys. Rev. Lett.* **114** (2015) 221801, [[1503.01789](#)].
- [188] T. Hurth, M. Fickinger, S. Turczyk and M. Benzke, *Resolved Power Corrections to the Inclusive Decay  $\bar{B} \rightarrow X_s \ell^+ \ell^-$* , *Nucl. Part. Phys. Proc.* **285-286** (2017) 57–62, [[1711.01162](#)].
- [189] M. Benzke, T. Hurth and S. Turczyk, *Subleading power factorization in  $\bar{B} \rightarrow X_s \ell^+ \ell^-$* , *JHEP* **10** (2017) 031, [[1705.10366](#)].
- [190] M. Benzke, *Factorization and non-local  $1/m_b$  corrections in the decay  $\bar{B} \rightarrow X_s \gamma$* , Ph.D. thesis, Mainz U., 2011.
- [191] M. B. Voloshin, *Large  $O(m_c^{-2})$  nonperturbative correction to the inclusive rate of the decay  $B \rightarrow X_s \gamma$* , *Phys. Lett. B* **397** (1997) 275–278, [[hep-ph/9612483](#)].
- [192] Z. Ligeti, L. Randall and M. B. Wise, *Comment on nonperturbative effects in  $\bar{B} \rightarrow X_s \gamma$* , *Phys. Lett. B* **402** (1997) 178–182, [[hep-ph/9702322](#)].
- [193] A. K. Grant, A. G. Morgan, S. Nussinov and R. D. Peccei, *Comment on nonperturbative  $O(1/m_c^2)$  corrections to  $\Gamma(\bar{B} \rightarrow X_s \gamma)$* , *Phys. Rev. D* **56** (1997) 3151–3154, [[hep-ph/9702380](#)].
- [194] G. Buchalla, G. Isidori and S. J. Rey, *Corrections of order  $\Lambda_{QCD}^2/m_c^2$  to inclusive rare B decays*, *Nucl. Phys. B* **511** (1998) 594–610, [[hep-ph/9705253](#)].
- [195] A. Gunawardana and G. Paz, *On HQET and NRQCD Operators of Dimension 8 and Above*, *JHEP* **07** (2017) 137, [[1702.08904](#)].
- [196] A. Gunawardana and G. Paz, *Reevaluating uncertainties in  $\bar{B} \rightarrow X_s \gamma$  decay*, *JHEP* **11** (2019) 141, [[1908.02812](#)].
- [197] M. Benzke and T. Hurth, *Resolved  $1/m_b$  contributions to  $\bar{B} \rightarrow X_{s,d} \ell^+ \ell^-$  and  $\bar{B} \rightarrow X_s \gamma$* , *Phys. Rev. D* **102** (2020) 114024, [[2006.00624](#)].
- [198] M. Neubert, *Renormalization-group improved calculation of the  $B \rightarrow X(s) \gamma$  branching ratio*, *Eur. Phys. J. C* **40** (2005) 165–186, [[hep-ph/0408179](#)].

- 
- [199] C. Greub, T. Hurth and D. Wyler, *Virtual  $O(\alpha_s)$  corrections to the inclusive decay  $b \rightarrow s \gamma$* , *Phys. Rev. D* **54** (1996) 3350–3364, [[hep-ph/9603404](#)].
- [200] M. Beneke, T. Huber and X.-Q. Li, *NNLO vertex corrections to non-leptonic  $B$  decays: Tree amplitudes*, *Nucl. Phys. B* **832** (2010) 109–151, [[0911.3655](#)].
- [201] T. Becher and M. Neubert, *Toward a NNLO calculation of the anti- $B \rightarrow X(s)$  gamma decay rate with a cut on photon energy. II. Two-loop result for the jet function*, *Phys. Lett. B* **637** (2006) 251–259, [[hep-ph/0603140](#)].
- [202] R. Brüser, Z. L. Liu and M. Stahlhofen, *Three-Loop Quark Jet Function*, *Phys. Rev. Lett.* **121** (2018) 072003, [[1804.09722](#)].
- [203] M. Beneke, P. Böer, J.-N. Toelstede and K. K. Vos, *Light-cone distribution amplitudes of heavy mesons with QED effects*, *JHEP* **08** (2022) 020, [[2204.09091](#)].
- [204] S. W. Bosch, B. O. Lange, M. Neubert and G. Paz, *Factorization and shape function effects in inclusive  $B$  meson decays*, *Nucl. Phys. B* **699** (2004) 335–386, [[hep-ph/0402094](#)].
- [205] M. Beneke, Y. Ji and X. Wang, *Renormalization of the next-to-leading-power  $\gamma\gamma \rightarrow h$  and  $g\gamma \rightarrow h$  soft quark functions*, *JHEP* **05** (2024) 246, [[2403.17738](#)].
- [206] M. Beneke, C. Bobeth and R. Szafron, *Power-enhanced leading-logarithmic QED corrections to  $B_q \rightarrow \mu^+ \mu^-$* , *JHEP* **10** (2019) 232, [[1908.07011](#)].
- [207] M. Beneke, P. Böer, J.-N. Toelstede and K. K. Vos, *QED factorization of non-leptonic  $B$  decays*, *JHEP* **11** (2020) 081, [[2008.10615](#)].
- [208] M. Beneke, P. Böer, G. Finauri and K. K. Vos, *QED factorization of two-body non-leptonic and semi-leptonic  $B$  to charm decays*, *JHEP* **10** (2021) 223, [[2107.03819](#)].
- [209] J. S. Schwinger, *Brownian motion of a quantum oscillator*, *J. Math. Phys.* **2** (1961) 407–432.
- [210] L. V. Keldysh, *Diagram technique for nonequilibrium processes*, *Zh. Eksp. Teor. Fiz.* **47**, 1515 (1964) .
- [211] T. Becher, M. Neubert and G. Xu, *Dynamical Threshold Enhancement and Resummation in Drell-Yan Production*, *JHEP* **07** (2008) 030, [[0710.0680](#)].
- [212] Y.-K. Huang, Y. Ji, Y.-L. Shen, C. Wang, Y.-M. Wang and X.-C. Zhao, *Renormalization-Group Evolution for the Three-Particle  $B$ -Meson Soft Function*, *Phys. Rev. Lett.* **133** (2024) 171901, [[2312.15439](#)].
- [213] G. Bell, T. Feldmann, Y.-M. Wang and M. W. Y. Yip, *Light-Cone Distribution Amplitudes for Heavy-Quark Hadrons*, *JHEP* **11** (2013) 191, [[1308.6114](#)].
- [214] V. M. Braun and A. N. Manashov, *Conformal symmetry of the Lange-Neubert evolution equation*, *Phys. Lett. B* **731** (2014) 316–319, [[1402.5822](#)].
- [215] S. J. Lee and M. Neubert, *Model-independent properties of the  $B$ -meson distribution amplitude*, *Phys. Rev. D* **72** (2005) 094028, [[hep-ph/0509350](#)].

- [216] Q. Qin, Y.-L. Shen, C. Wang and Y.-M. Wang, *Deciphering the Long-Distance Penguin Contribution to  $\bar{B}_{d,s} \rightarrow \gamma\gamma$  Decays*, *Phys. Rev. Lett.* **131** (2023) 091902, [[2207.02691](#)].
- [217] B. O. Lange and M. Neubert, *Renormalization group evolution of the B meson light cone distribution amplitude*, *Phys. Rev. Lett.* **91** (2003) 102001, [[hep-ph/0303082](#)].
- [218] G. Bell and T. Feldmann, *Modelling light-cone distribution amplitudes from non-relativistic bound states*, *JHEP* **04** (2008) 061, [[0802.2221](#)].
- [219] V. M. Braun and I. E. Filyanov, *Conformal Invariance and Pion Wave Functions of Nonleading Twist*, *Z. Phys. C* **48** (1990) 239–248.
- [220] V. M. Braun, Y. Ji and A. N. Manashov, *Higher-twist B-meson Distribution Amplitudes in HQET*, *JHEP* **05** (2017) 022, [[1703.02446](#)].
- [221] A. G. Grozin and M. Neubert, *Asymptotics of heavy meson form-factors*, *Phys. Rev. D* **55** (1997) 272–290, [[hep-ph/9607366](#)].
- [222] P. Böer and P. Hager, *On the gauge-invariance of SCET beyond leading power*, *JHEP* **08** (2023) 197, [[2306.12412](#)].
- [223] V. Shtabovenko, R. Mertig and F. Orellana, *New Developments in FeynCalc 9.0*, *Comput. Phys. Commun.* **207** (2016) 432–444, [[1601.01167](#)].
- [224] V. Shtabovenko, R. Mertig and F. Orellana, *FeynCalc 9.3: New features and improvements*, *Comput. Phys. Commun.* **256** (2020) 107478, [[2001.04407](#)].
- [225] V. Shtabovenko, R. Mertig and F. Orellana, *FeynCalc 10: Do multiloop integrals dream of computer codes?*, *Comput. Phys. Commun.* **306** (2025) 109357, [[2312.14089](#)].
- [226] R. Mertig, M. Böhm and A. Denner, *FEYN CALC: Computer algebraic calculation of Feynman amplitudes*, *Comput. Phys. Commun.* **64** (1991) 345–359.
- [227] K. G. Chetyrkin and F. V. Tkachov, *Integration by parts: The algorithm to calculate beta functions in 4 loops*, *Nucl. Phys. B* **192** (1981) 159–204, [[hep-ph/8102003](#)].
- [228] F. V. Tkachov, *A Theorem on Analytical Calculability of Four Loop Renormalization Group Functions*, *Phys. Lett. B* **100** (1981) 65–68.
- [229] A. V. Smirnov and F. S. Chukharev, *FIRE6: Feynman Integral REduction with modular arithmetic*, *Comput. Phys. Commun.* **247** (2020) 106877, [[1901.07808](#)].
- [230] R. N. Lee, *Presenting LiteRed: a tool for the Loop InTEgrals REDuction*, [1212.2685](#).
- [231] A. V. Kotikov, *Differential equations method: New technique for massive Feynman diagrams calculation*, *Phys. Lett. B* **254** (1991) 158–164.
- [232] A. V. Kotikov, *Differential equations method: The Calculation of vertex type Feynman diagrams*, *Phys. Lett. B* **259** (1991) 314–322.
- [233] T. Gehrmann and E. Remiddi, *Differential equations for two loop four point functions*, *Nucl. Phys. B* **580** (2000) 485–518, [[hep-ph/9912329](#)].

- 
- [234] J. M. Henn, *Multiloop integrals in dimensional regularization made simple*, *Phys. Rev. Lett.* **110** (2013) 251601, [[1304.1806](#)].
- [235] R. H. Lewis, *Fermat, computer algebra system*, 2008.
- [236] T. Gehrmann, E. Glover, T. Huber, N. Ikizlerli and C. Studerus, *Calculation of the quark and gluon form factors to three loops in qcd*, *Journal of High Energy Physics* **2010** (2010) 1–64.
- [237] C. Meyer, *Algorithmic transformation of multi-loop master integrals to a canonical basis with CANONICA*, *Comput. Phys. Commun.* **222** (2018) 295–312, [[1705.06252](#)].
- [238] C. Meyer, *Transforming differential equations of multi-loop Feynman integrals into canonical form*, *JHEP* **04** (2017) 006, [[1611.01087](#)].
- [239] S. Weinzierl, *Feynman Integrals. A Comprehensive Treatment for Students and Researchers*. UNITEXT for Physics. Springer, 2022, [10.1007/978-3-030-99558-4](#).
- [240] A. B. Goncharov, *Multiple polylogarithms, cyclotomy and modular complexes*, 2011.
- [241] X. Liu and Y.-Q. Ma, *AMFlow: A Mathematica package for Feynman integrals computation via auxiliary mass flow*, *Comput. Phys. Commun.* **283** (2023) 108565, [[2201.11669](#)].
- [242] ATLAS, CMS collaboration, G. Aad et al., *Measurements of the Higgs boson production and decay rates and constraints on its couplings from a combined ATLAS and CMS analysis of the LHC pp collision data at  $\sqrt{s} = 7$  and 8 TeV*, *JHEP* **08** (2016) 045, [[1606.02266](#)].
- [243] ATLAS collaboration, G. Aad et al., *Measurements of the Higgs boson production and decay rates and coupling strengths using pp collision data at  $\sqrt{s} = 7$  and 8 TeV in the ATLAS experiment*, *Eur. Phys. J. C* **76** (2016) 6, [[1507.04548](#)].
- [244] ATLAS collaboration, G. Aad et al., *A search for the  $Z\gamma$  decay mode of the Higgs boson in pp collisions at  $\sqrt{s} = 13$  TeV with the ATLAS detector*, *Phys. Lett. B* **809** (2020) 135754, [[2005.05382](#)].
- [245] ATLAS collaboration, G. Aad et al., *A search for the dimuon decay of the Standard Model Higgs boson with the ATLAS detector*, *Phys. Lett. B* **812** (2021) 135980, [[2007.07830](#)].
- [246] ATLAS COLLABORATION collaboration, *Measurements of Higgs boson production cross-sections in the  $H \rightarrow \tau^+\tau^-$  decay channel in pp collisions at  $\sqrt{s} = 13$  TeV with the ATLAS detector*, tech. rep., CERN, Geneva, Aug, 2021.
- [247] ATLAS collaboration, G. Aad et al., *Measurements of Higgs bosons decaying to bottom quarks from vector boson fusion production with the ATLAS experiment at  $\sqrt{s} = 13$  TeV*, *Eur. Phys. J. C* **81** (2021) 537, [[2011.08280](#)].
- [248] ATLAS collaboration, *Measurement of the Higgs boson decaying to b-quarks produced in association with a top-quark pair in pp collisions at  $\sqrt{s} = 13$  TeV with the ATLAS detector*, ATLAS-CONF-2020-058 (11, 2020) .

- [249] ATLAS collaboration, *Interpretations of the combined measurement of Higgs boson production and decay*, *ATLAS-CONF-2020-053* (10, 2020) .
- [250] ATLAS collaboration, *Measurements of gluon fusion and vector-boson-fusion production of the Higgs boson in  $H \rightarrow WW^* \rightarrow e\nu\mu\nu$  decays using pp collisions at  $\sqrt{s} = 13$  TeV with the ATLAS detector*, *ATLAS-CONF-2021-014* (3, 2021) .
- [251] ATLAS collaboration, M. Aaboud et al., *Search for Higgs boson pair production in the  $\gamma\gamma b\bar{b}$  final state with 13 TeV pp collision data collected by the ATLAS experiment*, *JHEP* **11** (2018) 040, [[1807.04873](#)].
- [252] ATLAS collaboration, M. Aaboud et al., *Search for pair production of Higgs bosons in the  $b\bar{b}b\bar{b}$  final state using proton-proton collisions at  $\sqrt{s} = 13$  TeV with the ATLAS detector*, *JHEP* **01** (2019) 030, [[1804.06174](#)].
- [253] ATLAS collaboration, M. Aaboud et al., *Search for resonant and non-resonant Higgs boson pair production in the  $b\bar{b}\tau^+\tau^-$  decay channel in pp collisions at  $\sqrt{s} = 13$  TeV with the ATLAS detector*, *Phys. Rev. Lett.* **121** (2018) 191801, [[1808.00336](#)].
- [254] CMS collaboration, *Combined Higgs boson production and decay measurements with up to 137 fb<sup>-1</sup> of proton-proton collision data at  $\sqrt{s} = 13$  TeV*, *CMS-PAS-HIG-19-005* (2020) .
- [255] CMS collaboration, A. M. Sirunyan et al., *Measurement of the inclusive and differential Higgs boson production cross sections in the leptonic WW decay mode at  $\sqrt{s} = 13$  TeV*, *JHEP* **03** (2021) 003, [[2007.01984](#)].
- [256] CMS collaboration, A. M. Sirunyan et al., *Evidence for Higgs boson decay to a pair of muons*, *JHEP* **01** (2021) 148, [[2009.04363](#)].
- [257] CMS collaboration, A. M. Sirunyan et al., *Measurement of the Higgs boson production rate in association with top quarks in final states with electrons, muons, and hadronically decaying tau leptons at  $\sqrt{s} = 13$  TeV*, *Eur. Phys. J. C* **81** (2021) 378, [[2011.03652](#)].
- [258] CMS collaboration, *Measurement of Higgs boson production in association with a W or Z boson in the  $H \rightarrow WW$  decay channel*, *CMS-PAS-HIG-19-017* (2021) .
- [259] CMS collaboration, *Measurement of Higgs boson production in the decay channel with a pair of  $\tau$  leptons*, *CMS-PAS-HIG-19-010* (2020) .
- [260] CMS collaboration, A. M. Sirunyan et al., *Measurements of Higgs boson production cross sections and couplings in the diphoton decay channel at  $\sqrt{s} = 13$  TeV*, *JHEP* **07** (2021) 027, [[2103.06956](#)].
- [261] CMS collaboration, A. M. Sirunyan et al., *Measurements of production cross sections of the Higgs boson in the four-lepton final state in proton-proton collisions at  $\sqrt{s} = 13$  TeV*, *Eur. Phys. J. C* **81** (2021) 488, [[2103.04956](#)].
- [262] CMS collaboration, A. M. Sirunyan et al., *Search for nonresonant Higgs boson pair production in final states with two bottom quarks and two photons in proton-proton collisions at  $\sqrt{s} = 13$  TeV*, *JHEP* **03** (2021) 257, [[2011.12373](#)].

- 
- [263] CMS collaboration, *Search for Higgs boson pair production in the four b quark final state*, *CMS-PAS-HIG-20-005* (2021) .
- [264] CMS collaboration, A. M. Sirunyan et al., *Search for Higgs boson pair production in events with two bottom quarks and two tau leptons in proton–proton collisions at  $\sqrt{s} = 13\text{TeV}$* , *Phys. Lett. B* **778** (2018) 101–127, [[1707.02909](#)].
- [265] ATLAS collaboration, G. Aad et al., *Differential cross-section measurements for the electroweak production of dijets in association with a Z boson in proton–proton collisions at ATLAS*, *Eur. Phys. J. C* **81** (2021) 163, [[2006.15458](#)].
- [266] CDF, D0 collaboration, T. A. Aaltonen et al., *Combined Forward-Backward Asymmetry Measurements in Top-Antitop Quark Production at the Tevatron*, *Phys. Rev. Lett.* **120** (2018) 042001, [[1709.04894](#)].
- [267] ATLAS, CMS collaboration, M. Aaboud et al., *Combination of inclusive and differential  $t\bar{t}$  charge asymmetry measurements using ATLAS and CMS data at  $\sqrt{s} = 7$  and 8 TeV*, *JHEP* **04** (2018) 033, [[1709.05327](#)].
- [268] CMS, ATLAS collaboration, G. Aad et al., *Combination of the W boson polarization measurements in top quark decays using ATLAS and CMS data at  $\sqrt{s} = 8$  TeV*, *JHEP* **08** (2020) 051, [[2005.03799](#)].
- [269] ATLAS collaboration, G. Aad et al., *Measurements of the charge asymmetry in top-quark pair production in the dilepton final state at  $\sqrt{s} = 8$  TeV with the ATLAS detector*, *Phys. Rev. D* **94** (2016) 032006, [[1604.05538](#)].
- [270] ATLAS collaboration, G. Aad et al., *Measurement of the  $t\bar{t}W$  and  $t\bar{t}Z$  production cross sections in pp collisions at  $\sqrt{s} = 8$  TeV with the ATLAS detector*, *JHEP* **11** (2015) 172, [[1509.05276](#)].
- [271] ATLAS collaboration, M. Aaboud et al., *Fiducial, total and differential cross-section measurements of t-channel single top-quark production in pp collisions at 8 TeV using data collected by the ATLAS detector*, *Eur. Phys. J. C* **77** (2017) 531, [[1702.02859](#)].
- [272] ATLAS collaboration, G. Aad et al., *Measurement of single top-quark production in association with a W boson in the single-lepton channel at  $\sqrt{s} = 8$  TeV with the ATLAS detector*, *Eur. Phys. J. C* **81** (2021) 720, [[2007.01554](#)].
- [273] ATLAS collaboration, G. Aad et al., *Measurement of the production cross-section of a single top quark in association with a W boson at 8 TeV with the ATLAS experiment*, *JHEP* **01** (2016) 064, [[1510.03752](#)].
- [274] ATLAS collaboration, G. Aad et al., *Evidence for single top-quark production in the s-channel in proton-proton collisions at  $\sqrt{s} = 8$  TeV with the ATLAS detector using the Matrix Element Method*, *Phys. Lett. B* **756** (2016) 228–246, [[1511.05980](#)].
- [275] ATLAS collaboration, M. Aaboud et al., *Measurement of top quark pair differential cross-sections in the dilepton channel in pp collisions at  $\sqrt{s} = 7$  and 8 TeV with ATLAS*, *Phys. Rev. D* **94** (2016) 092003, [[1607.07281](#)].
- [276] ATLAS collaboration, G. Aad et al., *Measurements of top-quark pair differential cross-sections in the lepton+jets channel in pp collisions at  $\sqrt{s} = 8$  TeV using the ATLAS detector*, *Eur. Phys. J. C* **76** (2016) 538, [[1511.04716](#)].

- [277] CMS collaboration, V. Khachatryan et al., *Observation of top quark pairs produced in association with a vector boson in pp collisions at  $\sqrt{s} = 8$  TeV*, *JHEP* **01** (2016) 096, [[1510.01131](#)].
- [278] CMS collaboration, V. Khachatryan et al., *Measurements of  $t\bar{t}$  charge asymmetry using dilepton final states in pp collisions at  $\sqrt{s} = 8$  TeV*, *Phys. Lett. B* **760** (2016) 365–386, [[1603.06221](#)].
- [279] CMS collaboration, A. M. Sirunyan et al., *Measurement of the semileptonic  $t\bar{t} + \gamma$  production cross section in pp collisions at  $\sqrt{s} = 8$  TeV*, *JHEP* **10** (2017) 006, [[1706.08128](#)].
- [280] CMS collaboration, V. Khachatryan et al., *Search for s channel single top quark production in pp collisions at  $\sqrt{s} = 7$  and 8 TeV*, *JHEP* **09** (2016) 027, [[1603.02555](#)].
- [281] CMS collaboration, *Single top t-channel differential cross section at 8 TeV*, *CMS-PAS-TOP-14-004* (2014) .
- [282] CMS collaboration, V. Khachatryan et al., *Measurement of the t-channel single-top-quark production cross section and of the  $|V_{tb}|$  CKM matrix element in pp collisions at  $\sqrt{s} = 8$  TeV*, *JHEP* **06** (2014) 090, [[1403.7366](#)].
- [283] CMS collaboration, S. Chatrchyan et al., *Observation of the associated production of a single top quark and a W boson in pp collisions at  $\sqrt{s} = 8$  TeV*, *Phys. Rev. Lett.* **112** (2014) 231802, [[1401.2942](#)].
- [284] CMS collaboration, V. Khachatryan et al., *Measurement of the differential cross section for top quark pair production in pp collisions at  $\sqrt{s} = 8$  TeV*, *Eur. Phys. J. C* **75** (2015) 542, [[1505.04480](#)].
- [285] CMS collaboration, V. Khachatryan et al., *Measurements of the  $t\bar{t}$  production cross section in lepton+jets final states in pp collisions at 8 TeV and ratio of 8 to 7 TeV cross sections*, *Eur. Phys. J. C* **77** (2017) 15, [[1602.09024](#)].
- [286] ATLAS collaboration, M. Aaboud et al., *Measurement of the cross-section for producing a W boson in association with a single top quark in pp collisions at  $\sqrt{s} = 13$  TeV with ATLAS*, *JHEP* **01** (2018) 063, [[1612.07231](#)].
- [287] ATLAS collaboration, M. Aaboud et al., *Measurement of the production cross-section of a single top quark in association with a Z boson in proton–proton collisions at 13 TeV with the ATLAS detector*, *Phys. Lett. B* **780** (2018) 557–577, [[1710.03659](#)].
- [288] ATLAS collaboration, M. Aaboud et al., *Measurement of the inclusive cross-sections of single top-quark and top-antiquark t-channel production in pp collisions at  $\sqrt{s} = 13$  TeV with the ATLAS detector*, *JHEP* **04** (2017) 086, [[1609.03920](#)].
- [289] ATLAS collaboration, *Inclusive and differential measurement of the charge asymmetry in  $t\bar{t}$  events at 13 TeV with the ATLAS detector*, *ATLAS-CONF-2019-026* (7, 2019) .
- [290] ATLAS collaboration, M. Aaboud et al., *Measurement of the  $t\bar{t}Z$  and  $t\bar{t}W$  cross sections in proton-proton collisions at  $\sqrt{s} = 13$  TeV with the ATLAS detector*, *Phys. Rev. D* **99** (2019) 072009, [[1901.03584](#)].

- 
- [291] ATLAS collaboration, G. Aad et al., *Measurements of inclusive and differential cross-sections of combined  $t\bar{t}\gamma$  and  $tW\gamma$  production in the  $e\mu$  channel at 13 TeV with the ATLAS detector*, *JHEP* **09** (2020) 049, [[2007.06946](#)].
- [292] CMS collaboration, A. M. Sirunyan et al., *Measurement of the production cross section for single top quarks in association with W bosons in proton-proton collisions at  $\sqrt{s} = 13$  TeV*, *JHEP* **10** (2018) 117, [[1805.07399](#)].
- [293] CMS collaboration, A. M. Sirunyan et al., *Observation of Single Top Quark Production in Association with a Z Boson in Proton-Proton Collisions at  $\sqrt{s} = 13$  TeV*, *Phys. Rev. Lett.* **122** (2019) 132003, [[1812.05900](#)].
- [294] CMS collaboration, A. M. Sirunyan et al., *Measurement of differential cross sections and charge ratios for t-channel single top quark production in proton-proton collisions at  $\sqrt{s} = 13$  TeV*, *Eur. Phys. J. C* **80** (2020) 370, [[1907.08330](#)].
- [295] CMS collaboration, A. M. Sirunyan et al., *Measurement of the  $t\bar{t}$  production cross section, the top quark mass, and the strong coupling constant using dilepton events in pp collisions at  $\sqrt{s} = 13$  TeV*, *Eur. Phys. J. C* **79** (2019) 368, [[1812.10505](#)].
- [296] CMS collaboration, *Measurement of differential  $t\bar{t}$  production cross sections in the full kinematic range using lepton+jets events from pp collisions at  $\sqrt{s} = 13$  TeV*, *CMS-PAS-TOP-20-001* (2021) .
- [297] CMS collaboration, A. M. Sirunyan et al., *Measurement of the cross section for top quark pair production in association with a W or Z boson in proton-proton collisions at  $\sqrt{s} = 13$  TeV*, *JHEP* **08** (2018) 011, [[1711.02547](#)].
- [298] CMS collaboration, A. M. Sirunyan et al., *Measurement of top quark pair production in association with a Z boson in proton-proton collisions at  $\sqrt{s} = 13$  TeV*, *JHEP* **03** (2020) 056, [[1907.11270](#)].
- [299] CMS collaboration, A. M. Sirunyan et al., *Search for resonant and nonresonant new phenomena in high-mass dilepton final states at  $\sqrt{s} = 13$  TeV*, *JHEP* **07** (2021) 208, [[2103.02708](#)].
- [300] ATLAS collaboration, G. Aad et al., *Search for heavy Higgs bosons decaying into two tau leptons with the ATLAS detector using pp collisions at  $\sqrt{s} = 13$  TeV*, *Phys. Rev. Lett.* **125** (2020) 051801, [[2002.12223](#)].
- [301] LHCb collaboration, R. Aaij et al., *Differential branching fractions and isospin asymmetries of  $B \rightarrow K^{(*)}\mu^+\mu^-$  decays*, *JHEP* **06** (2014) 133, [[1403.8044](#)].
- [302] CMS collaboration, V. Khachatryan et al., *Angular analysis of the decay  $B^0 \rightarrow K^{*0}\mu^+\mu^-$  from pp collisions at  $\sqrt{s} = 8$  TeV*, *Phys. Lett. B* **753** (2016) 424–448, [[1507.08126](#)].
- [303] LHCb collaboration, R. Aaij et al., *Differential branching fraction and angular analysis of  $\Lambda_b^0 \rightarrow \Lambda\mu^+\mu^-$  decays*, *JHEP* **06** (2015) 115, [[1503.07138](#)].
- [304] BABAR collaboration, J. P. Lees et al., *Measurement of the  $B \rightarrow X_s l^+ l^-$  branching fraction and search for direct CP violation from a sum of exclusive final states*, *Phys. Rev. Lett.* **112** (2014) 211802, [[1312.5364](#)].

- [305] A. Greljo, J. Salko, A. Smolkovič and P. Stangl, *Rare  $b$  decays meet high-mass Drell-Yan*, *JHEP* **05** (2023) 087, [[2212.10497](#)].
- [306] M. Misiak and M. Steinhauser, *Weak radiative decays of the  $B$  meson and bounds on  $M_{H^\pm}$  in the Two-Higgs-Doublet Model*, *Eur. Phys. J. C* **77** (2017) 201, [[1702.04571](#)].
- [307] HFLAV collaboration, Y. Amhis et al., *Averages of  $b$ -hadron,  $c$ -hadron, and  $\tau$ -lepton properties as of summer 2014*, [1412.7515](#).
- [308] BABAR collaboration, J. P. Lees et al., *Search for  $B \rightarrow K^{(*)} \nu \bar{\nu}$  and invisible quarkonium decays*, *Phys. Rev. D* **87** (2013) 112005, [[1303.7465](#)].
- [309] BELLE collaboration, D. Dutta et al., *Search for  $B_s^0 \rightarrow \gamma\gamma$  and a measurement of the branching fraction for  $B_s^0 \rightarrow \phi\gamma$* , *Phys. Rev. D* **91** (2015) 011101, [[1411.7771](#)].
- [310] PARTICLE DATA GROUP collaboration, R. L. Workman et al., *Review of Particle Physics*, *PTEP* **2022** (2022) 083C01.
- [311] LHCb collaboration, .  $\rightarrow K + + -$  et al., *Measurement of lepton universality parameters in  $B^+ \rightarrow K^+ \ell^+ \ell^-$  and  $B^0 \rightarrow K^{*0} \ell^+ \ell^-$  decays*, *Phys. Rev. D* **108** (2023) 032002, [[2212.09153](#)].
- [312] HFLAV collaboration, Y. Amhis et al., *Averages of  $b$ -hadron,  $c$ -hadron, and  $\tau$ -lepton properties as of summer 2016*, *Eur. Phys. J. C* **77** (2017) 895, [[1612.07233](#)].
- [313] PARTICLE DATA GROUP collaboration, M. Tanabashi et al., *Review of Particle Physics*, *Phys. Rev. D* **98** (2018) 030001.
- [314] LHCb collaboration, R. Aaij et al., *Measurement of  $CP$ -Averaged Observables in the  $B^0 \rightarrow K^{*0} \mu^+ \mu^-$  Decay*, *Phys. Rev. Lett.* **125** (2020) 011802, [[2003.04831](#)].
- [315] M. J. Dugan and B. Grinstein, *On the vanishing of evanescent operators*, *Phys. Lett. B* **256** (1991) 239–244.
- [316] G. Buchalla, A. J. Buras and M. E. Lautenbacher, *Weak Decays beyond Leading Logarithms*, *Rev. Mod. Phys.* **68** (1996) 1125–1144, [[hep-ph/9512380](#)].
- [317] S. Herrlich and U. Nierste, *Evanescent operators, scheme dependences and double insertions*, *Nucl. Phys. B* **455** (1995) 39–58, [[hep-ph/9412375](#)].
- [318] J. Aebischer, A. J. Buras and J. Kumar, *Simple rules for evanescent operators in one-loop basis transformations*, *Phys. Rev. D* **107** (2023) 075007, [[2202.01225](#)].

## *Acknowledgements*

The acknowledgments have been removed from the electronic publication of this dissertation for privacy reasons.

# Riccardo Bartocci

✉ [rbartocce@uni-mainz.de](mailto:rbartocce@uni-mainz.de)  [Inspire Profile](#)

**Address:** In der Neckarhelle 129, Heidelberg, 69118, Germany

**Nationality:** Italian



## Professional profile

---

I am a final-year PhD candidate and Mainz Physics Academy Fellow at Johannes Gutenberg University Mainz. My research interests lie in Effective Field Theory, Beyond the Standard Model physics, and Flavour Physics. My current work focuses on constraining New Physics through global analyses within the Standard Model Effective Theory and unveiling new phenomena in flavour physics using precision calculations within the Soft-Collinear Effective Theory.

## Education

---

- **PhD in Physics** *Nov 2022 - present*  
**Johannes Gutenberg University (MPA), Mainz, Germany**  
Thesis: “Synergies between Effective Field Theories: Global analyses of the Minimal Flavour Violating SMEFT and subleading NLO analysis of  $b \rightarrow s\gamma$  transitions”
- **Master’s degree in Physics** *Oct 2020 - Sep 2022*  
**University of Padua (Italy) and University of Heidelberg (Germany)**  
Thesis: “Probing LFV on all energy frontiers ”(SMEFT)  
Grade: 110/110 and honors
- **Bachelor’s degree in Physics** *Oct 2017-Sep 2020*  
**University of Padua, Padova (PD), Italy**  
Thesis: “Arithmetic of light: manipulating orbital angular momentum”  
Grade: 110/110 and honors
- **High school Diploma** *July, 2017*  
**Liceo scientifico “Galileo Galilei”, Ancona (AN), Italy**  
Grade: 99/100

## Teaching experience

---

- **Head tutor for “Advanced Quantum Mechanics”** *Winter semester 2024*  
**JGU, Mainz, Germany**  
Tutor, preparation of the exercise sheets, preparation and correction of the exams
- **Tutor for “Theoretical mechanics”** *Summer semester 2023*  
**JGU, Mainz, Germany**  
Tutor

## Administrative experience

---

- **Journal club organiser for the Theoretical High Energy Physics group** *Aug 2023-Oct 2025*  
**Johannes Gutenberg University, Mainz, Germany**

## Awards

---

- **Mainz Physics Academy (MPA) fellowship** *November, 2022*  
**JGU Mainz, Germany**  
PhD fellowship of the Cluster of Excellence PRISMA+
- **Erasmus+ scholarship** *Summer semester, 2021*  
**University of Padua (PD), Italy**  
One semester at University of Heidelberg (Germany)
- **Scholarship “Le mille e una lode”** *Summer semester, 2020*  
**University of Padua (PD), Italy**  
Within the best 3% of all students

## Conferences and talks

---

- **EPS-HEP conference** *July, 2025*  
**Marseille, France**  
NLO analysis of the  $Q_1 - Q_7$  interference in  $\bar{B} \rightarrow X_s \gamma$  at subleading power
- **EPS-HEP conference** *July, 2025*  
**Marseille, France**  
RGE effects on SMEFT global analyses
- **Workshop “Flavour for New Physics at Present and Future Colliders”** *June, 2025*  
**MITP, Mainz, Germany**  
SMEFT Global Analyses at the Energy Frontier: LHC and Beyond
- **HEFT 2025 Workshop** *June, 2025*  
**CERN, Switzerland**  
SMEFT Global Analyses at the Energy Frontier: LHC and Beyond
- **SMEFT-Tools 2025 Workshop** *January, 2025*  
**Mainz, Germany**  
NLO and RGE effects on SMEFT global analyses
- **Heidelberg theory group seminar (invited)** *January, 2025*  
**Heidelberg, Germany**  
SMEFT Global Analyses: NLO contributions, RGE Effects, and the Role of Flavour Physics
- **DISCRETE 2024** *December, 2024*  
**Ljubljana, Slovenia**  
SMEFT Global Analyses: NLO contributions, RGE Effects, and the Role of Flavour Physics
- **YOUNGST@RS - EFTs and Beyond** *December, 2024*  
**MITP, Mainz, Germany**  
SMEFT Global Analyses: NLO contributions, RGE Effects, and the Role of Flavour Physics
- **Particle Seminar (invited)** *October, 2024*  
**Radboud university, Nijmegen, Netherlands**  
SMEFT Global Analyses: NLO contributions, RGE Effects, and the Role of Flavour Physics
- **Workshop “New Physics Directions in the LHC era and beyond”** *April, 2024*  
**Max Planck Institute, Heidelberg, Germany**  
Global analysis of the *minimal* MFV SMEFT

- **Conference “Les Rencontres des Moriond” (invited)** *March, 2024*  
**La Thuile, Italy**  
 Global analysis of the *minimal* MFV SMEFT
- **MPA summer school** *August, 2023*  
**Chiemsee, Germany**  
 Global fit of the  $U(3)^5$  symmetric SMEFT

## Summer schools

---

- **Particle Physics Phenomenology after the Higgs Discover** *October, 2024*  
**Bingen, Germany**
- **CERN-FERMILAB summer school** *August, 2023*  
**CERN, Switzerland**
- **MPA summer school** *August, 2023*  
**Chiemsee, Germany**

## Competences and skills

---

- **Attended soft-skills workshops:** Presentation for the Virtual Stage, Scientific Publishing: Editor, Referee and Author responsibilities, Tutoring tutor (Training for teaching), Scientific writing.
- **Software:** MATHEMATICA (FEYN CALC, DSIX TOOLS, CODEX, FIRE, X), MADGRAPH (WITH PYTHIA AND RIVET), MATLAB, PYTHON, L<sup>A</sup>T<sub>E</sub>X, C++, MICROSOFT OFFICE.
- **Languages:** Italian (native), English (Professional proficiency/C1), German (Upper-intermediate proficiency/B2).

## Publications

---

- **“A global analysis of the SMEFT under the minimal MFV assumption”**  
**JGU, Mainz, Germany**  
 Published in JHEP 05 (2024) 07, Authors: Riccardo Bartocci, Anke Biekötter, Tobias Hurth
- **“Renormalisation group evolution of the shape function  $g_{17}$  in  $\bar{B} \rightarrow X_s \gamma$  and  $\bar{B} \rightarrow X_s \ell^+ \ell^-$  at subleading power”**  
**JGU, Mainz, Germany**  
 Published in JHEP 04 (2025) 066, Authors: Riccardo Bartocci, Philipp Böer, Tobias Hurth
- **“Renormalisation group evolution effects on global SMEFT analyses”**  
**JGU, Mainz, Germany**  
 Published in JHEP 05 (2025) 203, Authors: Riccardo Bartocci, Anke Biekötter, Tobias Hurth
- **“Global analysis of the  $U(3)^5$  symmetric SMEFT”**  
**JGU, Mainz, Germany**  
 Contribution to Moriond EW 2024, Author: Riccardo Bartocci
- **“Impact of NLO contributions and RGE effects on SMEFT global analyses”**  
**JGU, Mainz, Germany**  
 Published in Proceeding of Science (DISCRETE 2024)

- “NLO analysis of the subleading-power  $Q_1 - Q_{7\gamma}$  interference in  $\bar{B} \rightarrow X_s \gamma$  at large photon energies”

JGU, Mainz, Germany

Submitted to Proceeding of Science (EPS-HEP 2025)

